UNIVERSITÉ DE SHERBROOKE
Faculté de génie
Département de génie mécanique

Une approche systématique basée sur le pincement thermique pour une intégration optimale des sources intermittentes d'énergie renouvelable et résiduelle dans les bâtiments

A systematic thermal pinch-based approach for optimum integration of intermittent sources of renewable and waste energy in buildings

Thèse de doctorat
Spécialité: Génie Mécanique

SEYED MOJTABA HOSSEINNIA

Sherbrooke (Québec) Canada

juin 2022

MEMBRE DU JURY

Prof. Mikhail Sorin
Directeur

Prof. Dahai Qi
Rapporteur

Prof. Bernard Marcos
Évaluateur

Dr. Hervé Nouanegue
Évaluateur

RÉSUMÉ

Le secteur du bâtiment consomme une grande partie de l'énergie produite dans un pays et, par conséquent, il est responsable d'une grande quantité correspondante d'émissions de gaz à effet de serre dans l'atmosphère et du problème du réchauffement climatique. Au cours des dernières décennies, des efforts ont été déployés pour remplacer en partie l'énergie nécessaire au les charges de chauffage/refroidissement/eau chaude sanitaire dans les bâtiments par des sources d'énergie renouvelables, des sources de déchets disponibles et des pompes à chaleur. Cependant, une approche systématique capable de satisfaire toutes les charges mentionnées et d'assurer la récupération de chaleur interne maximale fait toujours défaut. De plus, il n'y a pas d'approche systématique pour le dimensionnement des équipements tels que la surface des panneaux solaires, la capacité d'une pompe à chaleur, la charge et la taille/configuration des échangeurs de chaleur au sol (GHE), etc. pour les bâtiments.

L'analyse par pincement est une technique d'intégration de chaleur bien connue qui a été utilisée pour la récupération de chaleur dans de grandes installations industrielles, principalement pour des processus en régime permanent. De plus, cette approche a été adoptée pour couvrir les processus batch, lorsque les flux chaud/froid avec des charges constantes représentent un comportement marche/arrêt pendant le temps batch. Néanmoins, les charges (c'est-à-dire les flux chauds/froids, y compris les sources renouvelables et les déchets) dans un bâtiment sont très dynamiques et dépendent du temps et les modèles de moyenne temporelle ou de tranches de temps actuellement disponibles ne peuvent pas gérer le dynamisme de charge mentionné. De plus, l'inadéquation temporelle entre les sources disponibles et les demandes nécessite l'intégration d'un ou plusieurs stockages d'énergie (par exemple, stockage d'énergie thermique/électrique).

L'objectif de cette thèse est de développer un modèle basé sur le pincement thermique pour inclure systématiquement la nature intermittente des sources d'énergie renouvelables et résiduelles dans les bâtiments. Par conséquent, dans cette thèse, une approche de pincement systématique est développée qui peut inclure toutes les charges dynamiques du bâtiment dans la récupération de chaleur et convertir le problème de dimensionnement des équipements en adéquation entre les flux chaud/froid. Dans ce contexte et au début, le modèle de tranche de temps disponible, qui a été essentiellement développé pour l'intégration thermique des processus industriels par lots, est adapté pour inclure les charges dynamiques d'un bâtiment via la chaleur directe et indirecte (via un stockage d'énergie thermique (TES)). récupération. Dans l'étape suivante, l'approche de pincement dynamique est proposée sur la base de l'approche de pincement originale. Le modèle de tranche de temps adapté et l'approche de pincement dynamique sont appliqués à un bâtiment d'essai multifamilial à Granby, au Québec. Comme la

récupération maximale de chaleur est garantie en appliquant les approches basées sur le pincement, le réseau extrait d'échangeurs de chaleur + TES + énergies renouvelables + pompe à chaleur + etc. passe la première couche d'une conception optimale à chaque jour parmi 365 jours dans une année. Cependant, un bâtiment n'a besoin que d'un réseau de travail de l'équipement mentionné. Par conséquent, l'analyse économique basée sur le coût annuel total (TAC) de chaque conception optimale quotidienne ouvre la voie à la deuxième couche d'optimisation. La conception avec le TAC minimum (c'est-à-dire en tant que fonction objectif) est sélectionnée comme réseau optimal final. Il convient de mentionner que l'approche par pincement est une méthode basée sur la thermodynamique. Par conséquent, elle ne peut pas voir les pertes d'énergie liées au transfert de chaleur dans les réservoirs de stockage d'énergie thermique stratifiés. En outre, l'approche de pincement proposée peut définir la charge minimale pour les GHE verticaux, cependant, elle ne peut pas aider à trouver la profondeur/configuration des GHE verticaux. Ainsi, la méthode de dynamique des fluides computationnelle est utilisée pour analyser avec précision les performances thermiques des réservoirs TES à eau stratifiée et des GHE verticaux. Les résultats de l'étude révèlent que le potentiel d'économie d'énergie pour la conception optimale du bâtiment d'essai peut réduire l'utilité chaude requise jusqu'à 70 %. De plus, la profondeur optimale des GHE est de 200 m avec la conception optimale quotidienne de mars et le coût moyen de l'électricité au Canada.

Mots clés: Analyse du pincement, Charges dynamiques, Énergie renouvelable, Stockage d'énergie thermique stratifié, Coût annuel total

ABSTRACT

Building sector consumes a large portion of produced energy in a country and, consequently, it is responsible for a corresponding large amount of greenhouse gas emissions into the atmosphere and the global warming issue. There have been efforts to partly replace the required energy for heating/cooling/domestic hot water loads in buildings by renewable sources of energy, available waste sources, and heat pumping in recent decades. However, a systematic approach that can satisfy all the mentioned loads and ensure the maximum internal heat recovery is still missing. Additionally, there is no systematic approach for sizing the equipment such as area of solar panels, the capacity of a heat pump, the load and size/configuration of ground heat exchangers (GHEs), etc. for buildings.

Pinch analysis is a well-known heat integration technique which has been utilized for heat recovery in large industrial plants, mostly for steady state processes. Furthermore, this approach has been adopted to cover the batch processes, when hot/cold streams with constant loads represent an on/off behavior during the batch time. Nonetheless, the loads (i.e., hot/cold streams, including renewable and waste sources) in a building are highly dynamic and time dependent and the current available time average or time-slice models cannot handle the mentioned load dynamism. Furthermore, the time mismatch among the available sources and the demands requires integration of one or several energy storages (e.g., thermal/electrical energy storage).

The objective of this thesis is to develop a thermal pinch-based model to systematically include the intermittent nature of renewable and waste energy sources in buildings. Therefore, in this thesis, a systematic pinch approach is developed that can include all building's dynamic loads in the heat recovery and convert the problem of equipment sizing into the matching between hot/cold streams. In this context and in the beginning, the available time slice model, which were basically developed for industrial batch processes heat integration, is adapted to include the dynamic loads of a building via direct and indirect (through a thermal energy storage (TES)) heat recovery. In the next step, the dynamic pinch approach is proposed based on the original pinch approach. Both adapted time slice model and dynamic pinch approach are applied to a multifamily test building in Granby, Quebec. As the maximum heat recovery is guaranteed by applying the pinch-based approaches, the extracted network of heat exchangers + TESs + renewable energies + heat pump + etc. is passed the first layer of an optimum design at each day among 365 days in a year. However, one building just needs one working network of the mentioned equipment. Therefore, the economic analysis based on the total annual cost (TAC) of each daily optimum design paves the way for the second layer of optimization. The design with the minimum TAC (i.e., as the objective function) is selected as the final optimum network. It worth mentioning that the pinch approach is a thermodynamic based method. Therefore, it

cannot see the heat transfer related energy losses in stratified thermal energy storage tanks. Also, the proposed pinch approach can set the minimum load for vertical GHEs, however, it cannot help on finding the depth/configuration of the vertical GHEs. Thus, computational fluid dynamic method is utilized to accurately analyse the thermal performance of the stratified water TES tanks and the vertical GHEs. The results of the study reveal that the energy saving potential for the optimum design for the test building can reduce the required hot utility up to 70 percent. Additionally, the optimum depth of GHEs is 200 m with the daily optimum design of March and the Canadian average electricity cost.

Keywords: Pinch analysis, Dynamic loads, Renewable energy, Stratified thermal energy storage, Total annual cost

ACKNOWLEDGMENTS

I would like to thank my supervisor, professor Mikhail Sorin, for all his support and considerations throughout the journey of this PhD program.

TABLE OF CONTENT

List of figures

List of Tables

Chapter 1: Introduction

1.1 Motivation

Residential buildings are responsible for around 40% of total consumed energy in a country [1]. A significant part of this energy consumption, i.e., 72%, is for heating, ventilation, and air conditioning (HVAC) systems [2]. This can be further narrowed down to more than 90 percent of the required energy for HVAC as for heating section in high latitude countries [3] such as Canada. Thus, building sector is responsible for a huge amount of greenhouse gas emission into the atmosphere and the global warming issue. Introducing renewable energies, alone or in combination with other available technologies such as heat pumping and drain or wastewater heat recovery, e.g., using gray water energy, are two main ways for reducing building energy usage.

Renewable energies such as solar or ground source have been proven to be effective in reducing house dependency on grid electricity supply, and consequently, reducing greenhouse gas emissions [4]. However, renewable energies have an intermittent nature. Solar energy, as an example, varies during a day based on some predictable variables such as building location, the considered day in a year, exact solar zenith angle in the given day time, solar collector's area/orientation, etc., and some unpredictable variables such as sky clearness factor, wind speed and outdoor temperature, etc. Regarding the ground source energy, the undisturbed temperature, deep enough in the ground, defines the practicality of the ground source in applications such as ground source heat pumping [5]. However, the ground source cannot survive long-term energy extraction during winter months. Adding a thermal energy storage can alleviate the intermittent nature of the solar energy. Also turning the ground into a solid thermal energy storage by charging it during summer and retrieving the stored energy during winter can ensure the sustainable integrating of the ground source into building energy system.

There can be found numerous studies in the open literature on integrating renewable energies into building. However, there are still basic questions about sizing the main components such as solar panel area, heat pump capacity, ground source load, etc. In other words, there is no systematic approach that can include all the available sources/sinks of energy involved in the building, included but not limited to renewable and waste sources, in the sizing of equipment or the optimum final design.

1.2 Objectives

Buildings can be assumed as energy systems, although strongly dynamic ones. Therefore, heat integration principles can be applied to them. One example of the heat integration technique is Pinch analysis [3] that successfully predicts the maximum possible heat recovery values for steady-state industrial processes via direct heat exchange by identifying and extracting hot/cold streams [6]. Pinch well-established guidelines help in designing heat exchanger network to achieve the predicted maximum heat recovery, resulting in an optimum hot utility utilization, consequently, reducing the GHG emissions. However, regarding the time dependent hot/cold streams, there are a few pinch-based models that demonstrate opportunities for modifications/improvements of heat exchanger networks coupled with heat storage (HX+TES). Some of them such as time slice model [7,8] or time pinch analysis [9,10] have been developed for industrial batch processes rather than for buildings.

What is the optimum interconnection (a network structure) between solar panels, thermal energy storage(s), heat pump and a Heat Exchanger Network (including the vertical ground heat exchanger) within a building and in a daily base load analysis that minimizes the overall building's energy consumption? Answer to this question is the main objective of this PhD research. The proposed approach is based on intermittent pinch analysis in order to systematically target and design the optimum HX (GHE) + TES + Solar Panel networks. The final optimum design should have the minimum total annual cost from the economic perspective. Furthermore, hydrodynamic modeling of stratified thermal energy storage tanks and vertical ground heat exchangers that considers the detail thermal performance (heat loss to ambient, thermocline thickness, working fluid properties, etc.) are developed in order to validate a preliminary design prompted by the proposed pinch analysis. Moreover, its application contributes to a detailed and robust design of the full network.

1.3 Thesis outline

This doctoral dissertation contains nine chapters. The state-of-the-art in heat integration techniques and the scientific gaps in the literature are presented in chapter two. The application of the adapted time slice model pinch analysis for just one day (a worst-case scenario in the winter) and the integration of a stratified water thermal energy storage tank into the energy system of a building equipped with solar thermal collectors, heat pumping, and gray water heat recovery are depicted in chapter three. The adapted pinch model delivers the ideal minimum volume of the TES units, where the thermocline thickness and the effects of charging/discharging diffuser types are missing. Hence, to better understand the thermal performance of the proposed stratified thermal energy storage units in the heat exchanger network, a computational fluid dynamic approach is performed that can evaluate the thermal performance of the stratified TES unit. The results are illustrated in chapter four. Further,

dynamic pinch analysis concept and its application as a robust framework for sizing the optimum network of TES+ Solar panel + GHE + HP in a residential building, especially for zero energy building, are depicted in chapter five. To shed light on the configuration of the vertical GHEs that are capable to deliver the predicted minimum ground load (i.e., predicted by the dynamic pinch analysis in chapter five) of a solar assisted ground source heat pump system, a three-dimensional CFD approach is performed and presented in chapter six. By calculating the exact size of the vertical GHEs in chapter six, chapter seven is devoted to the total annual cost economic analysis for the full network of equipment presented in chapter five. Energy targeting based on the dynamic pinch approach for a photovoltaic + thermal (PVT) solar panels in the ground source heat pumping system is presented in chapter eight. Finally, the conclusion and some suggestions for the future works are presented in chapter nine.

Chapter 2: State of the art

In this chapter, the basic pinch concept is provided. The challenges of applying this heat integration approach to time-dependent streams such as buildings' loads, and renewable energies are followed. Finally, the scientific gaps in the literature are explicitly presented. As the following chapters (i.e., chapter three to eight) have their own introduction and literature review section, the material presented in this chapter is concentrated on the main idea and on the entire perspective.

2.1 Pinch analysis, basic concept

Saving energy is one of the essential strategies for sustainable development, and the residential sector plays a prominent role in promoting energy conservation [11]. The residential sector accounts for nearly 15% of global final energy consumption, which results in nearly 27% of global CO_2 emissions [12]. Therefore, the reduction of energy consumption as well as the utilization of renewable energies within residential buildings can make an important contribution to addressing energy resource shortages and environmental issues.

Since the mid-1970s, heat integration techniques have received much research attention because of their ability to reduce the total energy requirement of the system [13]. These techniques continue to evolve from well-established methods that are highly valuable in dealing with steady-state processes in large industries such as crude oil refineries [14] and power plants [15], to include non-steady or batch processes in intermittently available streams in multipurpose batch plants [16] and, more recently, in residential buildings [17,18]. Among all heat integration techniques, the pinch methodology is the most practical and wide widespread analysis strategy, which guarantees maximum heat recovery within thermal systems by using several systematic thermodynamics-based steps [19,20]. Recently, it was shown that the application of pinch analysis to a residential building can lead to up to a 50% reduction in primary energy consumption [17]. Pinch analysis is relatively straightforward for steady-state processes, where the temperature is the only constraint in the procedure of determining the theoretical minimal energy requirements of a system, called "energy targeting" [21]. The application of pinch analysis for a system like a residential building is difficult due to the time-dependent behavior of the thermal streams, such as waste heat and solar thermal energy. In this case, time is another constraint, and there is a need for thermal energy storage (TES) units to accumulate available energy from available hot streams, hold the energy effectively, and release it at another time to

cold streams. Thus, an effective pinch analysis must be able to consider the dynamic behavior of the streams and identify the optimal specifications of TES units, including their number, volumes, and temperatures.

Systematic pinch approaches have been developed for calculating the energy targets, HSUs characteristics, and heat exchangers conductance in batch processes through several models, namely: the time average model (TAM) [22,23], the time slice model (TSM) [24–26], and time pinch analysis (TPA) [27]. Each approach provides a systematic methodology in batch-process heat integration. However, it should be emphasized that in almost all examples regarding batch processes in the open literature, during the presence of the streams for the batch period, the operating specifications of hot/cold streams are assumed constant: supply and target temperatures, mass flow rates, and specific heat capacities.

The TAM is the simplest approach and the backbone of a large portion of the studies conducted for energy targeting in batch processes and renewable energy integration [28,29]. Each variable stream load is converted into an average value by dividing the cumulative stream load by the batch period. Therefore, the time constraint is neglected, and the problem is approximated as a steady-state process, where the original pinch analysis, i.e., cascade analysis, can be applied to set the energy targets as well as determine the TES units characteristics and the heat exchangers conductances. The application of this model to highly dynamic streams such as solar thermal energy and waste heat integration in buildings [17] leads to an imprecise prediction of the energy targets and TES volumes. The intermittency and time-dependency characteristics of solar irradiation are fundamental aspects of solar thermal energy [30]. Thus, although the expected load from solar thermal collectors (STCs) is highly time-dependent, the TAM converts it to a constant value. The TAM defines an upper bound of heat recovery that a system can achieve by ignoring the time constraint [31].

The TAM has been improved to integrate TES units into batch processes. Olsen et al. [29] presented a systematic TAM pinch approach for TES integration in an energy system for full indirect heat recovery. In order to set the priorities among different streams, they introduced the concept of the indirect source/sink profile (ISSP), which defines the temperature shifting based on each stream's heat transfer coefficient and duration. The maximum and minimum temperatures for a pair of fixed-temperature variable-mass TESs or a stratified TES unit can be defined by an ISSP line and some degrees of freedom, and by some heuristic and engineering considerations. Recently, Abdelouadoud et al. [22] proposed the same systematic graphical approach based on the TAM for TES integration, which was earlier presented in [29,32], with some modifications. In their graphical model, they defined the aforementioned ISSP curve and added steps for defining restricted zones, extended zones, and a degree of freedom in selecting the temperature range for the assigned heat recovery amount. Additionally, the volume of TES

units and their types can be selected in this graphical approach. However, this model still has the oversimplification inherited from the TAM that makes it unsuitable for energy targeting for a system working with dynamic streams, such as heating loads in buildings or heat transfer fluids for solar energy applications.

The TPA proposed by Wang and Smith [27] is another approach to pinch analysis in HSU-integrated systems. In TPA, energy and time can be seen on the vertical and horizontal axis respectively, instead of temperature and enthalpy in the TSM. In other words, the hot/cold and grand composite curves show the time and energy at each temperature interval. This method can be very complex if several hot or cold streams exist in more than one temperature interval. In this particular case, the number of TES units can be as high as the number of temperature intervals, which may not be equivalent to the minimum number of TES units. Furthermore, since the heat transfer between external hot streams and the intermediate medium (the working fluid that stores thermal energy in the TES units) and the heat transfer between intermediate medium and external cold streams occur within the same temperature interval, double the minimum temperature difference between hot and cold streams must imposed, otherwise temperature difference penalties must be paid by using hot or cold utility. In this context, a "temperature penalty" means that the intended temperature difference will not be achieved, and the actual system performance will suffer. The TPA does not consider the resultant temperature difference penalties that will occur, due to the neglection of doubling the minimum temperature difference.

The TSM proposed by Kemp [33] was originally developed for batch processes. In this model, the conventional pinch analysis is applied to several specified time slices (TSs) defined based on the start and stop times of each stream (stream schedule or Gantt chart). In contrast to the TAM, the TSM has the advantage of including dynamic loads, such as hot water and heating in a residential building as well as the time-dependent use of solar energy [24]. However, finding the appropriate temperature for the TES units can be highly complex based on this model [31]. Another shortcoming of this model is that it neglects the fact that storing energy from hot streams into an intermediate storage medium and extracting it by cold streams within the same temperature interval not feasible, due to the minimum temperature difference constraints for charging and discharging processes. Another problem with the TSM presented in [33] is that it is not clear how to find an appropriate time slice duration for a system with highly dynamic loads, such as solar thermal collector duty [34]. The slice duration in the TSM must be selected in an appropriate way for a dynamic load, such that the heat recovery system is able to efficiently benefit from the short-terms minimum and maximum values of the changing steam loads (i.e., capture the extreme values, max. or min.) during a batch period.

Another important design consideration in batch process heat integration is the selection of the heat transfer configuration: direct heat exchange between time co-existing streams [35], indirect heat exchange by means of a TES unit [36], or a mixed approach [37]. In this choice, the economic profitability of each configuration option, among direct/indirect/mixed heat recovery, plays an important role. For instance, it was shown that the total annual cost for an industrial case study [32] with a mixed direct/indirect heat recovery was only 4% higher than that of purely direct heat exchange, and 18% lower in comparison to the purely indirect heat exchange. Moreover, the heat recovery configuration strongly influences the required volume of the TES units.

2.2 Buildings energy system specifications

Residential buildings need energy to provide heating (both space heating and domestic hot water) and space cooling. Every building has its own thermal characteristics such as form, structural materials, window to wall ratio, etc. However, the thermal comfort condition for the residents is the same. In other words, a building can be assumed as an energy system with some hot and cold streams. Moreover, renewable energy such as solar (in both thermal and electric form) and ground source can be combined with a heat pump system to reduce the dependency of the building energy use to external sources such as fossil fuel or grid line. There are some challenges regarding applying the described pinch integration technique on the buildings which are explained in the following sections.

2.2.1 Dynamic load

As mentioned earlier, the indoor condition of a building has to be maintained in a certain range of temperature and relative humidity for human thermal comfort. Nonetheless, the outdoor condition, i.e., mainly temperature and solar irradiance, changes with time during 0 to 24 hours of one day and 0 to 365 days of one year. Therefore, the heat loss/gain during one day is a time dependent variable. Moreover, the domestic hot water load is different based on residents' usage pattern/habits and city water temperature [38,39]. To conclude, both supply and target temperature of a water stream (for heating/colling/hot water) and the load amount can vary with time.

2.2.2 Renewable and waste sources of energy

Application of renewable energy such as wind, solar, and ground sources in buildings have been iterated in recent decade [40–42]. However, intermittency is the most important characteristics of renewable energies. In other words, there might be some time during a day that the energy produced by the renewable sources is more than what is needed in the building. Therefore, the extra energy should be stored in a storage system. This is called the indirect heat recovery. Furthermore, the energy from the used hot water, i.e., gray water or waste energy, can be

recovered by drain water heat recovery system [43–45]. Sizing the required area for the mentioned heat exchangers is not a trivial task. The main reason is the time dependency of the loads.

2.2.3 Heat pumping

According to the coefficient of performance (COP), a heat pump system can deliver an output energy by multiplying the input energy with the COP. Therefore, heat pumping has found its way into residential buildings [46]. Furthermore, if the heating application is considered, the evaporator load can be satisfied by several options such as gray water [47] and/or ground source [48]. It should be mentioned that the maximum pressure ratio (or temperature lift), the maximum temperature of the cycle, and the superheat energy of the refrigerant exiting the compressor are important design parameters. Additionally, the capacity of the heat pump can be selected based on different scenarios. There is still no systematic approach for sizing the heat pump capacity for a given building.

2.2.4 Thermal energy storage

Among available storage systems, sensible stratified thermal energy storage has been found their way into different applications ranging from domestic hot water storage in small scale in residential buildings [38,49,50] to high temperature molten salt storage in concentrated solar power plants [51–54].

The stratification condition occurs in liquid-sensible heat storage systems. The hot liquid tends upwards to the top of the storage due to the buoyancy force and the colder liquid stays below. Therefore, there is a gradient between the hot top and the cold bottom zones. If this temperature gradient zone is large and smooth, there will be a need for a higher storage volume to compensate for the lost volume due to stratification. On the other hand, if the mentioned gradient zone is small and steep, the required storage volume reads the value as predicted by thermodynamics. The sharp gradient area has been called thermocline zone. Presence of a small thermocline in a TES illustrates the important fact that there is very little mixing inside TES tank. Hence, a storage tank with a smaller thermocline thickness (TLT) has a higher thermal performance.

The available energy for storage in a tank is usually calculated based on thermodynamics and heat integration techniques such as pinch analysis [55,56]. This computed value for storage cannot include heat transfer effects such as mixing and thermocline (introduced by diffusion inside the tank). Therefore, there is a need to add some extra volume to the predicted one obtained based on thermodynamics analysis.

Fluid flow and heat transfer inside a stratified TES has been a subject of research interests. There is a good number of experimental studies which provide insights into the heat transfer performance of a stratified TES tank. Detailed review can be found in Chanrda and Matuska study [57]. Additionally, large size underground pit TES has been both experimentally and numerically studied in [58]. Computational fluid dynamic (CFD) studies are among the powerful tools which have been utilized to monitor, predict, and investigate different aspect of a stratified TES. Studies performed by Savicki et al. [59], Abdelhak et al. [60], Chandra and Matuska [61] are just some examples of full three-dimensional domestic hot water tank numerical studies. As an example, Chandra and Matuska used Ansys-Fluent software for their simulation. Full 3D Navier-Stokes equations have been solved inside a cylindrical TES tank with water as the heat transfer fluid. Effects of turbulence, diffuser or distributor types, and temperature profiles by considering variable thermophysical properties have been reported in their investigation. However, this type of detailed simulations required a good amount of computational time and equipment, as mentioned in their study [61].

Although water is the most utilized heat transfer fluid for sensible TES due to being cheap, its availability, having very good storage characteristics (high cp, low viscosity, etc.), it has limitations in storage at high temperatures, i.e., more than its boiling point. For storing energy at high temperatures, there are thermal oil, molten salt and ionic liquids as heat transfer fluids [62–67]. In all cases with thermal oil and molten salt, the main need for using these types of storage media is the high temperature of the heating source. Similar to the water tank, in high temperature stratified TES, the main goal is to maintain the stratification at highest possible degree. This fact shows the importance of thermal performance of a TES during charging/discharging process.

2.3 Scientific gaps in the literature

Based on the literature review presented in this chapter, the main scientific gaps in the literature can be listed as:

- The available pinch approaches are not suitable for heat integration and energy recovery within an energy system with time dependent characteristics. Therefore, this point is addressed in chapters three, five, seven, and eight.
- The available pinch approaches do not provide any priority regarding the direct/indirect heat recovery. It is tried to explain the effects of direct/indirect heat recovery in chapter three, by adding certain rules in heat recovery priority.
- The available pinch approaches cannot include the heat loss and presence of thermocline in the stratified TES tanks. This is the reason to include detail numerical analysis (i.e.,

CFD method) for evaluating the thermal performance of TES units and GHEs. The results are presented in chapters four and six.

- Sizing of equipment such as solar panels, heat pumps, ground heat exchangers, etc. for the maximum heat recovery is missing in the literature. As indicated earlier, several optimum networks of equipment (all extracted from the proposed pinch approach) can be found based on the maximum heat recovery concept. However, to select one final design, a techno-economic approach is presented in chapter seven.

Table 2-1 represents the gaps and the corresponding chapter that addresses it in the following chapters.

Table 2-1 Scientific gaps in the literature for sizing components for renewable/waste sources integration in buildings, corresponding chapters that fill the gap

Gap in the literature	Chapter(s) in this thesis
No pinch approach can deal with the time dependent loads/streams	3, 5, 8
Optimum sizing of the stratified TES units	3
thermocline thickness quantification and its evaluation according to the heat recovery concept	4
Definition for thermal performance of vertical GHEs, sizing based on the extracted load from the proposed dynamic pinch approach	6
Yearly optimum network of equipment based on the MHR concept for buildings	7

Chapter 3: A systematic pinch approach to integrate stratified thermal energy storage in buildings

Avant-propos

Auteurs et affiliation:

Seyed Mojtaba Hosseinnia: étudiant au doctorat, faculté de génie, département de génie mécanique, Université de Sherbrooke.

Mikhail Sorin: professeur, faculté de génie, département de génie mécanique, Université de Sherbrooke.

Date d'acception: 09 août 2020

État de l'acceptation: version finale publiée, 232 (2021) 110663

Revue: International Journal of Energy and Buildings

Titre français: Une approche systématique par pincement pour intégrer le stockage stratifié d'énergie thermique dans les bâtiments

Contribution au document: L'intégration du concept de stockage d'énergie thermique stratifié dans les bâtiments sur la base du modèle de tranche de temps adapté est présentée dans cet article

Résumé français:
Dans cette étude, des flux dynamiques comprenant le chauffage des locaux, l'eau chaude sanitaire, l'énergie solaire thermique renouvelable et la chaleur résiduelle telle que les eaux grises sont extraits d'un bâtiment multifamilial typique dans des conditions hivernales extrêmes pendant une journée ou 24 heures. La récupération de chaleur maximale (MHR) est ciblée par un modèle de tranche de temps (TSM) adapté d'analyse de pincement. Les tranches de temps sont sélectionnées de telle sorte que tous les changements dans les débits de capacité thermique dynamique puissent être inclus dans l'analyse de pincement. De plus, les flux de charge et de décharge du stockage d'énergie thermique (TES) sont calculés sur la base de l'approche graphique TSM adaptée. L'intégration d'un système de pompe à chaleur, d'eaux grises et de capteurs solaires thermiques par le biais d'une récupération de chaleur mixte directe/indirecte

(c'est-à-dire via TES) peut réduire jusqu'à 72 % l'utilisation des services publics d'eau chaude dans le cas étudié. Un échangeur de chaleur (HE) et un réseau TES appropriés sont proposés pour le bâtiment d'essai afin de bénéficier de cette ressource sous-utilisée. De plus, le comportement thermique dynamique du TES stratifié proposé est étudié numériquement. Les résultats révèlent que la combinaison de la perte de chaleur et de l'épaisseur de la thermocline peut réduire la récupération de chaleur du réservoir TES de 10 %, soit 2 % du MHR dans le bâtiment d'essai.

Mots-clés : Bâtiments, Analyse du pincement, Réservoir stratifié, Modèle de tranche de temps, Stockage d'énergie thermique

3.1 Abstract

In this study, dynamic streams including space heating, domestic hot water, renewable solar thermal energy, and waste heat such as gray water are extracted from a typical multi-family building under extreme winter conditions for one day or 24 hours. The maximum heat recovery (MHR) is targeted through an adapted time slice model (TSM) of pinch analysis. Time slices are selected such that all changes in dynamic heat capacity flow rates can be included in the pinch analysis. Moreover, charging and discharging streams of the thermal energy storage (TES) is calculated based on the adapted TSM graphical approach. The integration of a heat pumping system, gray water, and solar thermal collectors through mixed direct/indirect heat recovery (i.e., via TES) can reduce hot utility usage in the studied case by as much as 72 percent. An appropriate heat exchanger (HE) and TES network is proposed for the test building to benefit from this underutilized resource. Additionally, the dynamic thermal behavior of the proposed stratified TES is numerically investigated. The results reveal that combined heat loss and thermocline thickness can reduce the heat recovery from TES tank by 10 percent, which is 2 percent of MHR in the test building.

Keywords: Buildings, Pinch analysis, Stratified tank, Time Slice Model, Thermal energy storage

3.2 Introduction

Energy consumption in buildings is responsible for a significant portion of the total energy consumption in a country. Space heating/cooling, through various hydronic or air systems, and domestic hot water load are the main energy demands in a building, representing roughly 75 percent [68] of the building’s energy requirements. There are components and methods to improve energy efficiency in buildings, such as energy-efficient bulbs, installing light sensors, and regulating heating with programmable thermostats. There has also been some progress in incorporating waste heat, e.g., gray water [44,47], and renewable energies into the energy

balance of buildings, including solar [41,69], wind [40,70,71], and geothermal [72,73] sources. Solar energy, like other types of renewable energy, has an unsteady and intermittent nature due to several factors, such as outdoor temperature, sky clearness, orientation and location of solar panels, seasons, etc. This variable source of energy should ideally be accumulated in a storage system, to be used when needed. Thermal energy storage (TES) units have been designed to store solar thermal energy for large complex buildings [74,75]. It is still an open question as to how TES units should be optimally dimensioned and what level of thermal performance can be expected when they are part of a building energy system.

When an energy system and its optimization is being discussed, the application of pinch analysis, especially in large industries, comes to mind [6,76,77]. Pinch analysis is a mature method of heat integration used in large petrochemical, refinery, and power plants, where all streams are assumed to be in steady state. The pinch technology has been advanced to include the unsteady state process as well. In general, there are two main approaches that link both pinch analysis and TES size determination: graphical approach [55,56,78–80] and mathematical approach [81–83]. The latter is out of context of this study and readers are referred to [83] for more details. The graphical model uses hot/cold composite curves to determine the maximum possible heat recovery. The simplest approach in dealing with unsteady hot/cold streams is to neglect the time dependency of the streams and taking average over the time. This method is called time average model (TAM). There has been other method to include time as a restriction. Time pinch analysis (TPA) by Wang and Smith [9] and time slice model (TSM) [7,8,84,85] can be referred when time is a parameter in pinch analysis. These methods have been extensively studied to find the optimum energy targeting and heat exchanger networks in unsteady state streams, i.e., batch processes. Thus, pinch analysis application for time dependent streams such as renewable solar energy has been experienced and heat recovery practiced via TES units, i.e., indirect heat recovery [10,86–91].

The main available renewable energy source with a wide range of available temperatures is solar energy. Therefore, research into the integration of intermittent solar energy by designing a TES tank into industrial processes has been gathering momentum [92–98]. Due to not being continuous, surplus thermal solar energy needs to be stored in an appropriate TES system and finding its efficient size is a challenge to be solved.

Olsen et al. [55] proposed a modified TAM that utilizes an indirect source and sink profile (ISSP) and different minimum temperature differences based on characteristics of different hot/cold streams, i.e., their schedules, heat transfer coefficient, etc. They generalized their graphical method to provide a step-by-step algorithm applied to several industrial examples [56,78] to find the minimum number of TES units. After setting upper and lower temperature limits for the TES, the TES volume can be calculated based on the available energy to be stored,

obtained from the ISSP curve. They showed that the volume of TES tank can be significantly reduced by utilizing a hydraulically connected stratified tank, though they provided no insight into the actual working conditions and thermal performance of such a tank. Additionally, they assumed a constant CP (kW/°C, mass flow rate multiple by specific heat capacity) for all streams. Obviously, considering a constant mass flow rate for an intermittent and dynamic flow such as solar load is a simplifying assumption. Krummenacher and Favrat [79] proposed a graphical method, based on pinch analysis and TAM, for determining the minimum number of TES units and their range of heat recovery. They concluded that their method is more time efficient and provides significant insights into the optimization of industrial batch processes in spite of its simplicity. Despite the advantages of their approach, they assumed constant CP streams and implemented TAM in their graphical approach.

The practice of the pinch analysis has quite recently found its way into the building sector [3,99,100]. Reddick et al. [3] presented a novel waste heat recovery method by introducing gray water integration into the energy balance of a building. They divided gray water into warm and cold streams with different supply/target temperatures. Based on TSM with a time duration of one month, with average monthly values, they illustrated the heat integration potential of a solar thermal collector (STC), heat pumping and heat storage regarding heat recovery when there is a time mismatch between hot and cold streams. Although they extended the concept of thermal storage usage for the test building, they did not provide any TES volume calculation. By pure thermodynamic analysis, they reported a concept of thermal energy storage system which can store energy from summer and utilize it during winter. they considered different heat integration scenarios. In their best scenario, they calculated a reduction of 50% in annual primary energy consumption, i.e., electric energy. It is worth mentioning that seasonal heat storage, saving energy through one season (e.g., summer) and utilizing it for another season (e.g., winter), might be attractive based on thermodynamics analysis, however, from the practical point of view, it is not feasible. Even with a thick conventional insulation (mineral wool, polyurethane foam, etc.) layers for small to medium size TES tanks, they cannot hold high temperature energy of water (80~90°C) for more than several days in the best-case scenarios. This decay in the temperature level in a small size TES tank has been studied experimentally [39]. It is possible to reduce the heat loss to ambient by adding super insulating materials (SIMs) such as vacuum insulation panels (VIPs). VIPs are the most expensive SIMs; however, the price is not their only drawback: limited range of sizes, restricted flexibility, vacuum degradation, risk of damage and thermal bridge effects are just some that have been mentioned in the literature [101]. Even with this type of SIMs, the heat loss can be reduced 3 to 5 times that means a TES tank loses its thermal performance in two or three weeks which is still far less than the required time for seasonal storage.

Miseviciute et al. [99] considered the heating and ventilation system of a shopping center. They used actual building management system data and applied the pinch technique for the integration of available hot/cold streams. Based on their calculation of exergy demand in winter for the climate conditions of Lithuania, they found that the maximum exergy demand for HVAC system for heating duty happens when outdoor temperature is 3°C as the worst-case scenario. Their study showed a reduction of 26% in energy demand, achieved by applying a heat integration method. They did not assume any dynamic loads or time dependent streams in their case study of the shopping center.

Although the loads for heating or cooling in buildings are time dependent and dynamic, almost all available studies in the literature have assumed a constant value for the different loads while applying pinch analysis. Even when applying TSM to industrial processes, all streams are treated as having constant heat capacity rate, i.e., CP [kW/°C], with predetermined start and end times (schedules). This simplification leads to errors when dealing with solar thermal energy. Indeed, as a hot stream, there are two possible working designs for a STC system: a constant mass flow rate (i.e., variable outlet temperature) or a fixed outlet temperature (i.e., variable mass flow rate). In both scenarios assuming a constant solar load (duty) or a constant CP means ignoring the intermittent nature of STC stream. Consequently, pure thermodynamic analysis can attribute to undersizing or oversizing TES volume.

The main TES research has thus far focused on finding the minimum number of fixed temperature TES tanks based on TAM and then assigning an appropriate heat recovery capacity (again based on the TAM or a heuristic approach) to calculate each TES volume. The number of TES units is not an issue when one hydraulically connected stratified tank is chosen for TES. In this case, the inlet/outlet location of the intermediate heat recovery loops and their mass flow rates have the utmost importance. It is worth mentioning that the proposed sizing of stratified tanks in the literature (see [55,78] as examples) are highly simplified in spite of the complex hydrodynamics of a gravity driven fluid flow within a stratified tank, with several jets entering/exiting the tank in the form of intermediate heat recovery loops. Even for an initial economic assessment of applying a TES tank in an energy system, a highly simplified thermodynamic prediction for the volume of TES tank may results in a relatively large error in TES tank capital investment cost or maximum possible indirect heat recovery via the TES tank. Although heat loss to ambient is one problem, the combined effect of hydrodynamic-heat transfer in creating a region with high temperature gradient, i.e., thermocline region, cannot be suppressed. Thermocline thickness is a region where the hot and cold section of TES tank are separated. Thermocline thickness depends on tank geometry and shape, storage fluid type (thermal oil, water, molten salt, ionic liquid, etc.), charging or discharging mass flow rate (or bulk fluid velocity inside TES tank), and temperature difference between hot and cold part of a

stratified TES tank. This thickness can be as high as 30 percent of volume of a simple cylindrical water TES tank [102]. Therefore, having an estimate via at least one-dimensional modeling can help in addressing economic assessment and calculating maximum indirect heat recovery accurately.

In addition to the thickness of thermocline, when hot/cold streams are time variables in a single batch process (temperature or CP wise), the movement of local thermoclines up and down (based on the fixed location of charging/discharging ports of an intermediate heat recovery loop (IHRL)) may violate the predetermined minimum temperature difference for one or several IHRLs heat exchangers. As can be discerned from the mentioned points, the design of a stratified TES tank is not a trivial concept. A thermodynamics investigation is not sufficient, and a hydrodynamic validation and thermal performance analysis is required. The thermal performance of a TES tank can be briefly addressed in these references [103–109].

Building's thermal loads are highly stochastic in nature due to dependence on outdoor temperature (in case of heating load) or human behavior (domestic hot water heating load). These types of loads vary by time during one day. Also, the previous study of our research group revealed that winter heating demand for a test building was as high as 97.2 percent of the yearly required energy for heating and cooling [3], which is typical for high latitude countries. On the other hand, the required energy for domestic hot water remains almost constant through all seasons [3]. This means that occupant behavior is more important than the seasonal variation in city water temperature. However, the domestic hot water load is highly time dependent during one day. Hence, one needs to deal with at least three fully dynamic loads, i.e., space heating, domestic hot water, and renewable solar energy in a typical day in winter in buildings as an energy system. The reviewed literature so far suggests an averaging in application of pinch analysis which is not appropriate for dynamic loads. Thus, a systematic approach that determines the minimal energy requirements for a building, known as "targeting" in pinch analysis vocabulary, is still missing. In particular, there is a need for optimal energy targeting that focuses on the integration of renewable energy sources such as solar thermal energy into buildings.

The focus of this study is on the same test building as studied in [3] and on energy targeting for the coldest day in the winter. All hot/cold streams for the test building are extracted for the mentioned day in the heating season as continuous functions of time. TSM is modified with selecting appropriate time slices to cover all details and changes in mentioned dynamic loads in the test building. Furthermore, the energy targeting prioritizes direct heat exchange between hot and cold streams via heat exchanger units. After all cold streams are satisfied by direct heat recovery from hot streams, the extra energy of hot streams is calculated as a TES cold stream, i.e., an IHRL, to charge the TES tank. This prioritization makes the modified TSM highly useful

for building energy targeting process. To the best knowledge of the authors, this is the first application of TSM pinch analysis to a building by considering time-variable hot/cold streams in one day (i.e., 24 hours). The main objective of the present study is the development of a new approach that combines the energy targeting of dynamic loads in the test building and sizing the minimum volume of TES tank according to the maximum possible heat recovery.

Moreover, thermal performance of the designed stratified TES tank is evaluated by numerically solving the one-dimensional energy equation. The effects of TES heat loss to ambient and thermocline thickness, which cannot be taken into account in pinch analysis, are quantified as well. The remaining structure of the papers include four additional sections. In section 3.3, all hot/cold streams for a test building are extracted for the coldest day in winter. In section 3.4, the original time slice model is modified to allow three things: firstly, the direct heat exchange between time co-existence sources/sinks; secondly, charging the TES tank (when extra energy is available during each time slice); and finally, introducing TES discharging as an intermediate hot utility. The pinch analysis energy targeting result based on the detailed TSM will be used for computing the TES volume in the maximum possible heat integration scenario in the test building. In section 3.5, a heat exchanger + TES network is designed to accomplish the calculated maximum heat recovery with stratified TES as the heart of the proposed HE+TES network. Finally, section 3.6 presents the thermal performance of the designed stratified TES tank based on the TSM predicted volume for the test building.

3.3 Time dependent streams

The main hot/cold streams in a building show time-dependent characteristics during a year. Before presenting the energy targeting and TES sizing, here all hot and cold streams in the test building are derived for the worst-case scenario from a utility consumption point of view. Table 3-1 presents all possible streams in a typical building in the winter with suggested supply and target temperatures. The main loads in the test building are the hydronic floor heating and domestic hot water. All other streams are related to the heat integration assumptions. In other words, warm and cold gray water are due to heat recovery from used domestic hot water. A solar thermal collector can be used to integrate solar renewable thermal energy for the building to act as a substitution of the electrical heating hot utility. And the TES streams are responsible for charging (cold) and discharging (hot) the TES tank via intermediate heat recovery loops.

Sections 3.3.1 to 3.3.5 are intended to help visualize the hourly dynamic load for each stream in the test building.

Table 3-1 Hot and cold streams in the test building for a day in heating season

Stream descriptions	Acronyms	Supply → target temperature, °C
Space heating (Hydronic floor heating) (Cold)	*HFH*	30 → 35
Domestic hot water (Cold)	*DHW*	5 → 55
Warm gray water (Hot)	WGW	30 → 5
Cold gray water (Hot)	CGW	10 → 5
Solar thermal collectors (Hot)	STC	65 → 40
Heat pumping; condenser (Hot)	HP_Con.	50 → 45
Heat pumping; evaporator (Cold)	HP_Eva.	-5 → 0
Thermal energy storage – Hot Zone (Cold)	TES-HZ	35 → 60
Thermal energy storage – Hot Zone (Hot)	TES-HZ	60 → 35
Thermal energy storage – Cold Zone (Cold)	TES-CZ	0 → 7.5
Thermal energy storage – Cold Zone (Hot)	TES-CZ	7.5 → 0

3.3.1 Time-dependent ambient temperature function and hydronic floor heating

The test building was selected from a previous study by our group [3], and the building structural characteristics are repeated here for easier accessibility, shown in Table 3-2.

Table 3-2 Selected structural characteristics of the test building

Parameter description	Value
Foundation area	172 [m^2]
Outside wall area	356 [m^2]
Fenestration portion of wall area	0.15
Inclined roof area, one of two sides	145 [m^2]
Windows thermal resistance	0.7 [°C m^2/W]
Wall thermal resistance	4.9 [°C m^2/W]
Total thermal solar collector area	17.3 [m^2]
Reference solar collector efficiency	75 [%]

Energy losses in a building are due to heat transfer from the building envelope to the environment. Design energy losses or loads can be computed by considering the design outdoor temperature, which is available from long term meteorological data for a given city or location in conventional HVAC design. However, the outdoor temperature varies hourly, as do the energy losses. Eq. ((3-1) provides a simplified outdoor temperature profile for a typical day [110].

$$T_{amb} = \frac{T_{min} + T_{max}}{2} + \left(\frac{T_{max} - T_{min}}{2}\right) \times \sin(15t + 210) \qquad (3\text{-}1)$$

Where T_{min} and T_{max} are the minimum and the maximum daily temperatures, respectively. The parameter *t* is the time of the day in hours. The selected representative daily temperature extrema for a typical wintery day were entered in this equation from meteorological data [111] as -12.2 °C and -1.11°C (average of several years). Therefore, by assuming a constant indoor temperature (22°C), the time-variable heating load for the test building is shown in Figure 3-1. The heating duty is on a hydronic floor heating (HFH) system with 35°C and 30°C as its inlet and outlet temperatures, respectively.

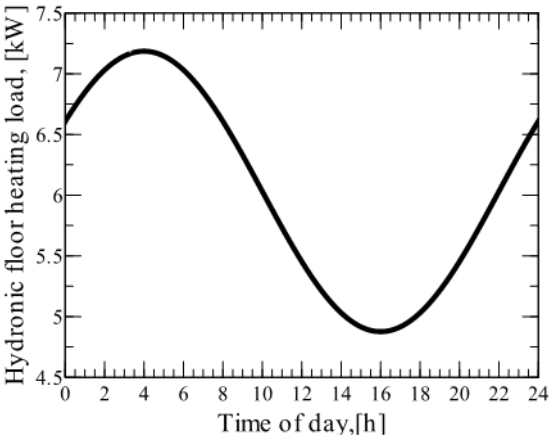

Figure 3-1 Hydronic floor heating load as a continuous function of time

3.3.2 Domestic hot water and gray water, as continuous functions of time

Another significant energy demand in the test building is the domestic hot water (DHW) load. To compute the time variable load the general hot water usage pattern proposed by [112] is used here. Considering the average city water entering the building as 5°C in winter and the target temperature of 55°C for DHW, the time variable DHW load is presented in Figure 3-2 for the multi-family test building. Additionally, this study supposes that the test building has a modified plumbing system for waste heat recovery wherein the gray water is separated and divided into warm and cold streams, as was previously proposed [3]. For pinch analysis purposes, the warm gray water (WGW) load can be extracted as a continuous function of time with the same pattern as the DHW load, but with different values due to the different supply and target temperatures, being 30°C and the city water temperature (5°C), respectively. The cold graywater (CGW) has the potential to be stored and used as a load for the evaporator of a possible heat pump in the test building. The CGW has an initial temperature of 10°C and can be cooled down to 5°C (city water temperature) in winter.

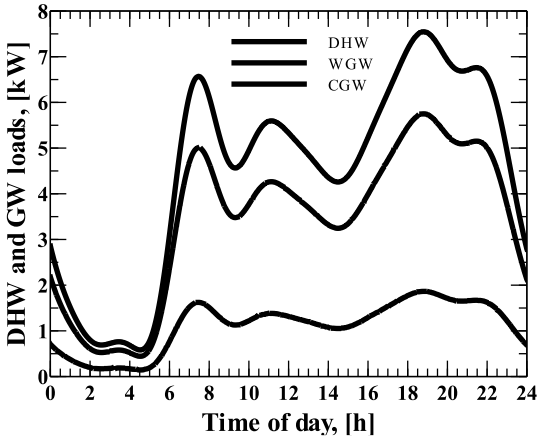

Figure 3-2 DHW, WGW and CGW loads as continuous functions of time

3.3.3 Solar thermal collector duty

The solar thermal collector load is the only hot stream that is a non-continuous stream during one analysis period (i.e., one day) in the test building. Solar irradiance provides a variable source of energy for solar collectors due to variable solar zenith angle and time duration of sunny hours per day. The time dependent solar irradiance function for a clear sky can be estimated based on the simplified yet sufficiently accurate Eq. (3-1) [113]

$$G(t) = 1362 \times \left(1 + 0.033 \cos\left(\frac{2\pi d_n}{365}\right)\right) \times \cos\left(\theta_z(t)\right) \times \sin\left(\frac{\pi(t - t_{rise})}{t_{set} - t_{rise}}\right) \qquad (3\text{-}2)$$

In Eq. (3-2), G is the solar irradiance (W/m^2), d_n is the day number in a year, $\theta_z$is the zenith angle, and t_{rise} and t_{set} are the local sunrise and sunset times, in hours. The zenith angle is a variable parameter regarding the time of a day. This function was calculated based on the available data [114] and is illustrated in Figure 3-3 for four winter months, namely December, January, February, and March for the test building, for the 21st of each month (values for November is very close to one for January). As seen in Figure 3-3, the minimum zenith angle occurs on the 21st of December and the maximum zenith angle is on the 21st of March. This value for all other days in the winter is between these two extremes. Therefore, these two days are the worst cases for STC load calculations.

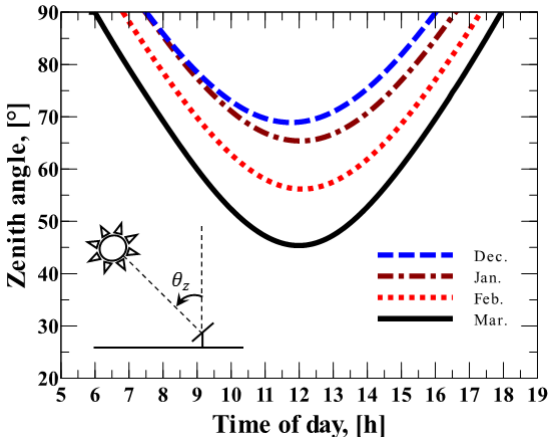

Figure 3-3 Time variable solar zenith angle (θ_z) for the location of the test building

As listed in Table 3-1, the solar thermal collector area is 17.3 m^2 for the test building. To calculate the solar collector duty, there are two different scenarios. First, fixing the collector's outlet temperature (temperature of heat transfer fluid) and the second, fixing the collector's mass flow rate of heat transfer fluid. Each scenario results in a different solar thermal collector performance. Eq. (3-3) is used to compute the performance of the flat plate solar collectors [95,97] of the test building.

$$Q_S = \eta_c G A_c = A_c(\eta_0 G - a_1(T_c - T_{amb}) - a_2(T_c - T_{amb})^2) = \dot{m}_{CHTF} \times c_p \times (T_{out} - T_{in}) \qquad (3\text{-}3)$$

Where, in this equation, η_c is the thermal performance of the solar collector. T_c is the collector temperature, i.e., $T_C = (T_{out} + T_{in})/2$, T_{amb} is the time-dependent ambient temperature. Eq. (3-1) is applied with different T_{max} and T_{min} values for each winter month. T_{in} is the inlet constant collector heat transfer fluid temperature, equal to 40°C. η_0, a_1, and a_1 are constants that can be found in the literature or from the collector's manufacturer. $\dot{m}_{CHTF}$ is the mass flow rate of the collector heat transfer fluid.

Eq. (3-3) is solved for each mentioned scenario. Figure 3-4 shows the collector performance at constant mass flow rate ($\dot{m}_{CHTF} = 0.1\ kg\ s^{-1}$) and constant T_{out} = 65°C for a typical day in winter with two different solar irradiance levels, one with minimum solar energy, i.e., in December, and the other with maximum solar energy, i.e., in March. As shown in Figure 3-4, the overall solar collector duty and performance in the case of constant T_{out} are higher than that of the constant mass flow rate. Therefore, the constant T_{out} has been selected in the rest of this study as the solar thermal collector (STC) load. Moreover, there is a time delay between the sunrise time and the time when solar collectors reach to their fully develop working condition. The time when the solar collectors start working is called *effective sunrise* in this study. The same delay has been observed before sunset, which is named *effective sunset*.

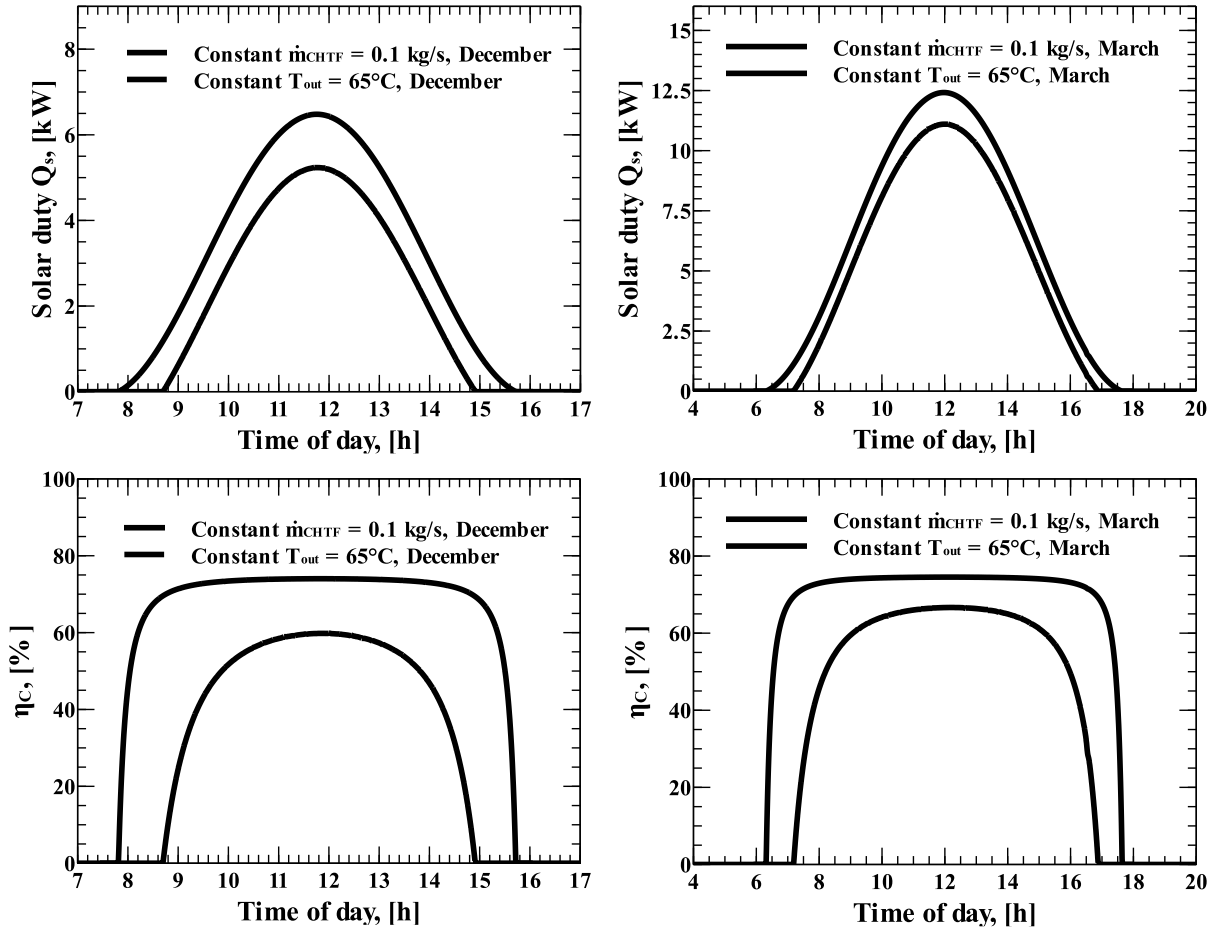

Figure 3-4 Solar collector load and performance for a constant $\dot{m}_{CHTF}$ and a constant T_{out} (for December and for March)

3.3.4 Heat pumping

Heat pumping is utilized for upgrading a low temperature heat source to a higher temperature and has been integrated in industrial processes in recent years. Reddick et al. [3] showed that the drained DHW stream can be reused (as a waste heat) by separating the gray water, and dividing it into two waste streams, namely, cold and warm gray water, where the available heating potential of both streams is depicted in Figure 3-2. The cold gray water (CGW) can only be integrated in a building as a load for the evaporator of a heat pump system, due to its low temperature. The general assumptions regarding heat pumping in this study are as followings:

- The COP is assumed constant, approximately 3
- The heat pump works continuously during one analysis period, i.e., 24 hours
- The temperature lift is around 50°C (condensation temperature at 45°C, evaporation at -5°C; both, the condenser and the evaporator may have 5°C of superheat)

- The constant evaporator load will be fully satisfied via gray water heat recovery through the TES tank, i.e., indirect heat recovery, therefore, there is no need for any external heating utility for evaporator.

Given the temperature ranges of WGW and CGW (Table 1), WGW can preheat DHW from the city water temperature up to 25°C. It is possible to mix the WGW (after preheating DHW) with CGW to provide a heat source for the evaporator of a heat pumping system. To find the optimum evaporator load that can be satisfied through a TES, the concept of time pinch analysis [9] is applied here. Figure 3-5 shows the available cumulative energy of this mixture as a hot stream that can be stored in a TES unit. A constant evaporator load that can be satisfied by this energy and can be found by a trial-and-error procedure. The maximum heat recovery by the constant evaporator load (shown in Figure 3-5 as the cold composite curve) is calculated as 2.75 kW through indirect heat recovery. To set up the time composite curve, first the energy (in kWh) with respect to time is calculated by integration of the time variable loads, i.e. WGW+CGW, and the same calculation is repeated for constant the evaporator load. Then the hot composite curve is shifted upward to touch the cold one at just one point (time pinch point). By subtracting the hot composite curve from the cold one, the grand composite curve is constructed. As can be seen in Figure 3-5, the amount of energy deficit and surplus are the same. However, the energy surplus needs to be saved in TES to be recovered when the energy deficit is dominant. In addition, the grand composite curve presents the maximum storable energy, which is an interesting point of time pinch analysis. In this specific case for the test building streams, the storable energy is 12.4 kWh (equal to the energy deficit, which is the same value as energy surplus depicted in grand composite curve).

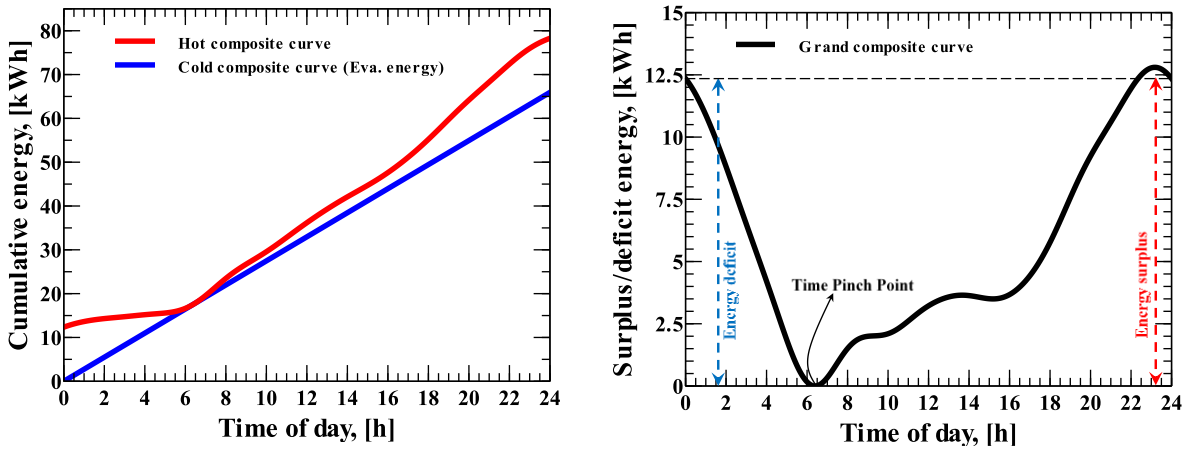

Figure 3-5 Time pinch analysis for optimum evaporator load calculation

It is worth mentioning that the same trial and error procedure for maximum heat recovery for evaporator load can be achieved by running the time slice model several times. As will be shown in section 3.4.3, the result is the same. The calculated evaporator load results in 4.12 kW as the available load of the condenser of the heat pumping system and requires 1.37 kW compressor workload from the electric power grid.

3.3.5 Intermediate heat recovery loops; thermal energy storage

The main and yet simple idea in the application of a thermal energy storage is to store extra energy when available and use it in another appropriate time interval. In order to accomplish this storage, a stratified tank as secondary medium is added to the heat exchanger network with several intermediate heat recovery loops to transfer energy from/to the main streams and the TES. The TES tank is divided into two main zones, the hot zone, and the cold zone. The buoyancy effect tends to prevent these two zones from mixing. The amount of energy to be transferred and the temperature limits can be calculated based on other parameters such as the supply and target temperatures of the hot and cold streams, their CPs, time duration, etc. Pinch TSM can shed some light on the optimum TES volume by extracting the maximum heat recovery in both direct and indirect forms. By “direct”, it means that heat exchange is done through a heat exchanger (without any flow mixing) between hot and cold streams; by “indirect”, it means that heat exchange happens through IHRLs connected to the TES tank.

3.4 Energy targeting based on adapted time slice model

Now that all time-dependent streams in the test building are derived, the concept of the time slice model can be applied. It is worth mentioning that time-variable CPs can be extracted for each stream due to known supply and target temperatures. The time slice model has the advantage of predicting the dynamic energy targeting for a system. The original TSM is here modified to perform the following steps systematically:

i. calculate the maximum direct heat recovery between time co-existing hot/cold streams at each time slice.

ii. identify the extra energy at each time slice where a cold stream as TES tank charging will remove this energy

iii. calculate CP for intermediates heat recovery loops in both TES hot and cold zones

These steps will now be demonstrated for the test building case study. The heat recovery between different hot/cold streams presented in Table 3-1 is demonstrated in Figure 3-6 before going forward.

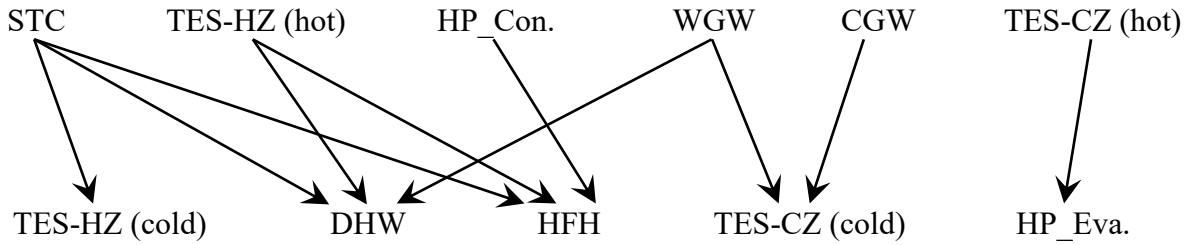

Figure 3-6 Heat transfer between different hot/cold streams in the test building

The streams presented at top row in Figure 3-6 are hot streams, while the streams at the bottom row are cold ones. The two main cold streams in the test building are DHW and HFH that should be satisfied through hot utility (mainly electricity) or via heat recovery from possible sources described in Table 3-1 and section 3.3.

3.4.1 Time slice duration selection

The time slice model has been used for energy targeting in industrial batch processes, as introduced by Kemp and Deakin [7]. In almost all industrial examples, the CP values were considered as constant quantities during their corresponding process time. However, as shown is section 3.3 for the case of different streams in the test building, the CPs can possess variable values with respect to time. Therefore, the selection of time slice duration in this case should be in a way that can recognize all variations in the time-dependent streams. In this study the minimum time slice duration that can cover all the details in the load variation has been assumed as 0.01 hour, i.e., 36 seconds, which with today's computer computational power can easily include all the local maxima and minima of the extracted data.

The average CP for each stream is computed by integration over the given time slice (TS) (Eq. (3-4)).

$$\overline{CP}_{TS_t} = \frac{\int_t^{t+TS} CP(t)\, dt}{TS} \tag{3-4}$$

3.4.2 Energy targeting for the test building

All hot and cold streams extracted for the test building are shown in Figure 3-7 (the minimum temperature difference is set as a fixed value of 5°C; in order to evaluate the "shifted temperatures" [6] half of this minimum temperature difference is subtracted from hot streams, and added to the cold streams). Solid vertical arrows are streams that are present during a full day, though with time-variable values. The vertical dashed arrows represent the intermittent stream, e.g., STC. The dash-dotted arrows present the four intermittent streams or intermediate heat recovery loops connected to the TES to charge or discharge energy from it. The IHRLs can be intermittent or continuous.

Here we assume that one repeatable analysis period is 24 hours for the test building. By considering very fine time slices, it is difficult to present the calculated values in one table as the problem table algorithm [6] suggests. Thus, here we first start with several selected time slices. Software code was developed in MATLAB software (R2020b) to store all the data for each time slice. This code can calculate the local pinch temperature at each time slice, the required hot and cold utilities (energy targeting), and the extra energy for storage (in both the high and low temperature zones). In the time slice model, the first priority is the direct heat exchange between time co-exist streams. If there is some remaining surplus energy, then the intermediate heat recovery loops will be activated to store this energy in the storage tank.

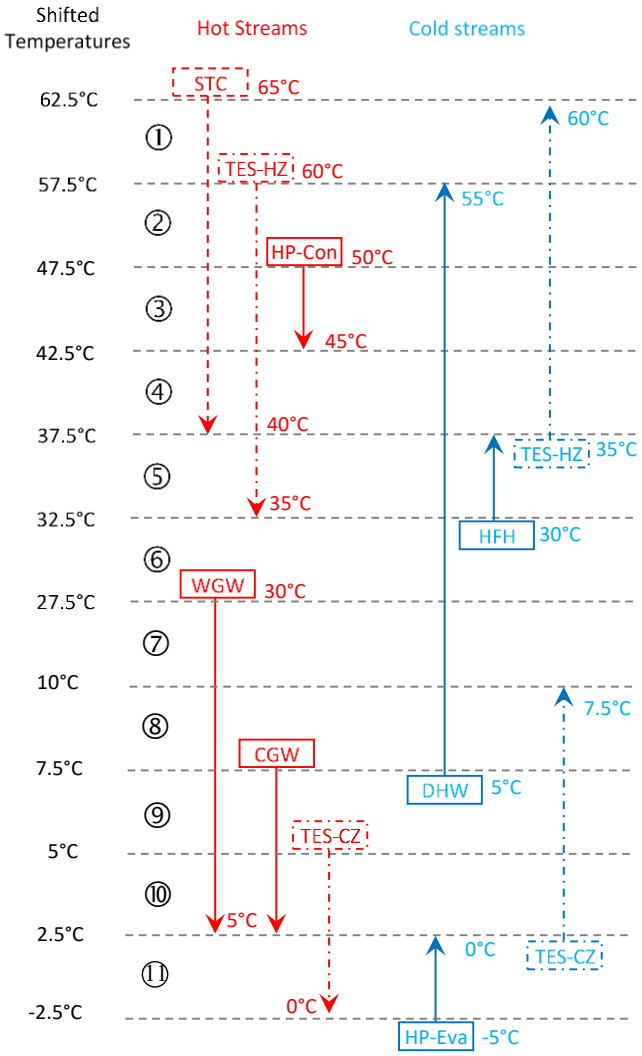

Figure 3-7 All streams in the test building with their corresponding supply and target temperatures (STC shown as dashed arrows indicating an intermittent source, IHRLS shown in dash-dotted arrows)

Based on the presence of streams, there are four distinct time durations in one analysis period. The main timing of events or schedules in a typical day (i.e., 0 to 24 hours) in winter for the test building is as follows:

- 0 to effective sunrise (when only streams with solid arrows + TES-CZ in Figure 3-7 are present)
- effective sunrise to a time when the test building experiences zero hot utility (when STC joins the streams of the previous time duration)
- Zero utility; TES charging to effective sunset (when TES-HZ 35°C→60°C joins the described streams)
- effective sunset; TES discharging to 24 (when solid arrows + TES-CZs + TES-HZ 60°C→35°C are present)

3.4.2.1 From beginning of analysis period to effective sunrise

shows representative composite curves for a time slice from the beginning of the analysis period to the effective sunrise interval (just on time slice from 6.99 hours to 7.00 hours; equals to 0.01 hours has been presented). In this time interval, there is no solar energy available. The condenser heat can preheat the HFH. DHW and HFH need hot utility, in this case electric energy, to reach their target temperatures.

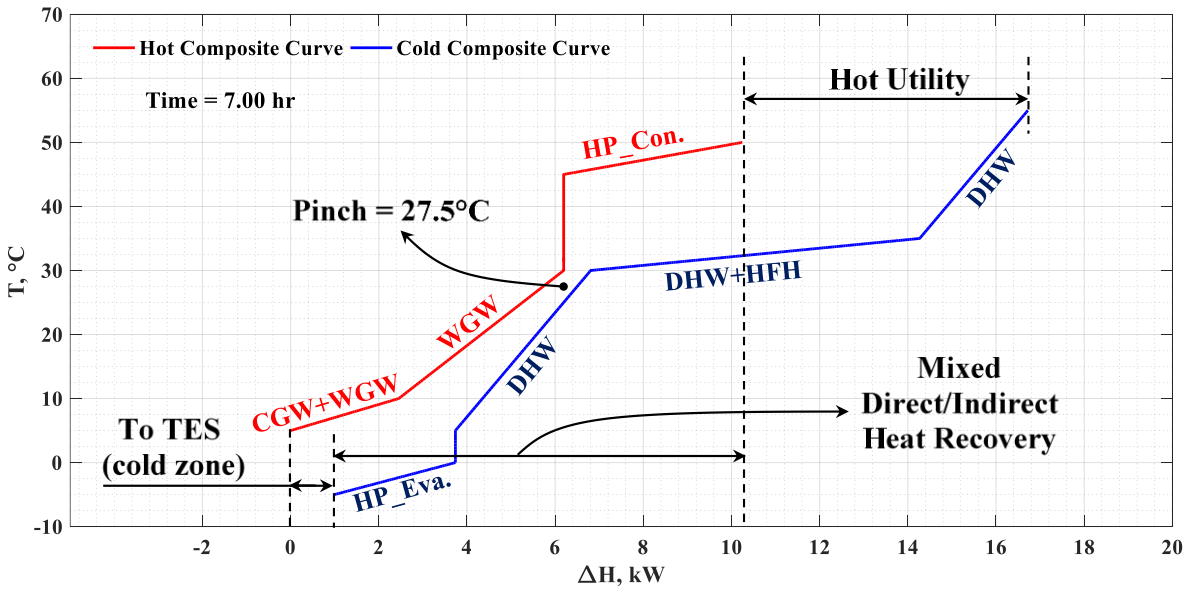

Figure 3-8 Representative composite curve for zero to effective sunrise in the test building

As shown in Figure 3-8, the pinch point in terms of a shifted temperature is 27.5°C. The heat recovery area is labelled as mixed direct/indirect, due to a combination of indirect heat recovery from the cold zone of the TES for the evaporator load and direct heat exchange between HP_Con.⇔HFH and WGW⇔DHW.

3.4.2.2 From effective sunrise to zero utility

After sunrise, solar thermal collectors provide a gradually increasing energy source. This energy can be used in direct heat recovery through heat exchanger networks. After some time, the integration of all possible hot streams in the test building reaches a point where there is no need for hot utility. Figure 3-9 illustrates representative composite curves for the time slice 10.33 hours to 10.34 hours at this time interval.

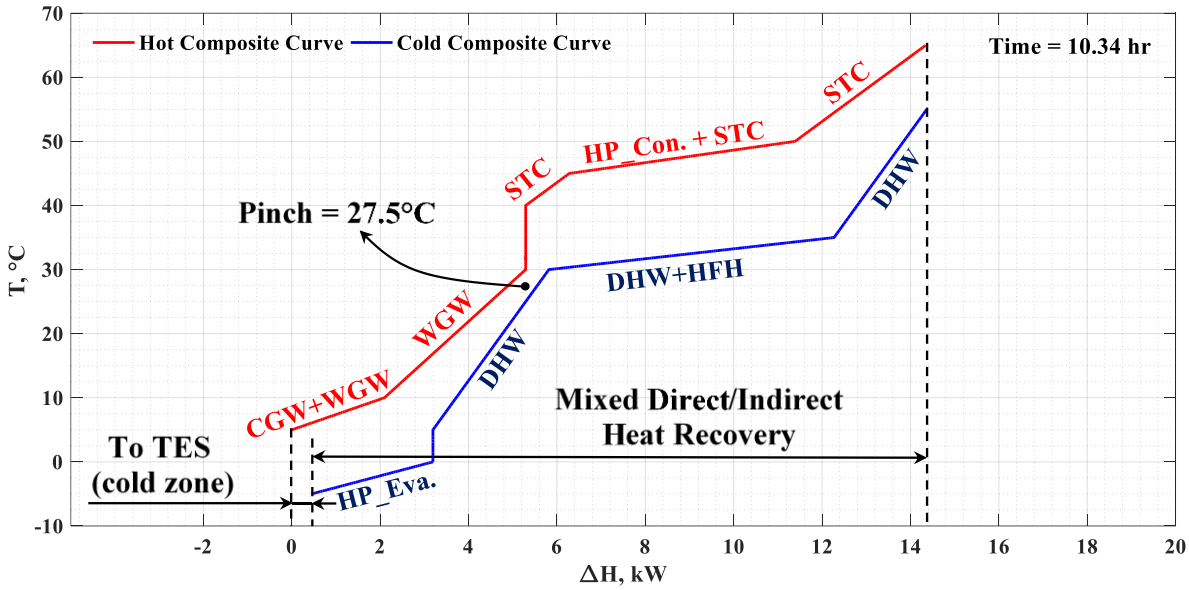

Figure 3-9 Representative composite curves for effective sunrise to zero utility

3.4.2.3 From zero utility and TES charging to effective sunset

When the test building energy system exhibits no need for hot utility (except the required compressor work for heat pumping), the extra solar energy can be stored in the hot zone of the stratified thermal energy storage tank. From this point, the TES-HZ stream will be introduced as an intermediate heat recovery loop to the streams of the test building. As long as the TES is charging, the zero-utility condition remains. Figure 3-10 shows the representative composite curves for this period. Introducing a TES charging stream as a cold stream keeps the hot utility at zero, as shown at the right-hand extremity of the cold composite curve in Figure 3-10. The supply/target temperatures of this TES charging stream are selected in a way that respects the minimum temperature difference (5°C). As the extra energy source is coming from the STC

stream, the TES-HZ as a cold stream can have 35°C to 60°C as supply and target temperatures, respectively.

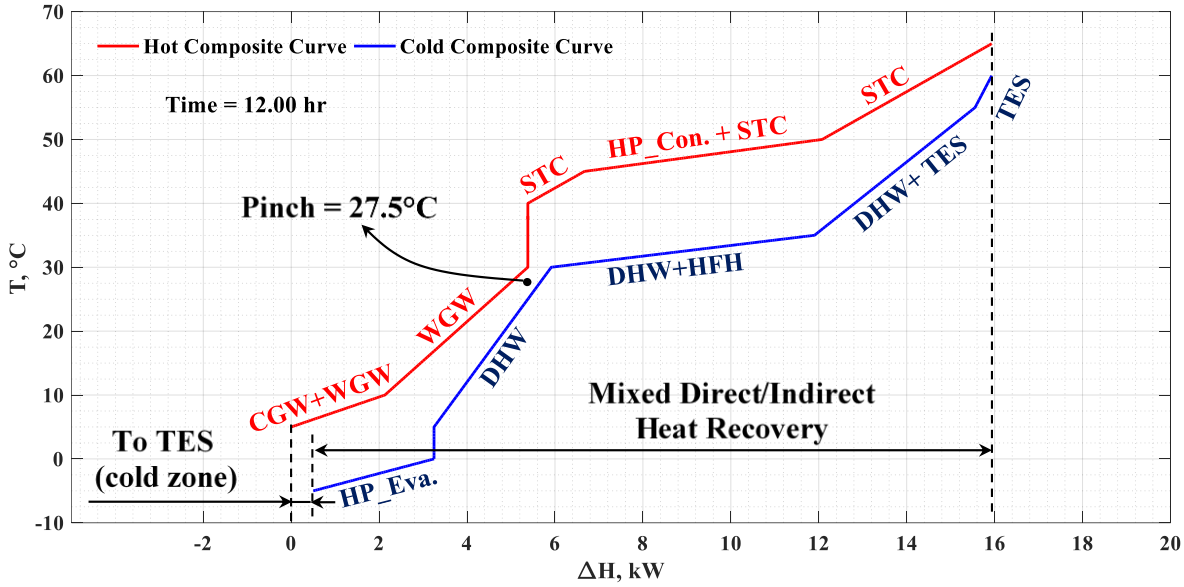

Figure 3-10 Representative composite curves for TES charging time interval

3.4.2.4 From effective sunset and TES discharging to end of analysis period

The TES charging continues until there is no extra solar energy. The test building needs hot utility to satisfy the domestic hot water and space heating loads. After effective sunset, the TES stored energy can be released as a hot stream and as long as this energy in addition to the heat pumping is sufficient, the building needs zero hot utility. The representative composite curves for this duration are shown in Figure 3-11. During TES hot zone discharging, the TES plays the role of a hot stream and is presented as an intermediate hot utility in Figure 3-11. The pinch temperature remains at 27.5°C, which guarantees the appropriate position of the heat pump. The TES discharging starts at effective sunset and heats up the demands in the test building to their target temperatures.

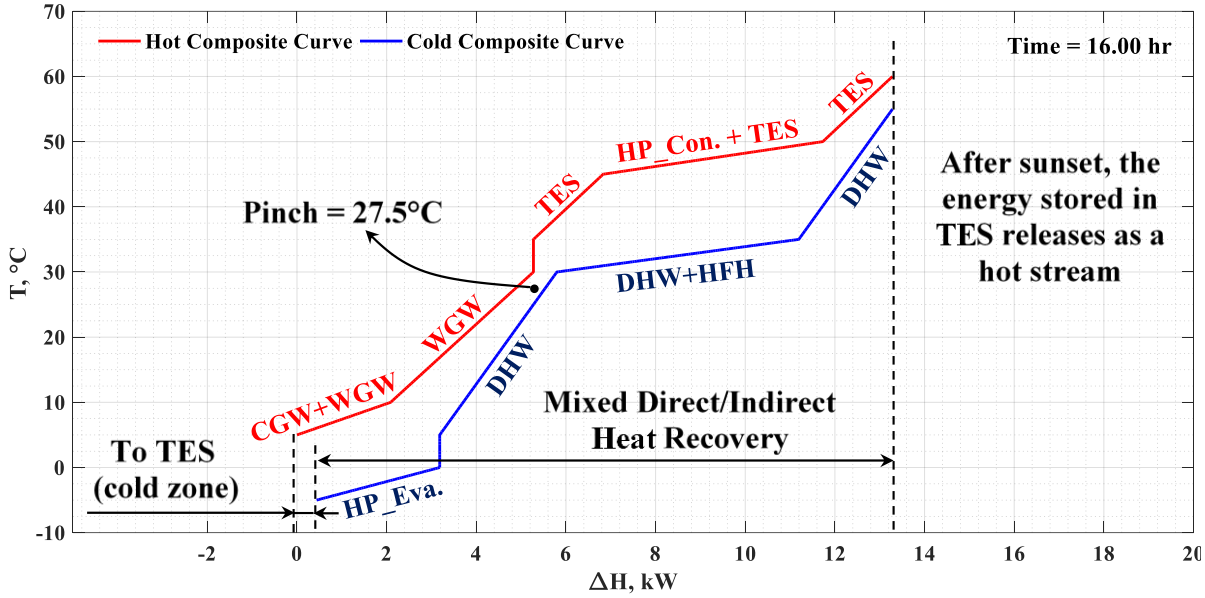

Figure 3-11 Representative composite curves for TES hot zone discharging

At the end of discharging, the composite curves will be the same as at the beginning of the analysis period and are illustrated in Figure 3-8. During the heating season, each complete analysis period (from 0 to 24 hours) will be repeated with different HFH loads (due to the effect of the outdoor temperature) and STC duty (due to varying solar zenith angles and hour of daylight). All other streams, i.e., DHW, WGW, CGW, and HP remain the same.

3.4.2.5 Obtained charge/discharge load of TES-HZ based on this graphical approach

Figure 3-12 shows the results of the explained graphical approach for obtaining the TES charge and discharge load with solar taken for March. The red area and the blue area represent the same amount of energy: 35.9 kWh. As it is presented in Figure 3-6, STC as a hot stream loads the TES-HZ through an IHRL. The discharging process happens through another IHRL and unload the TES-HZ by heating DHW and HFH.

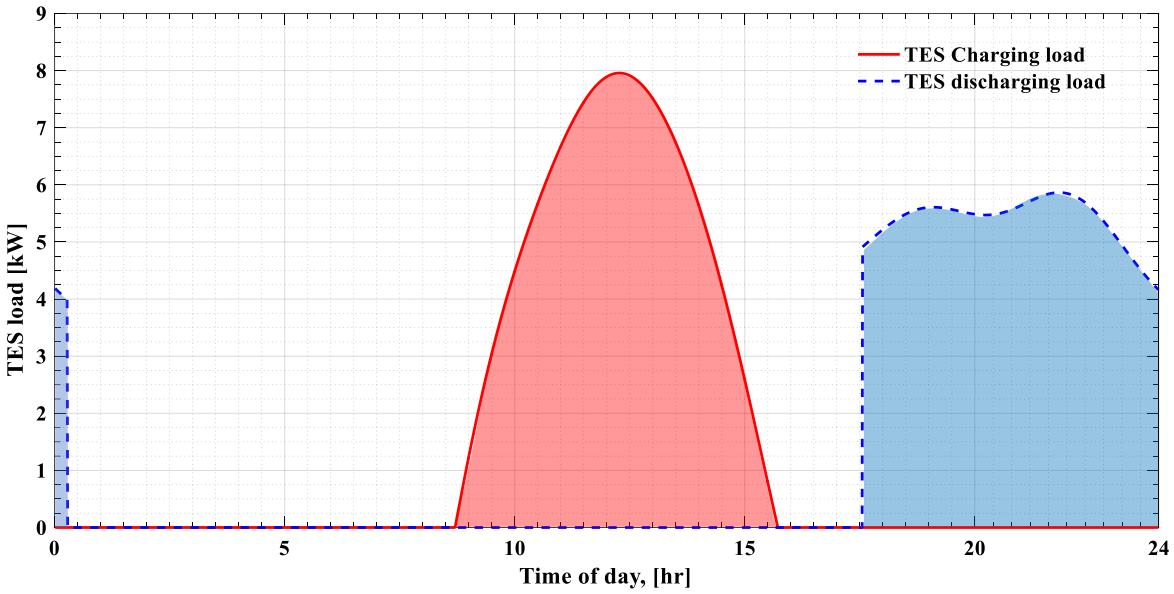

Figure 3-12 TES charging and discharging load from graphical approach (March solar energy)

3.4.3 Dynamic hot utility

When there is not enough energy from heat recovery, hot utility needs to be provided to the cold streams such as HFH and DHW. The required hot utility was shown in the representative composite curves, i.e., Figure 3-8 to Figure 3-11. Software code was developed and has the capability to calculate the required hot utility at any time. The dynamic hot utility is plotted in Figure 3-13. There are two time intervals where the test building needs zero utility. As shown here, while charging the TES hot zone, there is enough energy to satisfy all the cold streams, thus there is no need for hot utility. Also, when the TES (hot zone) starts discharging, this hot stream satisfies for a short time the test building energy requirement. This means that solar energy may be used even in December. Considering solar energy in the late March, the discharging period is longer. The stored energy can satisfy the demands after sunset up to some minutes (i.e., 0.28 hours) extended into next day. The existence of the extra energy defines the time duration of TES tank charging. For discharging, the energy balance between required energy by the test building (HFH+DHW as cold streams after direct heat exchange with available hot streams) and TES tank, defines the duration of TES tank discharging. It should be noted that the discharging process starts after sunset, no matter whether the solar data is from December or March. This is necessary to guarantee holding 35°C as the TES-HZ outlet temperature. To have a sense of how the heat recovery can reduce the hot utility requirements in a building, the case with no heat integration is plotted in Figure 3-13 (left figure shows the solar energy of December and the right one with solar energy of March).

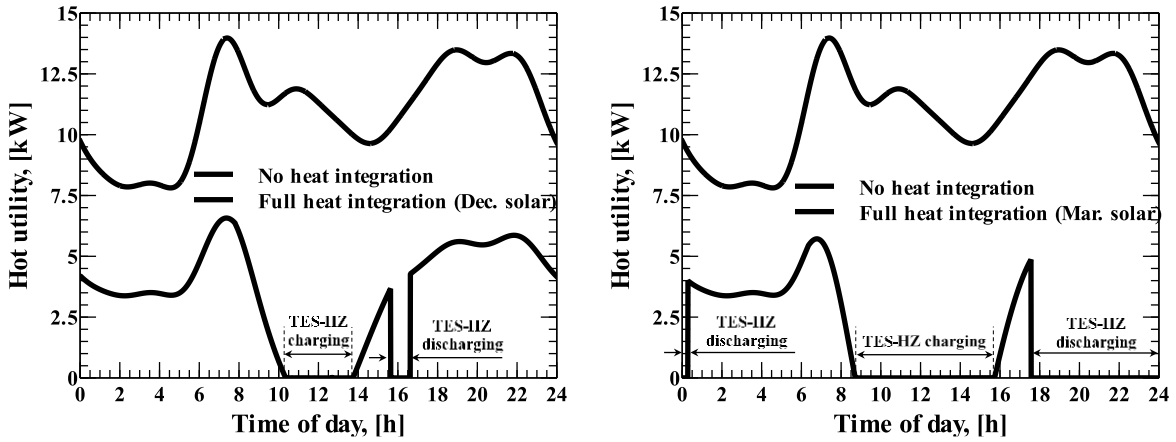

Figure 3-13 Comparison between full heat integration and no heat integration (minimum and maximum solar energy for December and March, left and right, respectively)

Moreover, Table 3-3 shows a summary of heat integration in the test building for both the December and March solar conditions. The required energy for satisfying all of the test building heating demands can be determined by calculating the area under the dashed line in Figure 3-13 or the no heat integration case. This value is 252.9 kWh and in no heat integration case should be provided by hot utility source, here electricity. The area under the solid curves in Figure 3-13 plus the required work needed for compressor of the heat pump in the energy demand based on the total heat integration. These values are 93.3 kWh and 70 kWh for solar in December and March, respectively.

Table 3-3 Summary of heat integration results

Solar energy in:	$Q_{utility}$, kWh	V_{TES}, L	***Utility reduction, %***
December	93.3	1580	63.1
March	70	2700	72.3

Additionally, the TES tank volume is calculated according to the available energy for storage at each zone of TES tank by Eq. (3-5).

$$V_{TES} = \frac{Q_{available}}{\rho c_p \Delta T} \tag{3-5}$$

Therefore, for the cold zone of the TES tank which is responsible for indirect heat recovery from a mixture of warm and cold gray water and provide this energy to the evaporator of the heat pump system have to store a maximum of 12.4 kWh energy. By considering the average value for density and specific heat of water + ethylene glycol (a mixture with 10 percent by mass) between 0°C and 7.5°C, the cold zone of TES tank volume can be computed as:

$$V_{cold\ zone} = \frac{(12.4\ \times 10^3 Wh) \times (3600 \frac{sec}{hr})}{1014 \frac{kg}{m^3} \times 4039 \frac{J}{kg\ °C} \times 7.5°C} = 1.445 m^3 = 1446 Lit \qquad (3\text{-}6)$$

The hot zone volume for STC in December and March can be calculated as 134 L and 1255 L, respectively. Therefore, the total mass of TES tank is 2700 L and 1580 L for each solar scenario. Due to higher solar energy in March, the reduction in hot utility is around 10 percent higher than that of December. However, the total volume of TES increases 41.5 percent by considering March solar energy. In other words, higher solar energy in winter will reduce the utility (operational cost), however, it will increase the initial investment cost due to the larger TES volume.

Figure 3-14 illustrates the energy surplus/deficit for the heat pump evaporator, extracted from graphical approach presented in Figure 3-8 to Figure 3-11. It is another way to calculate the maximum heat recovery from gray water (both warm and cold one, warm water after direct heat exchange with domestic hot water as can be seen in Figure 3-15 in section 3.5) for the evaporator load by noticing that the charging and discharging energy balance in cold zone of TES tank is zero (area below zero equals area above zero, and each area is 12.4 kWh). This means the amount of stored energy in the cold zone of TES is equal to the required energy during energy deficit time periods. Although all representative composite curves shown in section 3.4.2 presented the energy surplus for the cold zone, other composite curves during hours covering by blue area in Figure 3-14 are defined as “Energy deficit”, when energy is withdrawn from the cold zone of TES tank and supplied to the evaporator. Additionally, Figure 3-14 shows that the prediction of storable energy by time pinch analysis (shown in section 3.3.4 and Figure 3-5) and the calculated values by indirect heat recovery with the time slice model are the same.

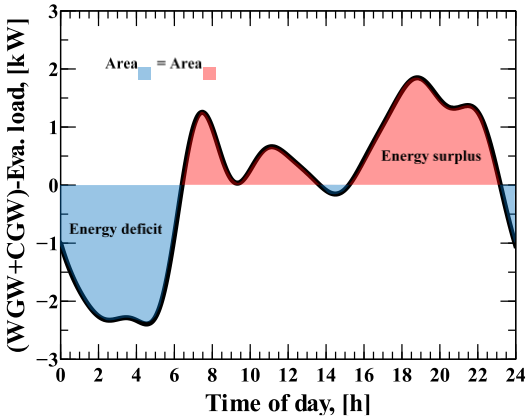

Figure 3-14 Load surplus/deficit for evaporator

3.5 Heat exchanger + TES network for full heat integration in the test building

In light of the previous composite curve analysis and discussion, and the following assumptions, the HE+TES network can now be designed. These assumptions will be helpful in deriving the HE+TES network from the Time Slice Model results:

I. First priority is direct heat exchange between time co-existing streams with a feasible temperature difference for heat transfer

II. Composite curves present the amount of energy for storage in both TES hot and cold zones

III. When assigning streams for hot zone thermal energy storage, priority goes to the stream with the highest temperature (i.e., STC) due to its higher quality (i.e., exergy)

IV. STC (65°C → 40°C) should first satisfy the DHW (25°C → 55°C), which was previously preheated by the WGW (from 5°C → 25°C), and if energy remains, it will be transferred to the HFH (30°C → 35°C). If there is still some extra STC energy, it will be stored in the TES hot zone.

The evaporator load will be fully provided by CGW and WGW from the TES cold zone (Always indirect heat exchange).

A superstructure that can make the calculated heat recovery possible (through both direct and indirect heat exchange) is designed following a "vertical heat transfer rule" [7,8], and is presented Figure 3-15. The TES has to have two zones or parts: the hot zone for storing high temperature solar energy and the cold zone for storing low temperature gray water waste energy in the test building. The dashed line heat exchangers (circles) are connected to the intermittent heat source, i.e., solar thermal collectors. The dash-dotted line heat exchangers are intermediate heat recovery loops connected to the TES.

To reduce the number of required heat exchangers, WGW (after heat exchanging with DHW) and CGW can be mixed and then exchange heat with the TES.

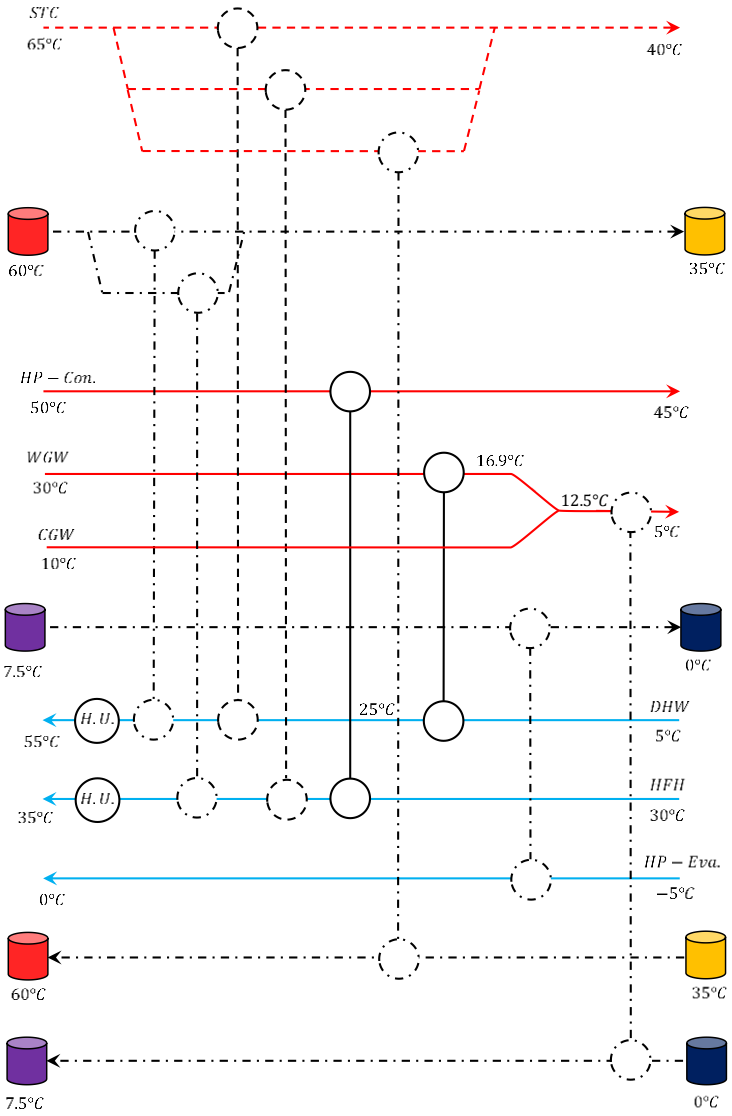

Figure 3-15 Proposed superstructure for the test building heat integration

3.6 TES design for buildings

TES can be classified into two main groups: fixed-mass variable-temperature (FMVT) stratified tanks and fixed-temperature variable-mass (FTVM) tanks. Although temperature control in FTVM is easier, the volume required by FMVT is approximately half that of FTVM, due to the natural separation of hot and cold temperature fluids within a stratified FMVT tank. Therefore, stratified tanks are selected in this study for the test building. However, stratification comes with its own difficulties, as will be addressed in this section.

3.6.1 Buoyancy effect and TES flow hydrodynamics

Hydrodynamics of the flow inside a TES tank is governed by gravity (i.e., buoyancy effect) [115,116], which simply means that the warmer current with lower density moves upward and the cooler medium flows downward. To take full advantage of this effect, TES charging and discharging access ports i.e., IHRLs, should be designed in a way that prevents mixing. In other words, the warmer streams should enter the TES always above the cooler ones.

Generally, there are three distinct regions in a stratified TES tank:

a) Top hot region
b) Thermocline region
c) Bottom cold region

The thickness of each region can be highly variable based on the available energy for storage, locations of inlet/outlet ports of IHRLs, tank height and diameter, and the thermophysical properties of the storage liquid. It is worth mentioning that TES performance can be defined by considering the thermocline thickness. A thermocline is a fluid region of high temperature gradient that separates hot and cold zones in a TES tank. It has been shown that at a fixed charging mass flow rate, the height of TES tank is an important parameter [117]. A shorter tank makes the diffusion heat transfer mechanism dominant, resulting in a large thermocline thickness and low TES volumetric efficiency. On the other hand, a taller tank contributes to a dominant advection mechanism and thus, ideally, result in a step-function like thermocline transition.

From the previous section, the maximum heat recovery contributes to the minimum tank volume determination. The integrated TES stratified tank design is completed according to the superstructure on Figure 3-15 and is illustrated in Figure 3-16. Here, it is assumed that the TES can be installed within the test building, therefore, the height of the tank was chosen as 2.2 m. Assuming the volume of 2700 liters, the tank diameter is chosen as 1.25 m.

The designed TES tank for the test building has two separate volumes: top hot zone and bottom cold zone. The hot and cold zones are separated by a 40 mm gap for mounting appropriate diffusers (please see details in Appendix A). Each zone has all three mentioned regions and the thermocline at each zone goes up and down during the charging/discharging process. The best design is to assure that the thermocline thickness remains as small as possible. Hence, 2.2 m has been selected for tank height, which results in H/D = 1.8.

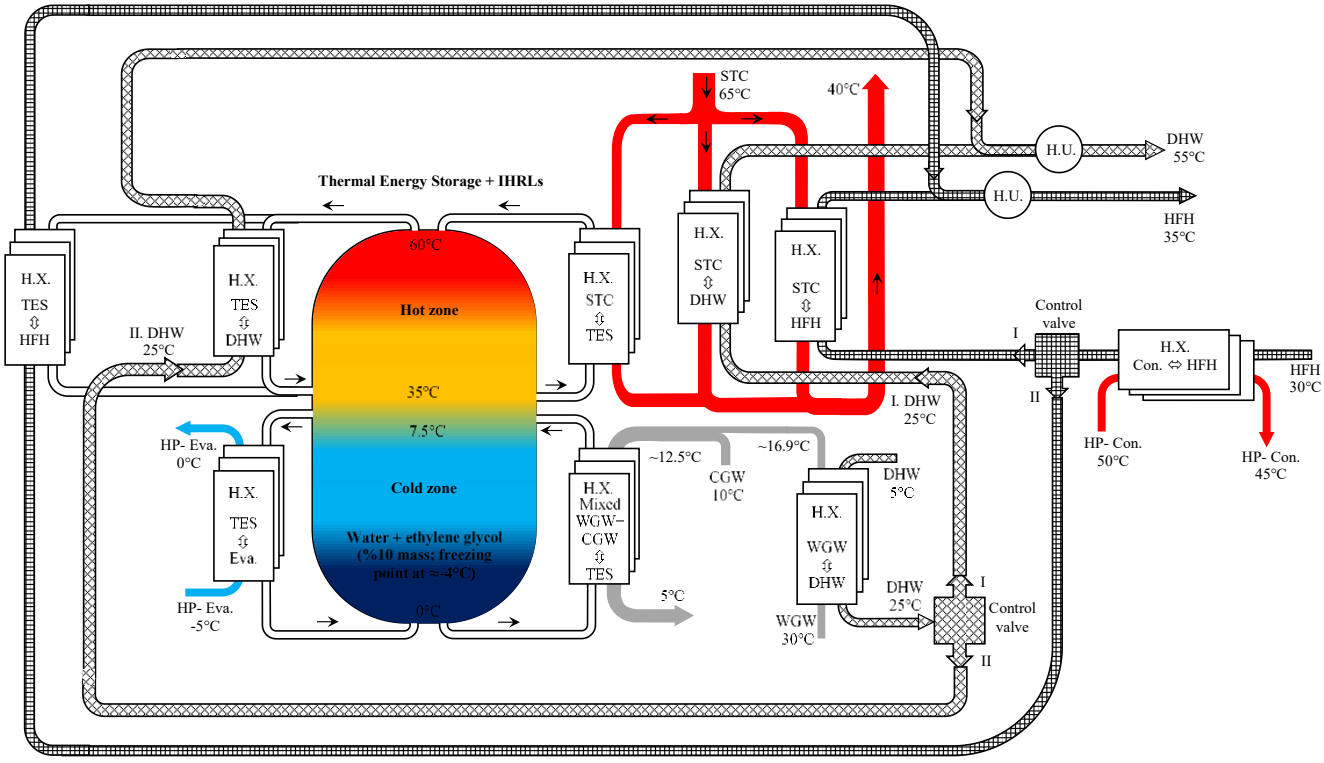

Figure 3-16 Stratified water + ethylene glycol tank integrated into heat exchanger network (temperatures in the TES are nominal, based on pure thermodynamics)

3.6.2 One-dimensional energy equation; advection-diffusion problem

Transient thermal behavior of the TES is performed in the literature in different ways according to the required accuracy and available computational capacity [118]. One dimensional modeling has been shown to be accurate enough, relatively fast and especially suitable for designing control systems [103]. Here, a one-dimensional simulation is performed to provide an acceptable estimation of thermal performance of the designed TES. In 1D modeling, the entire tank is divided into several segments with fixed cross-sectional area, where Figure 3-17 shows a schematic view of one segment (node).

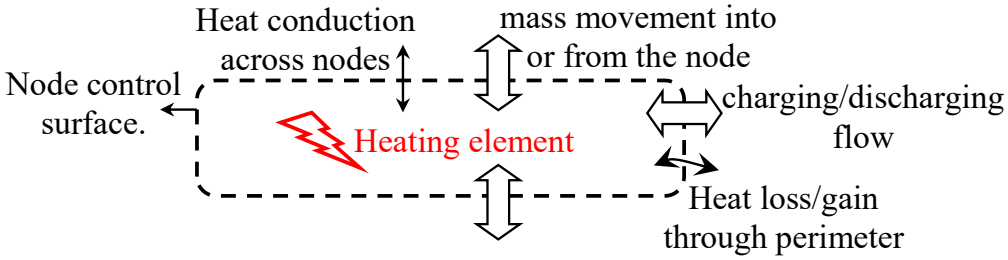

Figure 3-17 Control volume of node (i) of TES tank for 1D modeling

At each segment, the continuity equation must be satisfied, i.e., $\sum \dot{m}_{in} = \sum \dot{m}_{out}$. Temporal changes in temperature, convection term due to the bulk fluid motion, conduction between

layers, heat transfer to the environment, and auxiliary heaters are accounted for in the 1-D transient energy equation (Eq. (3-7)). Energy can enter/exit in/from the tank (via IHRLs) shown as $\dot{M}_{in}$ in Eq. (3-7)).

$$\frac{\partial T_i}{\partial t} = \alpha \frac{\partial^2 T_i}{\partial z^2} - \bar{u}\frac{\partial T}{\partial z} + \frac{A_{p,i}U_i}{\rho c_p A_i \Delta z}(T_i - T_\infty) + \frac{\dot{Q}_{Aux}}{\rho c_p A_i \Delta z} + \frac{\dot{M}_{in}(T_{in} - T_i)}{\rho A_i \Delta z} \quad (3\text{-}7)$$

Eq. (3-7) is linearized with finite difference techniques. For the second order conduction term on the right-hand side, depending on the node location, central, right sided or left sided, a second order finite difference scheme has been applied (See Table 3-4).

Table 3-4 Discretization of partial derivatives based on finite difference approximations

Nodes\Parameters	$\frac{\partial T_i}{\partial t}$	$\frac{\partial^2 T}{\partial z^2}$	$\frac{\partial T}{\partial z}$
First grid (i=1)	$\simeq \frac{T_{t+1,i} - T_{t,i}}{\Delta t}$	$\simeq \frac{2T_{t,i} - 5T_{t,i+1} + 4T_{t,i+2} - T_{t,i+3}}{\Delta z^2}$	$\simeq \frac{-3T_{t,i} + 4T_{t,i+1} - T_{t,i+2}}{2\Delta z}$
Middles		$\simeq \frac{T_{t,i+1} - 2T_{t,i} + T_{t,i-1}}{\Delta z^2}$	$\simeq \frac{T_{t,i+1} - T_{t,i-1}}{2\Delta z}$
Last grid (i=N)		$\simeq \frac{2T_{t,i} - 5T_{t,i-1} + 4T_{t,i-2} - T_{t,i-3}}{\Delta z^2}$	$\simeq \frac{3T_{t,i} - 4T_{t,i-1} + T_{t,i-2}}{2\Delta z}$

For the explicit method, the stability criteria should be considered ($\Delta t_1 \times \alpha/(\Delta z)^2 < 1/2$). Where, Δt_1 is time step, α is the thermal diffusivity and Δz is the thickness of each segment. Additionally, the well-known CFL stability criterion ($\bar{u} \times \Delta t_2/\Delta z < 1$) should be respected, where $\bar{u}$ is the maximum average velocity considering all nodes and, in all TES working hours. The final $\Delta t \leq \min(\Delta t_1, \Delta t_2)$ is selected as the working time step [119]. The mixing due to buoyancy effect is implemented in the generated code according to the model provided in [103]. At the end of each time step, when the temperature for each node is computed, all nodal temperatures are compared with the node above them. If the lower node has a higher temperature, the artificial mixing and buoyancy will be activated and the average temperatures of these two nodes will be assigned to each. These steps repeat until the difference between two consecutive nodes reaches to the desired accuracy.

3.6.3 TES performance analysis

To explore the thermal behavior of the stratified TES tank, a one-dimensional energy equation has been solved with explicit scheme, second order finite difference technique for all spatial partial differential terms and first order for the temporal one in 1D energy equation (Eq. ((3-7)).

The modeling accuracy is first validated with available experimental data with a simple cylindrical tank configuration, charging from the top [120], and as shown in Figure 3-18, very good agreement is observed. A grid independency study is performed (please see Figure A1 in Appendix A). The temperature profile with respect to the tank height did not change by reducing the grid size from 5 mm to 1 mm, therefore, this grid spacing ($\Delta z = 5mm$) is selected for the rest of this study.

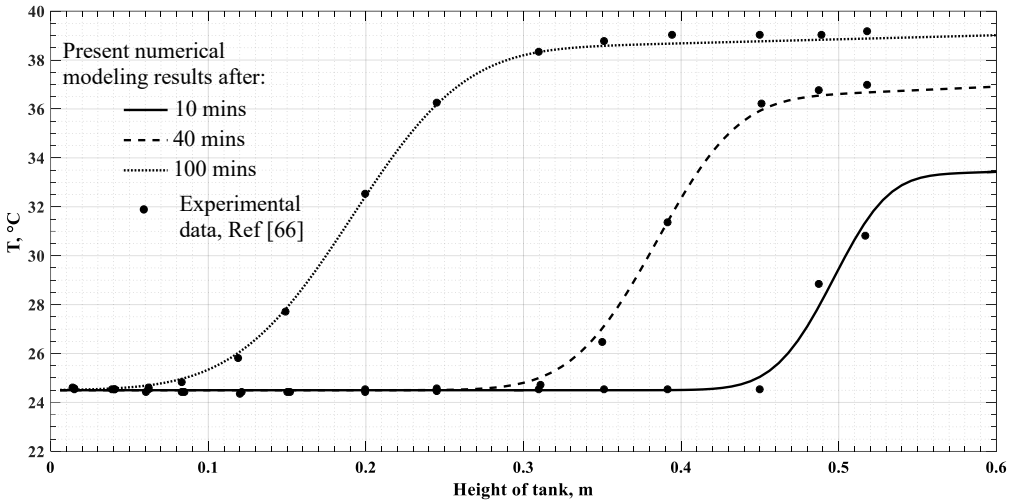

Figure 3-18 Model accuracy and validation against available experimental data [120]

Now the 1D model is applied to the configuration of Figure 3-16, with all mass flow rates variable with time. The initial temperature of the tank is set to 10°C (the tank is located inside the building, in an unconditioned space, with a nominal temperature of 10°C). Heat loss to the surrounding space is taken into account by using a U value for a typical insulation type [39] as 1 W/(m^2 K).

To attain results independent of the initialized values, three consecutive days are simulated. Figure 3-19 shows temperature versus TES height in different times of TES working hours. By starting from midnight (t = 0 hours), the evaporator is using the accumulated energy in the cold zone of the TES, therefore, this part of tank is undergoing a discharging process. The thermocline (in this zone) is moving upward during discharging process. Although mixed WGW+CGW is partially charging this part, the evaporator load (demand) is greater with respect to this small charging. Therefore, the higher energy removal results in discharging of the cold zone of the tank. This process will be reverse when the provided energy by WGW+CGW becomes higher than that of the required energy for the evaporator load. Hence, the cold zone starts accumulating energy. The exact timing can be seen in Figure 3-14 as well. Due to having a lower temperature than the surrounding environment, the cold zone can gain some energy from the environment, which is beneficial for the storage process for this zone.

The hot zone of the TES presents the same charging and discharging behavior similar to the cold zone as shown in Figure 3-19. However, there are some differences. First, despite the insulation, heat loss to the surrounding air (at 10°C) is significant. In other words, after the charging process is completed, the top tank temperature drops from 60° to 58.9°C. The heat loss continues during the discharging process. Moreover, the simulation results reveal that although the discharging intermediate heat recovery loop releases inside the TES at 35°, this temperature reduces to 32.5°C after 9 hours when the charging intermediate heat recovery loops starts loading the TES. Based on the proposed HX + TES network design (see Figure 3-15 and Figure 3-16) and pinch analysis, storage medium should enter the counter-current heat exchanger for TES-HZ charging at 35°C. However, as 1D simulation results reveal, storage fluid enters this HX at 32.5°C. Therefore, by considering fixed outlet temperature as 60°C and simple energy balance for this HX, the mass flow rate of this IHRL will reduce to recover the same amount of energy from STC hot stream. Furthermore, Figure 3-20 shows more details in the top temperature variations in both the TES hot and cold zones.

As the solar extra energy is a known value, then the higher temperature difference in the TES-HZ charging IHRL results in a smaller charging mass flow rate at 60°C. Based on the thermodynamics and pinch analysis, the hot zone can store 35.9 kWh of energy (solar in March) in a 25°C temperature difference, i.e., from 35°C to 60°C. Thus, higher temperature difference is attributed to a lower volume of the high temperature intermediate fluid, here water + ethylene glycol.

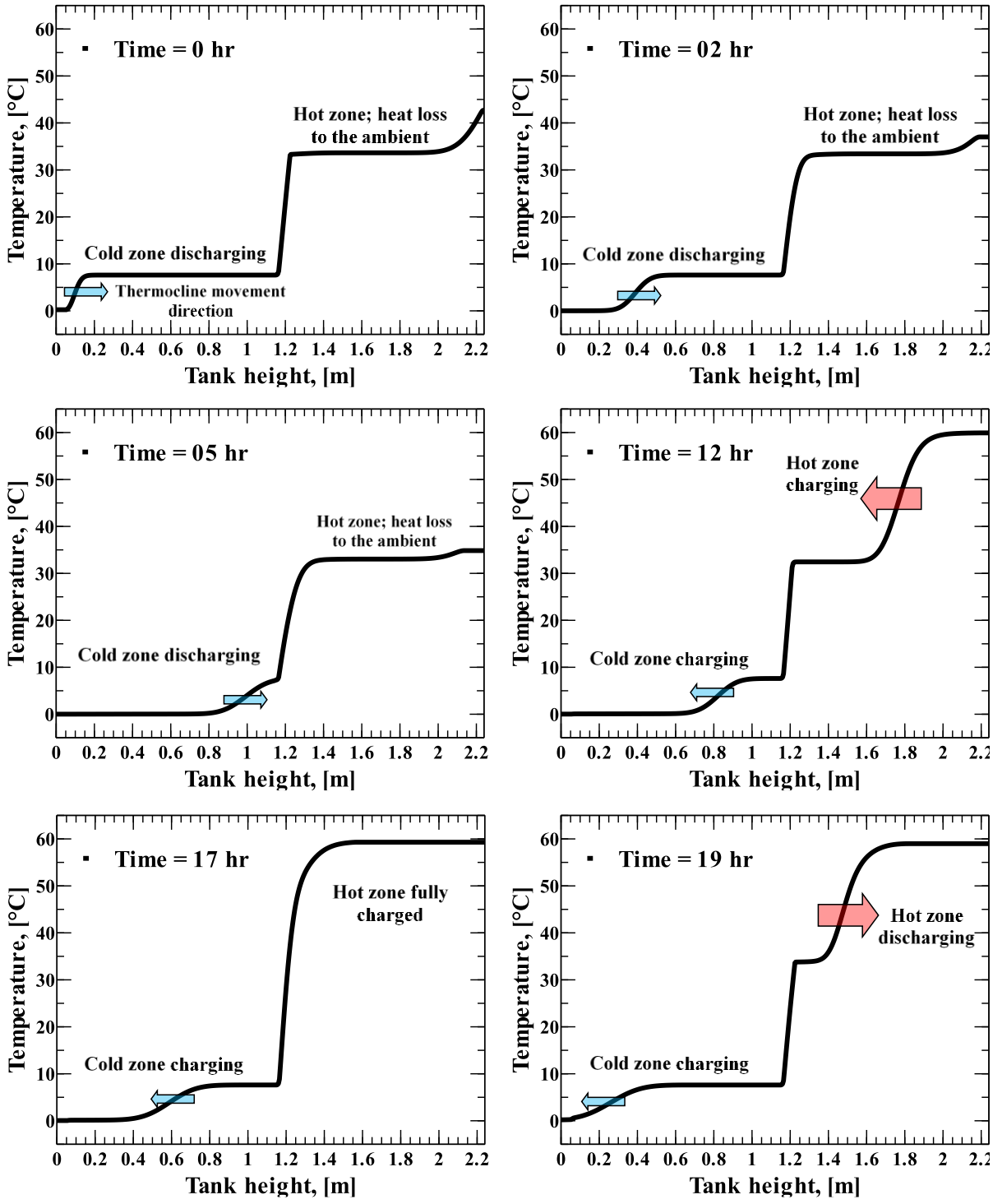

Figure 3-19 Tank temperature variation versus tank height at different hours (March solar values)

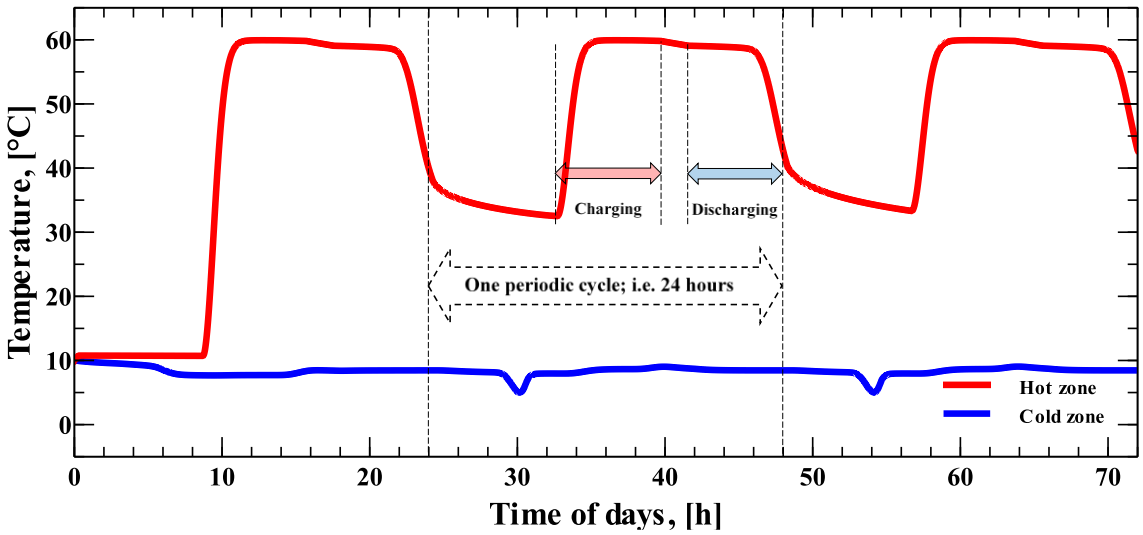

Figure 3-20 Top temperature of hot and cold zone of the designed stratified TES tank

In conclusion, there is a need to heat up both DHW and HFH by hot utility as a penalty produced by heat loss and thermocline thickness, as presented in Figure 3-21. This energy shows the importance of heat loss and thermocline thickness in designing TES systems. Thus, the proposed stratified TES can essentially provide the maximum predicted heat recovery, with less than a 2 percent reduction due TES heat loss.

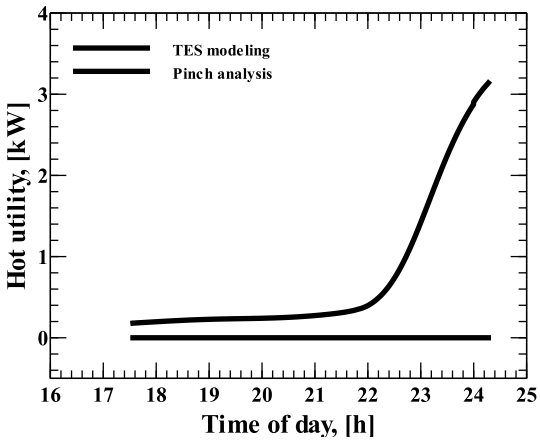

Figure 3-21 Additional hot utility penalty due to heat loss from hot zone of TES

However, it should be noted that the combined penalty of heat loss to ambient and thermocline thickness is in order of total amount of extra solar energy for storage by considering solar in December. This amount of energy can be calculated by computing the area under the solid line in Figure 3-21 as 3.7 kWh. This energy loss is 10 percent of total energy that needs to be saved in the hot zone of TES tank by considering March solar energy.

As remarked earlier, the surrounding air can heat up the cold zone of the TES, which means that the TES experiences some heat gain instead of heat loss in the lower cold part. This heat gain is not a meaningful value. The top temperature of the cold zone in Figure 3-20 shows that there is no need for an auxiliary heater for the evaporator of the heat pumping system. The minimum temperature in the uppermost part of the cold zone, from which the evaporator load is supplied, reaches 5.2°C, which is more than the required heat transfer minimum temperature difference.

3.7 Conclusion

In high latitude countries, both space heating and domestic hot water are the dominant heat sink in buildings. Possible heat sources for heat recovery can be categorized as solar energy, gray water, and heat pumping. The integration of intermittent renewable energies, such as solar thermal energy, into a building's energy system, makes the design of a TES tank a crucial task. Considering time dependent loads in a building, such as domestic hot water and hydronic heating, reveals the need for a systematic approach in the deployment of a building thermal storage system that can successfully account for all load variations during a single day. Time slice model used in pinch analysis of batch processes is adapted to include all time-varying details of the mentioned streams and to set fine time slices in order to calculate the maximum heat recovery. This strong graphical approach predicts the extra energy for a thermal energy storage tank through hot/cold composite curves. To show the capability of this approach, a cyclic analysis period of 24 hours is chosen for pinch analysis of a multi-family residential test building. There are several important concepts in designing an energy efficient stratified TES tank that have been introduced in this systematic study via a detailed time slice model. The main points in this study can be stated as:

1. All possible hot/cold streams are continuous functions of time for a test building.
2. The worst possible cases for winter are identified: December 21st (for solar energy), March 21st (for TES volume).
3. Adapted time slice model pinch analysis sheds light on computing maximum heat recovery through mixed direct-indirect heat recovery.
4. A proposed superstructure is designed to make the maximum heat recovery possible.
5. One dimensional TES modeling highlights the thermocline and heat loss effects on the predicted maximum heat recovery via TES.

For the test building case study, the TES volume of 2700 liters was calculated for the maximum energy storage in winter. Moreover, the thermal performance of the TES design was evaluated through one dimensional CFD modeling. Heat loss to ambient and presence of thermocline are two important issues which lessen the predicted indirect heat recovery through TES tank. It

worth mentioning that the pure thermodynamic analysis (pinch approach) cannot see these two adverse effects. Therefore, the results of the 1D modeling provided an insight into the thermal performance of the TES tank during charging and discharging hours. Even accounting for TES heat losses and thermocline thickness, a fully heat integrated test building equipped with a designed stratified TES tank revealed a hot utility reduction (electrical source) of at least 60 percent as compared with the non-heat integrated case.

3.8 Acknowledgements

The authors acknowledge the financial support of the Natural Sciences and Engineering Research Council of Canada for this project (RGPIN-2019-05826).

3.9 Nomenclature

a_1, a_2	Solar collector constants
A_c	Collector area
c_p	Specific heat capacity [J kg^{-1} K^{-1}]
CP = mass flow rate × c_p	Heat capacity rate [J K^{-1} s^{-1}]
d_n	Number of day in a year, starting with 1
G	Solar irradiance [W m^{-2}]
$\dot{m}_{CHTF}$	Collector heat transfer fluid mass flow rate [kg s^{-1}]
$\dot{M}_{in}$	External mass flow rate for TES Charging [kg s^{-1}]
$\dot{Q}_{Aux}$	Auxiliary hot utility [W]
t	Time [h]
t_{rise}	Sunrise time [h]
t_{set}	Sunset time [h]
T_{amb}	Ambient temperature [°C]
T_c	Average collector temperature [°C]
T_{in}, T_{out}	Collector inlet/outlet temperature [°C]
T_{max}	Maximum daily temperature [°C]
T_{min}	Minimum daily temperature [°C]
$\bar{u}$	Average node velocity [m s^{-1}]
U_i	Heat loss coefficient [W m^{-2} K^{-1}]
Greek	
α	Thermal diffusivity [m^2 s^{-1}]
Δz	Node thickness [m]
η_0	Nominal solar collector efficiency
η_c	Solar collectors efficiency
θ_z	Solar zenith angle [rad]
ρ	Density [kg m^{-3}]
Subscripts	

i	Node number

Acronyms

CFL	Courant–Friedrichs–Lewy condition
CGW	Cold Gray Water
COP	Coefficient Of Performance
DHW	Domestic Hot Water
FMVT	Fixed Mass Variable Temperature
FTVM	Fixed Temperature Variable Mass
HE + TES	Heat Exchanger + Thermal Energy storage
HFH	Hydronic Floor Heating
HP – Con.	Heat Pumping Condenser
HP – Eva.	Heat Pumping Evaporator
HU	Hot Utility
HX	Heat Exchanger
IHRL	Intermediate Heat Recovery Loop
ISSP	Indirect Source/Sink Profile
MHR	Maximum Heat Recovery
STC	Solar Thermal Collectors
TAM	Time Average Model
TES	Thermal Energy Storage
TES-CZ	Thermal Energy Storage – Cold Zone
TES-HZ	Thermal Energy Storage – Hot Zone
TPA	Time Pinch Analysis
TSM	Time Slice Model
TS	Time Slice
WGW	Warm Gray Water

Chapter 4: Numerical analysis of thermocline evolution during charging phase in a stratified thermal energy storage tank

Avant-propos

Auteurs et affiliation:

Seyed Mojtaba Hosseinnia: étudiant au doctorat, faculté de génie, département de génie mécanique, Université de Sherbrooke.

Hossein Akbari: stagiaire postdoctoral, faculté de génie, département de génie mécanique, Université de Sherbrooke.

Mikhail Sorin: professeur, faculté de génie, département de génie mécanique, Université de Sherbrooke.

Date d'acception: 07 mai 2021

État de l'acceptation: version finale publiée, 40 (2021) 102682

Revue: International Journal of Energy Storage

Titre français: Analyse numérique de l'évolution de la thermocline pendant la phase de charge dans un réservoir de stockage d'énergie thermique stratifié

Contribution au document: Les performances thermiques d'un réservoir de stockage d'énergie thermique à eau stratifiée ont été évaluées dans cet article.

Résumé français:
L'épaisseur de la thermocline (TLT) est le meilleur paramètre pour quantifier les performances thermiques des réservoirs de stockage d'énergie thermique stratifiés (TES) car elle définit la partie inactive d'un support de stockage. Une revue détaillée de la littérature révèle qu'il n'y a pas de consensus dans la communauté sur la bande de température où le TLT est quantifié. Dans cette étude, un nouveau critère de quantification de TLT est proposé qui traite de sa nature dynamique et est basé sur 1 K en dessous de T_{max} et 1 K au-dessus de T_{min} à l'intérieur d'un réservoir TES. De plus, un diffuseur de charge idéal est défini qui peut être attribué au TLT

théorique minimum à un certain rapport hauteur/diamètre du réservoir TES et débit massique de charge. Par conséquent, l'efficacité de toute stratégie d'amélioration pour améliorer les performances thermiques du TES dans des conditions de travail réelles peut être comparée au cas idéal. Le critère proposé est appliqué pendant le processus de chargement d'un réservoir TES cylindrique par dynamique des fluides computationnelle (DFC) en résolvant les équations hydrodynamiques couplées (continuité et quantité de mouvement) et énergétiques dans un domaine de calcul 2D axisymétrique pour un réservoir TES réel. La précision des résultats obtenus est validée par rapport aux données expérimentales disponibles et un bon accord est observé. L'observation principale est que le TLT minimum idéal évolue proportionnellement à la racine carrée du temps de charge sans dimension divisé par le nombre de Peclet, cependant, avec les diffuseurs réels lorsque la perte de chaleur vers l'air ambiant et l'effet de mélange sont présents, le TLT subit trois étapes de formation, à savoir, mêlant régions dominées, en développement et entièrement développées. L'évolution du TLT dans la dynamique du processus de charge du TES est rapportée dans différentes conditions de travail.

Mots clés: Épaisseur thermocline, Stockage d'énergie thermique, Réservoir stratifié, Dynamique des fluides computationnelle, Diffuseur idéal, Diffuseur de charge, Thermo-hydrodynamique

4.1 Abstract

Thermocline thickness (TLT) is the best parameter to quantify the thermal performance of stratified thermal energy storage (TES) tanks as it defines the inactive part of a storage medium. A detailed literature review reveals that there is no consensus in the community on the temperature band where the TLT is quantified. In this study, a new criterion for quantifying TLT is proposed that addresses its dynamic nature and is based on $1\,K$ below T_{max} and $1\,K$ above T_{min} inside a TES tank. Additionally, an ideal charging diffuser is defined that can attribute to the minimum theoretical TLT at a certain TES tank height to diameter ratio and charging mass flow rate. Therefore, the effectiveness of any enhancement strategies for improving TES thermal performance in a real working condition can be compared against the ideal case. The proposed criterion is applied during the charging process of a cylindrical TES tank through computational fluid dynamic (CFD) simulation by solving the coupled hydrodynamic (continuity and momentum) and energy equations in a 2D axisymmetric computational domain for a real TES tank. The accuracy of the obtained results is validated against available experimental data and a good agreement is observed. The main observation is that the ideal minimum TLT evolves proportional to the square root of dimensionless charging time divided by Peclet number, however, with the actual diffusers when heat loss to the ambient air and mixing effect are present, TLT undergoes three formation stages, namely, mixing

dominated, developing, and fully developed regions. The evolution of TLT in the dynamics of the TES charging process is reported at different working conditions.

Keywords*:* Thermocline thickness, Thermal energy storage, Stratified tank, CFD, Ideal diffuser, Charging diffuser, Thermo-hydrodynamics

4.2 Introduction

One issue regarding all types of renewable energies is their transient or intermittent nature which makes the application of a storage system significantly important. Among available storage systems, sensible stratified thermal energy storage (TES) tank has found its way into different applications ranging from domestic hot water storage in small- or large-scale residential buildings [38,49,50] to high-temperature molten salt storage in concentrated solar power plants [51–54]. The thermal efficiency of a stratified TES tank can be measured based on its stratification quality.

The stratification condition occurs in liquid-sensible heat storage systems based on the difference in density of the hot and cold liquid in a gravity field or the buoyancy force. Part of the storage medium with a smaller density tends upward to the top of the storage due to the buoyancy force and the one with higher density stays below. Therefore, there is a temperature gradient between the hot top and the cold bottom zones. This gradient zone is called the thermocline zone. The thermocline is highly influenced by fluid hydrodynamic inside a storage tank. The buoyancy force is the only force that holds the stratification inside the storage. In contrast, some other mechanisms such as momentum or turbulence-induced mixing result in fluid mixing inside the TES tank. These mechanisms are rooted in the charging diffuser, natural convection caused by heat loss to the ambient air, and heat conduction between fluid layers by diffusion mechanism inside the storage medium. All the mentioned mechanisms make the prediction of TLT a challenging task. Thus, fluid flow and heat transfer inside a stratified TES tank have been subjects of numerous research and investigations. A detailed review can be found in Chanrda and Matuska review [57].

The thermal performance of a stratified TES tank can be evaluated through numerical modeling. These can be categorized as one, two, and three-dimensional, i.e., 1D, 2D and 3D, numerical models. 1D models just solve the energy equation by considering an advection-diffusion partial differential equation with a constant average velocity inside a TES tank. This 1D equation can be solved either analytically [121,122] or numerically [103,118,123]. Both analytical and numerical 1D methods do not consider the turbulence-induced mixing inside the TES tank. This method can be improved by adding an algorithm that artificially introduces mixing effects in the 1D model in [123,124] or by including the turbulence-induced mixing as an effective diffusivity (ε_{eff}) function extracted experimentally [102]. However, in the area near the

diffuser, the numerically obtained results showed meaningful deviations from the experimental data [125–127]. Furthermore, there can be numerous different diffuser designs and it may not be feasible to experimentally extract an effective diffusivity function for each diffuser type. 2D and 3D modeling by means of computational fluid dynamic (CFD) have been performed to evaluate thermal performance of a stratified TES tank [59–61,128,129]. Common sources of error in CFD studies include the buoyancy effect via Boussinesq approximation and the adiabatic assumption for the sidewalls. Shin et al. [130] considered the buoyancy effect by using the Boussinesq approximation. This simplification inserts some errors in the simulation due to being valid in a limited temperature difference range inside a water TES tank. El-Amin et al. [131] reported the difference between the Boussinesq approximation (for buoyancy modeling) and considering the density as a polynomial function of temperature in their study. They proved that error between these two approaches is not negligible in certain cases.

Another important parameter that affects the prediction of thermocline thickness and thermal performance of a TES is diffuser shapes and types. Moncho-Esteve et al. [132] experimentally and numerically showed that changes in the diffuser shape from a simple cylinder to a cone shape one can improve the stratification performance. Al-Maraffie et al. [133] investigated the effect of different diffuser types on the charging and discharging thermal performance of a TES water tank. To damp the mixing-jet turbulent effect, they added layers of perforated plates (mesh) directly below and above the charging and intake diffusers, respectively. Chung et al. [134] numerically studied a rectangular TES water tank with three different charging diffusers: radial plates, adjusted radial plate, and H-beam shape. One main issue with their predicted results is that they assumed a laminar flow in their simulation. Recently, Findeisen et al. [135] worked on numerical simulation of different radial type diffusers in a large TES water tank (up to 6000 m^3). Their simulation results revealed that if the radial diffuser moves just 0.1 m below the top of the tank, the TLT doubles.

There is no solid definition for the ideal diffuser type that can lead to the minimum theoretical TLT in a fixed TES tank geometry and charging/discharging mass flow rates either. There have been reported studies on how changing different parameters and working conditions can reduce the TLT and improve the thermal performance of a TES tank. Nevertheless, the dynamics and evolution of the TLT during the charging process are not fully formulized, even with the ideal diffuser type. Moreover, from the reviewed studies, it can be discerned that still more investigations are required to fully understand the effect of turbulent mixing generated by the charging diffuser in TLT evaluation. As an example, it is still unclear whether the turbulence or momentum-induced mixing originated from a diffuser is a local event just affecting the area near the diffuser or its effect prolongs through the entire TES tank volume.

This study is an attempt to propose a new definition regarding TLT in a TES tank that is applicable for different TES mediums (water, thermal oil, etc.) and temperature ranges. The ideal conditions that lead to the minimum theoretical TLT are defined. The ideal TLT is related to the TES storage dimensionless numbers through a scale analysis and compared against obtained CFD results. The dynamic evolution of TLT is presented by detailed numerical modeling of a stratified water TES tank for the ideal and the real diffuser cases where the TLT is calculated by a home-made image processing code as part of CFD post processing task. Steel tank body and insulation material around it are parts of the computational domain. Therefore, the thermal performance of TES tank and the formation of thermocline can be obtained under more realistic boundary conditions in comparison to generally accepted adiabatic wall condition during the charging time of a TES tank in the literature.

4.3 A new criterion for quantifying thermocline thickness

In a stratified TES tank, the hot-charging flow enters the tank from its top through one or several diffusers or distributors. At a fixed charging flow rate, depending on the diffuser design, the turbulent mixing can be strong enough to alter the TLT through the charging process.

Figure 4-1 illustrates a schematic of a stratified TES tank that is equipped with two parallel-disks diffusers for the charging and discharging processes. Here it is tried to avoid the vertical jets by designing appropriate diffusers that guide the hot flow horizontally.

Due to the buoyancy effect the hot fluid accumulates at the top of the tank and a clear temperature gradient between the hot and cold parts inside the tank starts forming. Then, by continuous hot water charging, the mentioned gradient region develops and moves downward with a very small velocity that can be estimated by the charging mass flow rate divided by the tank cross-sectional area multiplied by the average density. There will be a section in the tank where there is a sharp temperature gradient from the hot top part to the cold bottom part as the thermocline. There is no universal formula that can predict the thickness of this temperature gradient region, i.e., TLT. This is mainly because there are several important design and working conditions which variations impact the TLT. TES tank geometrical shape and orientation, height to diameter ratio, tank wall thickness and material, insulation thickness and material, and design (configuration) of the charging diffuser are among the design variables. Storage medium, its temperature, charging mass flow rate, and the ambient air temperature are examples of storage working conditions.

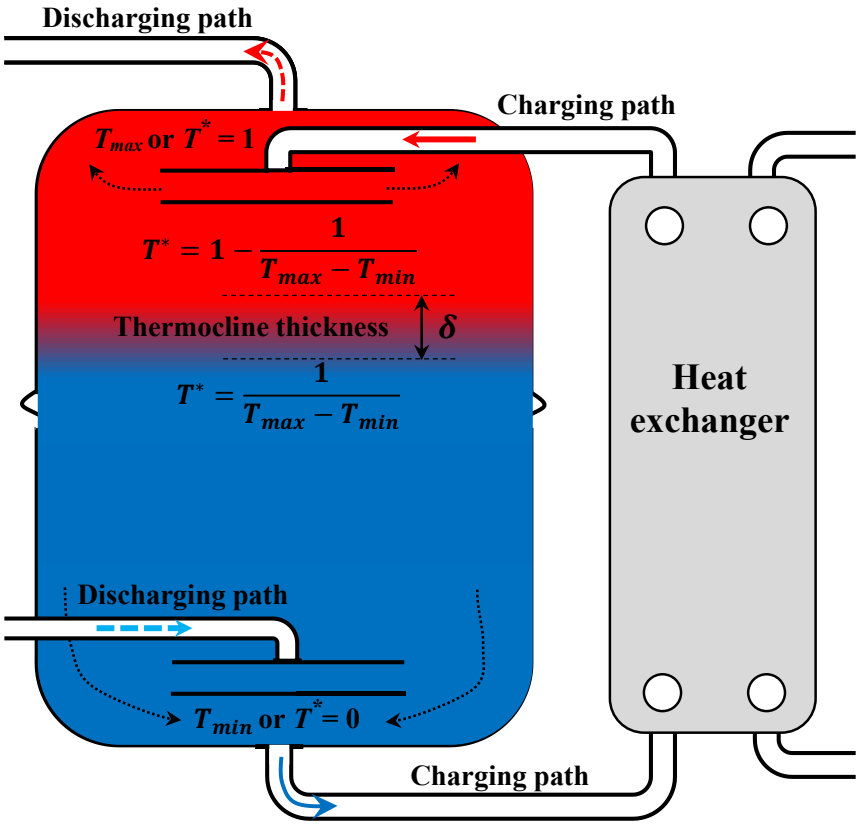

Figure 4-1 Thermocline definition (based on 1 Kelvin temperature increment/decrement) inside a stratified TES tank during charging from top

In almost all related studies, the TLT is linked to a specified value of dimensionless temperature ($T^* = (T - T_{min})/(T_{max} - T_{min})$). There is no consensus on the range of this temperature in the literature. This value has been defined in the range of $T^* = 0.01\ to\ 0.14$ for the bottom and $T^* = 0.86\ to\ 0.99$ for the top of the thermocline region [132,134,135], regardless of the maximum and the minimum temperatures inside the TES tank. In other words, the real temperatures corresponding to the top and the bottom of the TLT is directly connected to a predetermined or fixed percentage of the difference between T_{max} and T_{min} plus T_{min}. However, as mentioned in the introduction part, the higher temperature difference between T_{max} and T_{min} can attribute to a thinner TLT due to higher buoyancy force in the tank. This fact clearly shows that there is a need to define a temperature limit for TLT that is connected to the maximum and minimum temperature inside the tank.

Another important point is related to the charging and discharging of the TES tank by means of a heat exchanger. The storage medium needs to undergo a charge and discharge process by heat exchange with a high temperature source and a low temperature sink by means of passing the storage medium through heat exchangers. The heat transfer area of a heat exchanger is designed by taking nominal or design temperature values inside a TES tank. Therefore, when the fluid

inside the thermocline region enters the heat exchanger responsible for charging/discharging the TES tank, this heat exchanger performs in its off-design condition. As an example for an off-design response, at a constant mass flow rate in a counter flow heat exchanger, changing 1 K in the cold flow inlet temperature (at a fixed hot flow inlet temperatures), can attribute to a 0.75 K change in the cold flow outlet temperature [136]. Prediction of the off-design performance of a heat exchanger is no easy task [137]. Hence, to ensure the appropriate heat exchange during charging/discharging conditions, 1 K temperature difference is proposed for the definition of the thermocline thickness. In this way, based on T_{min} and T_{max} inside a TES tank, the T^* range identifying the TLT is not predetermined. These limiting temperatures can change based on the T_{min} and the T_{max} inside the TES tank. Therefore, the new proposed criterion band based on 1 K temperature difference links TLT to the maximum and minimum working temperatures.

These numbers for different thermal working conditions of TES tank are shown in Table 4-1, where $A \leq T^* \leq B$ are computed based on the proposed 1K criterion and $a \leq T^* \leq b$ is the original one assumed for TLT limits in the given reference. It can be seen that this 1 K criterion can predict the original assumed values in previous studies or provides a more accurate band for the TLT.

Table 4-1 Different criteria for TLT in the literature in comparison with the proposed one

Reference	T_{ini}, °C	T_{charg}, °C	A (1 K)	B (1 K)	a	b
Present study	25.9	50.8	0.04	0.96	-----	-----
Present study	25.9	90.8	0.015	0.985	-----	-----
Hatte et al. [67]	250	350	0.01	0.99	0.01	0.99
Wang et al. [52]	626	723	0.01	0.99	0.04	0.96
Chung et al. [134]	45	60	0.07	0.93	0.1	0.9
Kocijel et al. [105]	49	95	0.02	0.98	0.1	0.9
Moncho-Esteve et al. [132]	19.85	52.55	0.03	0.97	0.14	0.86

The followings describe the general assumptions used in this study:

- Charging and discharging does not happen at the same time, i.e., stagnant initial cold water inside the TES tank
- The discharge water flow as the submerged hot impingement jet is fully turbulent ($Re = \rho \bar{u} D_{pipe}/\mu \approx 12700 \gg 2000$) [138] in both diffuser types.

- All water thermophysical properties (density, specific heat capacity, thermal conductivity, and viscosity) are variables, functions of temperature (see Appendix)
- TES tank works at atmospheric pressure (TES tank is not a pressurized tank)
- TES tank body and insulation around it are parts of the computational domain, except for the adiabatic wall boundary conditions and the ideal case (section 4.4)
- TES wall is made of steel and the insulation is fiberglass.
- The ambient air temperature is set as the initial water temperature inside the TES tank, i.e., 25.9°C.

4.4 Ideal case for the minimum TLT

Significant efforts have been done to identify the influential parameters affecting the thermal performance of a stratified TES tank through numerous experimental and numerical studies as some have been reviewed in the introduction section. TES tank's geometrical characteristics such as shape, height to diameter ratio and diffuser design, the thickness of insulation around the tank, and finally temperature difference between top and bottom of the tank are the most influential TES tank specifications. Evaluation of the TLT in different working conditions of a TES tank can be the best way for its thermal performance assessment. Hence at a fixed working condition with a fixed geometrical design, there must be a minimum TLT that the real TLT asymptotically approaches to it via adjusting the mentioned influential specifications. Therefore, at a fixed volume and high enough height to diameter ratio, i.e., $H/D \geq 3.5$, the minimum TLT can be expected for the following ideal working conditions:

- No heat loss to the ambient air by means of perfect insulation, i.e., adiabatic wall boundary condition
- No mixing effect generated by charging/discharging diffusers, i.e., the ideal diffuser

The ideal diffuser is a diffuser that can provide a laminar flow with a velocity equal to the average bulk velocity inside the TES tank or $\bar{u} = \dot{m}_{charging}/(\rho A_{tank,cross})$. Clearly, this is an imaginary diffuser. Nonetheless, this definition helps to find the minimum possible TLT for a given set of tanks working conditions.

4.5 Numerical modeling

In this section, first, the studied geometries and mesh designs are presented. Aside from the ideal case that provides a uniform velocity and non-mixing condition which can be solved by

1D approach, the charging dynamic of the TES tank equipped with two other actual diffusers is investigated. The first one is a simple impingement jet aiming upward at the center of the top plate of a cylindrical TES tank. The second one is two-parallel disks with a gap of 1 cm and a diameter of 20 cm, (attached at the top of the just mentioned impingement-jet) where the hot charging stream enters the center of the bottom disk with the same diameter and mass flow rate as the impingement-jet diffuser.

4.5.1 Geometry and mesh design

A vertical cylinder is considered as the TES tank. Figure 4-2 illustrates several schematic views of the tank. The charging diffuser and flow outlet can be seen in the cross-sectional view. Hot water enters the TES tank through the diffusers and the cold water exits from the bottom of the TES tank.

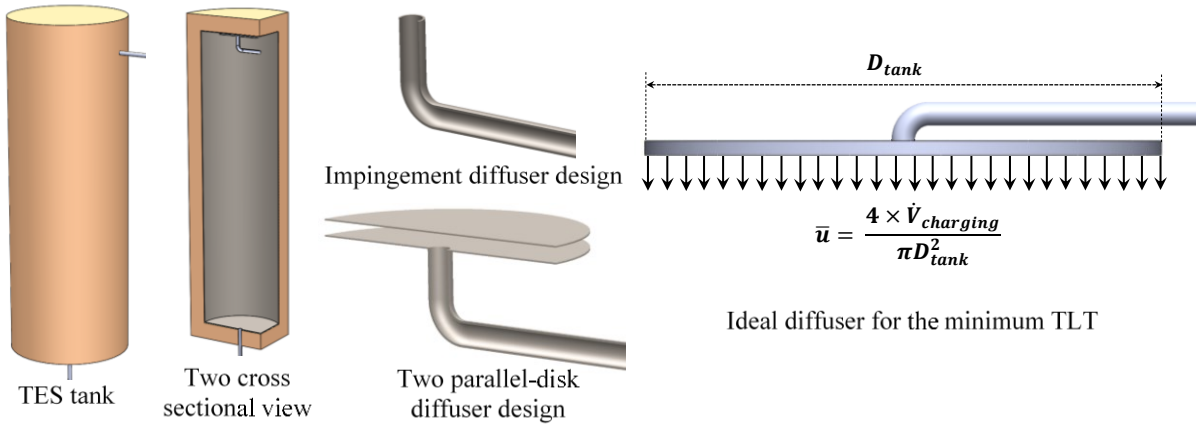

Figure 4-2 TES tank and its cross-sectional view, cross-sectional vies of all three charging diffusers

Dimensions of the tank and the mesh design are presented in Figure 4-3 and Figure 4-4. The computational domain is divided into structured non-uniform quadrilateral cells. The grids are very fine near all walls to capture are gradient and boundary layer formation near walls.

Both grid and time step independency analyses are performed. Details of the grid and time step independency analysis are presented in section 4.5.4.1.

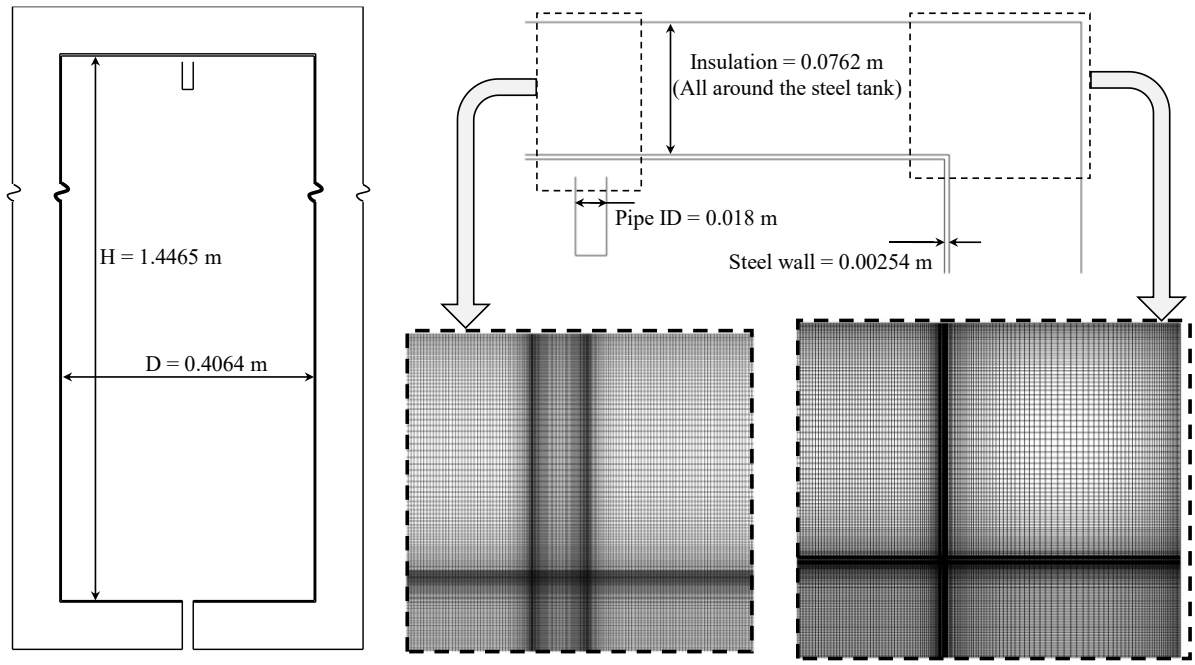

Figure 4-3 Impingement-jet diffuser in the TES tank and the mesh design

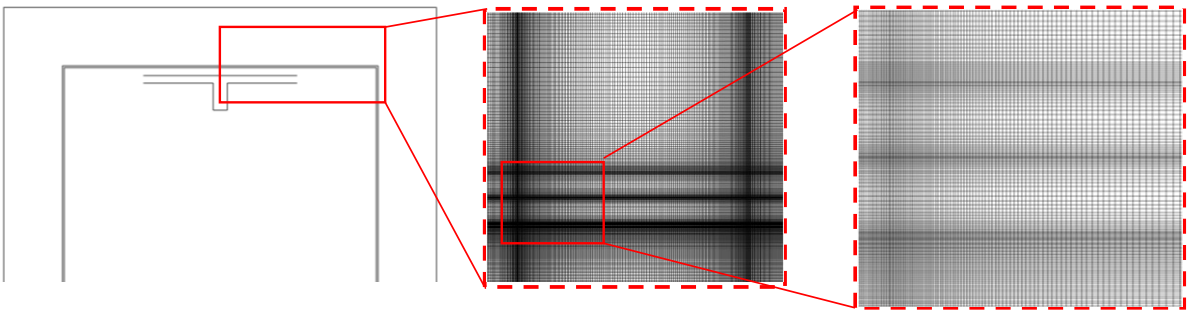

Figure 4-4 Parallel-disks diffuser in the TES tank and the mesh design

4.5.2 Governing equations

The water is the working fluid in the TES tank. The continuity equation is presented in Eq. (4-1).

$$\frac{\partial \rho}{\partial t} + \nabla.(\rho \vec{V}) = 0 \qquad (4\text{-}1)$$

where ρ is the density of water. Water is assumed incompressible and a Newtonian fluid with a density as a function of temperature, not a function of pressure (see Appendix B). $\vec{V}$ is the velocity vector. The momentum equation is presented in Eq. (4-2).

$$\frac{\partial}{\partial t}\left(\rho\vec{V}\right) + \nabla.\left(\rho\vec{V}\vec{V}\right) = -\nabla p + \nabla.\tau + \rho\vec{g} \quad (4\text{-}2)$$

In Eq. (4-2), g is the gravitational acceleration, taken fixed as 9.806 m s^{-2}. τ is the viscous stress. The momentum equation can be rewritten in the form of unsteady Reynolds-Averaged Navier-Stokes (URANS) equations [139,140]. As the impingement jets is both two real diffuser types are fully turbulent flows, the momentum equations need additional equations for turbulence modeling (closure problem) to compute the Reynolds stress terms. As the flow falls in the turbulent regime inside the connected tube to the charging diffuser with a Re number of 5000, there is a need to include appropriate turbulence model. In this study, the two-equation model $(k-\omega)$ [141] is selected for turbulence modeling. This turbulence model has been shown better results in comparison with experimental data as shown in [142]. The energy equation for the water is:

$$\frac{\partial}{\partial t}(\rho E) + \nabla.(\vec{V}(\rho E + p)) = \nabla.(k_{eff}\nabla T) \quad (4\text{-}3)$$

where E is total energy (enthalpy plus kinetic energy), k_{eff} is the effective thermal conductivity which is thermal conductivity plus the turbulent induced conductivity [141]. As the velocity is relatively small, the viscous dissipation terms are neglected. For the solid parts, the energy equation can be written as Eq. (4-4).

$$\frac{\partial}{\partial t}(\rho c T) = \nabla.(k\nabla T) \quad (4\text{-}4)$$

4.5.3 Boundary and initial conditions

The TES water tank is assumed as an axisymmetric geometry for all studied diffuser types. Therefore, the computational domain is selected as a two-dimensional axisymmetric form. Figure 4-5 shows the boundary conditions for each entity of the computational domain. From hydrodynamics point of view, all walls are assumed as no-slip condition and impermeable. The hot charging flow enters from the bottom of the diffuser at a constant mass flow rate and constant temperature. As there is no heat source inside the solid walls and the insulation layer, the heat flux that passes through all layers should be conserved. Thus, Eq. (4-5) depict the thermal boundary conditions between the insulation and the ambient air. At the discharge port, there is no information about the flow. Therefore, an extrapolation from the inner grids' values for calculating all flow variables is allowed. This is the so-called outflow boundary condition.

The initial temperature for all cases is set as the ambient air temperature that is equal to 25.9°C. The thermal boundary condition for the insulation layer adjacent to the ambient air is set as the convection boundary condition with a constant heat transfer coefficient of 30 W m^{-2} K^{-1}.

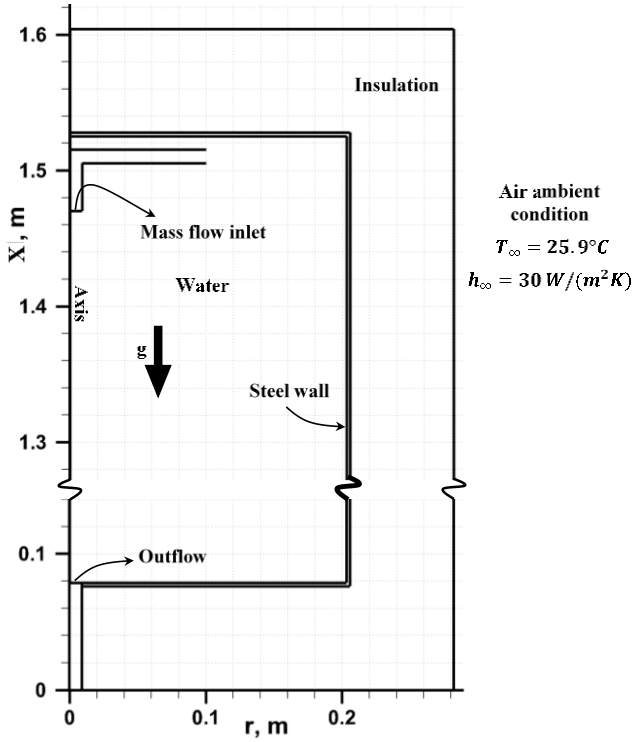

Figure 4-5 Numerical boundary conditions for the real diffusers

$$h_\infty \times (T - T_\infty) = -k_{ins}\frac{\partial T}{\partial n}\ between\ insulation\ wall\ and\ ambient\ air \qquad (4\text{-}5)$$

Figure 4-2 shows the thermophysical properties of the solid wall of the Steel tank body and fiberglass insulation material.

Table 4-2 Material properties of TES tank and insulation

material	ρ, $\mathbf{kg\ m^{-3}}$	k, $\mathbf{Wm^{-1}K^{-1}}$	cp, $\mathbf{Jkg^{-1}\ K^{-1}}$	*Thickness*, m
Steel tank	8030	16	502	0.00254
Fiberglass	22	0.038	840	0.0762

Water thermophysical properties including density, viscosity, thermal conductivity, and specific heat capacity are extracted from Engineering Equation Solver (EES) at atmospheric pressure as a function of absolute temperature. For more details, the readers are referred to the Appendix B. These functions were introduced to the finite volume solver Ansys-Fluent 2020R1 as user-defined function (UDF) code written in C++ language.

4.5.4 Solving procedure

A commercially available finite volume solver (ANSYS-FLUENT 2020R1) is utilized for the numerical analysis. Eqs. (4-1) to (4-3) and turbulence kinetic energy (κ) and dissipation (ω) are discretized with a second order upwind scheme to minimize the numerical diffusion. The well-

known SIMPLE algorithm is utilized for coupling between the pressure and the velocity fields [143]. All the equations are solved implicitly through time marching with the appropriate time step size. The convergence criteria are set as 1×10^{-6} for all equations, except for the continuity equation, where the convergence criterion is set as 1×10^{-5}. Simulations were run on two separate Intel® Core (TM)i7 (6700 CPU@3.40GHz with 16Gb RAM each) workstations, using a parallel solver. The average simulation run time was about two days.

4.5.4.1 Grid and time step independency analysis

To quantify the best number of grids, a grid independency analysis is performed. The results are compared, and the best cell number is selected for the rest of the simulations. The grid size near all walls is very fine, approximately 0.00005 m for the first cell, adjacent to the wall. Three main sizes in the axis direction of the cylinder are selected as 0.00025 m, 0.0005 m, and 0.001 m, while the cell width varies from 0.0005 m to 0.002 m in the r-direction, resulting in 2.5, 1.25, and 0.6 million cells, respectively. The variation in the temperature at different times during charging of the TES tank are compared and the results show that the maximum deviation between 0.0005 m grid size and 0.00025 m is less than 0.1%. Therefore, the main grid size of 0.0005 m has been selected for all of the reported simulations.

Although the implicit scheme is selected to solve the discretized equations numerically, a time step independency analysis is performed. It is observed that the small time steps are required in the very beginning of the simulation (during the mixing dominated region) in order of 10^{-6} to 10^{-4} seconds and the time step size can be increased to an order of 10^{-2} seconds in the fully developed thermocline region. In all grid sizes, the changes in the time step size are applied. This dynamic change in the time step size is compared with the constant small time step in one analysis to compare the accuracy of the obtained numerical data with a gradually increasing time step. The maximum value of the constant time step size was set as 2×10^{-5} sec. The maximum deviation between these two solutions is less than 0.085% in the temperature on the axis of the tank and a vertical line parallel to the axis of the TES tank (0.1 m away from the axis). Hence, the gradually increased time step values have been applied for all the reported simulations.

4.6 Results and discussion

4.6.1 Validation of CFD simulation

To illustrate the accuracy of the numerical results obtained in this study, the results are compared with the experimental data [102] and it is shown in Figure 4-6. The CFD simulation was performed for a cylindrical tank with geometrical and boundary conditions identical to the mentioned experimental study. The geometry of the TES tank is described in section 4.5.1. The

TES tank is equipped with the impingement-jet diffuser type, and it undergoes a charging process. Table 4-3 shows all the charging parameters and *H/D* of the base case numerical simulation. The CFD results are in good agreement with the experimental data.

Table 4-3 Charging parameters of the base CFD case according to the experimental case studied in [61]

Charging flow rate (lit/min)	Charging temperature (°C)	Initial temperature (°C)	TES tank volume (lit)	*H/D*
5.92	50.8	25.9	188	3.5

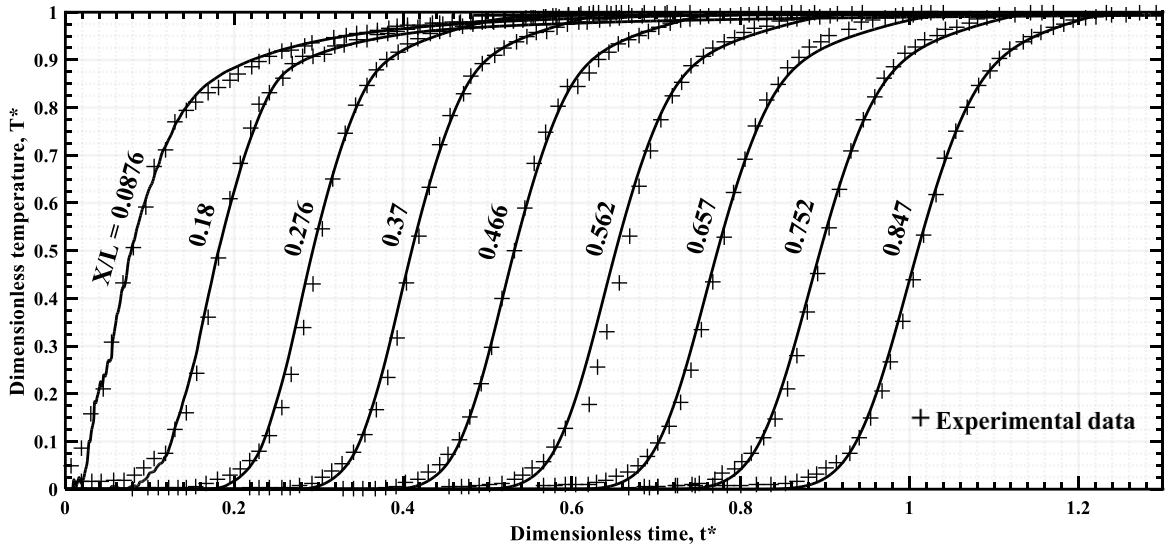

Figure 4-6 Comparison between the present study and experimental data [14]

It is worth mentioning that Zurigat et al. [102] used their obtained experimental data to extract the effective diffusivity coefficient for their 1D simulation. In their 1D model, it was observed that adding an effective diffusivity factor can predict the effect of turbulent mixing induced by the diffuser in the areas far enough from the charging diffuser. In other words, with the modified model, still, the area close to the charging diffuser experiences a higher mixing effect that makes it considerably hard if not impossible for a 1D model to predict the temperature profile correctly. It should be added that although their 1D model (equipped with an experimentally obtained effective diffusivity) predicts the temperature profile far from the charging diffuser reasonably accurate, there are some deviations from measured experimental data. This type of error is part of simplified 1D modeling nature. This inherent nature can lead to a higher error percentage especially in TES tanks with large diameters where even a 1 cm error in predicting TLT can result in meaningful volume changes. Therefore, a 2D CFD simulation that includes all hydrodynamic, turbulence, mixing and buoyance effects predicts the thermocline dynamic behavior and variations with higher accuracy than any modified 1D model.

4.6.2 Thermocline thickness dynamics in the ideal case

In section 4.4 the conditions for an ideal diffuser capable to address the minimum theoretical TLT are discussed. The TES tank working conditions for the ideal case are as presented in Figure 4-7. Constant velocity is the boundary condition for the entire top plate of the TES tank that resembles the ideal diffuser functionality.

Figure 4-7 presents the time dependent TLT based on the proposed 1 K criterion extracted from CFD simulation with the ideal case conditions at four different *H/D* ratios, at a constant charging volumetric flow rate, i.e., 5.92 lit/min, and at a fixed charging temperature of 50.8°C. For the specific case of *H/D* = 3.5, the ideal constant velocity is 0.000761 m s^{-1}. The volumetric flow rate is constant for all simulated *H/D*s, therefore, the ideal velocity can be easily calculated for all other *H/D* ratios.

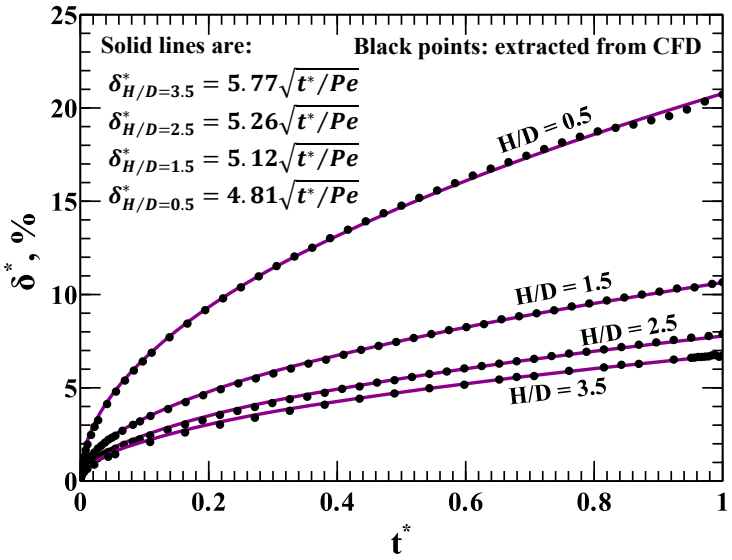

Figure 4-7 Dimensionless TLT for the ideal case of the TES tank configuration

As it can be seen, the TLT follows a dynamic behavior that can be predicted as a function of the second root of the dimensionless time, i.e., *t**. Clearly, the ideal TLT is not constant during the charging process, it varies from a thin layer at the beginning of the charging process to a relatively thick one at the end of the charging process. There are three main concluding points here:

1. The maximum TLT is 21% of the height of the tank at the worst-case *H/D* ratio, i.e., 0.5, and 7% of the tank height at *H/D* = 3.5.
2. H/Ds above 3.5 (not shown in Figure 4-7) can marginally reduce the TLT. This finding is in accordance with the reported experimental data in [144]

3. In the ideal case where the mixing and heat loss to the ambient air is completely ignored, one dimensional advection-diffusion energy equation, i.e., Eq. (4-6), is the governing one. As a strong temperature gradient locates the thermocline zone, the first term on the left-hand side can be scaled with the diffusion term or the right-hand side.

$$\frac{\partial T}{\partial t} + \bar{u}\frac{\partial T}{\partial x} = \alpha \frac{\partial^2 T}{\partial x^2} \tag{4-6}$$

Therefore, the TLT can be scaled with the square root of time or in a dimensionless form as derived in Eq. (4-7).

$$\begin{gathered} \frac{\partial T}{\partial t} \sim \frac{\Delta T}{t}, \qquad \alpha \frac{\partial^2 T}{\partial x^2} \sim \alpha \frac{\Delta T}{\delta^2}, \qquad yields\ to\ \ \delta \sim \sqrt{\alpha}\, t^{\frac{1}{2}} \\ \delta^* = \frac{\delta}{H}, \qquad t^* = \frac{t}{t_{max}}, \quad then \quad \delta^* \sim \frac{\sqrt{\alpha t_{max}}}{H}\,(t^*)^{\frac{1}{2}} \end{gathered} \tag{4-7}$$

The obtained CFD results for the ideal case are in good agreement with the predicted ones based on the scale analysis. In a broader sense, by defining dimensionless Peclet number as $Pe = \bar{u}H/\alpha$, the dimensionless TLT can be scaled as Eq. (4-8).

$$\delta^* \sim \sqrt{\frac{t^*}{Pe}} \tag{4-8}$$

The scale sign can be converted into an equality sign by multiplying with a constant factor depending on *H/D*, see Figure 4-7, for the TES tank charging conditions described in Table 4-3. Moreover, it worth mentioning that the thickening behavior of TLT has been observed in the previous studies [54,135] as well. However, it is for the first time that the exact dependency of the TLT on time in the ideal case condition is quantified here.

Thus far it has been shown that there can be defined a minimum TLT at a specified working condition of a TES tank. There is no way to have a smaller TLT than that of the estimated one via Eq. (4-8). As the thermocline behavior is generalized by 1D advection-diffusion equation for the ideal case, the resulting dynamic behavior of TLT can be extended to other storage mediums such as thermal oils, ionic liquids, and molten salts as well. This formula provides a quick estimate for the minimum TLT that can be added to the required tank volume prediction calculated by the thermodynamics-based approaches. It worth mentioning that the ideal case does not need a sophisticated 2D CFD simulation due to taking simplified assumptions and the presented results in Figure 4-7 can be obtained by solving simple 1D advection-diffusion equation as well. However, by taking the turbulence mixing induced by diffuser type and heat

loss to the ambient air, a 2D CFD model generates more realistic results, as will be presented in the following sections. Finally, the thermal performance of a stratified TES tank can be linked to δ^* as presented in Eq. (4-9) by calculating the ratio of stored energy to the maximum storable energy.

$$\eta_{st} = 1 - \delta^* \tag{4-9}$$

Due to the thickening nature of TLT during the charging phase, the ideal thermal performance of the TES tank reduces during the charging time. For instance, the ideal thermal performance can be as high as 93% at the end of the charging process in a stratified water TES tank at *H/D* = 3.5 ratio. The performance formula can encompass the actual TES tanks as well.

4.6.3 Thermocline formation inside the TES tank - impingement-jet diffuser case

Aside from the ideal case, the TLT varies with time in real cases not only due to the diffusion mechanism that is already discussed in section 4.6.2, but also due to the momentum/turbulence induced mixing and heat loss from the tank's walls. At the top of the TES tank, the turbulent mixing is strong due to the presence of the impingement-jet. The continuous charging jet generates circulations at the top part of the TES tank, expanding in all directions toward the walls of the tank. There is an ongoing competition between inertia force (hot jet tries to get mixed with the stationary cold environment) and buoyance force to hold the hot and cold fluid separated. By marching forward in time, the top part rises to higher temperatures, heat loss to the ambient air gets stronger. The heat loss contribution in the TLT evolution can be quantified by running one more simulation, this time with adiabatic walls. Competition among buoyance force, turbulent mixing, natural convection, and heat diffusion results in three different stages in thermocline formation from the beginning of the charging process to a fully stabilized temperature gradient inside the tank. These stages can be defined as mixing dominated region, developing, and fully developed one.

4.6.3.1 Mixing dominated region

Before the charging process begins, the entire TES tank is at a constant temperature of 25.9°C at t = 0 sec. Then, the hot water starts entering the TES tank with a hot vertical impingement jet at a temperature of 50.8°C. Figure 4-8 depicts some contours of the temperature field at different times during this stage of the thermocline formation. The generated density current propagates symmetrically toward the side walls and after colliding with the tank's walls, loses part of its momentum where the buoyancy force bends this wave upward. The main mixing between hot and cold areas happens during this reflective motion. After some fluctuations, it settles at the top of the TES tank and a relatively distinct region between the cold stationary part and the higher temperature part forms. However, the effect of the impingement jet on the temperature field can still be seen in the relatively higher temperature areas.

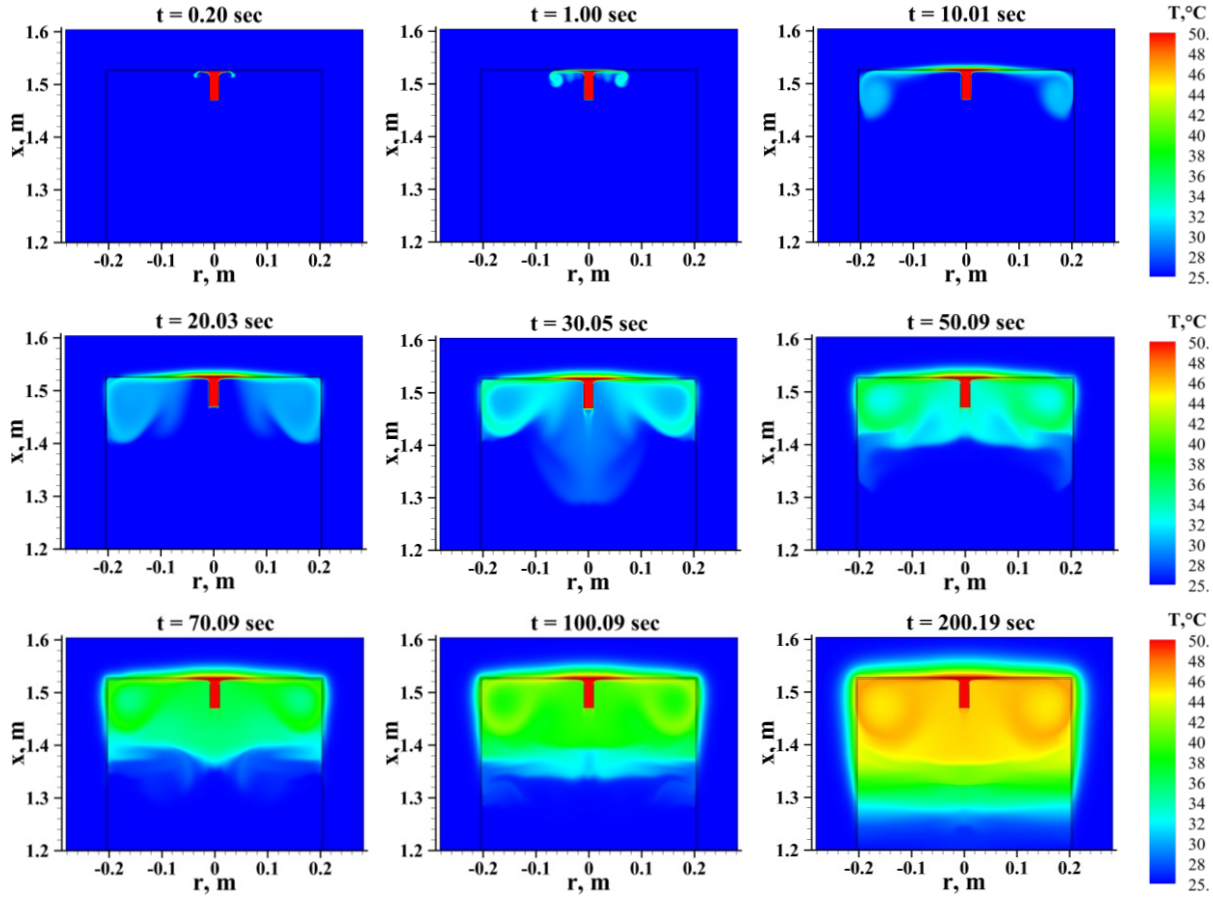

Figure 4-8 Temperature field inside TES tank at the mixing dominated region, impingement-jet diffuser

As the bulk temperature inside the top part of the tank is still lower than the charging temperature, the hydrodynamic of the flow is affected by buoyance force. As the charging continues, the top part of the tank experiences a higher temperature. When the top temperature reaches the upper boundary of defined for TLT, i.e., $T_{max} - 1$, it can be considered as the end of mixing dominated region.

4.6.3.2 Thermocline developing region

The TLT is defined as the region where $T_{min} + 1 \leq T \leq T_{max} - 1$, where in this case, TLT is defined between 26.9°C and 49.8°C, that reads as $0.04 \leq T^{*} \leq 0.96$. By considering this criterion, Figure 4-9 illustrates several contours of temperature field, limited to the defined temperature range for TLT. For a better understanding of this stage, the temperature field inside the solid wall and the insulation are not shown in this figure. The thermocline gradually takes its shape. The top part of the tank is still affected by the charging jet flow, however, after 700 seconds, a sharp temperature gradient inside the tank is recognizable. There are still some waves on the top surface of the thermocline which shows the circulations in the velocity field.

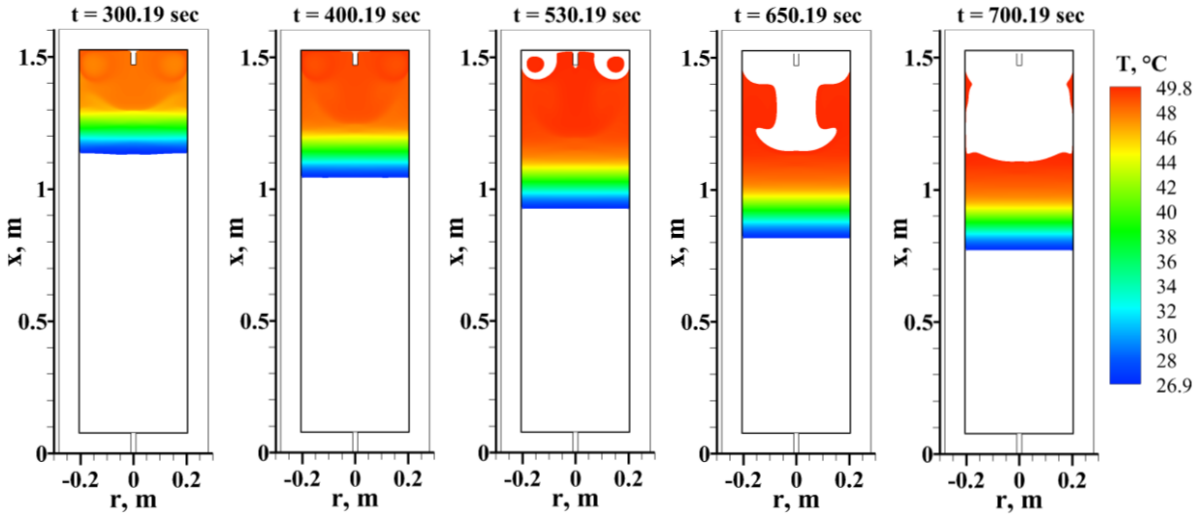

Figure 4-9 Thermocline developing region in the TES tank equipped with the impingement jet diffuser

4.6.3.3 Fully developed thermocline region

Figure 4-10 shows the downward movement of the fully developed thermocline during the charging process. There can be found slight waves on the high temperature side of the thermocline due to the turbulent mixing induced by the impingement jet. Additionally, near the full charging time, the lower part of the thermocline shows a vortex shape because of the suction from the TES tank outlet. The TLT is slightly increasing. Nevertheless, this thickness is 4 times larger than the ideal case at the end of the charging process. It shows how the combined effect of mixing, buoyancy, heat loss and heat conduction inside the TLT can increase its thickness.

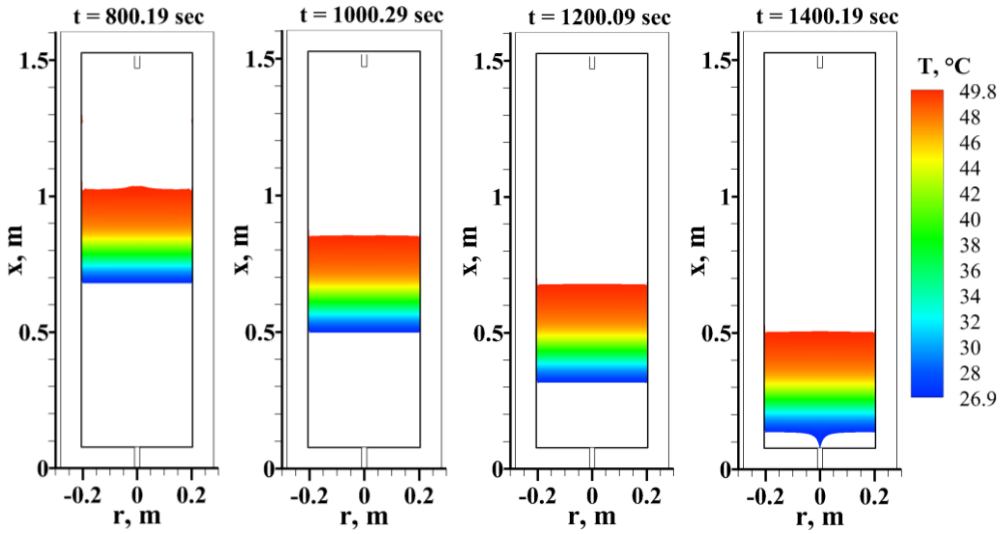

Figure 4-10 Fully developed thermocline; impingement-jet diffuser case

4.6.4 Thermocline formation inside the TES tank - parallel-disks diffuser case

Thermocline formation in the impingement-jet diffuser has been presented so far. The TLT is about 25% of the entire tank volume at the end of the charging process which can be translated into a low thermal performance of the storage tank, comparing with the ideal case. Replacing the charging diffuser from impingement-jet type to a parallel-disks type can shed light on the role of diffuser design, i.e., turbulence induced mixing, on the TLT evolution. If the main reason for such a large TLT is because of the strong mixing effect generated by the relatively high velocity inside the TES tank due to impingement jet, then this issue can be solved by avoiding propagation of the generated waves within the confines of two parallel disks. In this section, the thermocline evolution in the TES tank equipped with the parallel-disks diffuser is discussed.

4.6.4.1 Mixing dominated region

The parallel-disks diffuser fulfills several tasks. First, it avoids any vertical jet stream inside the TES tank. Second, it reduces the charging velocity. The distance between the parallel disks is 0.01 m with a diameter of 0.2 m. Water is incompressible, then the fluid passage area is 25 times larger in comparison with the impingement-jet diffuser. In other words, at the same charging flow rate, the parallel-disk diffuser discharges hot flow at 1/25 of the impingement's velocity. Therefore, the inertia force for turbulent mixing is significantly weaker. Nevertheless, the Reynolds number based on the average outlet velocity of the charging tube is high enough to be classified as a turbulent jet. The third and the main important task is that it prevents the propagation of the waves and circulations observed in the impingement-jet diffuser case. Figure 4-11 shows how small the mixing dominated region grows inside the TES tank armed with the parallel-disks diffuser. Due to the smaller discharge velocity, the mixing dominated region is smaller than that of the impingement one. Additionally, the mixing dominated phase in the charging process is shorter in comparison with the impingement-jet diffuser. In other words, 100 seconds after charging starts, a clear separation between the hot and cold parts can be seen.

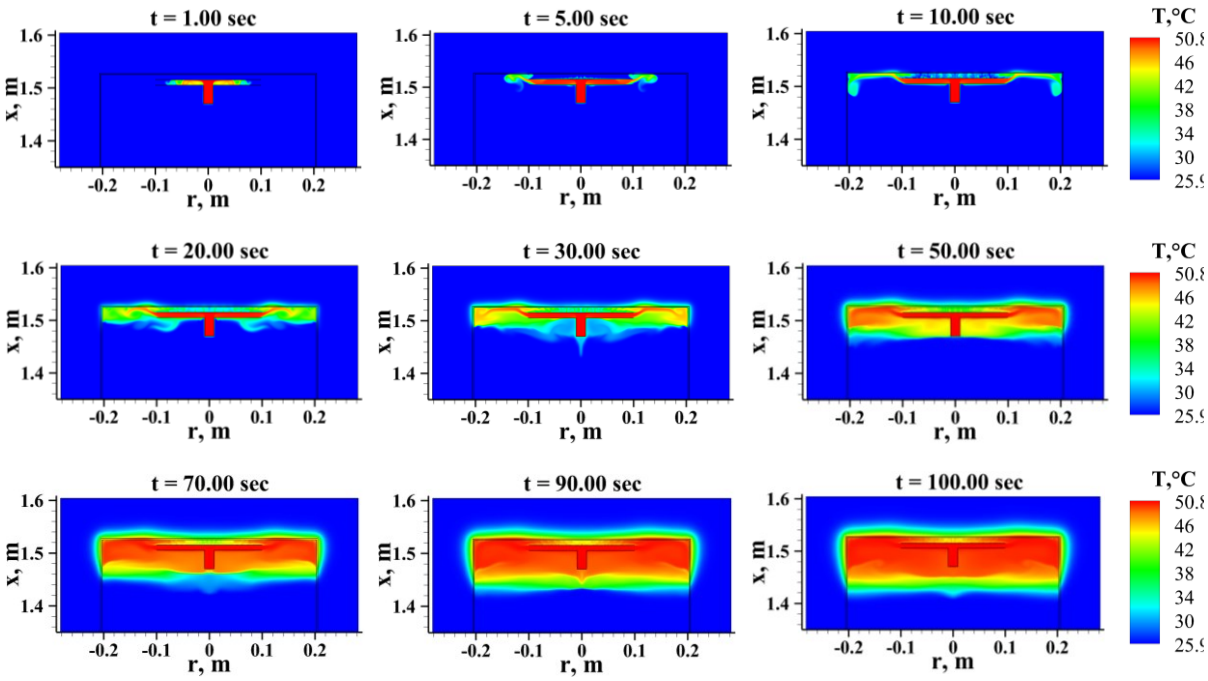

Figure 4-11 Mixing dominated region with parallel-disks diffuser

4.6.4.2 Thermocline developing region

The change in diffuser design has a very important thermo-hydrodynamics effect on the development of the thermocline inside a stratified TES tank. The parallel-disks diffuser configuration redirects the upward charging impingement jet ninety degree and limits the generated wave propagation inside the TES tank by confining it within the area between two disks. The diffuser design ramifications persist in the thermocline developing stage. The lower velocity at the same charging flow rate presents a faster and smaller thermocline developing stage. This stage in the thermocline formation with parallel disks is depicted through temperature contours in Figure 4-12.

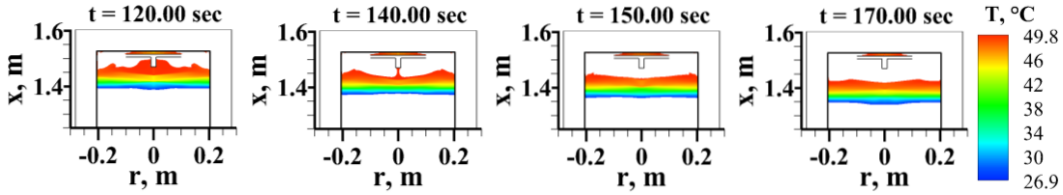

Figure 4-12 Thermocline developing stage in parallel-disks diffuser case

A glance at Figure 4-9 and Figure 4-12 reveals how diffuser design can reduce the thermocline developing stage in a TES tank, where in this case, the developing stage region shows a 1/3 reduction in the required volume.

4.6.4.3 Fully developed thermocline

As mentioned in the introduction section, one important question regarding stratified tanks is whether the diffuser design can affect TLT in the area far from the diffuser. The numerical analysis presented in this study answers this question. If one compares the fully developed thermocline at different charging times between impingement-jet and parallel-disks diffusers, it is obvious that the turbulent mixing induced by the diffuser alters the TLT in the entire charging process. Comparison between Figure 4-10 and Figure 4-13 indicates this finding. Additionally, Figure 4-13 shows that the fully developed thermocline grows up in length continuously during the charging time. The dynamics of TLT variation is discussed in the next section.

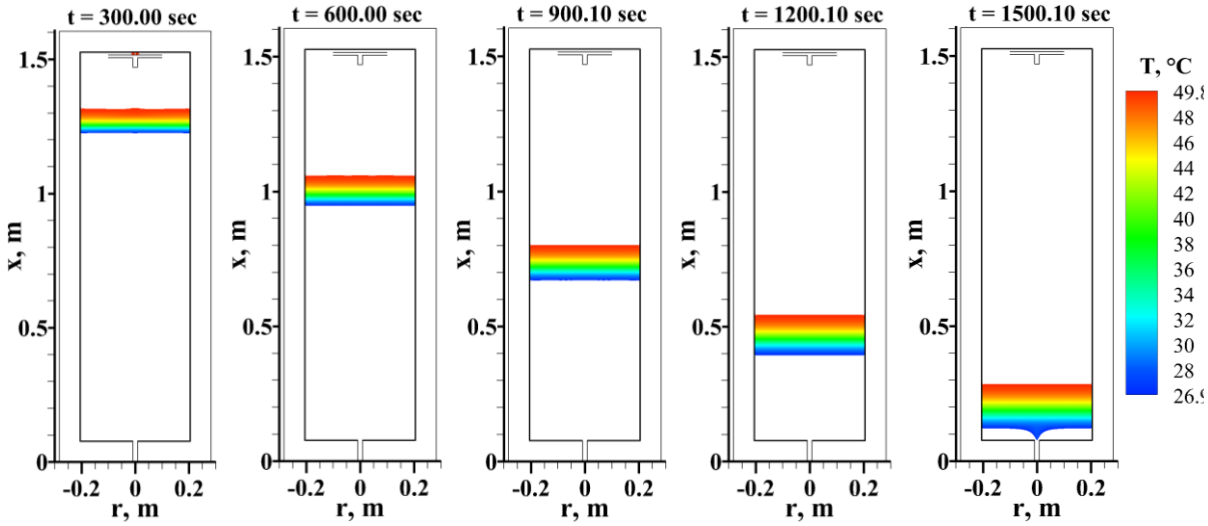

Figure 4-13 TLT in fully developed region with parallel-disks diffuser

4.6.5 TLT evolution with time

Different stages of the thermocline formation during the charging process of a TES tank are illustrated in the previous sections. It should be noted that the volume occupied by the thermocline is highly dynamic with a complex shape in the first two stages as can be seen from Figure 4-8, Figure 4-9, Figure 4-11, and Figure 4-12. Hence, a home-made code is developed by using the image processing toolbox of MATLAB 2020R2, as part of CFD post processing, that can calculate the exact volume of the tank defined as the TLT. The average TLT is assigned to the early two stages before the formation of the fully developed thermocline by dividing this volume to the tank's cross-sectional area. Figure 4-14 shows the procedure for calculating the average TLT during charging of the TES tank.

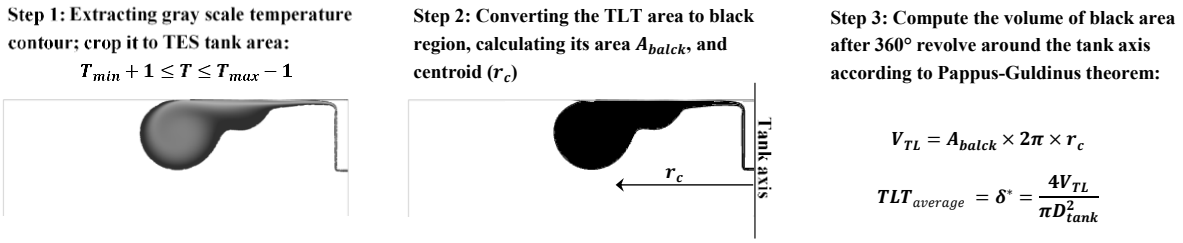

Figure 4-14 Image processing procedure for average TLT computation

The average thickness of thermoclines during the charging phase of the TES tank is shown in Figure 4-15 for the two different diffuser types. All parameters (TES tank geometry, charging mass flow rate and its temperature, insulation thickness, simulation models, etc.) are the same and just the type of the diffuser is changed. The main observations are reported here:

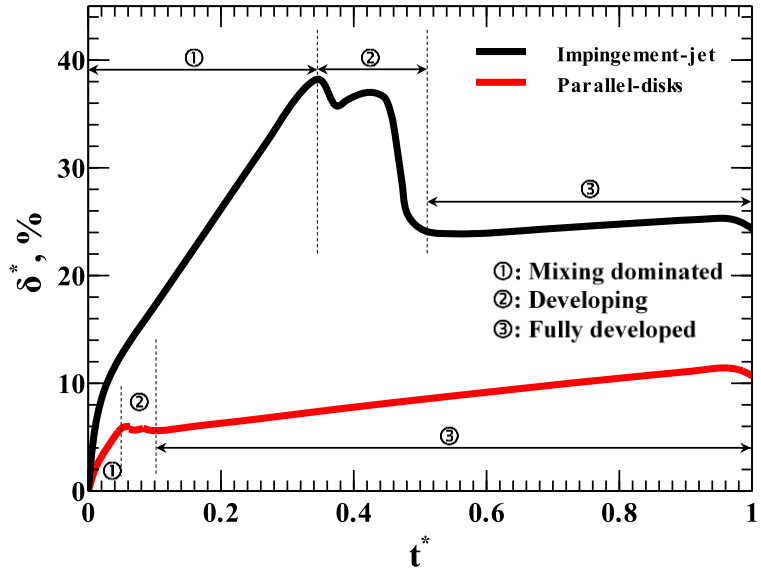

Figure 4-15 Dynamic of dimensionless average TLT

1. Average TLT in TES tank equipped with parallel-disks diffuser is approximately 2.5 times smaller than that of impingement-jet diffuser at fully developed region.
2. Thermocline can reach its fully developed form in a shorter time by a proper diffuser type, in this case, parallel-disks type.
3. In both diffuser cases and at fully developed region, TLT shows a linear increase by marching to the bottom of the TES tank. This linear increase in TLT has been seen in other studies [135]. The slope of the observed linear increase is approximately twice in parallel-disks diffuser in comparison to impingement-jet diffuser. This is mainly due to faster heat diffusion in shorter TLT.

4. Mixing induced by the impingement-jet diffuser is strong enough to affect the average TLT in the area far from the top of the tank.

Moreover, to evaluate the heat loss effect on the TLT evolution and at the same working conditions of the simulated TES tanks, two more cases with perfect insulation around the tank, i.e., adiabatic walls, are simulated. In this way the effect of heat loss on the TLT evolution can be quantified. Figure 4-16 illustrates the TLT evolution with the cases with no heat loss for both real diffuser types (results of 1D equation) and for the sack of comparison, the TLT corresponding to the ideal case is repeated in this figure.

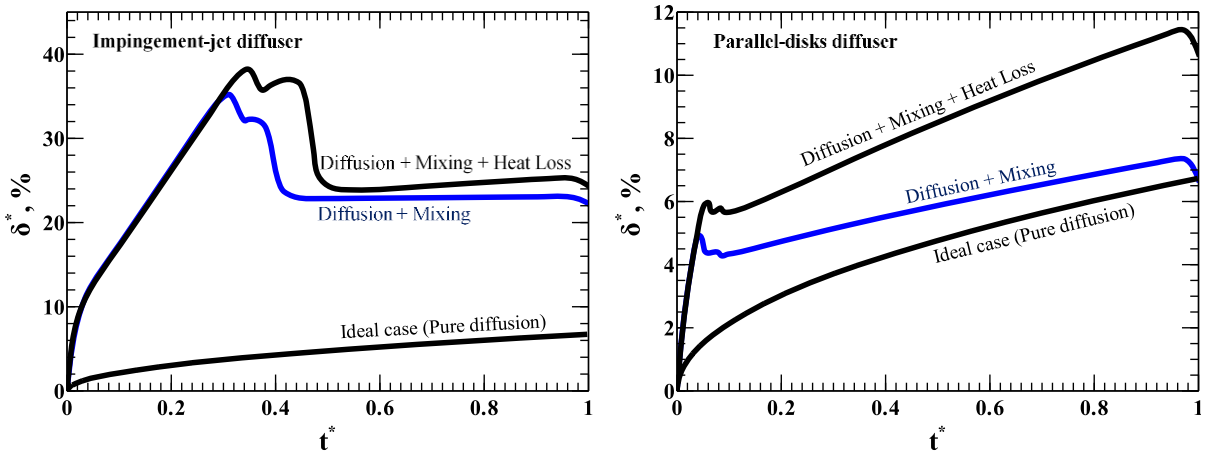

Figure 4-16 Dimensionless average TLT evolution in different scenarios, comparison between minimum possible TLT (ideal case) and actual TLT

The adiabatic wall means that there is no heat loss from the TES tank to the ambient air. Therefore, there is no natural convection boundary layer on the side walls of the TES tank and consequently, the TLT is smaller compared with the presence of the heat loss in both diffuser types. Moreover, it was shown that the generated mixing by the impingement-jet diffuser is stronger compared to the parallel-disks diffuser. This fact can be clearly seen in Figure 4-16 as well. The adiabatic wall condition can be useful in evaluating the mixing effect on the thermocline if compared with the ideal diffuser case. The TLT evolution in the ideal case is just due to heat diffusion inside the downward movement of the temperature gradient inside the TES tank. Therefore, the momentum induced mixing effect on the TLT in the actual diffuser types can be quantified by eliminating heat loss to the ambient air and comparing the result with the ideal case. In the adiabatic-wall impingement-jet diffuser case, the mixing effect multiplies the TLT by a factor of four at the end of the charging process by comparison with the ideal case. Additionally, the presence of the heat loss to the ambient air delays formation of the fully developed thermocline and makes the enlargement rate of the TLT faster.

Heat loss to the ambient air can have a profound effect on the TLT evolution when the mixing is not the dominant parameter as can be seen in Figure 4-16 with the parallel-disks diffuser case. On the contrary to the impingement-jet diffuser, the heat loss to the ambient air is the main parameter responsible for the TLT deviation from the ideal case in the parallel-disks diffuser. Elimination of the heat loss by setting the wall boundary conditions to the adiabatic one shows that the parallel-disks diffuser can achieve a TLT just 2% thicker than that of the predicted one by the ideal case.

4.6.6 Effect of height to diameter ratio (*H/D*)

Four numerical experiments are run to assess how different height to diameter ratios influence the thermal performance of a TES tank by evaluating the TLT. The working conditions such as charging flow rate, its temperature, the diffuser type, insulation thickness and all other parameters are constant and just *H/D* ratios are increased from 0.5 to 3.5. Because of a constant volume and a constant charging flow rate, after a fixed charging time, e.g., 1000 sec, a constant amount of energy is charged into the tank. Therefore, the temperature fields inside the tanks with different *H/D* ratios after 1000 sec are plotted in Figure 4-17. To have a better idea about the thermocline region in each tank, the temperature limits indicating TLT are separately shown in this figure, as well. At a low *H/D* ratio, the thermocline is still in mixing dominated region, as is predicted from Figure 4-9. It is shown that the mixing dominated region is around half of the TES tank height that is 0.6 m approximately. Therefore, if at a constant volume, with the same charging flow rate and diffuser type, the tank height stays in this limit, then there will be no fully developed thermocline, even at the end of the charging process. In other words, this shows how the turbulence induced mixing is the most influential parameter in the thermal performance of a TES tank. The dependency of thermocline height at each formation stage on the diffuser design can be seen in *H/D* = 1.5 as well, where after 1000 sec, the thermocline is still in developing stage.

At higher *H/D* ratios, e.g., 2.5 and higher, after 1000 sec in the charging process, there is a fully developed thermocline region. The TLT will be smaller at higher *H/D* ratios. This is mainly due to higher average downward velocity in the TES tank. Although the potential for heat diffusion is the same, the diffusion mechanism needs time to take effect. At higher *H/D*s, the fluid residence time is smaller due to higher average downward thermocline velocity.

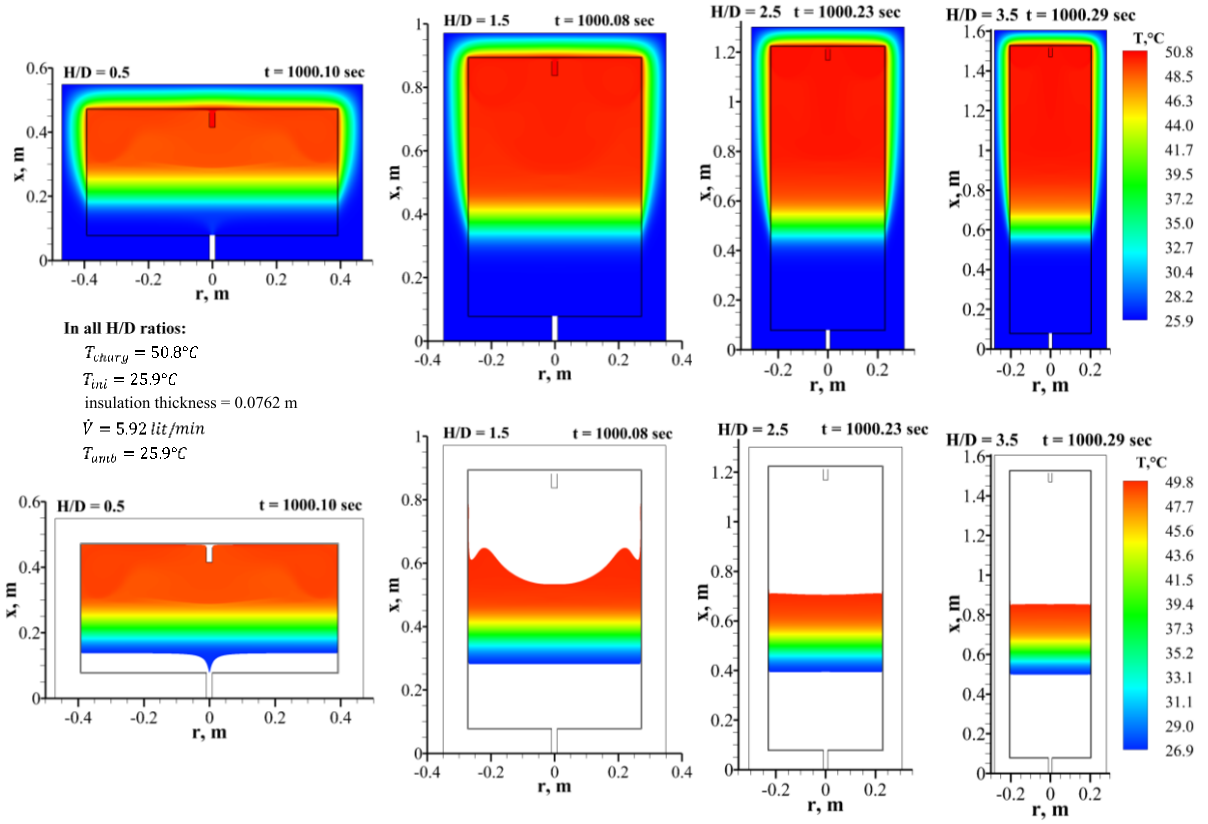

Figure 4-17 Temperature contours (top row: entire field, bottom row: thermocline region) in different *H/D* ratios at constant tank volume

Average TLT is extracted from the simulations and is plotted in Figure 4-18 for all studied *H/D* ratios. At small *H/D* ratios, the mixing effect of the diffuser prevents the formation of the fully developed thermocline. Therefore, TES tanks with small *H/D* ratios have the poorest storage thermal performance, i.e., η_{st} less than 5%. By increasing *H/D* ratio, the thermocline has the opportunity to reach its fully developed stage. The *H/D* ratios higher than 3.5 result in a very slender tank that does not reduce the TLT effectively. Even the increase in the *H/D* ratios from 2.5 to 3.5 shows a reduction in the average TLT to less than 3% at the end of the charging process.

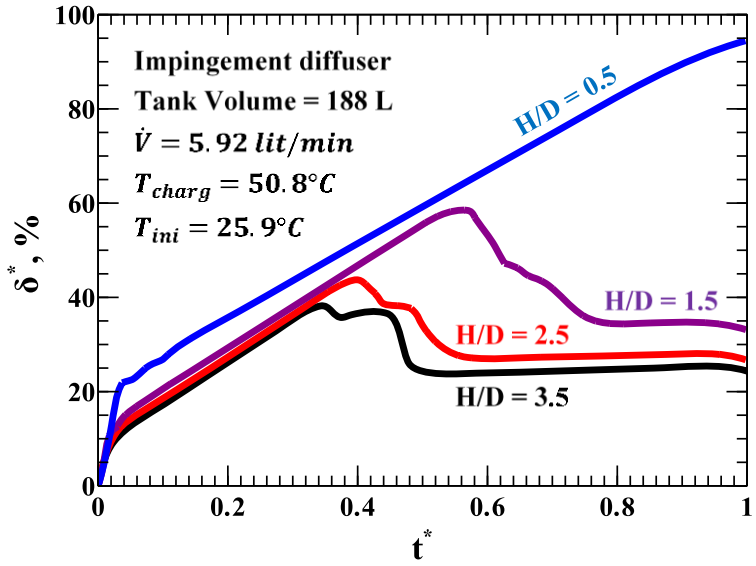

Figure 4-18 Average TLT at different *H/D* ratios - impingement-jet diffuser

4.6.7 Effect of charging-initial temperature difference (ΔT_{t-b})

A higher temperature difference between upper and lower parts inside a TES tank results in a stronger buoyancy force and consequently, a smaller TLT. In this section, at a fixed TES tank geometry (volume, *H/D*, diffuser, tank thickness and insulation thickness), fixed charging flow rate and initial temperature (25.9 °C), the charging temperature is increased, from 50.8 °C to 90.8°C, i.e., from $\Delta T_{t-b} = 24.9°C$ to $\Delta T_{t-b} = 64.9°C$. For ordinary (not pressurized) water TES tanks, 90.8°C temperature is very close to the maximum nominal charging temperature, i.e., 100°C. In addition to these cases, a TES tank with perfect insulation, i.e., adiabatic wall boundary condition, is also simulated to numerically evaluate the heat loss effect on the TLT at high charging temperatures. According to the proposed 1 K criterion for TLT, when the charging temperature is 90.8 °C, the dimensionless temperature is limited in $0.015 \leq T^* \leq 0.985$ range. The TLT is extracted during the charging phase of the TES tank. Figure 4-19 shows the TLT variations at mentioned ΔT_{t-b} and the adiabatic wall condition. As in previous cases, the TLT is not a constant value, it increases in a linear pattern after the formation of a fully developed thermocline. However, the average TLT becomes 25.3 mm smaller (at minimum difference) when ΔT_{t-b} goes up by 40 °C. Another interesting observation is the effect of heat loss to the ambient air during the charging process at high charging temperature. As is described in the introduction section, there are numerous numerical studies that assumed adiabatic wall condition for tanks' side walls. They claimed that the heat loss during the charging process is negligible. However, the TLT value and its dynamic change with perfect insulation, i.e., adiabatic wall boundary condition, shows a meaningful deviation in comparison with the case taking into account a heat loss.

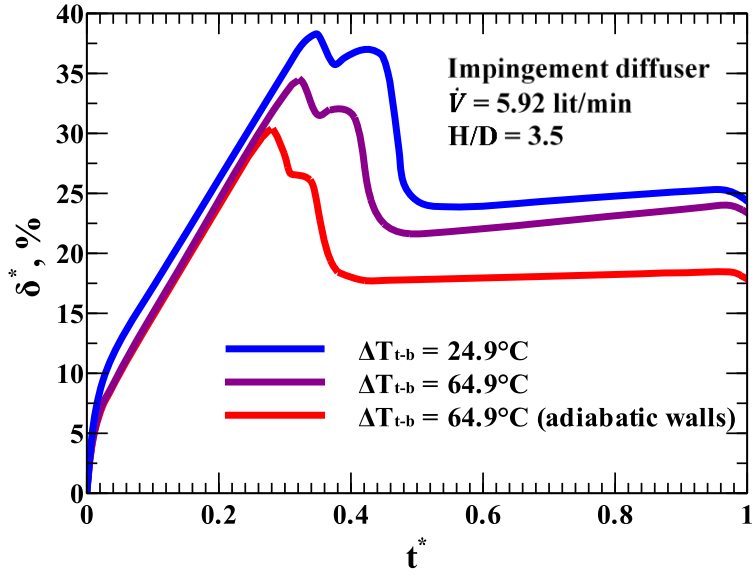

Figure 4-19 TLT variations at higher charging temperature difference

Furthermore, it is a fact that a higher ΔT promotes stratification inside a TES tank, however, it increases the heat loss to ambient as well. Figure 4-20 shows the amount of heat loss per square meter of the side wall of the TES tank for both ΔT_{t-b}. Average heat loss per square meter is 2.5 higher at a charging temperature of 90.8 °C with respect to the 50.8 °C one.

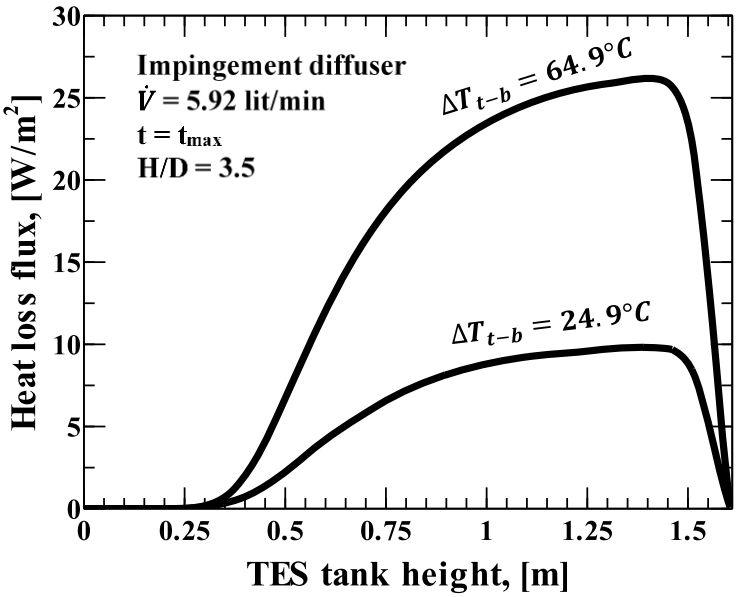

Figure 4-20 Heat loss to the ambient air in different charging temperatures

4.7 Conclusion

A TES tank is an integral part of renewable energy integration into energy systems. In all liquid sensible TES tanks, there is a region inside the TES tank with a strong temperature gradient, named thermocline. The thermal performance of a TES tank can be quantified by measuring the thermocline thickness inside the tank, especially during the charging process, as this is an inactive or dead part of the storage system. A detailed literature review reveals that there is no consensus about the temperature limits where the TLT can be measured. Therefore, in the first step a new criterion for quantifying the TLT is proposed. This criterion is based on 1 K above the minimum temperature and 1 K below the maximum one. In this way the off-design condition of the charging heat exchanger can be avoided. As it is impossible to completely get rid of the thermocline in a TES tank, many attempts have been made to minimize its thickness. Thus, there is a strong need to have an idea about the minimum possible TLT in an ideal case. In this paper, the ideal case is presented through the introduction of an ideal charging diffuser. The time dependent TLT in the ideal case is found to be scaled with the square root of dimensionless charging time divided by Peclet number. Finally, the time-dependent TLT in a TES tank equipped with two actual diffuser types (impingement-jet and parallel-disks) are numerically investigated under several TES tank working conditions.

The dynamics of the TLT with time is extracted from the numerical data by calculating the volume of the TES tank where the temperature is in the range of $T_{min} + 1 \leq T \leq T_{max} - 1$. The average TLT is computed by dividing this volume by the tank's cross-sectional area. The formation of a stable thermocline is divided into three stages: mixing dominated, developing, and fully developed. Mixing effect originated from a real diffuser and heat loss to the ambient air are two main reasons for the TLT to deviate from the ideal minimum one. The numerical results show the combined effect of two phenomena: 1. heat loss to the ambient air and 2. turbulence induced mixing on the TLT development during the charging process. The latter increases the TLT by a factor of 2 and 4 with parallel-disks and impingement-jet diffuser types, respectively, in comparison with the ideal minimum TLT at the end of the charging process. The evolution of thermocline in the TES tank equipped with the parallel-disks diffuser suggests that for well-insulated large volume storage tanks and with high charging flow rates, a cluster of parallel-disks diffusers guarantee a low momentum induced mixing, resulting in a small TLT and consequently, and can pave the way for a high storage thermal performance.

4.8 Acknowledgment

The authors acknowledge the financial support of the Natural Sciences and Engineering Research Council of Canada for this project (RGPIN-2019-05826).

4.9 Nomenclature

c_p, c	specific heat capacity [J kg^{-1} K^{-1}]
D	TES tank diameter [m]
E	Total energy [J kg^{-1}]
H	TES height [m]
L	effective length [m]
$R = H/D$	TES Tank height to diameter ratio
$Re = \rho \bar{u}_{pipe} D_{pipe}/\mu$	Reynolds number
$Pe = \bar{u}H/\alpha$	Peclet number
r_c	centroid of area occupied by thermocline region
t	time [s]
t^*	Dimensionless time; t/t_{max}
t_{max}	Maximum charging time when tank outlet reaches to $T_{min} + 1$
T	Temperature [°C]
T^*	Dimensionless temperature
T_{amb} or T_∞	Ambient temperature [°C]
T_{ini}	TES tank initial temperature [°C]
T_{max}	Maximum TES temperature (at top) equal to charging temp. [°C]
T_{min}	Minimum TES temperature (at bottom) equal to initial temp. [°C]
$\bar{u}$	Average velocity inside TES tank [m s^{-1}]
V	TES volume [m^3]
$\dot{V}$	Volumetric charging mass flow rate [lit/min]
V_{TL}	Volume occupied by thermocline region [m^3]
Greek	
α	Thermal diffusion [m^2 s^{-1}]
δ	average TLT [m]
δ^*	δ/H
η_{st}	Thermal performance of storage tank
ρ	Density [kg m^{-3}]
Subscripts	
t-b	Top mines bottom
Acronyms	
CFD	Computational Fluid Dynamics
TES	Thermal Energy Storage
TL	Thermocline
TLT	Thermocline Thickness [m]

Chapter 5: Energy targeting approach for optimum solar assisted ground source heat pump integration in buildings

Avant-propos

Auteurs et affiliation:

Seyed Mojtaba Hosseinnia: étudiant au doctorat, faculté de génie, département de génie mécanique, Université de Sherbrooke.

Mikhail Sorin: professeur, faculté de génie, département de génie mécanique, Université de Sherbrooke.

Date d'acception: 17 février 2022

État de l'acceptation: version finale publiée, 248 (2022) 123528

Revue: Energy

Titre français: Approche de ciblage énergétique pour une intégration optimale des pompes à chaleur géothermiques assistées par énergie solaire dans les bâtiments

Contribution au document: Dans cet article, l'approche de pincement dynamique est proposée pour le dimensionnement optimal de l'équipement d'une pompe à chaleur géothermique à assistance solaire dans les bâtiments.

Résumé français:
L'application de pompes à chaleur géothermiques à assistance solaire (SAGSHP) dans les bâtiments a augmenté ces dernières années. Cependant, une approche systématique pour intégrer le système SAGSHP optimal dans les bâtiments afin de répondre aux charges de chauffage/refroidissement des locaux et d'eau chaude sanitaire fait toujours défaut. Une nouvelle approche de ciblage dynamique est proposée. Il peut prévoir et garantir la récupération de chaleur directe et indirecte maximale possible dans un bâtiment donné en introduisant un réseau interconnecté d'échangeurs de chaleur (y compris l'échangeur de chaleur au sol) + stockage d'énergie (énergies électriques et thermiques) + pompe à chaleur (HP) + solaire

photovoltaïque (PV) basés sur les courbes composites chaudes et froides (CC) en temps réel. La principale nouveauté de cette approche consiste dans le fait que les charges dynamiques du bâtiment et la variation temporelle des énergies renouvelables et résiduelles sont intégrées dans la procédure de ciblage. L'approche est appliquée à un bâtiment test multifamilial, où l'irradiance solaire et les demandes de chauffage et de refroidissement du bâtiment sont prises en compte. En plus de la récupération de chaleur maximale, l'approche proposée calcule la surface minimale des panneaux solaires photovoltaïques, le volume minimal de TES et la capacité minimale de stockage d'énergie électrique pour chaque jour représentatif.

Mots clés: Source au sol, Solaire photovoltaïque, Pincement dynamique, TES stratifié, Ciblage énergétique

5.1 Abstract

Application of solar assisted ground source heat pumps (SAGSHP) in buildings have been increased in recent years. However, a systematic approach for integrating the optimum SAGSHP system in buildings in order to meet the space heating/cooling and the domestic hot water loads is still missing. A novel dynamic targeting approach is proposed. It can predict and guarantee the maximum possible direct and indirect heat recovery in a given building by introducing an interconnected network of heat exchangers (including ground heat exchanger) + energy storage (both electric and thermal energies) + heat pump (HP) + solar photovoltaic (PV) panels based on the real-time hot and cold composite curves (CCs). The main novelty of this approach consists in the fact that the dynamic building's loads and the time variation of renewable and waste sources of energies are included into the targeting procedure. The approach is applied to a multifamily test building, where the solar irradiance and building's heating and cooling demands are taken into account. In addition to the maximum heat recovery, the proposed approach computes the minimum area of the solar photovoltaic panels, the minimum volume of TES, and the minimum capacity of the electric energy storage for each representative day.

Keywords: Ground source, Solar photovoltaic, Dynamic pinch, Stratified TES, Energy targeting

5.2 Introduction

Renewable energies such as ground source and solar can be integrated in the energy system of residential buildings through introducing a heat pump (HP) to the system [48,145–148] that reduces required utilities, which results in lower greenhouse gas emissions. A recent study shows that ground source heat pump (GSHP) is the first option to provide heating for buildings

in China and the second option in European union and the US in zero energy buildings [149]. In addition to the renewable energies, low grade energies such as waste heat recovery from the used domestic hot water (i.e., gray water) is another option that has been recently iterated [3,123,150] that can preheat the city water and provide the required refrigerant evaporation energy of the HP. Also, the compressor load can be satisfied by solar energy via photovoltaic (PV) panels that introduces the solar assisted GSHP. Moreover, it should be emphasized that due to the intermittent nature of the solar energy and time-dependent characteristics of building's load such as domestic hot water, space heating (SH), space cooling (SC), integration of one or several thermal and electric energy storages (TES and EES) are required [123,151]. A SAGSHP can satisfy the required building's SC load in the summer, SH load in the winter, and the domestic hot water (DHW) load year-round [3,152,153]. As these loads are highly variable throughout a year, the optimum capacity of a heat pump system is an absolutely critical design point to be addressed.

If the SAGSHP capacity is selected based on the maximum SH + DHW loads in the coldest day of year, it is automatically guaranteed that both mentioned loads in all other days in a year can be met through heat pumping. At the same time the integration of HP system should be done in the way to minimize the total energy consumption for the building. It should be noted that this HP capacity may or may not be enough to satisfy the SC requirement in the summer. On the other hand, the SAGSHP capacity can be sized according to the maximum SC load, where again this capacity may or may not be sufficient for heating loads in the winter. No matter what load is selected as the design load for sizing the HP, sizing the optimum area of the PV panels and the capacity of the thermal and electric storages are other challenges. These challenges have their root in the intermittent nature of the solar energy during a year. In other words, the required PV panel area and EES capacity depend not only on the compressor load, but also on the daily/yearly solar irradiance and the available area for panel mounting [154].

Another important component of a SAGSHP is the ground heat exchangers. Adding ground source (GS) to HPs shows an increasing trend in recent years [155]. The GS energy has been utilized in a HP system via vertical ground heat exchangers (GHE) [156–158], mainly due to small land requirement in contrast to the horizontal GHEs. At a certain underground depth, the ground temperature can be assumed constant. The constant temperature, which is called undisturbed temperature, depends on the air temperature swing and other geographical characteristics of the area [159]. The undisturbed temperature is a good source for heat extraction/injection in heating/cooling working modes of a HP system. Moreover, the underground can be used as a solid thermal energy storage in an imbalanced building's heating/cooling loads that can reduce the depletion rate of the ground source potential in continuous and long-term energy exchange with the HP system [160].

Separate studies in the literature have been performed that present utilization of gray water + HP + TES + solar thermal collectors (STC) [3], HP + PV panels [161], GHEs + HP [153], PV panels + EES + ground source HP [154,162,163], and GHEs + PV/Thermal + TES + HP [157,164] in a building's energy system. A full list of all studies and different types of renewable energies introduced in buildings energy system can be found in [165]. All the mentioned studies are done by inspection of different integration scenarios. No one investigates the overall heat recovery from all possible sources and sinks regarding a SAGSHP integration in a building in a systematic way. Furthermore, connecting all the equipment and sizing them according to the maximum heat recovery is completely missing in the mentioned studies. The main reason is that the different integral parts of a SAGSHP are not only connected to each other from energy point of view, but also are interconnected to the other building energy streams such as gray water, SC, and SH. Therefore, there is a need to a systematic approach to integrate all of the mentioned energy sources and sinks into buildings energy system.

Pinch analysis (PA) is one of the heat integration techniques for calculating the maximum possible heat recovery in an energy system [166–168]. This technique is based on the thermodynamics laws and rigorous mathematical algorithms that allows to evaluate the minimum energy targets or the minimum number of heat exchangers (HXs) while respecting the maximum heat recovery among the hot and cold streams in an energy system for a given minimum temperature difference among streams [167]. Steady state PA, where the target and supply temperatures as well as heat capacity flowrates (CP) (i.e., mass flow rate multiplied by specific heat capacity) has been applied to buildings to evaluate the heat integration possibility. Herrera [100] extracted all hot and cold streams in a hospital at steady state condition with constant CPs. Of course, the heating is a dynamic value for a building as the outdoor condition is varying day in day out. However, in the hospital case and similar cases, they assumed constant heating load as a rough estimation to apply the basic pinch technique and understand the heat recovery opportunities. Misevičiūtė [99] applied PA to a ventilation system of a non-residential building. They extracted heating data with constant CP which means the load are not considered dynamic ones. Additionally, they did not include any renewable energies or heat pumping system in their case study.

There are also some limited pinch-based models such as time PA [9], time average model [78], time slice model [7] and adapted time slice model [123] for time-dependent streams of batch processes. Reddick et al. [3] conceptually introduced pinch technique via time average model for integrating warm and cold gray water, STC, HP and TES in a building. Different heat integration scenarios have been studied in their investigation and the profitability of each scenario is estimated based on the life cycle analysis. They did not include the TES volume and pricing in their life cycle analysis. Hosseinnia and Sorin [123] presented a systematic approach

based on the adapted time slice model PA for integration of the stratified TES in buildings. Their model successfully predicted the maximum heat recovery via both direct and indirect (through a stratified TES tank) heat exchange in buildings by constructing a TES + HX network that can achieve predicted maximum heat recovery goal. However, the entire study just focused on one single day in the winter, they did not consider the solar PV and the ground source energies.

In this study, a systematic graphical dynamic pinch approach is introduced that can provide a model for integrating all the mentioned sources of energy into the energy system of a building equipped with a SAGSHP system, where the maximum heat recovery, the minimum required hot utility, and the optimal equipment sizing can be achieved. To avoid a tedious running of the proposed approach for 365 days of a year (each day from 0 to 24 hours), 12 days are selected, each representing the dynamic building's loads, the outdoor conditions and the solar irradiance of 12 months in a year for a test building. In other words, the HP capacity, the PV panel area, the required load of GHE, the volume of TES tanks, and the EES capacity is extracted according to the dynamic hot and cold CCs via the proposed graphical dynamic pinch approach. To the best of the author's knowledge, this is the first time that a systematic pinch approach is applied for sizing and energy targeting of a SAGSHP system in buildings. Moreover, this approach has the possibility to include all possible sources and sinks of energy through the set of hot and cold streams with variable *CP* capacities. The latter gives an opportunity to design the net zero-energy buildings.

5.3 Graphical dynamic pinch approach

Figure 5-1 shows the procedure to derive the dynamic-pinch based optimum SAGSHP system for buildings. The highlighted steps are performed in this study. Therefore, the first step is to extract the time-dependent heating and cooling loads of buildings.

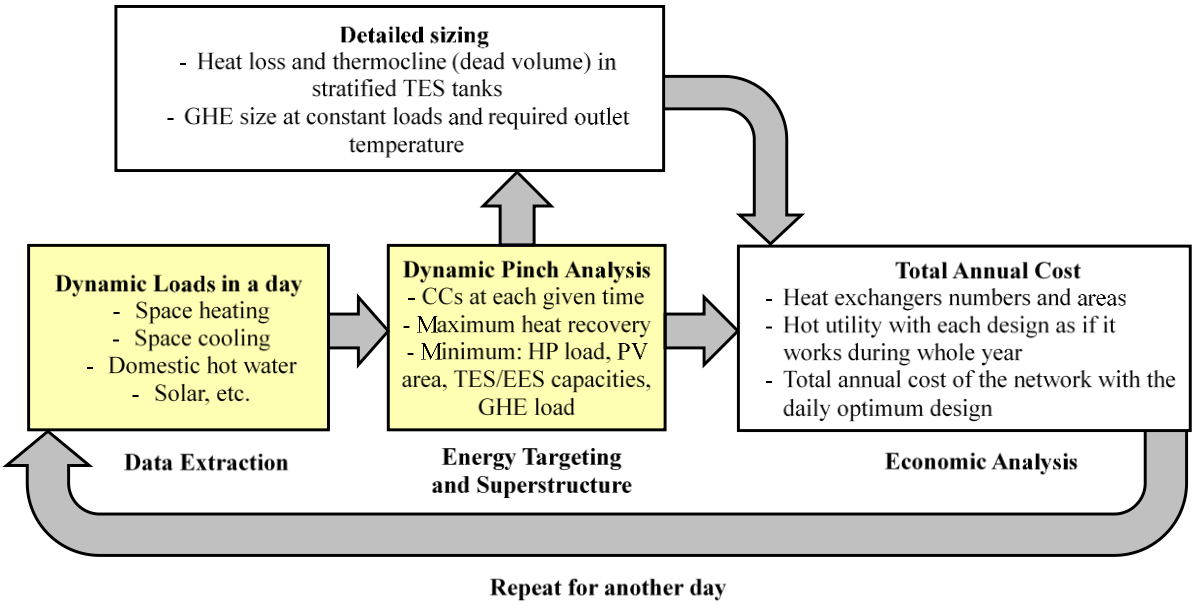

Figure 5-1 General approach for selecting dynamic pinch base optimum SAGSHP for buildings

It should be noted that the output of the energy targeting step gives the ideal minimum volume of the TES tanks and the minimum loads of the GHEs, however, for the total annual cost analysis, the practical volume of TES tanks and depth/configuration/number of the GHEs are required. The detailed sizing of these components needs a thorough hydrodynamic and heat transfer modeling/simulation [169,170].

5.3.1 Data extraction phase

In data extraction phase, all dynamic loads of a building should be computed as precise as possible. Shape, form, orientation, envelope materials, residents' expectations, the outdoor temperature, and the solar irradiance dictate the dynamic SH and SC, that a building energy system needs to address the thermal comfort in the conditioned areas. Regarding DHW load, the city water temperature, residents' usage pattern, and the desired hot water temperature can define the DHW dynamic load, and consequently, the gray water loads. These loads have been extracted for a test building and the details can be found in [3,123]. In brief, the test building is a multifamily residential building located in Granby, Quebec in Canada. The building is equipped with a hydronic floor heating (HFH) system as the SH system. An independent air conditioning system provides the thermal comfort in the hot and humid summer days.

Dynamic loads are extracted for 12 days corresponding to the outdoor conditions of 12 months. The representative days are on 21st of each month. The days are selected in a way that can cover the longest and shortest possible sunny hours (i.e., solar solstices). Figure 5-2 presents the dynamic heating, cooling, and DHW loads during one year in the representative days. It should

be noted that the cooling load in summer is assumed the same for both representative days in July and August, as the indoor/outdoor condition remains the same with a good precision. Moreover, the variations in DHW loads are close for 12 representative days. Therefore, just two general loads are shown in this figure.

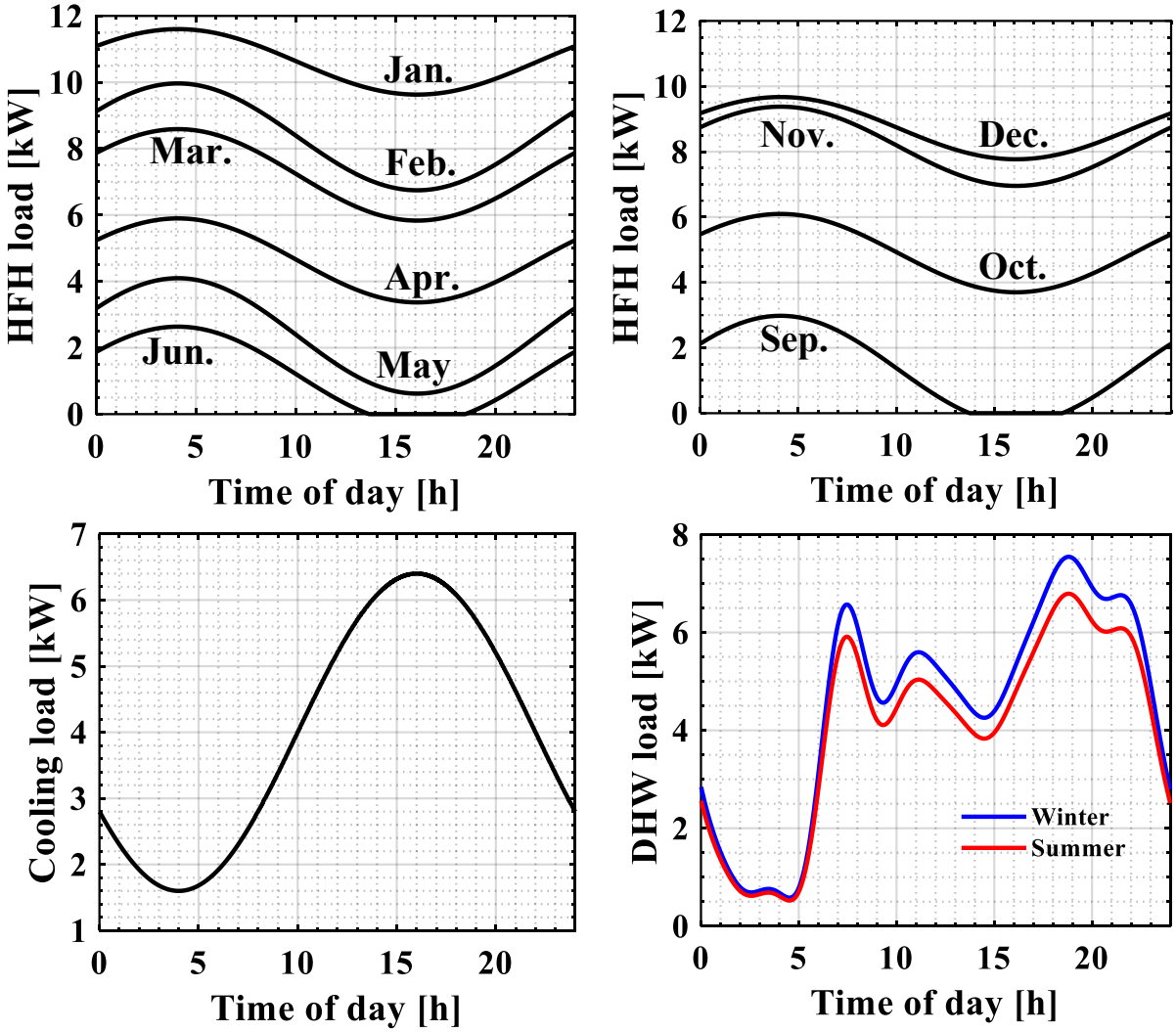

Figure 5-2 Dynamic loads of the test building in 12 representative days, cooling load extracted for a typical summer day

5.3.2 Possible renewable and waste energies

5.3.2.1 Gray water

The city water inlet temperature varies from month to month, so does the required DHW load. The outlet temperature of DHW should reach to 55°C, regardless of the city water temperature. The average city water temperatures are presented in Table 5-1 [3].

Table 5-1 Average city water temperature at different months [3]

Parameter (unit)	Jan.	Feb.	March	April	May	June	July	Aug.	Sep.	Oct.	Nov.	Dec.
T_{city} (°C)	5	5	5	8	9	10	10	8	8	8	7	6

The DHW is mixed with city water to reach to the desire temperature for bath, kitchen, etc. This used DHW is called gray water [171].The gray water can be divided into two types: warm gray water (WGW) and cold gray water (CGW) [3]. The temperature of the warm gray water is close to 30°C, while the temperature for the cold gray water is 10°C. Figure 5-3 shows the average daily flow rate (for January as an example) of the WGW and CGW. The corresponding loads can be calculated via $\dot{m}c_p\Delta T$. It should be noted that the flow pattern of both WGW and CGW are as the DHW. Therefore, WGW can be used to preheat the city water by direct heat exchanging. Both WGW and DHW are presented asterisked (i.e., DHW* and WGW*) when the preheating is performed. Furthermore, the cold gray water can be used for evaporator load via indirect heat exchange through a TES tank.

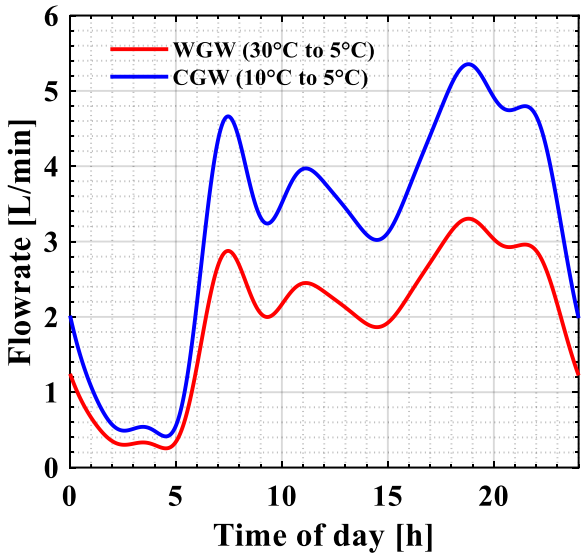

Figure 5-3 Warm and cold gray water flow rate in the test building (day in January)

5.3.2.2 Solar energy

Solar energy can be integrated into a building's energy system in two forms: electric form via PV panels or thermal form via solar thermal collectors. Here we focus on the integration of PV panels as there is a need for electricity to run the compressor of a HP. PV panels converts the solar radiation into direct current (DC) electricity. As the solar irradiance is a time-dependent parameter, the outlet power of the PV panels, Eq. (5-1), will be time-dependent.

$$PV\ Electric\ Power = A_{PV} \times G(t) \times \eta_e \quad (5\text{-}1)$$

Where A_{PV} is the solar PV panel area (m^2), $G(t)$ is the solar irradiance (W/m^2) as a function of time (Eq. (5-2) [113]), and η_e is the energy efficiency of PV panels, electric device, and inverter that varies from sunny days to cloudy days, however, it is shown that the average value can be assumed as 15% for a typical PV panel [172,173].

$$G(t) = 1362 \times CI \times \left(1 + 0.033 \cos\left(\frac{2\pi d_n}{365}\right)\right) \times \cos\left(\theta_z(t)\right) \times \sin\left(\frac{\pi(t - t_{rise})}{t_{set} - t_{rise}}\right) \quad (5\text{-}2)$$

CI is the clearness index presented in Table 5-2 as the average values [174], d_n is the number of day in a year, and t_{rise} and t_{set} are the sunrise and sunset time in hour, respectively. θ_z is the zenith angle, shown in Figure 5-4.

Table 5-2 Average *CI* values

Parameter (unit)	Jan.	Feb.	Mar.	Apr.	May	June	July	Aug.	Sep.	Oct.	Nov.	Dec.
***CI* (--)**	0.3	0.35	0.45	0.5	0.55	0.6	0.65	0.65	0.6	0.5	0.4	0.3

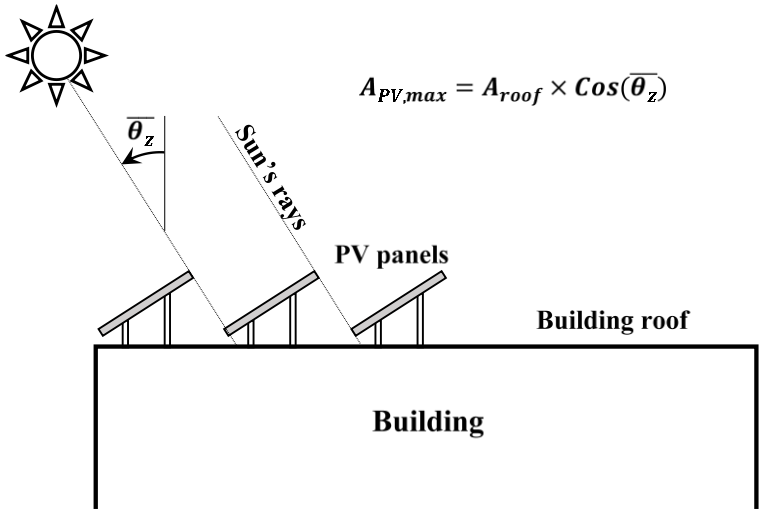

Figure 5-4 PV panel mounting area limits on the roof of buildings

The dynamic PV panel power output is plotted in Figure 5-5 for representing days in December, March, and July. In this study, the PV panel area is computed to satisfy the compressor load of the HP system solely based on the solar energy. However, there could be a limit mounting area for the PV panels. The PV panel tilt angle and building's roof area define the maximum available mounting area. To have the sun's rays always normal to the PV panels, the tilt angle should vary according to the changes in the zenith angle during each day.

However, this needs a relatively sophisticated servo motor equipment and other control systems. Therefore, an average tilt angle of 45° is selected for all 12 representative days. This value is an

average among the optimum tilt angles for all seasons [175] obtained for Montreal which is close to the location of the test building.

It should be noted that depending on the solar irradiance and the compressor load, the required PV panel area can be less, equal, or above the maximum mounting area. In the latter case, the maximum area will be assigned to the PV panel area and the rest of the required electric energy should be provided by the hot utility (i.e., grid electricity).

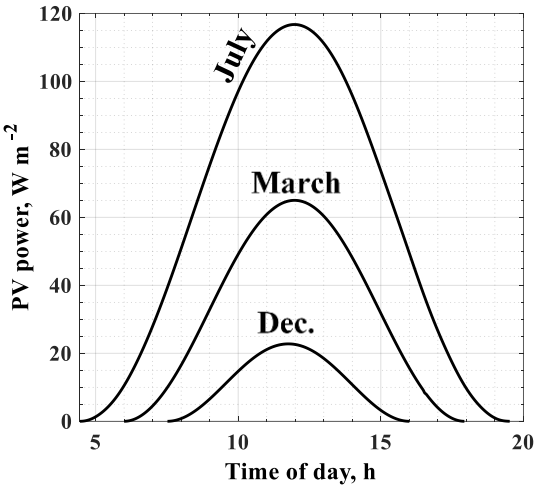

Figure 5-5 Dynamic PV panel power output in three representative days in March, July, and December

5.3.2.3 Heat pumping

HP should have the following characteristics to effectively satisfy the building loads:

- Condensation temperature should be high enough for viable heat transfer to SH+DHW loads
- Evaporation temperature should be low enough for viable heat transfer to SC
- Refrigerant environmental impact should be minimum, therefore, the available and widely used but phased out refrigerants (e.g., R410A) are not appropriate.
- The minimum pressure in the cycle should be above the atmospheric pressure to prevent air penetration into different components
- Compressor pressure ratio should be in an acceptable range, under 8, approximately [176]

- The pinch temperature of all possible streams in all times from 0 to 24 hours must be between the evaporation and the condensation temperatures
- HP is connected to TES tanks; therefore, it can work at constant load from 0 to 24 hours

In light of these facts, HP condensation and evaporation temperature with R466A [177] is proposed in Table 5-3.

Table 5-3 HP working parameters with R466A as refrigerant

Process	Temperature, °C	Pressure, kPa	Pressure ratio
Condensation	55	3594.9	5.8
Evaporation	-10	619.9	

Figure 5-6 presents the T-S diagram for the proposed HP system. Although the condensation temperature is 55°C, the maximum temperature reaches to 110.1°C. The superheat part of condensation should have enough energy to heat up the DHW to 55°C. It can be checked in hot/cold composite curves whether this level of refrigerant superheat can effectively heat up the DHW via direct or indirect heat exchange, according to the pinch minimum heat transfer temperature difference, as it is explained in section 5.3.5.1.

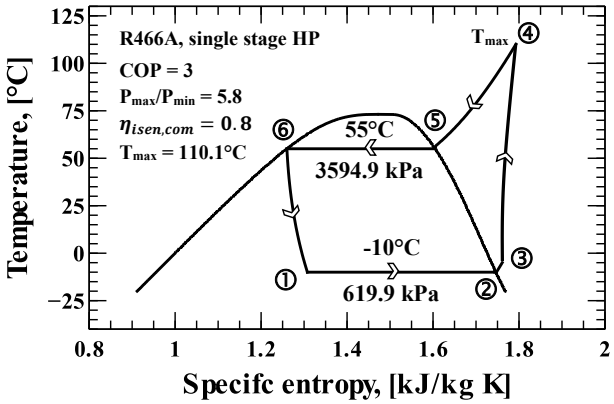

Figure 5-6 T-S diagram for the proposed HP system

Engineering Equation Solver software (Academic V10.836) is used for the HP thermodynamic modeling with R466A as the working fluid. The condenser of the HP system can deliver useful heat from point ④ to ⑥, as shown in Figure 5-6. The superheat energy is from point ④ to ⑤, where the refrigerant thermodynamic states are known as superheat and saturated vapor, respectively. According to the design load of the condenser or the evaporator, the refrigerant mass flow rate can be determined.

5.3.2.4 Ground source energy

Depending on the geographical characteristics of the ground and the maximum and the minimum air temperature in a year, the temperature of the underground can be assumed constant

below a certain underground depth [178]. There is a need for a heat exchanger for an effective heat transfer between the underground and building's energy system. This heat exchanger can have different configurations such as horizontal serpentine tubes buried 2 m underground, approximately, or long vertical GHEs with a depth of 30 m to 200 m [179]. Conventional vertical GHEs consist of a single or double long PVC U-tube embedded deep inside a vertical hole (i.e., borehole), as it is illustrated in Figure 5-7. The heat transfer fluid passes through the U-tube and exchange heat with the constant temperature medium of the underground.

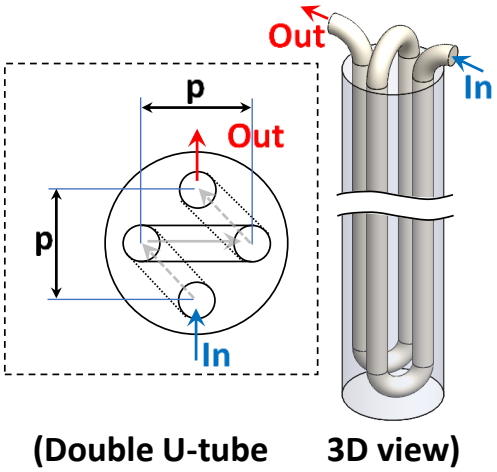

Figure 5-7 A schematic of a double U-tube GHE with a cross-section view, p = 4 inch and borehole diameter is 6 inch, PVC U-tube diameter is 1 inch, the depth of GHE defines the GHE's load and outlet temperature [170]

Two working modes for the vertical GHEs should be defined: heat extraction mode which works during the building's heating months and heat injection mode which works during the building's cooling months. In the former, the energy is extracted from the ground by means of circulating a cold heat transfer fluid (HTF) inside the vertical GHEs, while in the latter, all or part of the extracted energy during the heat extraction mode is replenished into the vertical GHE by circulating a hot HTF into the vertical GHE. The HTF is water + ethylene glycol with freezing point of -8°c as will be explained in section 5.4.2. The heat injection part can be of crucial importance because if the heat extraction process continues for a long period of time (e.g., for several months in the heating months) without any active replenishment, the heat transfer potential of the vertical GHE diminishes and the outlet temperature and/or the delivered load cannot meet the design set points [170,180]. The term active charging or energy replenishment is used versus the passive charging by the solar energy heating the ground surface. The passive charging is, in contrast, meaningfully slow.

In this study, the required load and outlet temperature of the vertical GHEs are computed based on the dynamic PA requirement, given that the load and temperature should be evaluated in the

context of the energy targeting by considering all hot/cold streams of the system. The temperature set points of a GHE can be obtained based on two main parameters: the undisturbed ground temperature and the minimum temperature difference for effective heat transfer. The effective heat transfer is guaranteed by considering a minimum temperature difference in the PA. In this study, it is set as ΔT_{min}= 5°C. Therefore, the nominal or design inlet and outlet temperatures of a GHE is determined as is shown in Figure 5-8. The undisturbed ground temperature is considered as 10°C in the case of the test building location as it is relatively close to Montreal, where the undisturbed temperature is measured in [181,182], experimentally. The red solid line in Figure 5-8 presents the temperature range of HTF in the GHE energy injection working mode and the blue solid line shows the temperature limits in the GHE energy extraction working mode.

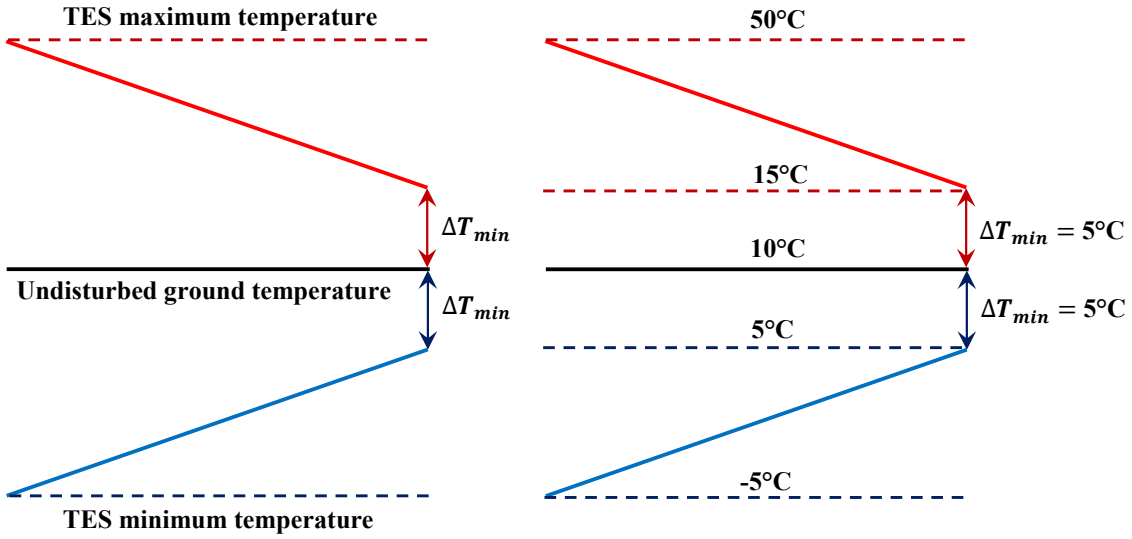

Figure 5-8 Temperature ranges for TES connected to the GHEs, the part below undisturbed temperature is for energy extraction, the part above it is for energy injection mode

5.3.3 Intermediate heat recovery loops and stratified thermal energy storage tanks

The building's different loads (i.e., SH, SC, and DHW) are time-dependent due to the variations in the outdoor conditions and the residents' expectations. However, in this study, the HP system is set to continuously work in a nominal steady state load. Thus, there will be moments in the mention time duration that the available energy and the demands are not in a balance. In other words, there will be a time mismatch between supply and target energy. It is shown in [123] that stratified TES tanks are a reliable solution for heat transfer among different energy sources and sinks with time mismatch, at least in the short-term usage, e.g., 24 hours. TES tanks can be charged and discharged via several intermediate heat recovery loops (IHRLs). The minimum temperature difference defined in the PA, the maximum and the minimum temperatures of the available sources and sinks determine the top and the bottom temperatures of a stratified TES

tank, which is the supply and target temperatures of IHRLs as hot and cold streams. The energy balance between the main stream and the corresponding IHRL is helpful in computing *CP(t)* of an IHRL.

5.3.4 Temperature ranges of all energy sources and sinks

The main sources and sinks have been identified thus far. Table 5-4 presents the supply and target temperatures of these streams. It should be emphasized that although the supply and target temperatures are constant, the loads are dynamic and time dependent.

Table 5-4 Hot and cold streams with supply and target temperatures

Streams	**Hot/Cold**	**Supply (°C)**	**Target (°C)**	**CP (kW/°C)**
HFH	C	30	35	Dynamic
DHW	C	City water	55	Dynamic
WGW	H	30	5	Dynamic
CGW	H	10	5	Dynamic
CL	H	12	7	Dynamic
Con-HP	H	110.1	55	constant
IHRL-H	H	60	30	Dynamic
IHRL-C	C	30	60	Dynamic
Eva-HP	C	-10	-5	constant
GS-Ext	H	≥5	-5	constant
GS-Inj	C	≤15	50	constant

The temperature range of each stream in the building's energy system can define it as a hot or a cold stream. Accordingly, the possible heat exchange among them can be arranged for both heating and cooling modes, as shown in Figure 5-9. The IHRLs, are not shown here.

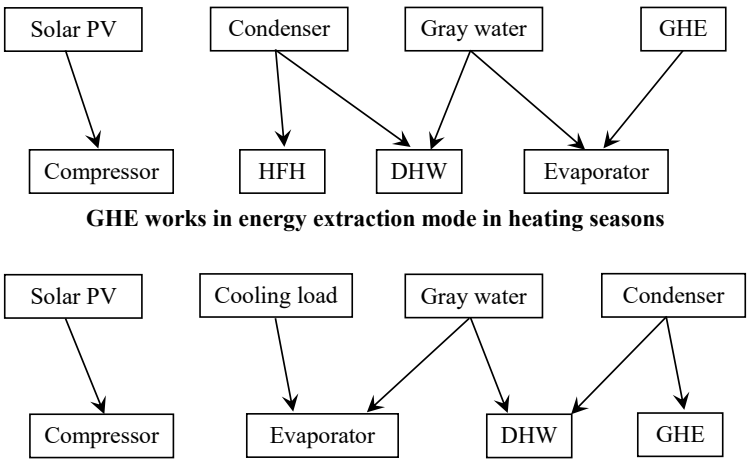

Figure 5-9 Possible energy/heat exchanges among hot/cold streams

In the heating months, the GHE can be used for heating the evaporator of the HP system and in the cooling months the GHE can partly contribute to providing the required cooling for the condenser. This is especially important in an imbalanced energy extraction/injection mode. In other words, the GHE can be treated as a solid thermal energy storage. Thus, this fact may justify some criss-crosses and cross pinch heat transfers [166] to store high temperature energy of the condenser into the ground. Having this in mind, two distinct scenarios are possible for the cooling months. First, directing all possible low temperature sources such as gray water (after preheating city water for DHW use) and building cooling load towards the evaporator. This maximizes the evaporator load; hence, the condenser load can be conveyed to the ground for recharging it. This case is named Summer C1. Second, the evaporator load is just enough to satisfy the building cooling load (i.e., Summer C2). In this case the condenser can satisfy the DHW, however, there will be less energy for recharging the ground.

5.3.5 Energy targeting; dynamic pinch analysis

Almost all presented loads in a building energy system represent a time-dependent nature, therefore, the conventional PA, which has been successfully applied to steady-state energy systems, should be modified to be utilized for a system with dynamic loads. The modification can be introduced through an adapted time slice model [123], where the 24 hours of a day is divided into small time slices (TSs). Nonetheless, the conventional PA can be applied for all TSs by taking the average values of CPs, as presented in Eq. (5-3).

$$\overline{CP}_{TS_t} = \frac{\int_t^{t+TS} CP(t)\,dt}{TS} \; for\ small\ TS \;\Rightarrow\; \overline{CP}_{TS_t} = CP(t) \tag{5-3}$$

According to the definition of the integration provided in Eq. (5-3), for an infinitesimal TS, the $\overline{CP}_{TS_t}$, will be equal to the instantaneous $CP(t)$. A better look at the dynamic loads reveal that

all loads can be assumed as continuous function of time. Thus, there is a finite value for $CP(t)$ at a given time. By way of explanation, there is no need for calculating the integral in Eq. (5-3), and the real-time value of the CPs can be evaluated according to the instantaneous loads. Then, the PA can be performed at each specific time from 0 to 24 hours. This approach is named as dynamic PA in this study. The graphical approach is based on the vertical heat transfer from hot streams to the cold ones. Therefore, all streams should be plotted based on the shifted temperature concept [167]. Figure 5-10 shows the shifted temperature intervals for all the hot/cold streams in two typical days in the heating and cooling months, respectively.

It should be noted that the temperatures are constant as the indoor thermal comfort condition needs to be constant. In other words, loads can vary by time, however, the supply and target temperature remain constant. Regarding the ground temperature, the more the energy extracted from the ground during the energy extraction mode, the lower the outlet temperature will be. However, the outlet temperature should not go below/above the design set point in the energy extraction/injection working modes (i.e., 5°C in heat extraction mode and 15°C in energy injection mode) as discussed in section 5.3.2.4.

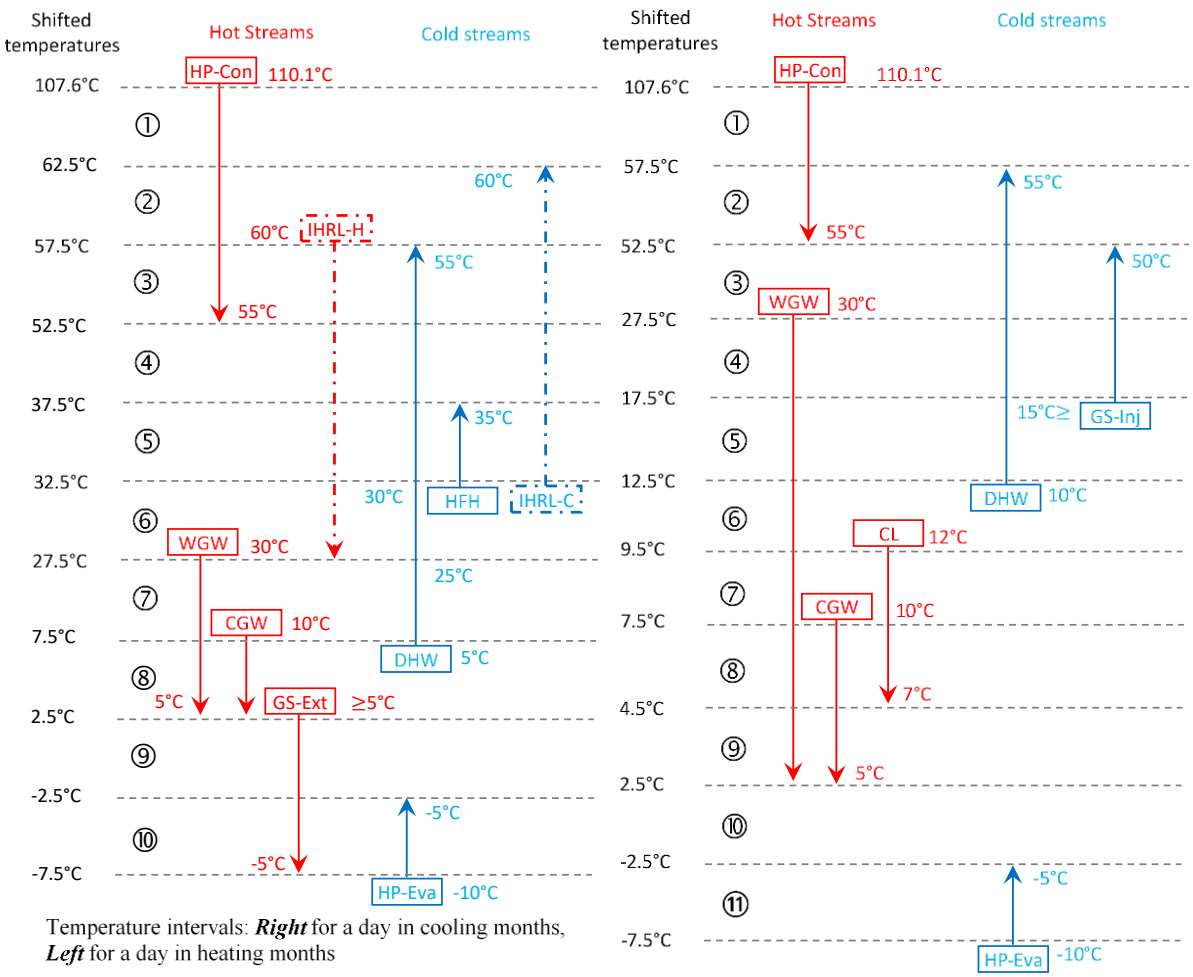

Figure 5-10 All streams in shifted temperature intervals for ΔT_{min} = 5°C for both heating and cooling months

5.3.5.1 Condenser and evaporator loads in heating and cooling months

HP capacity is the vital parameter in a SAGSHP design. As it is mentioned in section 5.3.2.3, the condensation and the evaporation temperatures of the HP system are designed as shown in Table 5-3 and Figure 5-6. Next step is to determine the load of the HP system. The required energy of the HFH+DHW* loads (in total) define the condenser load in the winter, when the gray water and the GHEs should satisfy the evaporator load.

One way of computing the constant condenser load is by calculating the cumulative energy of all demands that the condenser supposed to satisfy. As an example, Figure 5-11 presents the cumulative energy of HFH+DHW* for the day in January.

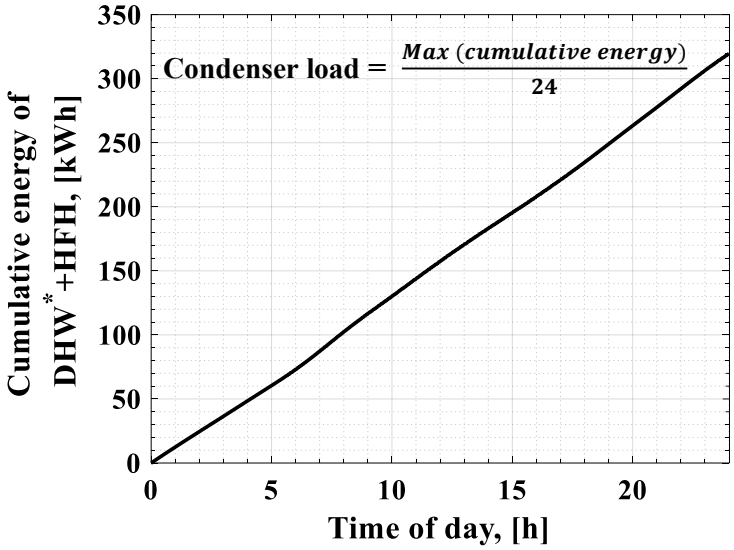

Figure 5-11 Computing the constant condenser load based on the cumulative energy of HFH+DHW*, day in Jan. (DHW* refers to DHW after being preheated by WGW)

As both building's cooling and heating demands are time dependent, there will be a need for a heat pump system with variable load characteristics to satisfy the mentioned loads. However, we can compute the total required energy (cumulative energy as presented in Figure 5-11) of space heating + domestic hot water and extract the corresponding constant load of the condenser that can meet the maximum cumulative require energy of the building. There will be hours in the buildings that the condenser load is more than what is required by building's loads. The excessive energy of condenser will be stored in a stratified TES tank. Also, there will be hours during the day that the constant load of the condenser is not enough to meet building's demand. Therefore, the stored energy can be retrieved to satisfy the loads. Therefore, the constant condenser load is calculated based on the building required energy demand via charging and discharging of the TES tank(s).

5.3.5.2 Hot and cold composite curves

At a given time during the 0 to 24 hours of a day, the hot and cold composite curves can be plotted at each temperature interval. The slop of the line at each temperature interval is calculated by Eq. (5-4) [167].

$$\Delta H = \sum (CP)_i \times \Delta T_{interval} \Rightarrow \left(\frac{dT}{dH}\right)_{interval} = \frac{1}{\sum CP_i} \tag{5-4}$$

ΔH is the enthalpy difference, i is the number of hot or cold streams presented at each temperature interval. $CP(t)$ of each hot and cold streams can be extracted from the corresponding load at a given time. Many CCs can be plotted during 0 to 24 hours of a day. If all the instantaneous CCs attached to each other, an animation can be generated (see the

supplementary data) that provides details about the maximum direct + indirect heat recovery, the GHE required load, and the dynamic heat transfer area between hot and cold streams. As an example, the hot/cold CCs for the day in the heating months is presented in Figure 5-12.

Relying on the stored energy in the high temperature TES tank (IHRL_H), it is not necessary for the HP system to meet the required energy at peak demand for the SH + DHW. In this way the SH + DHW load is satisfied just by the heat pumping.

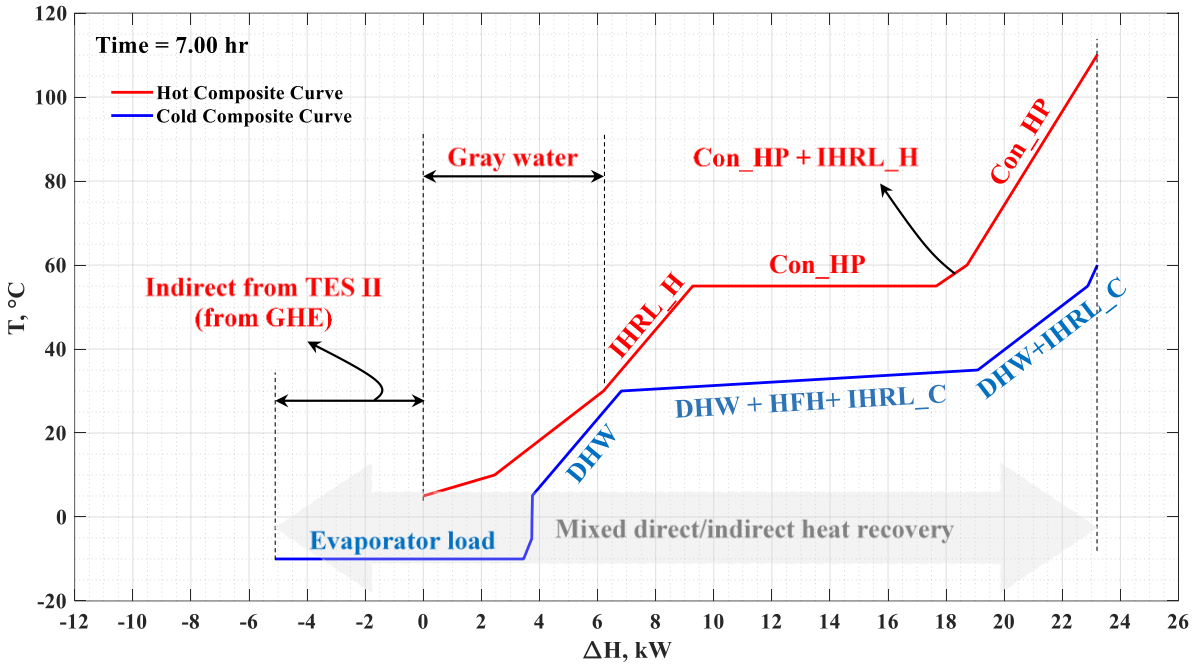

Figure 5-12 Real-time hot and cold CCs at 7 AM for Jan. 21st in the heat extraction working mode of GHEs

The low temperature energy surplus is stored inside the low temperature TES tank (i.e., TES II). This TES tank have to be connected to the GHEs. As the undisturbed ground temperature is above the evaporation temperature, the HTF inside the TES II tank can extract energy from the ground. The heat extraction working mode continues during the heating months. Figure 5-13 shows the hot and cold CCs at two moments in a day in summer. In some hours the energy surplus from CL+GW is stored in a TES II tank and when the evaporator needs this stored energy, it can be used by TES energy discharge.

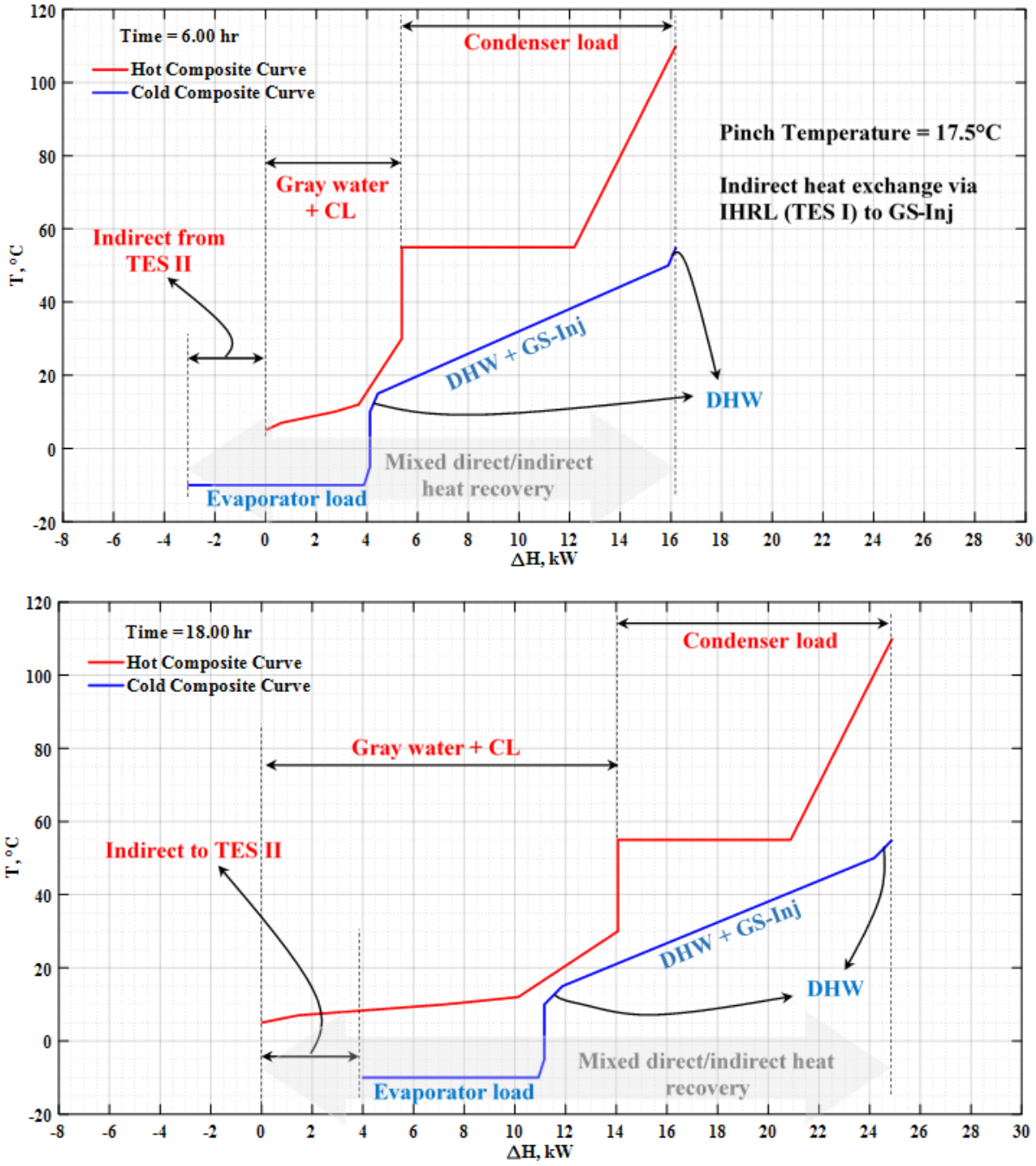

Figure 5-13 Real-time hot and cold CCs at 6 AM and 6 PM for 21st of July in the heat injection working mode of GHEs

The pinch temperature remains constant as 27.5°C and 17.5°C in heat extraction and heat injection working mode of the GHEs, respectively, for all times during 0 to 24 hours. The presented CCs are plotted for all other representative days, and the HP capacity, the required hot utility, the volume of the TESs, the area of PV panels, the capacity of the EES, and the GS

loads will be different based on building's load and the solar irradiance at different representative days.

5.3.6 Proposed superstructure or HX+GHE+TES+EES+PV+HP network

According to the CCs, the amount of heat that can be transferred between hot and cold streams is defined at each given time from 0 to 24 hours in each representative day. Therefore, a heat exchanger network can be extracted for each moment according to the corresponding CCs. Hence, there can be an immense number of networks. In this study CCs are produced from 0 to 24 hours at each 0.01 h. In other words, there are 2400 CCs for each representative days, and 2400 networks for each day. In spite of the large number of possible networks, the overall number of heat exchangers remain the same because the number of the hot/cold streams are the same in each working mode and the heat transfer possibility among them is governed by the second law of thermodynamics. If we consider the energy extraction working mode, Figure 5-14 shows the grid diagram of the HX+TES+GHE network that can make real the predicted MHR by the dynamic PA during the heating months. The dash-dotted lines illustrate the indirect heat exchange (i.e., IHRLs). The ground source is presented as a symbolic stream. It should be noted that the size (or even existence) of the HXs is different at different hours of the day. Furthermore, in some representative days, e.g., June and Sep., there is no need for the GHE, as the gray water can satisfy the evaporator load via the TES II tank.

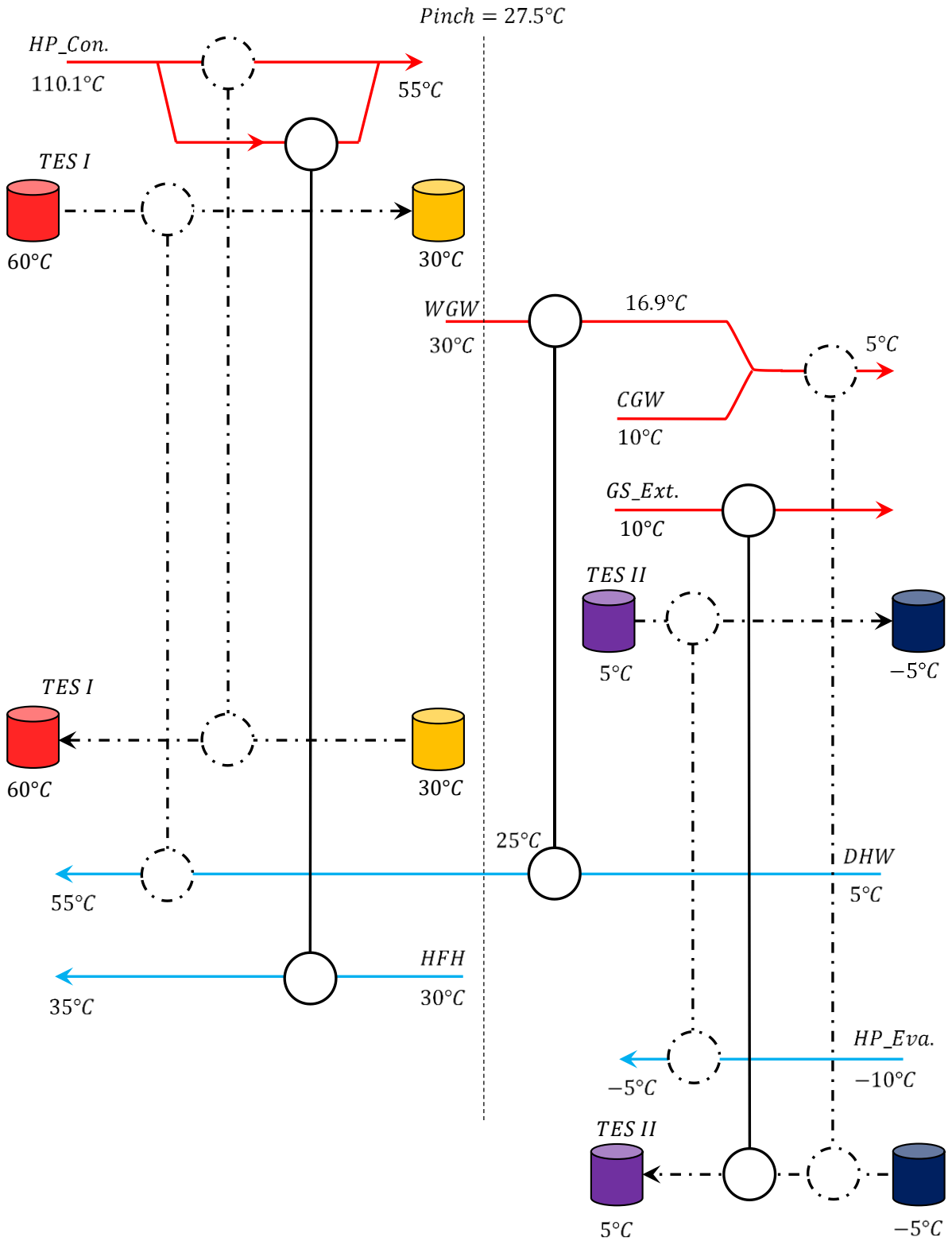

Figure 5-14 Grid diagram for the energy extraction working mode (the GS-Ext is a symbolic line)

Likewise, the grid diagram for the summer day can be set up as shown in Figure 5-15.

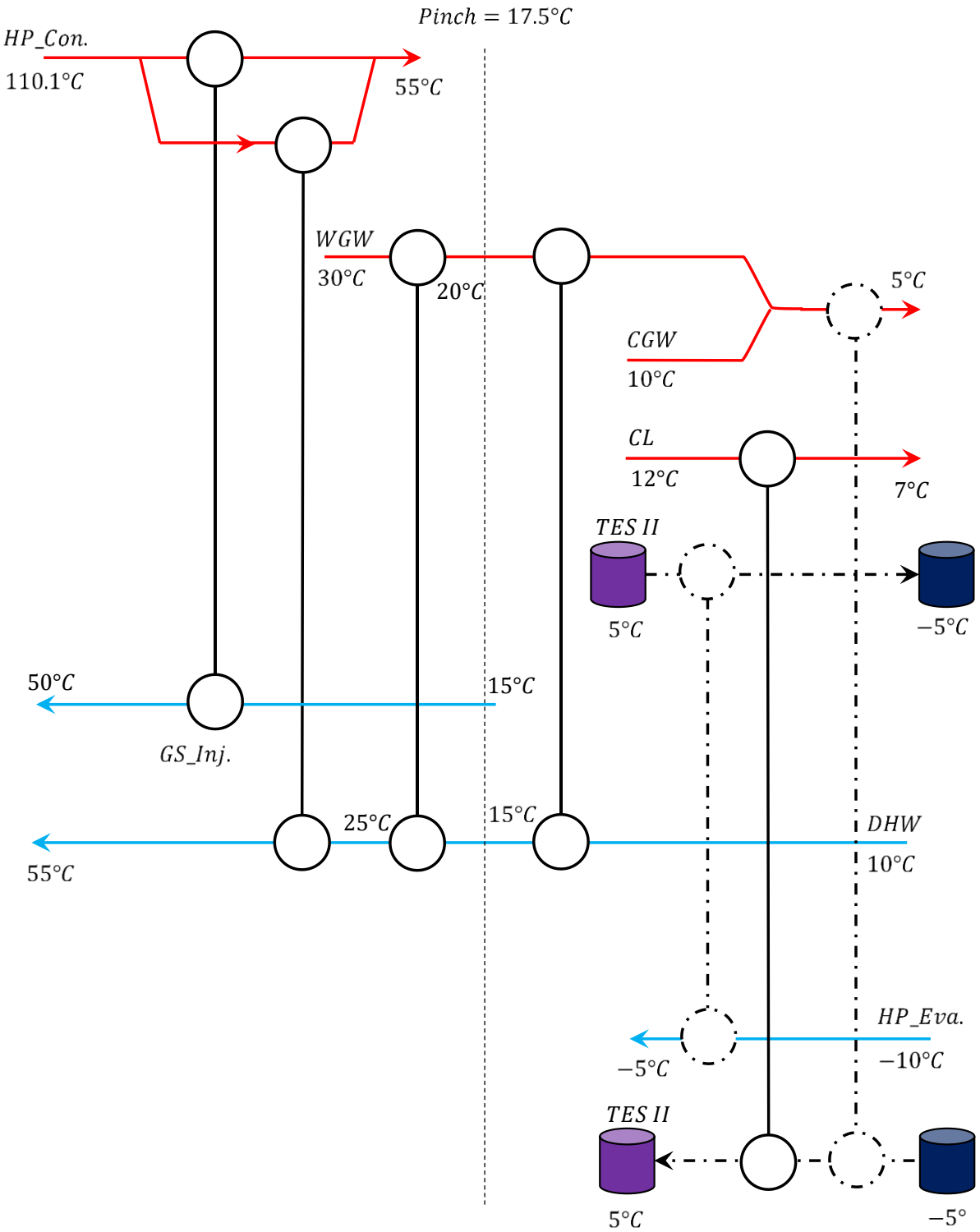

Figure 5-15 Grid diagram for the energy injection working mode (the GS-Inj stream is symbolic)

All of the grid diagrams can be illustrated in one superstructure by adding other parts such as the solar panels, the compressor, the EES, and the TESs to the HX network. The superstructure of all required HX+GHE+TES+EES+PV+HP network is demonstrated in Figure 5-16. There are two working modes for a SAGSHP system in a building: heating and cooling working modes, corresponding to the energy extraction and energy injection working modes of the GHEs, respectively. The proposed superstructure can achieve the MHR as predicted by CCs introduced in section 5.3.5, for both working modes and throughout the year. It should be noted that there might be one or several heat exchangers that are not required in one particular time in a representative day, yet they should be presented in the superstructure.

The proposed superstructure consists of two stratified TES tanks and a cluster of EESs, e.g., lead-acid batteries. The network requires 7 HXs to achieve the MHR by a mixed or the direct/indirect heat exchange. It should be noted that the temperature shown in this superstructure are based on the pinch approach that is based on pure thermodynamics.

Additionally, this superstructure has the capability to integrate other types of renewable energies such as wind energy, solar thermal energy, etc. For instance, in case of the wind energy, the dynamic electric energy output of a wind turbine can be stored in the EES. Therefore, reduces the required grid electricity.

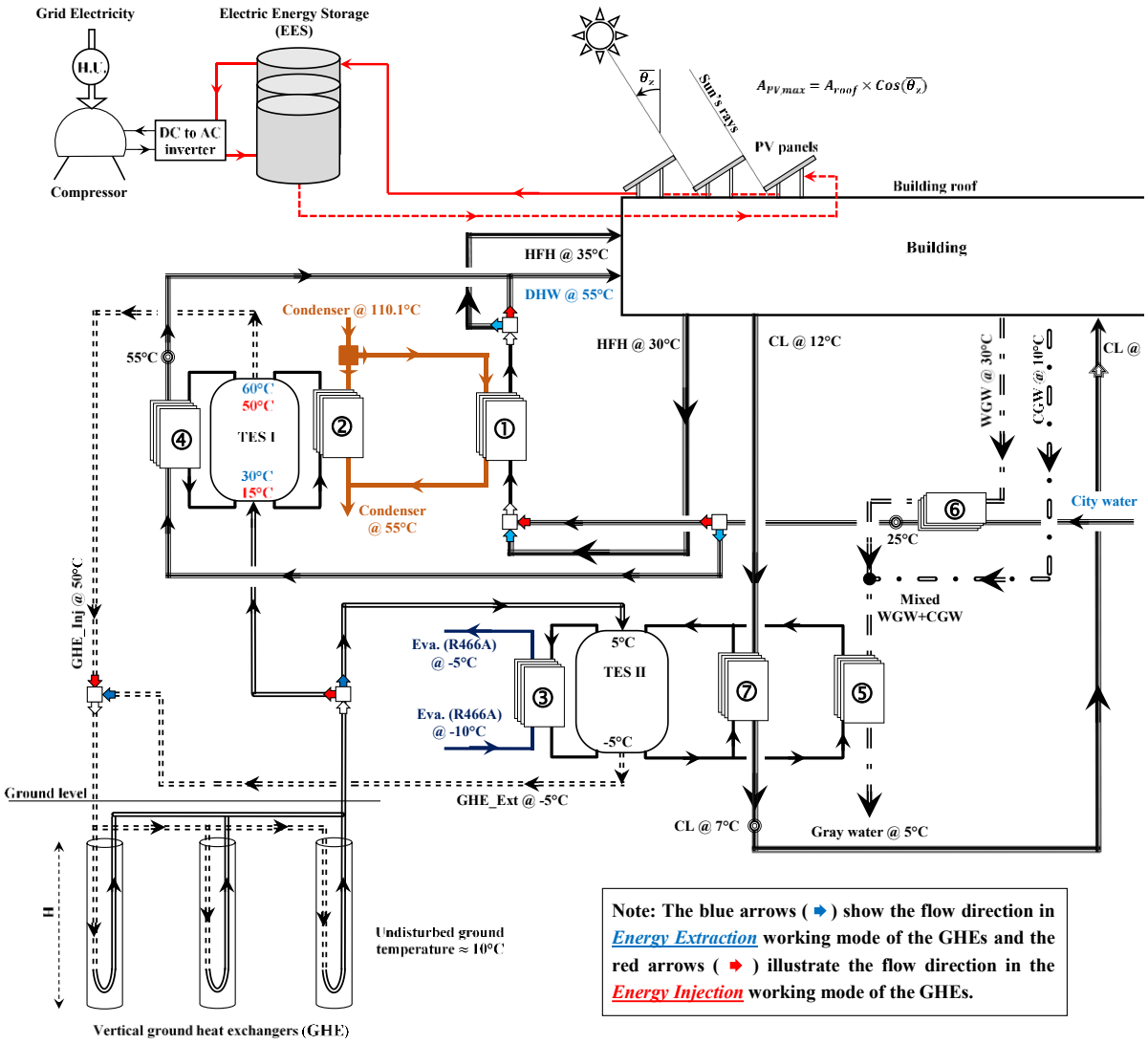

Figure 5-16 Proposed superstructure for the SAGSHP system extracted from the dynamic PA for both energy extraction/injection working modes

5.4 Results and discussion; energy targeting for each representative day

Based on the proposed dynamic PA, the daily targeted values of the HP capacity, the volume of each TES, the capacity of the EES, the GHE loads, and the total daily hot utility, are computed and presented here.

5.4.1 Heat pump capacity

Figure 5-17 shows the required constant condenser and evaporator loads of the proposed HP system based on the dynamic PA. Both loads represent a reducing pattern from the cold winter days (i.e., from Jan.) towards the hot summer days. As explained earlier, both the condenser and evaporator loads in Summer C1 are higher than that of the Summer C2 due to charging extra energy into the ground via the heat injection working mode of GHEs.

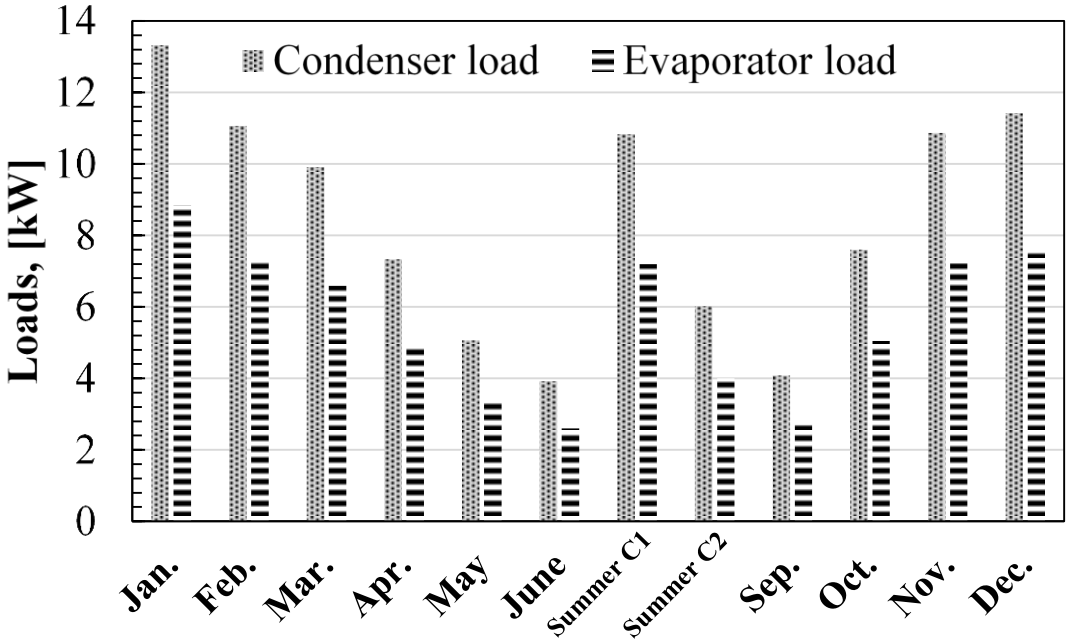

Figure 5-17 The HP loads for each representative day in each month

The HP capacity shows an increasing pattern after the summer month, in order to satisfy the heating demands of the test building, the HP capacity varies by the required load. Nonetheless, the output of the dynamic PA at each day for the HP capacity is based on the MHR concept. In other words, the building energy demands can be successfully satisfied by the condenser or the evaporator loads.

5.4.2 Volume of TES tanks

The amount of energy that can be stored into the TES tanks can be calculated from the composite curves by subtracting the IHRL_H from the IHRL_C loads. The result is shown in Figure 5-18. This figure shows that the blue area is equal to the red area at condenser load of 13.3 kW, therefore, the constant capacity of the heat pump computed by the cumulative energy load is in line with the dynamic PA. Either the blue or the red areas can be used for computing the volume of the TES I tank. The same procedure is repeated for the TES II.

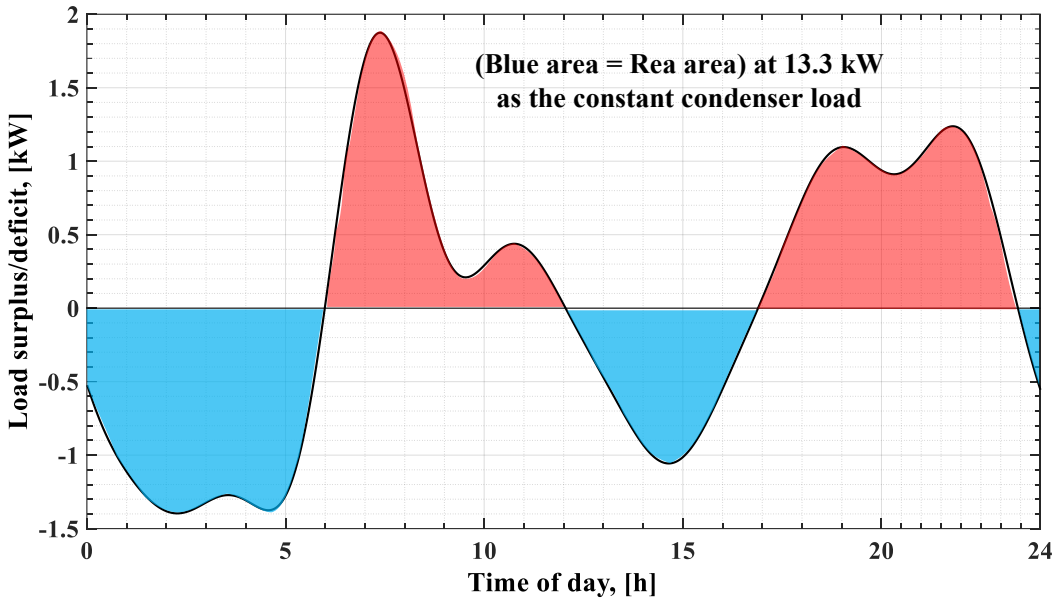

Figure 5-18 TES I loads during charging (positive values) and discharging (negative values) time (the day in Jan.)

The top and bottom temperatures of the TES tank is defined based on the minimum temperature difference defined in the PA and the temperature of the charging/discharging IHRLs, therefore, the theoretical value of the TES tank volume (V_{TES}) for each representative day can be calculated with Eq. (5-5).

$$V_{TES} = \frac{Q}{\bar{\rho}\bar{c_p}\Delta T} \tag{5-5}$$

Where, the Q is the amount of energy to be stored. The $\bar{\rho}$ and $\bar{c_p}$ are the average density and specific heat capacity of the intermediate heat transfer medium, that is a mixture of water and ethylene glycol (20% by weight) in both the TES I and the TES II. This mixture has a freezing point of - 8°C. The ΔT in Eq. (5-5) is the temperature difference between the top and the bottom of the tank (i.e., hot zone and the cold zone). It should be noted that the liquid in the TES I can be pure water from temperature perspective, however, as this liquid should circulate inside the GHE during the energy injection mode, to avoid using two different working fluids in the GHE and eliminating unnecessary efforts for tanking/detanking the TES I, the same water + ethylene glycol is considered as the HTF for the TES I during both energy extraction/injection modes.

The volume of TES I and II (in liter) are computed for each representative day and illustrated in Figure 5-19. The nominal temperature difference between top and bottom of the TES II is only 10°C that makes its volume larger than the TES I tank, where the nominal temperature difference is 35°C.

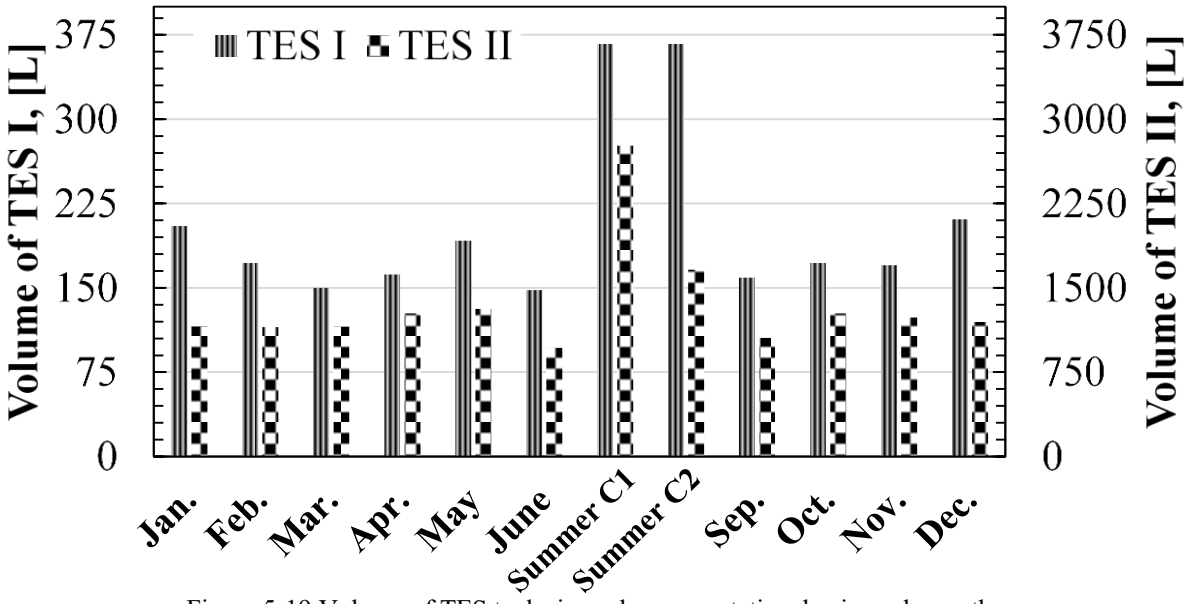

Figure 5-19 Volume of TES tanks in each representative day in each month

The computed V_{TES} is the minimum theoretical value which the heat transfer phenomena such as the effect of heat loss to the ambient air and the lost volume due to presence of a temperature gradient between the maximum and the minimum temperatures inside the stratified TES tank (i.e., thermocline thickness) are not taken into account. A recent numerical study by the authors that investigated the thermocline thickness development inside a stratified TES tank [169], showed that by considering the heat loss to the ambient air and the turbulent or momentum mixing effect of the charging diffuser type, the practical volume has to be 15 percent higher than that of predicted by Eq. (5-5) (in a TES equipped with radial type charging and discharging diffusers at the minimum height to diameter ratio of three). As the volumes of TES I and II are different, and to respect the minimum height to diameter ratio for each tank, the tanks cannot be merged into one.

5.4.3 PV area and EES capacity

According to the required compressor load ($Q_{con} - Q_{eva}$), and the deliverable energy by PV panels (see Figure 5-5), the panels area and the capacity of the EES are computed. Figure 5-20 shows the required PV area to have a building not relying on the grid electricity for SH, SC, and DHW.

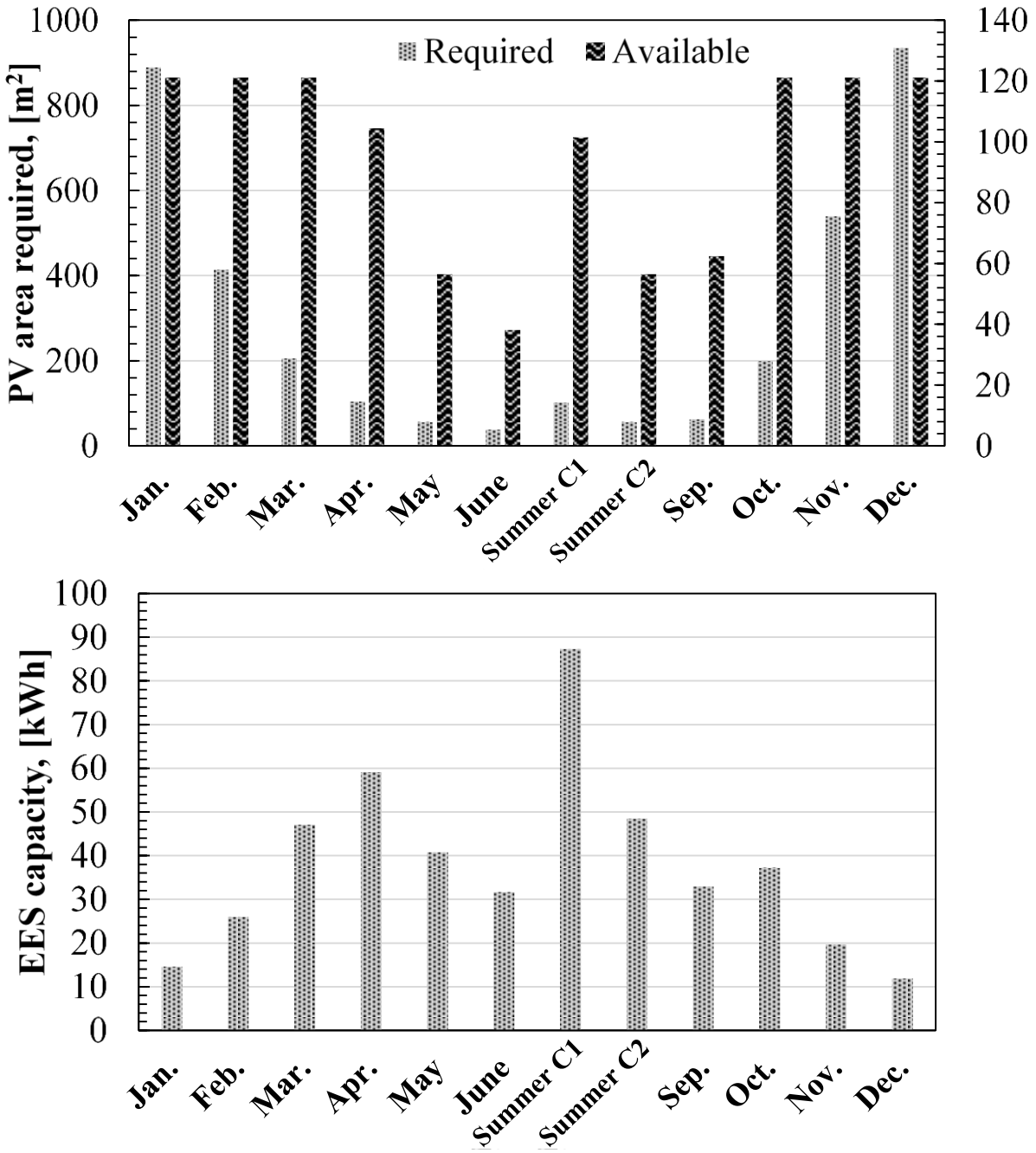

Figure 5-20 Top: required and available PV panel area, Bottom: EES capacity at each representative day

The area of 121.2 m^2, is assumed the maximum available area for mounting the PV panels on the flat roof of the test building. Therefore, for the representative day in six months of January, February, March, October, November, and December in the heating months, the maximum available area for mounting the PV panels is taken into account. The compressor load could be satisfied solely based on the solar energy with panel area of 889, 414, 205, 199, 540, and 935 m^2 for the mentioned months, respectively, if there was enough effective mounting area on/around the test building. With these area of PV panels, the building hypothetically does not need any

grid electricity for SH and DHW loads. However, these PV areas might not be the optimum ones from economic aspect, especially considering full-year operation. When the system needs a panel area above the maximum available mounting area, the solar energy cannot meet the compressor load in full, thus the rest of the required compressor energy needs to be provided by the grid electricity as the hot utility.

The EES capacity, shown in Figure 5-20, is computed based on the available area for the PV panels multiplied by the area under Figure 5-5, for each representative day. Additionally, during the cold months, the EES batteries undergo a charging/discharging process once per day. Different modules of the batteries may undergo more than one time of load/unload phases per day in the summer months.

5.4.4 GHE load evaluation

The proposed dynamic PA predicts the required time dependent GHEs load. For instance, the solid black line in Figure 5-21 illustrates the dynamic GHEs load for the representative day in January. By connecting to a TES tank, the constant load of the GHEs is computed when the blue and red areas in Figure 5-21 are the same, therefore, a constant load of 6.1 kW is enough for the cluster of GHEs to satisfy the evaporator load when it adds to the WGW^{*}+CGW. Similarly, Figure 5-22 presents the constant GHE loads for other representative days. The GHE load goes down as the SH + DHW load reduces. This pattern continues until the GHE load is zero in two months of June and September. It means that the gray water can satisfy the evaporator load without any needs to the GS.

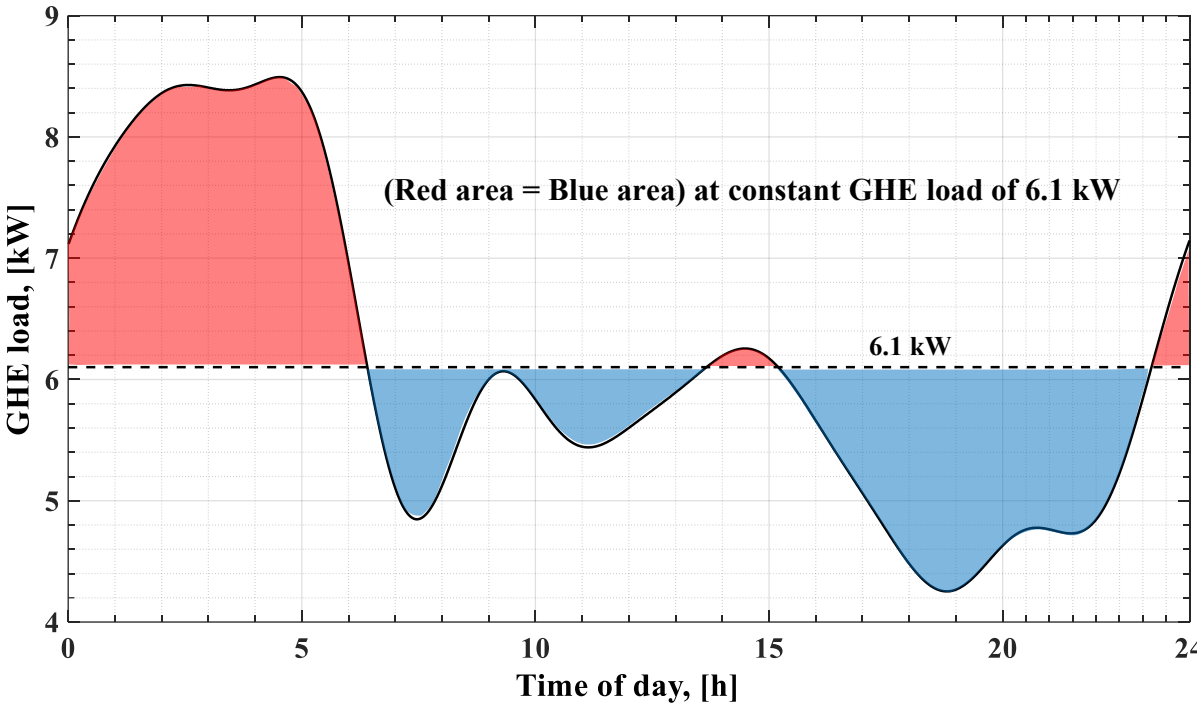

Figure 5-21 Dynamic and constant load of GHEs computed for the day in Jan.

In the heat injection working mode of the GHEs (i.e., in Summer-C1 and C2), the hot HTF enters to the GHE and charges part of the removed energy in the heat extraction working mode. However, as the heating load is dominant in the test building, this imbalance workload will alter the GHE outlet temperature in a long term run such as 20 years. It worth mentioning that the depth and configuration of a cluster of GHEs that can deliver the constant design load at the desire outlet temperature can be found in [170], where the computational fluid dynamic (CFD) simulation is utilized to compute the thermal performance of the GHEs.

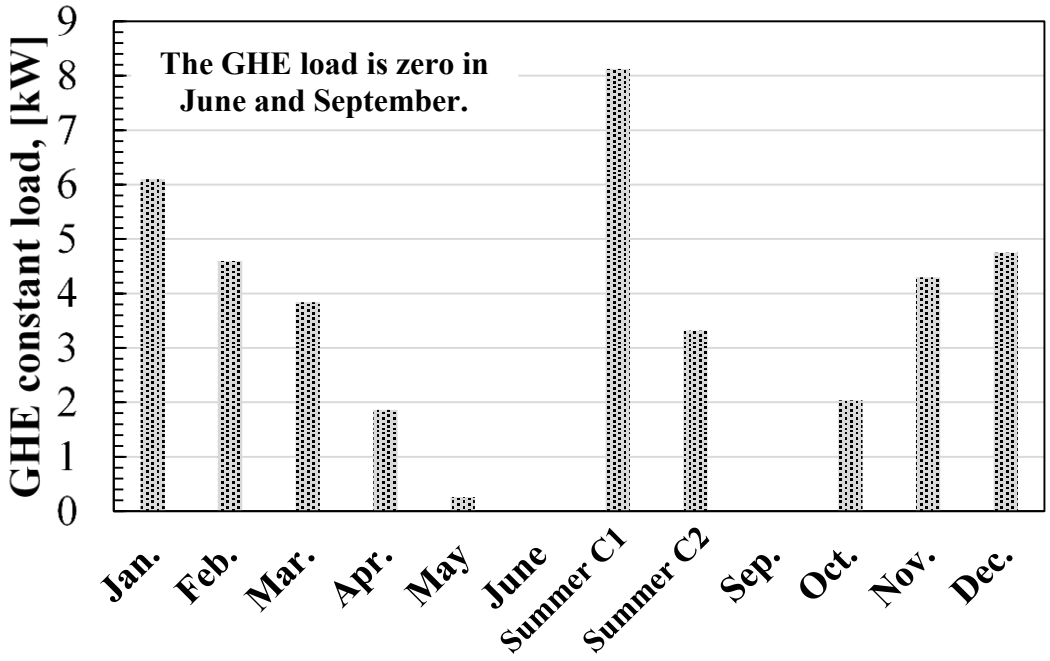

Figure 5-22 GHE loads for all representative days, heat injection mode in Jul. and Aug., zero load in June and Sep., other months are in the heat extraction mode.

5.4.5 Hot utility and energy use intensity (EUI)

The main idea behind the SAGSHP is to satisfy the building loads by renewable energy and heat pumping. However, as the solar irradiance in some heating months are low and the performance of commercially available PV panels degrades in the cloudy days, the building needs to have a source of energy for the compressor of the heat pump which is the grid electricity. Table 5-5 presents the required energy from the grid electricity in each representative day. The bottom row of Table 5-5 shows the amount of grid electricity for each day in no-heat integration case.

Table 5-5 Daily hot utility at each representative day

Day in Month ➔	Jan.	Feb.	Mar.	Apr.	May	June	July & Aug.	Sep.	Oct.	Nov.	Dec.
$\boldsymbol{Q}_{\text{Utility}}$(kWh)	92.7	63	32.8	0	0	0	0	0	24	68	80
$\boldsymbol{Q}_{\text{no-HI}}$(kWh)	362.9	308.6	281.1	212.8	156	126.5	131.5	134.7	219.2	299.7	315.2

When the required energy from the grid (i.e., $\boldsymbol{Q}_{\text{Utility}}$) is zero, the proposed SAGSHP successfully functions without any need to the hot utility. In other words, based on the proposed full network of a HP system, two stratified TES tanks, a cluster of GHEs, the solar PV panels + the corresponding electrical batteries, and the waste energy recovery of the gray water, the space heating/cooling and the domestic hot water can be satisfied in 6 months of a year purely on the renewable and waste energies. Furthermore, in cases when the hot utility is needed (i.e.,

highlighted months in Table 5-5), the SAGSHP provides a substantial reduction in the required energy. As an example, considering the day in January, the test building equipped with the proposed SAGSHP system needs a quarter of the total energy required in the no-heat integration case ($\boldsymbol{Q}_{\text{no-HI}}$).

Moreover, the energy use intensity (EUI) as a key performance indicator (KPI) for the proposed SAGSHP system is computed and compared against the Canadian average value. It should be noted that the computed value is for the case if the final selected design for the test building is a design that all the involved components are selected with their maximum load/volume/area (e.g., maximum volume for TES tanks, maximum capacity of HP, maximum GHE load, etc.). Then the EUI can be computed via Eq. (5-6):

$$EUI^* = \frac{\sum_{i=1}^{12}(N_{days} \times Q_{utility})_i}{Building\ floor\ area} \tag{5-6}$$

In this equation, i shows the number of the month, N_{days} is the number of days in each month, $Q_{utility}$ is the daily required hot utility (i.e., grid electricity, see Table 5). The test building habitable floor area is 308 m^2 [3]. The presented EUI^* is asterisked to indicate that just SH/SC + DHW loads are included (not lighting nor miscellaneous plug loads). The yearly average EUI^* is 35.45 kWh/m^2 for the test building equipped with the proposed SAGSHP system. This number is 131 kWh/m^2 for the Canadian average [183]. Therefore, the proposed SAGSHP system can reduce the building EUI^* by 3.7 times in comparison to the Canadian average.

5.5 Conclusion

Renewable energies such as solar and ground source along with the energy recovery from waste sources such as gray water can be integrated into a building's energy system via thermal/electrical energy storage and heat pumping to reduce the building dependency on the hot utility such as the grid electricity or the fossil fuels. Furthermore, building's main loads such as SH/SC and DHW are time-dependent loads that change not only on an hourly base, but also during one year from day 1 to day 365. Although there can be found a significant number of studies regarding application of the SAGSHP in buildings, they are not based on a systematic approach and cannot systematically include all available sources and sinks in a building. In this study, a systematic dynamic targeting approach based on pinch concept is proposed that can include all time-dependent and intermittent nature of the involved energy sources and sinks in buildings during 0 to 24 hours of 12 days, each representative of the loads and solar condition of each month during a year. In other words, sizing different components of a SAGSHP is converted into matching and selecting different sources and sinks in a building where the PA can effectively predict the maximum heat recovery values. Current graphical model is based on the dynamic composite curves at each given time from 0 to 24 hours in each representative day,

thus, it predicts the minimum solar PV panel area, the minimum TES volume and EES capacity, the minimum GHE load, and the minimum hot utility for each representative day, which it can be called the daily optimum design. Moreover, application of TES allows designing HP and GHEs as constant loads, working for full day. A proposed network of HX+GHE+TES+EES+PV+HP in form of a superstructure facilitates achieving to the promised maximum heat recovery in both heating and cooling months. In the studied test building, heating load is the dominant one. Hence, the test building drains the heating potential of the ground source by extracting energy continuously for 8 consecutive months at different extraction rates. To replenish some removed energy during the heating months, the summer design not only satisfies the building cooling load and the domestic hot water, but also it charges part of the condensation energy into the ground during the heat injection working mode. In other words, the ground can be treated as a solid thermal energy storage for long term application. This energy injection is helpful for long term (i.e., 20 years) functionality of the proposed system. Additionally, according to the proposed dynamic pinch model and the full network of equipment, it is shown that there is no need for the hot utility, for 6 months of a year, from April to September, in the test building. This proves that this approach can be used as a framework for designing zero energy buildings.

It should be noted that detailed design/configurations of the GHE for delivering the targeted constant load at desired temperature set points are presented in another study [170]. Moreover, among all extracted 12 optimum daily designs, the building just needs one design. The techno-economic analysis base on the total annual cost, which will be performed in a future study, sheds some light on selecting the final optimum design for the test building.

5.6 Acknowledgement

The authors acknowledge the financial support of the Natural Sciences and Engineering Research Council of Canada for this project (RGPIN-2019-05826).

5.7 Supplementary data

The graphical dynamic pinch approach code is written in MATLAB R2021a. This software is used for generating the animation by putting all the CCs together. One example of this video is provided as the supplementary data. This video is for day 21st of January (heat extraction working mode of the GHE). Definitions of each segment of the hot/cold CCs are as depicted in Figure 5-12.

5.8 Nomenclature

A	Area [m^2]	DHW	Domestic Hot Water
c_p, c	specific heat capacity [J kg^{-1} K^{-1}]	EES	Electric Energy Storage

CP	heat flow rate [W/°C]
d_n	Number of days in a year from 1 to 365
G	Solar irradiance [W m^{-2}]
H	Enthalpy [kW]
N	Number of days in each month
Q	Energy to be stored [J]/ hot utility [kWh]
t	Time [s]
T	Temperature [°C]
V	TES volume [L]
Greek	
Δ	Difference sign
η_e	PV energy conversion efficiency [-]
$\eta_{isen,com}$	Compressor isentropic efficiency
θ_z	Zenith angle [°]
ρ	Density [kg m^{-3}]
Subscripts	
t	time [s]
city	City water
max	maximum
min	minimum
PV	Photovoltaic
rise	Sunrise time
roof	Roof area of building
set	Sunset time
utility	Hot utility, grid electricity
no-HI	No-Heat Integration
Superscripts	
*	after pre-heat exchange - SH/SC+DHW in *EUI* calculation
Acronyms	
CCs	Composite Curves
CFD	Computational Fluid Dynamics
CGW	Cold Gray Water
CI	Clearness Index
CL	Cooling Load
Con-HP	Condenser of Heat Pump
COP	Coefficient of Performance
DC	Direct current
Eva-HP	Evaporator of Heat Pump
EUI	Energy Use Intensity [kWh/m^2]
GHE	Ground Heat Exchanger
GS	Ground Source
GS-Ext	Ground Source in Heat Extraction working mode
GS-Inj	Ground Source in Heat Injection working mode
GSHP	Ground Source Heat Pump
GW	Gray Water
HFH	Hydronic Floor Heating
HP	Heat Pump
HTF	Heat Transfer Fluid
HU	Hot Utility
HX	Heat Exchanger
IHRL	Intermediate Heat Recovery Loop
KPI	Key Performance Indicator
MHR	Maximum Heat Recovery
PA	Pinch analysis
PV	Photovoltaic panel
PVT	Photovoltaic-Thermal collector
Ref	Refrigeration system
SAGSHP	Solar Assisted Ground Source Heat Pump
SC	Space Cooling
SH	Space Heating
STC	Solar Thermal Collector
TES	Thermal Energy Storage
TS	Time Slice
WGW	Warm Gray Water

Chapter 6: Numerical approach for sizing vertical ground heat exchangers based on constant design load and desired outlet temperature

Avant-propos

Auteurs et affiliation:

Seyed Mojtaba Hosseinnia: étudiant au doctorat, faculté de génie, département de génie mécanique, Université de Sherbrooke.

Mikhail Sorin: professeur, faculté de génie, département de génie mécanique, Université de Sherbrooke.

Date d'acception: 18 décembre 2021

État de l'acceptation: version finale publiée, 48 (2022) 103932

Revue: Journal of Building Engineering

Titre français: Approche numérique pour le dimensionnement des échangeurs de chaleur souterrains verticaux en fonction d'une charge de conception constante et de la température de sortie souhaitée

Contribution au document: Cet article révèle les performances thermiques des échangeurs géothermiques pour un dimensionnement optimal.

Résumé français: Des échangeurs de chaleur géothermiques verticaux (GHE), dans le cadre d'un système de pompe à chaleur géothermique, ont été utilisés pour l'extraction/l'injection d'énergie depuis/vers le sol, c'est-à-dire une source d'énergie renouvelable, pendant les mois de chauffage/refroidissement afin de réduire l'utilisation de l'énergie du bâtiment. . Les méthodes de dimensionnement GHE actuellement disponibles sont principalement basées sur plusieurs analyses unidimensionnelles ou bidimensionnelles trop simplifiées, qui ne peuvent pas prédire son comportement thermique avec des conditions aux limites précises et réalistes ou dans des configurations en série. Dans cette étude, les performances thermiques des GHE verticaux sont

étudiées numériquement à une charge constante donnée en résolvant les équations de Navier-Stokes 3D transitoires complètes à l'intérieur des tubes en U et l'équation d'énergie dans tout le domaine de calcul, c'est-à-dire les parties fluides et solides. Il existe trois paramètres interconnectés, à savoir la charge GHE, la température de sortie du fluide caloporteur et la profondeur GHE qui influencent ses performances thermiques et, par conséquent, le coût d'investissement requis. Par conséquent, la performance thermique des GHE est calculée pour différentes charges constantes à différentes profondeurs, et il est montré qu'à chaque charge constante, il existe un compromis entre le coût d'investissement et la performance thermique. De plus, les performances thermiques des GHE en configuration parallèle et série sont étudiées à une profondeur fixe et à différentes charges. À la lumière des données obtenues, la taille requise des GHE pour un bâtiment test avec un taux d'extraction/injection d'énergie déséquilibré est dérivée et la performance thermique du groupe de GHE proposé est simulée numériquement pendant 20 ans.

Mots-clés : GHE verticaux parallèles, GHE verticaux en série, pompe à chaleur, analyse CFD, profondeur GHE optimale

6.1 Abstract

Vertical ground heat exchangers (GHE), as part of a ground source heat pump system, have been utilized for energy extraction/injection from/to the ground, i.e., a renewable source of energy, in the heating/cooling months to reduce building energy utilization. The current available GHE sizing methods are mostly based on several over-simplified one- or two-dimensional analyses, which cannot predict its thermal behavior with the accurate and realistic boundary conditions or in series configurations. In this study, thermal performance of vertical GHEs is numerically investigated at a given constant load through solving full transient 3D Navier-Stokes equations inside the U-tubes and the energy equation all over the computational domain, i.e., both fluid and solid parts. There are three interconnected parameters, namely GHE load, the heat transfer fluid outlet temperature, and the GHE depth that influence its thermal performance and consequently, the required investment cost. Therefore, the thermal performance of GHEs is computed for different constant loads at different depths, and it is shown that at each constant load, there is a trade-off between the investment cost and the thermal performance. Furthermore, the GHEs thermal performance in parallel and series configuration is investigated at a fixed depth and different loads. In light of the obtained data, the required size of the GHEs for a test building with an imbalanced energy extraction/injection rate is derived and the thermal performance of the proposed cluster of GHEs is numerically simulated for 20 years.

Keywords: parallel vertical GHEs, series vertical GHEs, heat pump, CFD analysis, optimum GHE depth

6.2 Introduction

At a specific depth below the ground surface, the underground temperature is above the air temperature in the winter, and, with the same approximate differential magnitude, it is below the air temperature in the summer. Therefore, the ground source energy can be assumed as a constant temperature solid storage medium for a heat pump system for both heating and cooling purposes during a year [184]. One available way of energy exchange between the ground and the condenser/evaporator of a heat pump system is through one or several vertical ground heat exchangers (GHE). Each vertical GHE consists of one or more U-tubes fitted inside a borehole. The borehole can be as deep as 30 m to 100 m, for residential building applications [5]. In the winter, the GHE provides the required energy (or part of it) for the evaporation process in the evaporator. From the ground side, this is called the energy extraction mode. In the energy extraction working mode, the low temperature heat transfer fluid (HTF) enters the U-tubes and extracts heat from the ground. In the summer, the GHE dissipates the required energy (in part or total) of condensation process in the ground. This process is called the energy injection. In the energy injection working mode, the GHEs should provide the required cooling for the condenser of the heat pump system. The HTF in a typical GHE can be either the heat pump refrigerant [185,186] or water + antifreeze mixture [187–189] as a secondary medium.

Thermal performance of the GHE is a crucial parameter in total performance of the heat pump system. Both of the mentioned heat exchange processes between U-tubes/borehole and the ground, i.e., energy extraction and injection, are complex and highly dynamic and should be treated as a three-dimensional problem due to the time-dependent thermal boundary conditions, spatial and temporal temperature variations in all three dimensions, i.e., x, y, and z. Being a transient three-dimensional problem is not the only hindrance in predicting the GHE thermal performance in an accurate manner. The number of involved parameters also matters.

Vertical GHEs should be designed to such an extent that they satisfy the required load of a heat pump system which calls for an acceptable temperature difference. At a fixed length of the GHEs, the deliverable load and the outlet temperature of the HTF are the GHE's two main interdependent specifications. The GHE thermal performance is affected by its working conditions and its design specifications. From working condition's perspective, heat transfer fluid type, inlet temperature and mass flow rate can be named as the most influential parameters. The thermophysical properties of grout, soil and U-tube material, length, and configuration of U-tubes inside the borehole, and the boreholes distribution (center-to-center spacing, parallel or

connected in series) in the field can be named as the design specifications. Consequently, these parameters influence the investment and operational cost of the project including but not limited to drilling cost, grout and cement filler magnitude and cost, piping, and required pumping power. The available studies in the literature have been focused on GHE thermal performance prediction by taking some parameters/boundary conditions as constant values which is especially required for analytical modeling.

Analytical solutions describe the vertical borehole as a vertical infinite or finite line source with constant temperature, and the results are the temperature field around the source line [190,191]. As a recent example, Rivera et al. [192] expanded the finite line source model by modifying the top temperature boundary condition from Dirichlet type to Cauchy type. Although they analytically solved the temperature field inside a three-dimensional geometry around the line, the main simplification in their study is that the GHE is assumed as a finite line with uniform heat flux. Moreover, analytical solutions cannot include the fluid flow inside the GHE U-tubes.

2D models are based on the thermal resistance concept. Several comprehensive reviews have been carried out on different 2D modeling methods for computing the thermal performance and sizing of the GHE [155,158,193–195]. As an example, the method explained in American Society of Heating, Refrigeration and Air-Conditioning Engineers' guide (ASHRAE) [196] is reviewed here. Similar to all 2D models, there are several simplifications in the ASHRAE's method for sizing the depth of the boreholes. To reduce the complexity of the problem and provide a more practical way for sizing the required length (and number) of the boreholes, ASHRAE proposed a modified two-dimensional heat transfer study originally developed for steady state condition in Ingersoll et al. work [197]. This model offers calculation of the borehole equivalent resistance in single and double U-tube GHEs. The proposed borehole load computation is entirely based on average values; average value of borehole wall temperature, average temperature of the inlet leg of the U-tube, average temperature of the outlet leg of U-tube, etc. Additionally, the axial heat transfer along the borehole is neglected and setting the temperature of both legs of a single U-tube as one constant value is the main simplification in 1D and 2D modeling [198]. These simplifications are in the nature of the 1D and 2D modeling as can be seen even in very recent studies such as [199–201].

Numerical studies in the form of computational fluid dynamic (CFD) analysis has been applied for predicting the thermal performance of GHEs. Although the CFD approach may take more computational time in comparison with the simpler models, today's powerful computers can reduce the necessary run time reasonably and the results will bear less relative error against the experimental data. Serageldin et al. [202,203] applied 3D CFD finite volume approach for solving the continuity, momentum, and energy governing equations for one vertical GHE equipped with oval cross-section U-tubes. They concluded that according to their numerical

results the oval shape U-tube can reduce both thermal resistance and pressure drop by 18.47% and 32% in comparison with conventional circular U-tube, respectively. However, they imposed an adiabatic boundary condition for the top surface of the simulation domain, which is not accurate for long term applications, or an area drilled with several boreholes. It should be noted that they extended the computational domain just 1 meter around the center of the borehole and imposed the symmetry or a predefined temperature profile boundary condition all around the computational domain. It means that the center-to-center spacing between boreholes in the considered computational domain is just 2 m. This will impact the thermal performance of the GHE during long term run, e.g., 1 month. Also, they did not mention the thermal performance of this new oval cross-section U-tube GHE in series configuration. Zhang et al. [204] studied the effect of borehole spacing and groundwater presence on the thermal performance of nine GHEs in just parallel configuration. They showed that a higher spacing (from 3.5 m to 5.5 m) can increase the heat pump coefficient of performance by 2.2% and 15.4% in cooling and heating mode, respectively. The thermal performance of the GHEs in series configuration is not presented in their study.

There are a few other 3D numerical studies that investigated different design specifications of a single GHE such as heat transfer fluid type and the fluid Reynolds number on the GHE thermal performance [205], changing the U-tube design as a spiral corrugated tube [206], an elliptical U-tube [207], or a single GHE fitted with double U-tubes connected at different configurations [208]. Pu et al. [209] and Qi et al. [210] investigated thermal performance of three GHEs in parallel and series configurations, numerically and experimentally. The boundary condition of the side walls in their computational domain is not stated in the studies. Moreover, in the numerical study of [209], the GHE is at the center of a 1×1 m^2 (with a depth of 3 m) that means a center-to-center spacing between GHEs in series as 1 m and the entire GHE is located in the transient ground temperature. With this small spacing between GHEs, it is not clear how the thermal interaction between GHEs is accounted in the simulations. Both [209] and [210] performed simulations at constant mass flow rates of the HTF. This means the GHE load in both energy extraction and injection working modes changes with time, so does the HTF outlet temperature.

The reviewed available studies show the following gaps in the literature:

- Realistic boundary and initial conditions are missing for several GHEs in parallel or series configurations
- The load of the GHEs are assumed variable or time-dependent rather than a constant load
- Information regarding the thermal performance of the GHEs in series configuration is scarce

- The available sizing method pay little attention on the temperature of the HTF exiting from the GHEs
- Long-term and accurate enough simulation for a test building with different load of GHE during a year is rare.

It should be emphasized that almost in all the simulations performed regarding the GHE thermal performance, the simulated cases are not based on a systematic heat integration in buildings. In other words, the GHEs studied in the literature are just connected to the heat pump system, and they are not connected to the building energy system, directly. It is shown that a stratified thermal energy storage tank can be integrated into a building energy system equipped with a heat pump system [123] based on the heat integration technique such as pinch analysis (PA).

Buildings can be assumed as an energy system with several hot and cold streams. Space heating, space cooling, and domestic hot water are the main energy streams in buildings which are time dependent and highly dynamic in nature. The mentioned loads should be satisfied to provide indoor comfort condition for residents. The required energy demand can be reduced by integrating waste and renewable sources such as gray water, ground source, solar energy, and heat pumping. PA is a tool that can systematically determine the maximum heat recovery (MHR) in an energy system among all possible hot/cold streams based on first and second laws of thermodynamics and a set of rigorous mathematical algorithms [6]. Furthermore, PA approach can be adapted for a time-dependent energy system such as building by introducing a network of heat exchangers and thermal energy storage tanks [3,123] to compensate the time mismatch among energy sources and sinks.

Introducing a TES tank into a building energy system brings a powerful advantage. It can dampen the fluctuations in the dynamic heating/cooling demands of a building, therefore, allows a constant heat pump capacity and constant ground source (GS) load. The surplus energy of the heat pump can be stored in the TES tank and it will return to the system when it is needed by discharging the TES tank. The same functionality of the TES tank help defining a constant load for GHEs. However, the outlet temperature of the HTF circulating inside the GHE should be in an acceptable range (see Appendix C).

The main objective of this study is to pave the way for sizing the vertical GHEs to deliver the design constant load at the acceptable outlet temperature range in both energy extraction/injection working modes. Therefore, first the thermal performance of the GHEs is defined according to the heat exchange between the heat transfer fluid and the ground. Then, the thermal performance of the GHE at three typical constant loads but at different depths is computed in the worst case which means the GHE is surrounded by other similar GHEs with accurate boundary and initial conditions. By defining an objective function as investment cost

divided by the thermal performance, it is shown that there is a trade-off between the thermal performance, the investment cost, and the depth of the GHE. Effect of parallel or series configurations on the thermal performance are presented in the next step for single and double U-tube GHEs at constant depth, but different working loads. Finally, the sizing procedure is applied to the test building with imbalanced GHEs energy extraction/injection rate and the thermal performance of the selected cluster of GHEs is investigated numerically for 20 years.

6.3 GHEs in different configurations

GHEs can be equipped with one single U-tube, double U-tube, or more. Additionally, the required duty or load can be share between several GHEs. In this way, the heat transfer fluid enters to each GHE with the same mass flow rate and the same temperature. This configuration is called parallel. However, it is possible to connect two GHE in series. In series configuration, the outlet of first GHE enters the second GHE.

6.3.1 Parallel configuration

A predetermined load can be delivered with several GHEs arranged in parallel configuration. Figure 6-1 shows the top view of several GHEs in parallel configuration. To obtain realistic results from numerical simulations the borehole that is surrounded with other boreholes is selected for simulation. Due to thermal interaction between neighboring boreholes, especially in long term applications, the thermal performance of a borehole surrounded with other ones closely resembles the worst-case scenario. In this numerical study the minimum center-to-center spacing is set as 6 m as recommended in [196].

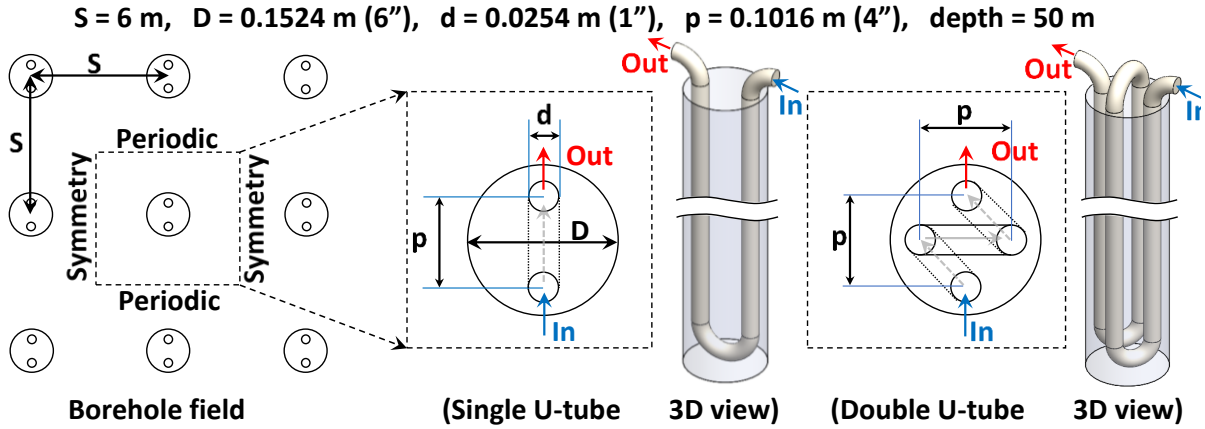

Figure 6-1 GHEs in parallel configuration (each inlet receives the same mass flow rate and temperature)

It should be noted that the single U-tube GHE in the parallel configuration is shown in Figure 6-1, however, the GHE equipped with double U-tube can have exactly the same parallel configuration. The interaction between adjacent GHEs is taking into account by setting a periodic boundary condition at the side walls, shown in Figure 6-1.

The inlet and outlet fluid pathways are illustrated as three-dimensional view in Figure 6-1, as well. There are several possible ways to connect U tubes in a double U-tube GHE. In this study, the heat transfer fluid enters from one side, passes through both U tubes that are connected in series. The arrows show the fluid flow direction.

6.3.2 Multiple pairs of vertical GHEs in series

As mentioned earlier, the outlet temperature of the HTF can be higher in the energy extraction working mode or lower in the energy injection mode if two GHEs, regardless of the U-tube configurations, are connected in series in comparison with the two parallel GHEs, where each receives the HTF at the same temperature. In series case, the HTF with the original inlet temperature enters to the first GHE, it exchanges the energy with the ground, then through an adiabatic connecting tube flows into the second GHE. This configuration is depicted in Figure 6-2. The double U-tube GHE is not shown in this figure, but the connection and the flow direction are the same. To simulate the worst-case scenario, which means the land is covered by several other GHEs connected in series, the symmetry and periodic boundary conditions are necessary. It worth mentioning that like the parallel case, the center-to-center spacing is assumed 6 m in series case.

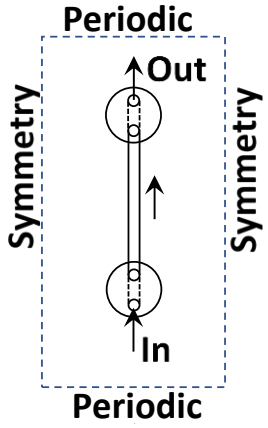

Figure 6-2 Schematic top view of two GHEs connected in series (arrows show flow direction)

It is possible to connect more than two GHEs in series. However, two problems will emerge. First, an effective heat transfer needs a reasonable temperature difference between the undisturbed ground temperature and the HTF, that might be missing in the last and/or several boreholes located before the last one. The second issue is the higher pressure loss as the HTF must flow through longer path that can be attributed to the higher required pumping power.

Therefore, just two GHEs in series equipped with single and double U-tube are considered in this study.

6.4 Numerical modeling

In this section the computational domain, mesh design, and other numerical details are discussed. The commercial finite volume solver ANSYS FLUENT 2020 R2 is used for all the presented results in this study. Several user-defined functions (UDFs) are hooked to the software regarding some specific boundary conditions and temperature dependent thermophysical properties of the HTF as a mixture of water and ethylene glycol.

6.4.1 Geometry and mesh design

The computational domain is discretized with hexahedral and tetrahedral 3D elements. Fine grid sizes are used in the volume inside the U-tube(s) and around it, and near borehole wall. The grid size is gradually increased toward the area far from the boreholes. Figure 6-3 shows the computational domain of the two GHEs in series configuration and some cross-section and closed views of the utilized grids in selected areas. The details of the grid size are provided in section 4.5.4.1.

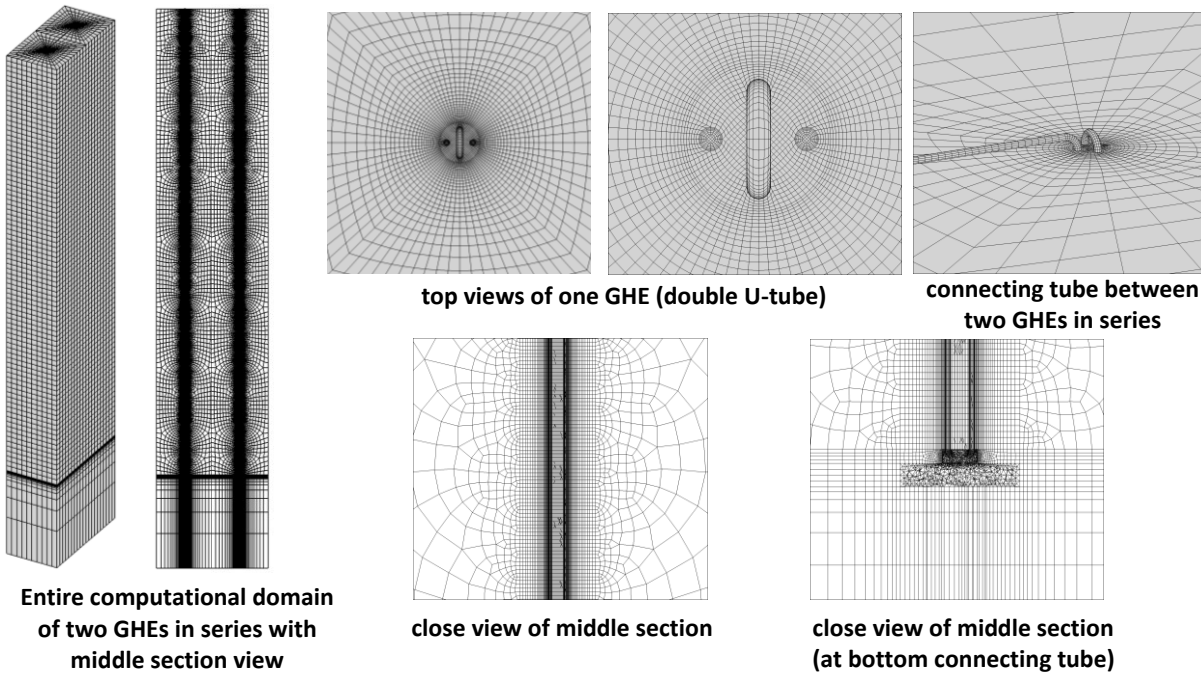

Figure 6-3 General grid design for the computational domain

The center-to-center spacing between each borehole is fixed as 6 m, therefore, the 3D computational domain is a rectangular prism with $6 \times 6 \times H$ m^3 corresponding to $-x, -y$, and $-z$, respectively. Regardless of the GHE depth, the computational domain is expanded 10 m below the bottom of the borehole. The simulations have been performed at different grid sizes to ensure that the obtained results are independent of the grid size. It worth mentioning that for

the parallel configuration, one rectangular prism with $6 \times 6 \times H$ is simulated where the GHE is at its center, while for two GHEs connected in series, two $6 \times 6 \times H$ are joint together, and a connecting tube connects the outlet of the first GHE to the inlet of the second GHE. Thus, the computational domain will be $12 \times 6 \times H$ for the series configuration.

6.4.2 Governing equations

Water + ethylene glycol (20% by mass), with freezing point of -7.95°C, is the working fluid for all the simulated GHEs. For this part of the computational domain, the continuity, the momentum, and the energy equations are presented in Eqs. (6-1) to (6-3), respectively.

$$\frac{D\rho}{Dt} + \rho \nabla \cdot \vec{V} = 0 \tag{6-1}$$

$$\rho \frac{D\vec{V}}{Dt} = -\nabla P + \mu \nabla^2 \vec{V} \tag{6-2}$$

$$\rho c_p \frac{DT}{Dt} = \nabla \cdot (k \nabla T) \tag{6-3}$$

where $D/Dt = \partial/\partial t + u\,\partial/\partial x + v\,\partial/\partial y + w\,\partial/\partial z$ is the material derivative [211], ρ is the density of the working fluid and a continuous function of temperature (see Appendix D), $\vec{V}$ is the velocity vector, i.e., (u, v, w) inside the U-tube, μ is the dynamic viscosity, P is the pressure, k is the thermal conductivity, and T is the temperature. As the Reynolds number is less than 2300 in all simulated loads, the fluid flow inside the U-tube is assumed to be laminar. It is worth mentioning that the Re number is between 500 to 2000 in different assigned load to the GHEs.

In the solid part of computational domain, i.e., the borehole + soil around it, just the energy equation (Eq. (6-4)) should be solved.

$$\frac{\partial}{\partial t}(\rho_s c_s T) = \nabla(k_s \nabla T) \tag{6-4}$$

where ρ_s, c_s, and k_s are the density, the heat capacity, and the thermal conductivity of the grout or the soil.

6.4.3 Boundary and initial conditions, modeling assumptions

As it was shown in section 6.3, the worst-case scenario is considered for all the simulations unless otherwise stated. Therefore, it is assumed that the field is covered by a large number of boreholes in different configurations, e.g., parallel or series. Two lateral vertical side walls can

be considered as symmetrical plane and other two sides are periodically repeated, as shown in Figure 6-1 and Figure 6-2. Therefore, the thermal interaction between adjacent GHEs is included in the simulation. The inner side of the PVC U-tube is no-slip condition and impermeable. The fluid flow enters with a specific temperature and mass flow rate. The top surface is located about 1.5 m below to the ground surface. The time dependent temperature profile of this top surface is computed based on the well-known Eq. (6-5) [182].

$$T(z,t) = T_{mean} - T_{amp} \times exp\left(-z\sqrt{\frac{\pi}{365\alpha}}\right) \times cos\left(\frac{2\pi}{365}\left(t - t_{min} - \frac{z}{2}\sqrt{\frac{365}{\pi\alpha}}\right)\right) \quad (6\text{-}5)$$

Where z is the depth , t is time in days, T_{mean} and T_{amp} are $T_{mean} = (T_{max} + T_{\min})/2$, and $T_{amp} = (T_{max} - T_{min})/2$, respectively. t_{min} is the number of day when the $T_{\min}$ occurs. In this study, the minimum temperature is on 21st of January, thus $t_{min} = 21$. α is the thermal diffusivity in m^2 day^{-1}. Based on the Eq. (6-5), the temperature at the top boundary condition is shown in section (a) in Figure 6-4. The energy extraction simulations start from day 21st of the year and is extended for 60 days. The energy injection simulations start from day 213th of the year, and it continues for 60 days.

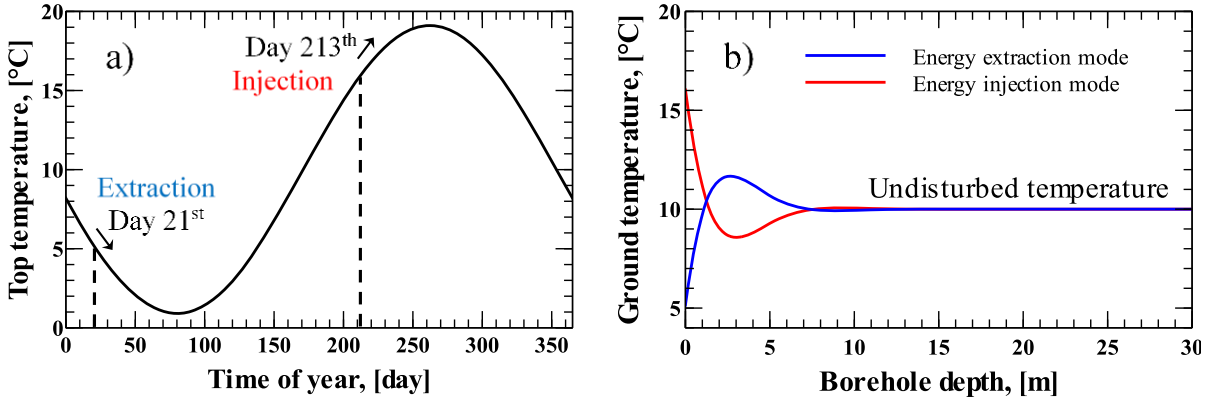

Figure 6-4 a) top boundary condition for each mode b) initial temperature profile for each working mode

The computational domain is initialized with the temperature profiles as shown in Figure 6-4 (b) corresponding to the mentioned days of 21 and 213 in the year. The undisturbed ground temperature is set as 10°C. The inlet temperature for the energy extraction and the energy injection are set to -5°C and 50°C, respectively. These temperatures are extracted from the dynamic pinch analysis, where the GHEs are connected to the building energy system via TES tanks. The readers are referred to Appendix C for the details of the superstructure, hot/cold streams, and all involved components.

The outlet temperature of GHEs varies according to the energy extraction or injection rate. In other words, it is possible to maintain a constant GHE load by adjusting the inlet mass flow rate.

Therefore, a variable mass flow rate makes sure that the GHE delivers the required load by taking feedback from the outlet temperature. Eq. (6-6) is applied at the beginning of each time step to adjust the required mass flow rate corresponding to the constant GHE load.

$$\dot{m}(t) = \frac{GHE\ constant\ load}{\left|c_{p,in}(t)T_{in} - c_{p,out}(t)T_{out}(t)\right|} \tag{6-6}$$

In all of the performed simulations, it is assumed that:

- The GHEs are located 1.5 m (60 inches) below the ground surface, at the same depth of the city water pipes, approximately
- The soil is dry, therefore, the convective effect is negligible in the underground
- The GHE inlet temperature is constant. -5°C in energy extraction mode and 50°C in energy injection mode
- The flow regime is laminar inside the U-tube pipes (except for the case considered in the validation section, where the flow is turbulence and the well-known standard $k-\varepsilon$ model [212] is applied)

Table 6-1 presents the thermophysical properties of underground, borehole grout, and PVC U-tube that are used for the modeling in this study. The temperature dependent thermophysical properties of water + ethylene glycol are presented in Appendix D. These data are extracted from Engineering Equation Solver (EES) software.

Table 6-1 Underground, grout, and PVC properties

Parameter		**Value**
Underground and grout	density	1600 kg/m^3
	thermal conductivity	1.5 W/(m K)
	heat capacity	2400 J/(kg K)
PVC (U-tube)	density	950 kg/m^3
	thermal conductivity	0.48 W/(m K)
	heat capacity	2100 J/(kg K)

6.4.4 Solving procedure

The governing equations are solved on staggered grids and are discretized with a second order upwind scheme. The SIMPLE algorithm proposed by Patankar [143] is applied for coupling between velocity and pressure on the computational domain inside the GHE. To ensure the accuracy of the obtained results, the convergence criteria for continuity, momentum and energy equations are set as 1×10^{-4}, 1×10^{-6}, and 1×10^{-10}, respectively. The discretized equations

are solved with implicit scheme as it is unconditionally stable over the computational domain. However, to capture the temperature variation over a meaningful time, the maximum time step is set as 864 seconds. For the very beginning of the transient simulations, the time step is set as 1 millisecond and it is gradually increased to the 864 seconds over a smooth curve.

6.4.4.1 Grid independency analysis

The dependency of the obtained results on the number of grids in a numerical analysis should be investigated. In other words, the numerical results have to be independent of the grids or meshes design. The general pattern of the grid distribution is shown in Figure 6-3. The computational domain inside the U-tube is assigned with the finest grid size. The height of the cells alongside the vertical GHE are 30 mm, 20 mm, 10 mm, 5 mm, and 2.5 mm. The cross section of the U-tube is meshed with a so-called butterfly grid [213] and the borehole area is covered with the radial grid distribution, where the grid at the area near the solid part is finer than the center of U-tube with a size of 0.5 mm × 2 mm. Furthermore, the maximum grid size is at the area far from the U-tube, with the sizes of 50 mm × 50 mm × 60 mm in $-x$, $-y$, and $-z$, respectively. Figure 6-5 presents the outlet temperature of a 50 m double U-tube GHE at different grid numbers at a constant load of 1000 W. The average outlet temperature is independent of the number of grids in grid sizes above 2 million, corresponding to the cell height of 10 mm. Therefore, this grid distribution is the base for all of the performed simulations.

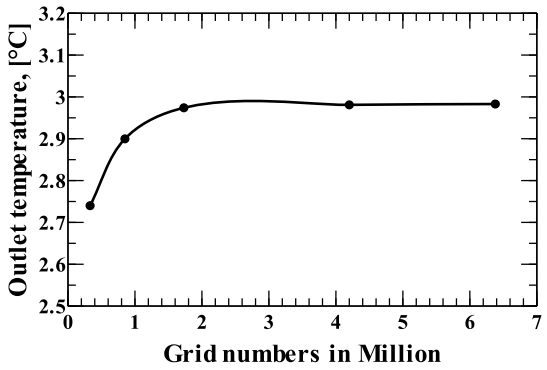

Figure 6-5 Grid independency analysis results

6.5 Results and discussion

6.5.1 Validation of the CFD simulation

The accuracy of the numerical approach needs to be validated against available experimental data. Hence, the obtain results from a Thermal Response Test (TRT) of a vertical GHE [214] are used to check the accuracy of the presented numerical data. Water was used as the heat transfer fluid. Dimensions and the other thermophysical properties are presented in Table 6-2.

Table 6-2 Experimental GHE characteristics, used for CFD results validation only

Parameter	Value
Borehole depth	50 m
Borehole radius	57.5 mm
U-tube inner diameter	35.2 mm
U-tube thickness	2.4 mm
Average ground density	2600 kg/m^3
Average ground heat capacity	850 J/(kg K)
Average ground thermal conductivity	2.9 W/(m. K)
Water mass flow rate	0.27 kg/s

A new numerical geometry with the dimensions and thermophysical properties as presented in Table 6-2 are simulated to evaluate the accuracy of the current CFD study. Figure 6-6 shows the test data and the numerical simulation results. The inlet temperature for the CFD study is the same as the experimental data, i.e., the blue line in Figure 6-6, however, the inlet temperature is used as a continuous function of time in the CFD study. The numerical outlet temperature is in an agreement in comparison to the experimental ones, with the maximum relative error less than 0.7%.

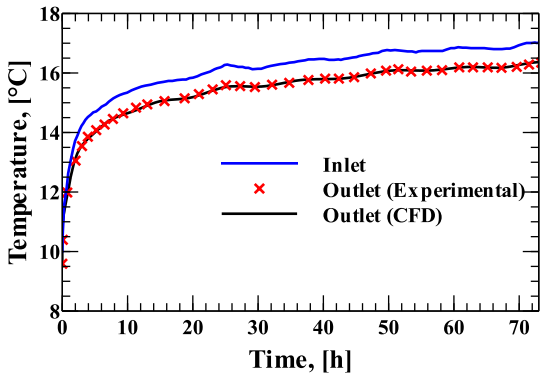

Figure 6-6 Comparison between the numerical and the experimental data

6.5.2 Optimum vertical GHEs depth; trade-off between cost and thermal performance

As mentioned in boundary condition section, the GHE can keep a constant load by adjusting the inlet mass flow rate based on the difference between inlet and outlet temperatures. The most important question that should be answered here is: at a constant load of GHE, how does the outlet temperature change by time? Due to the transient nature of the problem, a steady state answer might not exist, even after a long time. Hence, a long enough time is set for all the simulations that is set here as 60 days or two months. It should be noted that the dynamic GHEs duty can be computed based on the average monthly loads in a building. As the buildings heating

and cooling loads are not constant, the maximum GHE load should be considered as the design load. This maximum load lasts for one month or less. Therefore, the two months for the simulation time is a reasonable time duration at each constant load. This design load should be divided among all the GHEs in parallel configuration. The depth of the GHE can define the cost and the thermal performance of it.

The final cost of a vertical GHE is a function of drilling depth ($\mathrm{A} \times H$), U-tubes ($2\mathrm{B} \times H$) and other installations/distribution system ($\mathrm{C} \times H$), filling materials, i.e., cement, grouts, transport of extracted dirt ($\mathrm{D} \times H$), and labor cost ($\mathrm{E} \times H$). Drilling deeper boreholes results in the higher total cost. Therefore, the final cost is directly connected to the depth of the borehole. The cost can be assumed as a linear function of depth [188,215], as it is presented in Figure 6-7.

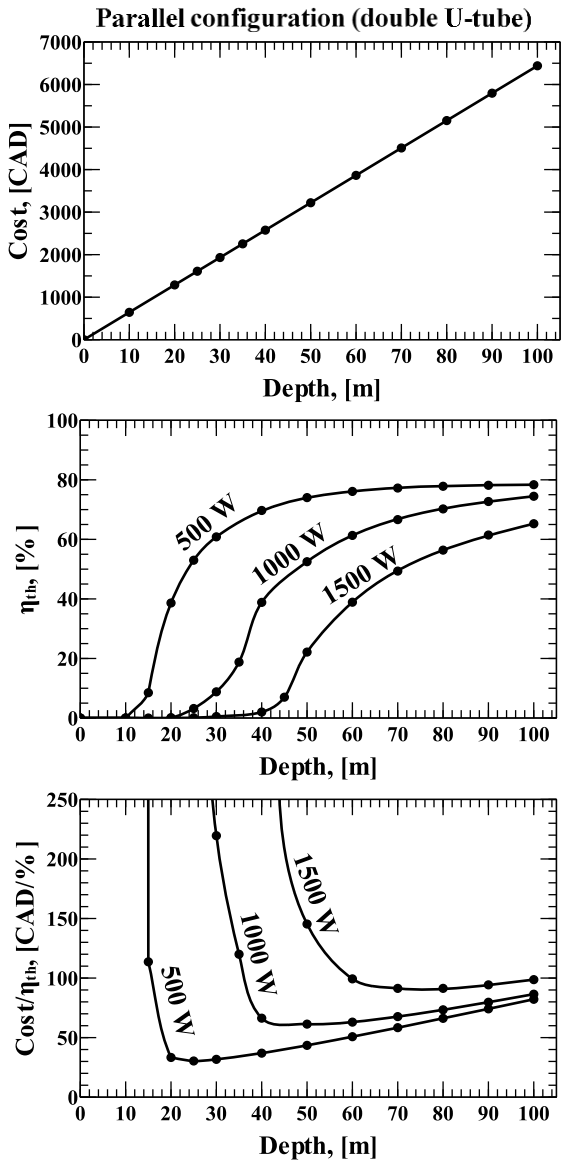

Figure 6-7 Cost, thermal performance, and trade-off between cost and performance at constant loads (parallel double U-tube GHEs)

The thermal performance (η_{th}) of a vertical GHE can be defined as presented in Eq. (6-7). In this equation the h_{in} and h_{out} are the inlet and outlet enthalpy of the HTF, i.e., water + ethylene glycol. The h_{undis} is the enthalpy of the HTF at the constant undisturbed underground temperature, i.e., far from the surface and the GHE, at 10°C in this case. Several simulations are performed with the GHE fitted with double U-tube at different depths for 60 days in energy extraction working mode. The loads are kept constants for all depths as 500 W, 1000 W, and 1500 W. All thermal performances are plotted in Figure 6-7. The vertical GHE cannot deliver

the desired constant load in depths below 15 m, 25 m, and 40 m for 500 W, 1000 W, and 1500 W, respectively.

$$\eta_{th} = \frac{h_{out} - h_{in}}{h_{undis} - h_{in}} \tag{6-7}$$

The thermal performance increases sharply from 0 % to 40 % almost in all constant loads, however, it increases slowly at higher depths. If we divide the capital investment cost of the GHE to its thermal performance, as an objective function, there is a minimum point that can be taken as the trade-off between its cost and the thermal performance at each given constant load. As an example, at constant load of 1000 W, the minimum cost/η_{th} can be achieved in H = 50 m. The optimum depths are 25 m and 75 m in loads equal to 500 W and 1500 W, respectively. Another interesting observation is that for the GHE load of 6 kW, as an example, one needs 12 GHEs with the optimum depth of 25 m (each deliver 500 W), or 6 GHEs with the optimum depth of 50 m (each deliver 1000 W), or 4 GHEs with the optimum depth of 75 m (each deliver 1500 W). In other words, the total length of the vertical GHEs is constant as 300 m when the optimum depth is the primary parameter for GHEs sizing at the required constant load. Nonetheless, the outlet temperature is another important factor that should be taken into account in sizing the GHEs.

Figure 6-8 illustrates the outlet temperature of the GHEs at the different depths and the different loads. The GHEs are connected to the TES tank as it is proposed in the superstructure extracted based upon energy targeting pinch procedure (see Appendix C). Therefore, the outlet temperature of the GHEs should be above or equal to 5°C in the energy extraction working mode, i.e., the dashed line in Figure 6-8. By applying this temperature limit, it can be found that the required length of the vertical GHEs for satisfying 6 kW load with the outlet temperature above 5°C is 480 m: 12 GHEs each 40 m (500 W each), 6 GHEs each 80 m (1000 W each), or 4 GHEs each 120 m (1500 W each). This observation suggests that the total required length of the GHE is more less the same, regardless of the depth of each individual borehole depth.

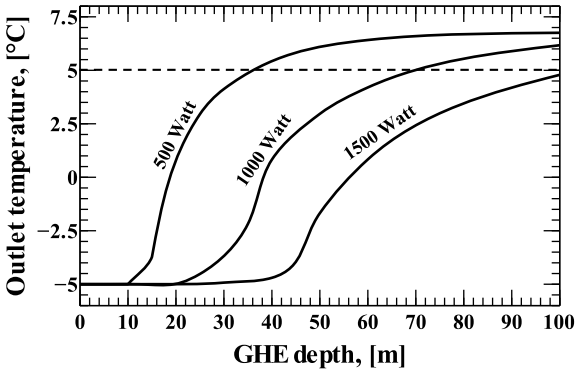

Figure 6-8 Outlet temperature versus depth at different loads (parallel double U-tube GHEs)

From the results presented in this section, it can be inferred that although there is an optimum depth for the GHE at a given load, the GHE at this depth may not be able to deliver the required minimum outlet temperature that is set by the pinch integration technique. In order to achieve to the maximum heat recovery in a building, these temperature limits should be respected. Therefore, the outlet temperature of the GHE plays an important role in sizing the required depth.

6.5.3 Performance of parallel GHEs at a fixed depth

The thermal performance of the GHEs at fixed depth of 50 m and in the parallel configuration are presented in this section. In parallel configuration, all of the GHEs receive the same mass flow rate and the inlet temperature of -5°C in the winter or the energy extraction working mode. Figure 6-9 presents the three most important parameters of GHEs arranged in parallel configuration: the outlet temperature, the inlet mass flow rate, and the pressure drop. The GHE thermal behavior is different at each constant load. At small loads, e.g., 250 W to 500 W, the outlet temperature is close to each other for both single U-tube and double U-tube GHEs as the difference between them is less than 0.25°C after 60 working days. This temperature difference gets larger by increasing the load. The fall in the outlet temperature is higher in the single U-tube in comparison to the double U-tube GHE. Another point is that at higher loads, the outlet temperature of the double U-tube GHE is higher than that of single U-tube. As an example, at a constant load of 1000 W, the heat transfer fluid reaches to 3°C with the double U-tube GHE, that is 1.25°C greater than the outlet temperature of the GHE equipped with the single U-tube at the same load. Moreover, an increasing pattern in the mass flow rate can be recognized at higher loads in both single and double U-tube GHEs. The better performance regarding outlet temperature in double U-tube GHE is mainly due to having higher heat transfer area, i.e., twice the area that the single U-tube. It should be noted that the inlet temperature is constant in the energy extraction mode, i.e. -5°C, for both single and double U-tube ones.

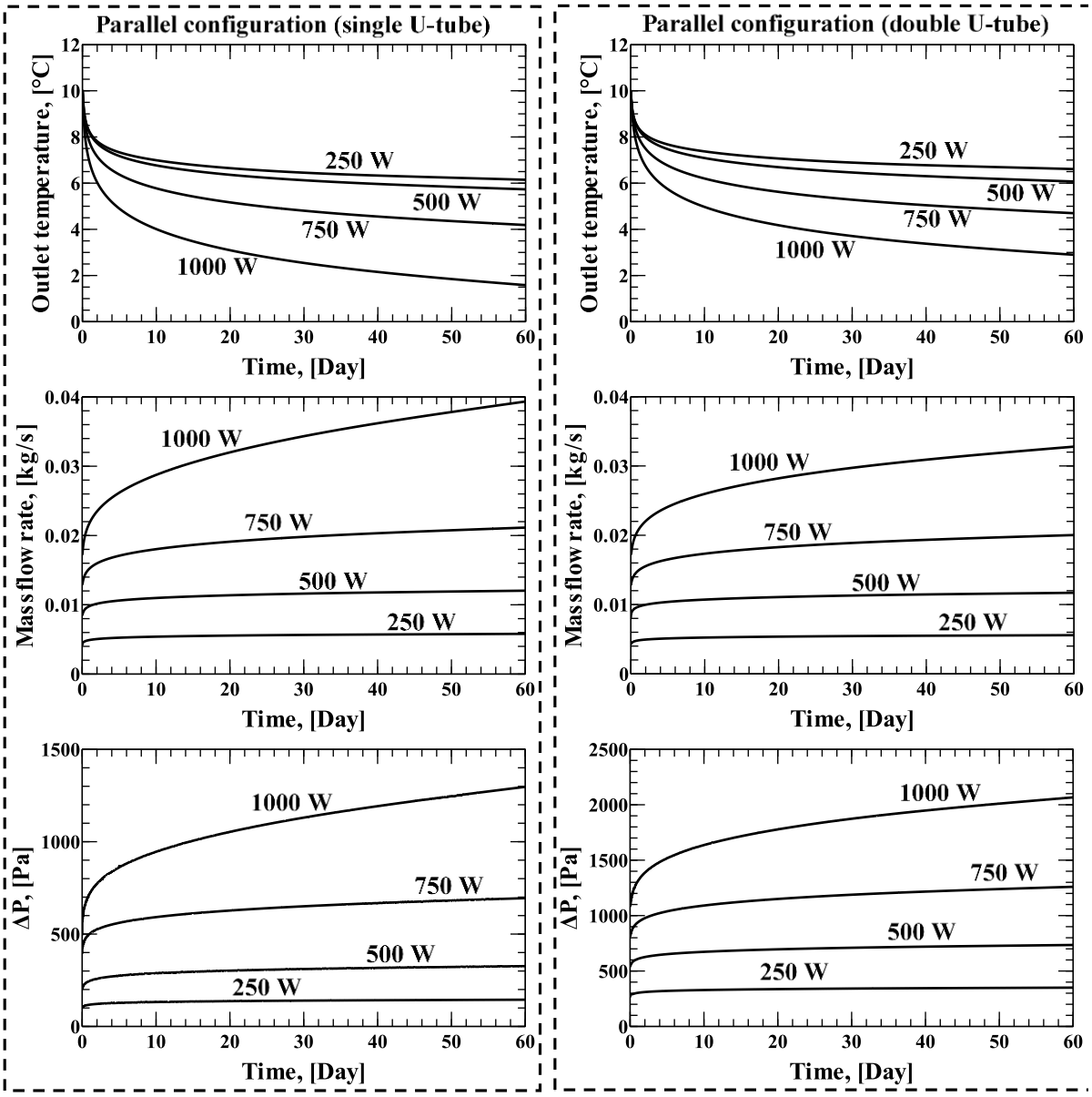

Figure 6-9 Thermal performance of single (left graphs) and double (right graphs) U-tube GHEs in parallel configuration, energy extraction mode

Moreover, the heat transfer fluid needs to go in a longer path to exit from the GHEs equipped with the double U-tube. Therefore, the pressure loss is two times higher in double U-tube case with respect to the one equipped with single U-tube. As the pumping power is directly related to the pressure loss, thus the required pumping power is approximately two times higher in the double U-tube GHE versus the single U-tube GHE. This can be expected especially when in all presented simulations the fluid flow regime is laminar based on the inlet Reynolds number, e.g., $Re = 515 \ll 2300$, at 1000 W in the single U-tube GHE.

Figure 6-10 illustrates thermal performance of the single and double U-tube GHEs in parallel configuration in the energy injection working mode.

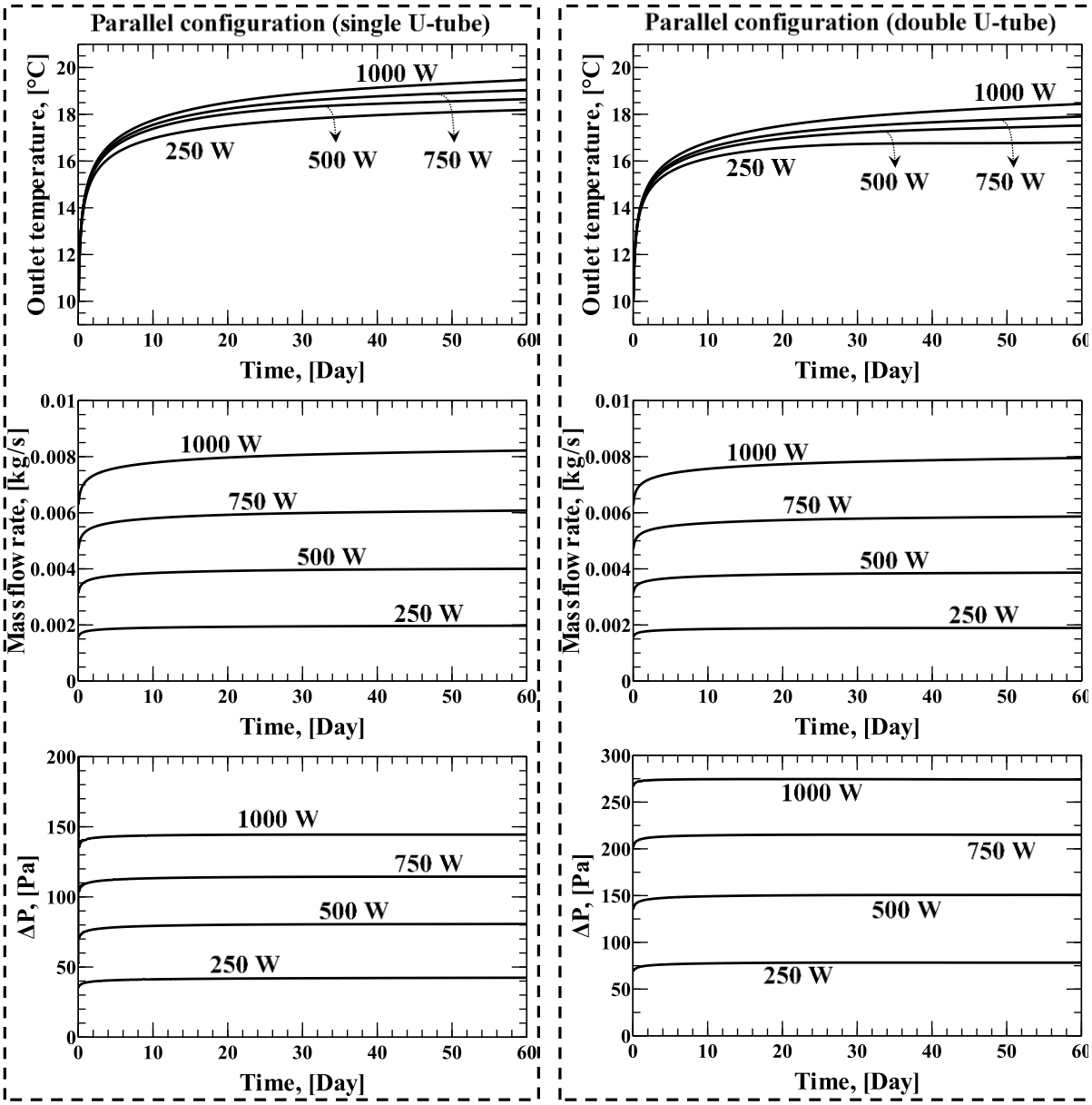

Figure 6-10 Thermal behavior of single (left graphs) and double (right graphs) U-tube GHEs in parallel configuration, energy injection mode

In this case, the inlet temperature is relatively high, i.e., 50°C. According to the dynamic pinch analysis, the outlet temperature of the GHE should be below or equal to 15°C in the energy injection working mode. However, this temperature is higher in all the simulated cases in the parallel configuration, from 250 W to 1000 W load. As can be seen in Figure 6-10, the overall performance is slightly better when the GHE is equipped with a double U-tube in comparison to the single U-tube GHEs.

6.5.4 Performance of two GHEs in series at fixed depth

It is practical to connect two GHEs in series to achieve higher outlet temperatures in comparison with two GHEs in parallel. Figure 6-11 and Figure 6-12 illustrate the thermal performance of two GHEs in series.

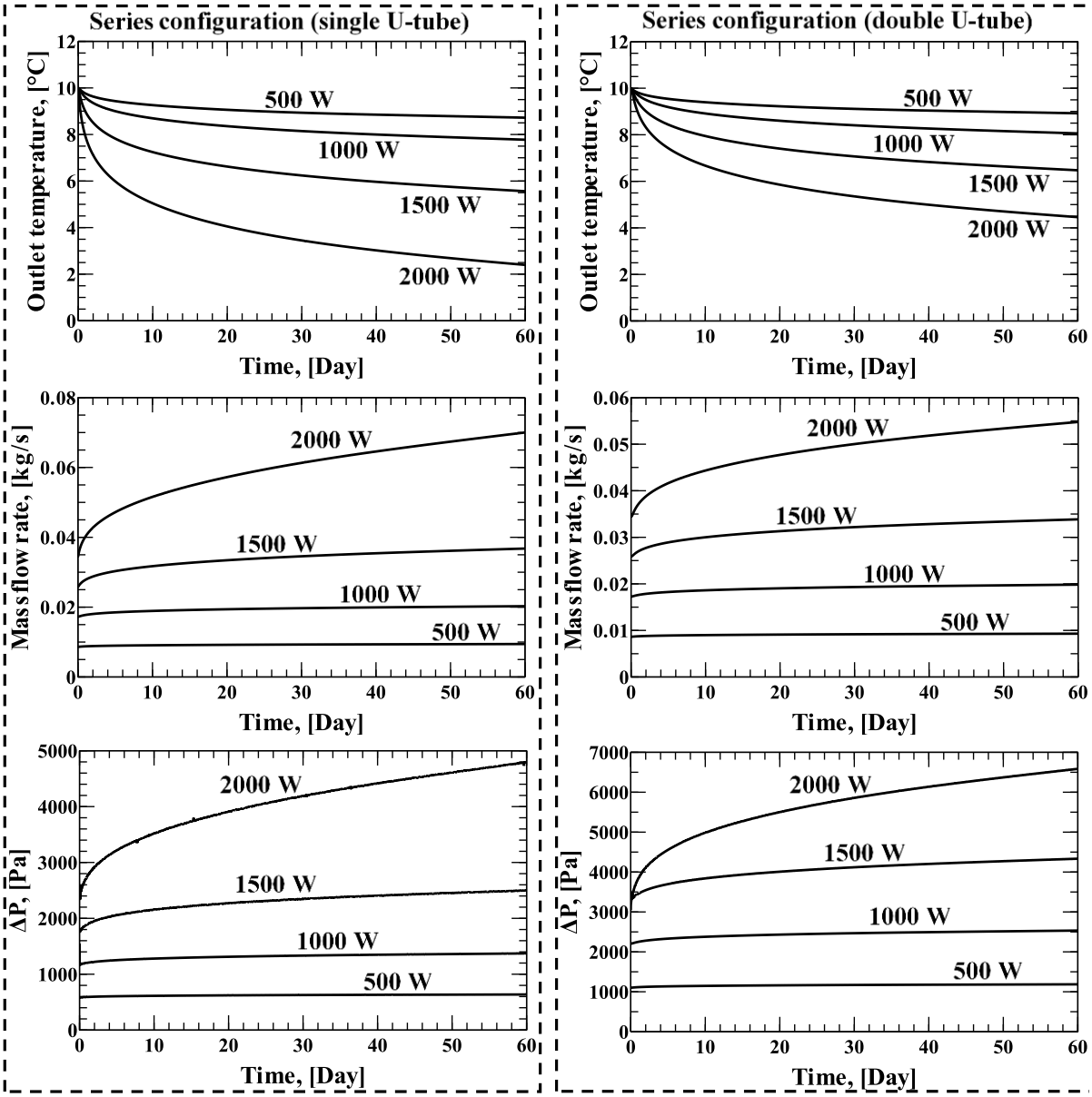

Figure 6-11 Thermal behavior of a pair of single (left graphs) and double (right graphs) U-tube GHEs in series configuration, energy extraction mode

It should be noticed that in the series configuration, the loads are doubled to have a fair comparison with the parallel GHEs. Simulations are performed for both single and double U-tube GHEs. Similar to the parallel case, here in series configuration, the outlet temperature is very close to each other in single and double U-tubes in small GHE load, e.g., 500 or 1000 W.

Nevertheless, at higher GHE loads, the difference between these two designs is noticeable. As an example, at constant load of 2000 W, the outlet temperature of the HTF circulating inside two GHEs connected in series, but one equipped with the single U-tube and another equipped with the double U-tube are 2.5°C and 4.5°C, respectively. Although the outlet temperature is not increased twice, it still shows the better performance of the GHEs equipped with double U-tubes.

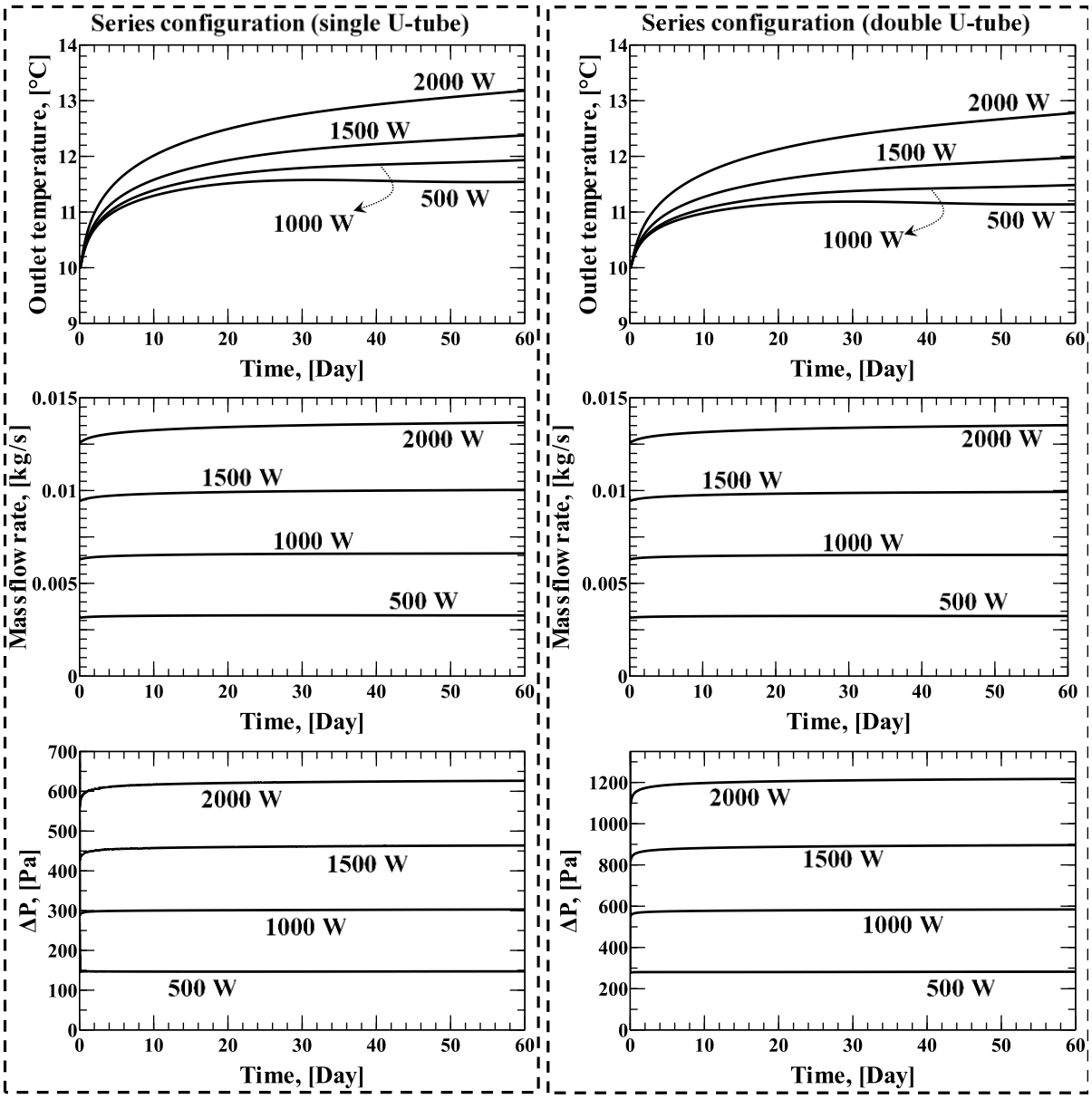

Figure 6-12 Thermal behavior of a pair of single (left graphs) and double (right graphs) U-tube GHEs in series configuration, energy injection mode

Furthermore, the results show that the outlet temperature of two GHEs in series is higher than the outlet temperature of two GHEs in parallel at the same equivalent load. In other words, the outlet temperature of two double U-tube GHEs in series at 2000 W after 60 days, is 4.5°C,

where this value for two double U-tube GHEs in parallel (each delivering 1000 W), is 2.95°C. As the maximum outlet temperature in the series configuration in the energy extraction mode are higher with respect to the parallel configuration, therefore, it can be attributed to the higher thermal performance.

From energy injection perspective, the series configuration can meet the outlet temperature requirement imposed by the pinch analysis and the connection with a TES tank. The outlet temperature is less than 15°C in all the simulated loads at a constant depth of 50 m. If the thermal performance of the GHE for delivering 2000 W is considered, the outlet temperature limit of below or equal to 15°C is achieved by providing 4.4 times higher pressure drop versus two double U-tube in the parallel configuration when each deliver 1000 W.

6.5.5 GHE configuration for a test building; A design case study

GHE load is a variable quantity during the heating or cooling days in a year. As it is presented in the proposed superstructure in Appendix A, the GHEs can be integrated into the energy system of a building through heat integration techniques such as pinch analysis. Therefore, the monthly average value of the GHE load is a known value in the context of reaching to the maximum possible heat recovery in buildings. The test building has been described in previous studies of the authors [3,123]. The required GHE size to meet the maximum GHE load is presented in this section. It is assumed that the GHE is going to be sized to satisfy its maximum load that occurs in January. It worth mentioning that the sizing procedure is the same if a smaller GHE load is selected.

6.5.5.1 Possible GHE sizing based upon the CFD results

The average minimum GHE load at each month for the test building is shown in Figure 6-13. These loads are obtained based on a full heat integration among all possible hot/cold streams in the test building (see Appendix C). This is a building with a dominant energy extraction rate. The ground source needs to provide the required energy for eight consecutive months. The extracted energy can be partly replenished from June to September. This energy replenishment is just by warm atmospheric air and solar radiation in June and September, i.e., passive recharge. In addition to the passive charging, the condenser of the heat pump system injects energy into the GHE during the summer, i.e., July and August. This is called the active ground source energy recharge.

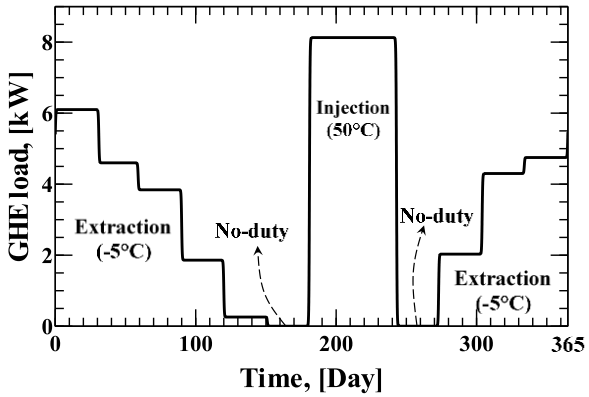

Figure 6-13 Dynamic GHE load during one year

The maximum GHE load during the energy extraction mode occurs in January with a value of 6 kW. Therefore, this load is the design load for selecting the GHE's number and configuration. The desired outlet temperature of the GHEs is assumed to be 5°C, in integration with a TES, thus Figure 6-9 and Figure 6-11 can help in selecting the number and configuration of GHEs. Table 6-3 shows several possible designs for a cluster of GHEs.

Table 6-3 Number and configuration of GHEs (each 50 m deep) for 6 kW energy extraction

Configuration	**Single U-tube (Parallel)**		**Double U-tube (Parallel)**		**Single U-tube (Series)**			**Double U-tube (Series)**		
Load (W)	250	500	250	500	500	1000	1500	500	1000	1500
Number	24	12	24	12	24	12	8	24	12	8
Approximate outlet temperature (°C)	6	5.8	6.5	6	8.8	7.75	5.5	9	8	6.5

The maximum GHE load in the energy injection mode is 8 kW and the temperature should be less than or equal to 15°C. Therefore, just series configuration is suitable based on the provided data in Figure 6-10 and Figure 6-12. If just energy injection mode is considered, the best case is four sets of two GHEs (both double and single U-tube are acceptable) in series, each pair works at 2000 W.

The final design of GHE for the test building is the common denominator of possible arrangement of the GHEs between the energy extraction and injection working modes. In this case, it is four sets of two double U-tube GHEs, where each pair of GHEs are connected in series. The reason for selecting double U-tubes over single one is that the latter can provide higher outlet temperature that is a key point in the energy extraction working mode.

As the final design consists of just eight GHEs, there can be several arrangements for the selected design. Figure 6-14 shows three possible arrangements for the eight GHEs (4 sets of two double U-tube GHEs in series). All three clusters respect the minimum borehole center-to-center distance of 6 m. However, the proposed configuration in case c has the maximum distance of the HTF inlets in comparison to the case a and b. This distance is 8.5 m, 6 m, and 14.5 m, in case a, b, and c, respectively. Hence, this configuration is selected for the final consideration. It is worth noting that this number of GHEs and the corresponding arrangement will satisfy the maximum GHE load in both energy extraction and injection modes if the extracted and injected energies were the same, i.e., balanced extraction/injection rate, which in this case study it is not a balanced rate. The imbalanced energy rate results in deviation from the expected design outlet temperatures. To quantify this depletion rate and understand the thermal performance of the selected cluster a long-term simulation is performed.

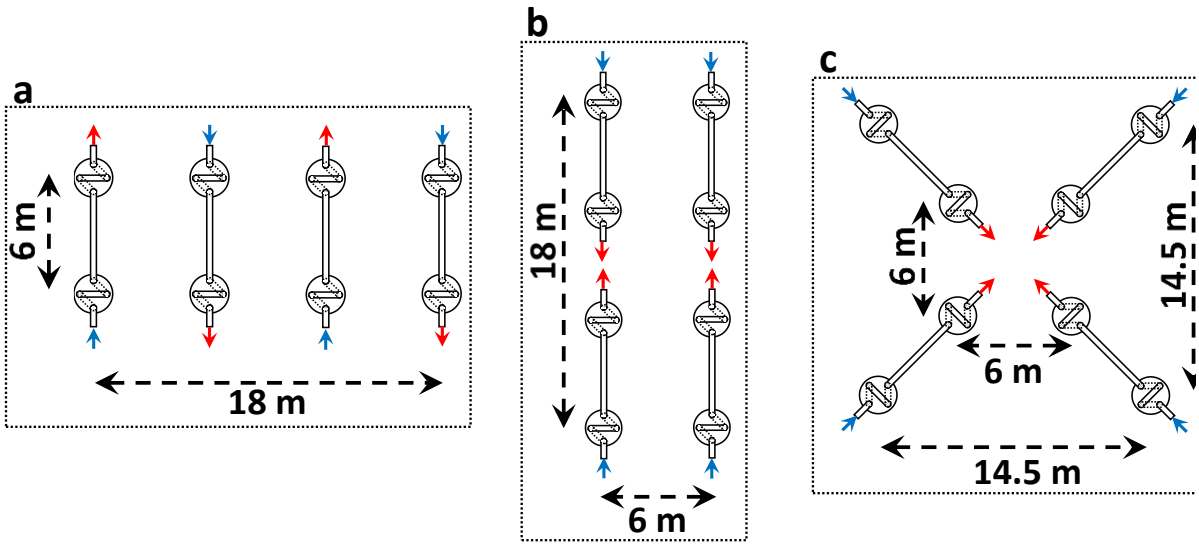

Figure 6-14 Top view of possible clusters of four sets of two double U-tube GHEs in series for the test building (the minimum center-to-center spacing of 6 m), the blue arrows indicate inlet and the red arrows show outlet

6.5.5.2 Depletion of ground source potential at imbalanced energy extraction/injection rate

So far it is shown that at a constant load, the outlet temperature and the mass flow rate can vary in different GHEs configurations. There is another factor that should be taken into account. When there is a deficit between the extracted energy and the injected energy in a year, the ground source potential regarding effective heat transfer will eventually deplete. In other words, it eventually loses its functionality to meet the design outlet temperatures in both working modes. Therefore, based on the difference in total extracted and injected energy and the

designed working time, e.g., 20 years, a safety factor should be defined to ensure the GHEs viability in long term applications. This safety factor can be adding an electric heating element inside the TES tank where the GHEs are connected to. This heating element represents a hot utility and can easily compensate the energy deficit due to an imbalance energy extraction/injection rate.

Due to the limited number of GHEs, a new simulation domain needs to be set to include the most accurate boundary conditions (see Appendix E). The thermal performance of the proposed cluster of the GHEs that can satisfy the dynamic load illustrated in Figure 6-13, are presented for selected years in Figure 6-15 (the full results are shown in Figure E2). The minimum temperature is obtained at the end of the January in each year when the GHE load is the maximum value. There are two months that the GHE load is zero. In these two months, the mass flow rate is zero, where the temperature is shown as dashed line in Figure 6-15.

The effect of the imbalanced energy extraction/injection rate on the outlet temperature can be seen in the long-term simulation data. The outlet temperature decreases during time at different rates. In the beginning, the reduction rate is significant, e.g., from 7°C to 5.5°C in first three years, however, the reduction rate reaches to an almost constant value after 10 years that is 0.05°C per year.

It should be noted that the minimum outlet temperature should not go below 5°C in energy extraction working mode. However, it goes below this design set point in some days in the end of January each year (after 7th years). This issue can be solved in two ways. First, if there is a need to use 100 percent of the ground source renewable energy, another set of two GHEs in series can be added to the proposed design. In this way, it can be guaranteed that the design temperature will be respected, even after 20 years. The second solution is adding one auxiliary electric heating element inside the TES tank to make sure that the top temperature in the TES tank is always 5°C. The economic analysis, which is a subject of the next part of this study, will shed light on the best solution.

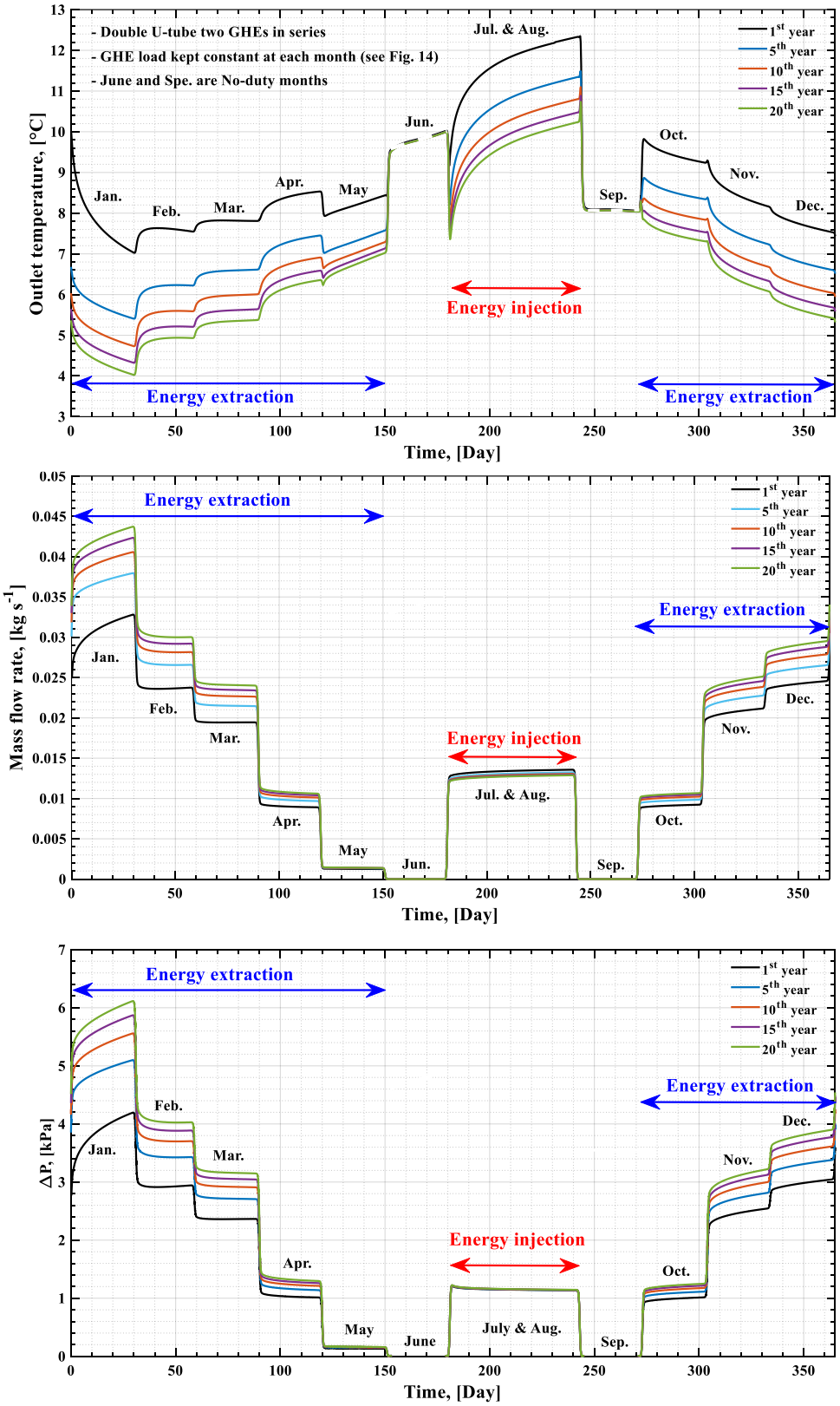

Figure 6-15 Outlet temperature, mass flow rate, and pressure loss for selected years during 20 years of simulation

6.6 Conclusion

The optimum load for the GHEs in integration with the building energy system can be extracted through heat integration techniques such as pinch analysis. To achieve the maximum heat recovery from direct and indirect heat exchange, the GHEs need to be connected to a stratified TES tank. This connection results in constant load and constant inlet temperatures of the circulating HTF of the GHEs in both energy extraction and injection working modes. At the same time, by integrating the GHEs into the building energy system, the outlet temperature of the circulating HTF exiting the GHEs should be in a certain range, above or equal to 5°C in the energy extraction working mode and below or equal to 15°C in the energy injection working mode. Determination of the depth and configuration of the vertical GHEs that can fulfill the mentioned constant load and the temperature limits is not a trivial task, also these requirements cannot be satisfied based on the available sizing methods in the literature. Thus, in this study extensive 3D CFD simulations are performed to evaluate thermal behavior of the GHEs at different constant working loads in both energy extraction and injection working modes.

The results reveal that at constant GHE loads, there is a trade-off between the investment cost and the thermal performance where the objective function, defined as cost divided by thermal performance, is minimum. It has been shown, as an example in the energy extraction working mode, that at constant loads of 500 W, 1000W, and 1500 W, the optimum depths that correspond to the minimum cost over thermal performance are as 25 m, 50 m, and 75 m, respectively. However, by considering the desired outlet temperature of the HTF, the GHEs depth should be 40 m, 80 m, and 120 m, for the mentioned loads, respectively. Another important aspect of sizing the depth of the GHEs are their configuration as parallel or series. Hence, the thermal performance of the GHEs in two configurations, namely parallel and two GHEs connected in series, are simulated at a constant depth of 50 m, but at different constant loads. Therefore, four different cases as single U-tube in parallel and series, and double U-tube in parallel and series are investigated numerically. According to the obtained results, the thermal performance of two GHEs in series equipped with double U-tube is superior in comparison to the two parallel GHEs at an equivalent load.

Finally, the sizing procedure is performed for a test building with an imbalanced extracted-injected energy rate. In light of the obtained outlet temperature at each constant load in the present numerical study, four pairs of two GHEs (double U-tube) connected in series are selected for the test building. The numerical results reveal that the outlet temperature goes below the minimum design set point after seven years, in limited days in each year, due to the ground source potential depletion. To overcome this issue, the building can be equipped with more pairs of GHEs or the energy deficit can be compensated be an auxiliary electric heating element. The

economic analysis, which clears up the best solution for this issue, will be performed in another investigation.

6.7 Acknowledgement

The authors acknowledge the financial support of the Natural Sciences and Engineering Research Council of Canada for this project (RGPIN-2019-05826).

6.8 Nomenclature

A, B, C, D, E	constant values for GHE cost
c_p, c_s	specific heat capacity [J kg^{-1} K^{-1}]
D	borehole diameter [m], material derivative
d	U-tube diameter [m]
H	GHE depth [m]
P	pressure
S	borehole center-to-center spacing [m]
t	time [s]
T	Temperature [°C]
T_{top}	Temperature at 1.5 m below ground surface [°C]
T_{ini}	Initial temperature [°C]
$T_{in,Ext}$	Inlet temperature at energy extraction working mode [°C]
$T_{in,Inj}$	Inlet temperature at energy injection working mode [°C]
$\vec{V}$	Velocity vector ($u\vec{\imath} + v\vec{\jmath} + w\vec{k}$) [m s^{-1}]
Greek	
μ	Dynamic viscosity [kg m^{-1} s^{-1}]
ρ	Density [kg m^{-3}]
Subscripts	
in	inlet
out	outlet
s	solid (U-tube, soil, and grout)
$undis$	Undisturbed temperature
Acronyms	
CAD	Canadian Dollar
CFD	Computational Fluid Dynamics
GHE	Ground Heat Exchanger
GS	Ground Source
GSHP	Ground Source Heat Pump
HTF	Heat Transfer Fluid
HP	Heat Pump
HX	Heat Exchanger
TES	Thermal Energy Storage
TRT	Thermal Response Test

Chapter 7: Techno-economic approach for optimum solar assisted ground source heat pump integration in buildings

Avant-propos

Auteurs et affiliation:

Seyed Mojtaba Hosseinnia: étudiant au doctorat, faculté de génie, département de génie mécanique, Université de Sherbrooke.

Mikhail Sorin: professeur, faculté de génie, département de génie mécanique, Université de Sherbrooke.

Date d'acception: -----

État de l'acceptation: Soumis à Journal

Revue: Energy Conversion and Management, An International Journal

Titre français: Approche technico-économique pour une intégration optimale de la pompe à chaleur géothermique assistée par énergie solaire dans les bâtiments

Contribution au document: Cet article ouvre la voie à la recherche d'un seul réseau optimal parmi tous les optimaux quotidiens possibles pour un bâtiment.

Résumé français: Une approche en deux étapes pour une intégration optimale de la pompe à chaleur géothermique assistée par énergie solaire dans les bâtiments est proposée. Lors de la première étape, une procédure spéciale d'analyse de pincement dynamique permet de cibler la taille de l'équipement de transfert d'énergie et de chaleur en fonction des demandes d'un bâtiment, des sources d'énergie renouvelables/déchets disponibles et des spécifications d'une pompe à chaleur géothermique assistée par énergie solaire (SAGSHP) système. En conséquence, plusieurs candidats à la conception quotidienne éconergétique sont sélectionnés. Lors de la deuxième étape de la démarche proposée, une conception finale fonctionnant pour toute l'année est sélectionnée parmi tous ces candidats en calculant le coût annuel total (TAC).

Un algorithme spécial est proposé pour calculer la pénalité annuelle moyenne en termes d'énergie et de coût en capital pour les services complémentaires chaud/froid afin d'adapter les conceptions mensuelles à la conception globale de l'année. En tant que fonction objective, le TAC est défini pour une durée de vie de 20 ans. Dans le contexte du marché canadien, il est illustré que le choix de la conception globale de l'intégration annuelle dépend principalement du coût de l'électricité. Par exemple, avec le coût de l'électricité au Québec, la conception pour le mois de septembre est optimale pour toute l'année, où l'intégration du SAGSHP n'est pas économiquement justifiée. Cependant, si l'on considère le coût moyen de l'électricité au Canada, la conception pour le mois de mars est optimale pour toute l'année. La taille optimale de l'échangeur de chaleur au sol est de 200 m^2 dans ce cas.

7.1 Abstract

Two-step approach for optimum solar assisted ground source heat pump integration in buildings is proposed. At the first step a special procedure of a dynamic pinch analysis allows to target the energy and heat transfer equipment size based on a building's demands, the available renewable/waste sources of energy and the specifications of a solar assisted ground source heat pump (SAGSHP) system. As a result, several energy efficient daily design candidates are chosen. At the second step of the proposed approach, a final design working for the whole year is selected among all these candidates by calculating the total annual cost (TAC). A special algorithm is proposed to compute the yearly average energy and capital cost penalty for complementary hot/cold utilities in order to adapt the monthly designs to the overall year design. As an objective function, TAC is defined for a 20-year lifetime design. In the context of Canadian market, it is illustrated that the choice of the overall year integration design depends mainly on the electricity cost. For example, with Quebec electricity cost, the design for the month of September is optimal for the whole year, where the integration of SAGSHP is not economically justified. However, if Canadian average electricity cost is considered, the design for the month of March is optimal for the whole year. The optimal size the ground heat exchanger is 200 m^2 in this case.

Keywords: Daily optimum design, Dynamic pinch, Heat exchanger sizing, Maximum heat recovery, Total annual cost

7.2 Introduction

Energy utilization in buildings can be reduced by integrating waste and renewable energy sources into the building energy system via a solar assisted ground source heat pump (SAGSHP)

system. SAGSHP systems have been shown as an enticing and capable system that can satisfy buildings space heating (SH) and domestic hot water (DHW) loads even in severely cold climate [216–218] or space cooling and DHW loads in hot or temperate climate [48,219]. The main reason behind the attraction towards the SAGSHP system is mostly due to the fact that the heat pump system converts the input electric energy into thermal energy. The output thermal energy is several times higher in value than the input electric energy, in other words, the heat pump system multiplies it by its coefficient of performance (COP), e.g., around 3 as a typical value. However, as a SAGSHP system consists of several vital components such as PV panels, ground heat exchangers, thermal energy storages, condenser, evaporator, etc., combined with the dynamism of the building heating/cooling loads and the intermittent nature of renewable energies during a single day/throughout a year, SAGSHPs inherit the challenge of evaluating an optimum size/capacity, especially from economic perspective.

Despite being available for several decades, a quick survey in the literature reveals that the performance and configuration of the SAGSHP for a particular building is still the main subject of investigation. Lazzarin [220] and James et al. [221] have provided a very detail and the state-of-the-art review of different configurations regarding solar energy and heat pumping in buildings. Some very recent examples are scrutinized here. Yao et al. [222] investigated the overall performance of a SAGSHP system in a residential building. In their design, the condenser of a heat pump is directly connected to the building heating system. The combined solar PV and thermal panels (PVT) provides both the heating load for the evaporator and the electric energy for the compressor. They showed that the overall COP of the studied case can reach up to 7.4. However, they provided no clue regarding sizing of different components of the system or how to determine the capacity of the heat pump (HP) system. Chen et al. [46] introduced a combination of PV/thermal panels and GSHP system into a hotel and an office building. They determined the capacity of the system based on the maximum heating load. They concluded that the energy saving potential of the proposed system is 33% and 19% in the residential and office building, respectively. Sakellariou and Axaopoulus [223] and Sakellariou et al. [224] introduced a new index for performance evaluation of the PVT+GSHP as renewable power fraction (RPF) in contrast to the generally utilized seasonal performance factor (SPF). They showed that SPF index neglects the electricity produced by PV panels and solely includes the amount of thermal energy produced by the solar thermal collectors. Sommerfildt and Madani [146] investigated the techno-economic feasibility of a PVT+GSHP system for a multifamily building in Sweden, where the heating load is the dominant one. In their total life cycle cost analysis, they reported that application of PVT into a traditional GSHP can reduce the borehole length up to 20% for their specific multifamily test case. Sakellariou et al. [225] compared a SAGSHP system with a natural gas boiler in both energy performance and the economic analysis via the life cycle cost analysis for a central England location and for the domestic

heating purpose. The economic analysis results reveal that the natural gas boiler is a better option in comparison to the SAGSHP system as the natural gas price is low in that area. This clearly shows that the utility price plays an important role in the economic viability of the renewable energy integration into buildings.

Naili and Kooli [226] performed the annualized total cost of a SAGSHP system working in both heating and cooling mode in Tunisia. They showed that the system is cost benefit in comparison to the conventional heating and cooling system. It should be noted that the solar energy is integrated as a thermal collector into the GSHP system not as the PV panels. Emmi et al. [227] presented the performance of a SAGSHP system for a residential two-story building. They considered four months of January, April, July, and October; each represents the condition of a season. Their HP system was able to meet the space heating, DHW, and the cooling load of the studied case. They concluded that the overall COP of a system equipped with PVT is higher than that of the conventional solar thermal collectors (STC) + GSHP system. They did not include any waste energy such as gray water in their model. Also, no economic analysis was provided.

Mehrpanahi et al. [228] studied different configurations of STC + GSHP system in Tehran climate condition to satisfy a building heating load. They used the COP of the heat pump system as the main objective function in all different studied configurations. Based on this criterion, they concluded that the optimum COP occurs when the STC and ground heat exchanger (GHE) provide the required load for the evaporator, and the condenser satisfy the building heating loads. A similar configuration was experimentally investigated for a building in Indian winter climate condition for a single day, as well [229]. However, they did not address the ground source potential depletion rate [230] at the energy imbalanced working condition (i.e., working only in heat extraction for several years) in their studies.

From the reviewed examples, it can be discerned that the focus is on the performance of the system rather than providing a systematic approach for sizing the SAGSHP system. Moreover, the reviewed examples clearly shows that there is a need for a systematic sizing approach that can include waste heat, e.g., gray water, or other types of the renewable energy sources. The main focus in the literature regarding the SAGSHP system has been on the building with the heating dominant load, so the equipment sizing has been concentrated on the maximum required heating/hot water loads.

The graphical dynamic pinch model, proposed in the first section of this study [231], can fill the gap in the literature by providing a systematic approach in which the sizing problem can be converted into a matching procedure between different source/sink streams in a building energy system, based upon the pinch heat integration rules [3,123,168,232,233]. The maximum heat

recovery (MHR), the energy targeting in the real-time based on the dynamic hot and cold composite curves, and a superstructure of all possible network of SAGSHP+ thermal energy storage + Heat exchangers are the outcomes of this approach. However, the provided superstructure can have different heat exchangers and thermal energy storage (TES) sizes in different hours from 0 to 24 hours in each representative days, and even different heat exchanger (HX) numbers and sizes in different representative days. In other words, one superstructure has been extracted from the pinch-based approach, however, the size of each component in the single final structure is still under debate. Therefore, if all days in a year is considered, there would be 365 optimum networks or structures for each single building as there are unique sources and sinks conditions (i.e., the heating/cooling loads and the waste/solar/ground source of energies) throughout the year. As a building just needs one network/structure with a known equipment capacity and HX/TES size, thus the valid question is: what is the best structure amongst all 365 daily optimum ones? The economic analysis of each daily optimum design (DOD) can shed some light to answer this question. It has been shown that the total annual cost is the best criterion for selection among all possible networks [234–237]. In this context, the total annual cost of each design or working scenarios is defined as the objective function.

Annualized total cost as an economic analysis tool has been used to determine the most cost-effective scenario in retrofitting projects. Toffanin et al. [238] applied the annualized total cost in the economic analysis of different regulations for DHW temperatures in district heating in Swiss. However, their study is not a pinch approach. Pina et al. [239] combined the pinch analysis principle with a mathematical approach, i.e., mixed integer linear programming, to achieve to the minimum total annual cost in different possible heat integration scenarios in a Brazilian university hospital. Although they used the dynamic loads such as hot water and chilled water in their analysis, they did not include any renewable energy sources, e.g., solar, ground source, or thermal energy storage in their analysis. Reddick et al. [3] applied the time average model pinch analysis for a multifamily test building. They investigated several scenarios for including a waste energy source such as gray water, and heat pumping, integrated with a thermal energy storage concept into the building energy system. The life cycle cost analysis rather than the TAC is performed to compare different retrofitting scenarios in the test building.

In this study, the size of each heat exchanger of the extracted superstructure, proposed in the energy targeting phase, is computed for each representative day in a way that the predicted MHR is respected. This is also performed for the two TES tanks, the electric energy storage (EES) and PV panel area. Then the required hot/cold utility (HCU) for each daily network is computed as if the selected DOD runs for the entire year. In other words, the designer should pay the penalty for the extra HCU if the undersize network is selected as the final design. This

coin has the other side, too. If an oversized network is chosen as the final network, then, although there is no need for extra HCU, the capital cost of the final design will be higher. Finally, the TAC of each network is derived from the annualized capital costs, operational costs, and maintenance costs. Hence, the network with the minimum TAC is the best SAGSHP system for the test building.

7.3 Method and assumptions

7.3.1 First layer of optimization

The details of the proposed graphical dynamic pinch analysis are presented in [231], which can be assumed the first part of this study. Furthermore, the main results are illustrated in Appendix F. It includes the data extraction and energy targeting steps, as shown in Figure 7-1. In brief, the following steps need to be performed to extract the dynamic pinch-based DOD:

- All the energy streams (sources/sinks) and their supply and target temperature should be computed as a continuous function of time (see Table 7-1)

Table 7-1 All hot/cold stream in the test building [231]

Streams description	Hot/Cold	Supply (°C)	Target (°C)	CP (kW/°C)
Space Heating (Hydronic Floor Heating, HFH)	C	30	35	Dynamic
Domestic hot water (DHW)	C	City water	55	Dynamic
Warm Gray Water (WGW)	H	30	5	Dynamic
Cold Gray Water (CGW)	H	10	5	Dynamic
Space Cooling (Cooling Load, CL)	H	12	7	Dynamic
Condenser of Heat Pump (Con-HP)	H	110.1	55	constant
Intermediate Heat Recovery Loop-Hot (IHRL-H)	H	60	30	Dynamic
Intermediate Heat Recovery Loop-Cold (IHRL-C)	C	30	60	Dynamic
Evaporator of Heat Pump (Eva-HP)	C	-10	-5	constant
Ground Source in energy extraction (GS-Ext)	H	≥5	-5	constant
Ground source in energy injection (GS-Inj)	C	≤15	50	constant

- The hot/cold composite curves should be set up at any given time during 0 to 24 hours of each representative day.
- The periodic time for all the streams in a building is 24 hours, this time interval can be attributed equivalent to the batch period in industrial energy systems. Therefore, the total amount of surplus energy can be computed from each hot/cold composite curves, and by integration over 0 to 24 hours can yield the volume of TES tanks and the capacity of the EES units.
- The integration of TES tanks into the energy system provides the freedom of designing heat pump and the load of the GHEs as constant values during 0 to 24 hours. In other words, when the condenser of the HP system delivers energy more than what the building

demand is, this surplus energy can be stored into the TES tanks. The same pattern has been practical regarding the electric energy output of PV panels. The stored energy will be retracted when there is a need.

- Although the proposed dynamic pinch approach can set the constant ground source load (when the vertical GHEs are connected to the TES tanks), it cannot provide details about the depth and configuration of the vertical GHEs. Furthermore, even the ground source can be treated as solid energy storage units which can charge/discharge energy via the vertical GHEs. In this way there are two scenarios for summer design: 1. sizing the ground source load based on the building energy demands plus saving extra energy into ground (i.e., storing energy for winter) 2. sizing the ground source load based on just the building's energy demand. The former is called summer-C1 (or SC1), and the latter is named as summer-C2 (or SC2) in this study.
- The proposed dynamic pinch approach is thermodynamics-based one. In other words, the heat transfer phenomena such as thermocline thickness and heat loss to the ambient air in the TES tanks or the transient heat conduction between the soil and the vertical GHEs cannot be addressed by this approach. This is the reason why there is a need for detail sizing as shown in Figure 7-1.The detail sizing for specific components has been performed by computational fluid dynamics tool in [169,170].

By performing the energy targeting phase, the first layer of finding the optimum SAGSHP system for a test building is completed. In other words, the daily based energy targeting and finding the DOD for 12 representative days (i.e., one day in each month) have been predicted. Nevertheless, a building only needs one design for the entire year. Thus, the second layer of finding the optimum network/design (i.e., economic analysis) should be performed.

7.3.2 Second layer of optimization

The second layer optimization is important because it is related to computing the required HCU for the entire year and the TAC analysis of each DOD, the highlighted part in Figure 7-1. The outputs of the energy targeting phase are the designs with MHR for that very representative day. Hence, there will be 12 optimum networks for the unique solar and loads of the 12 studied representative days. Each DOD has the minimum: HP capacity, TES volume, PV area, EES capacity, and GHE load/size.

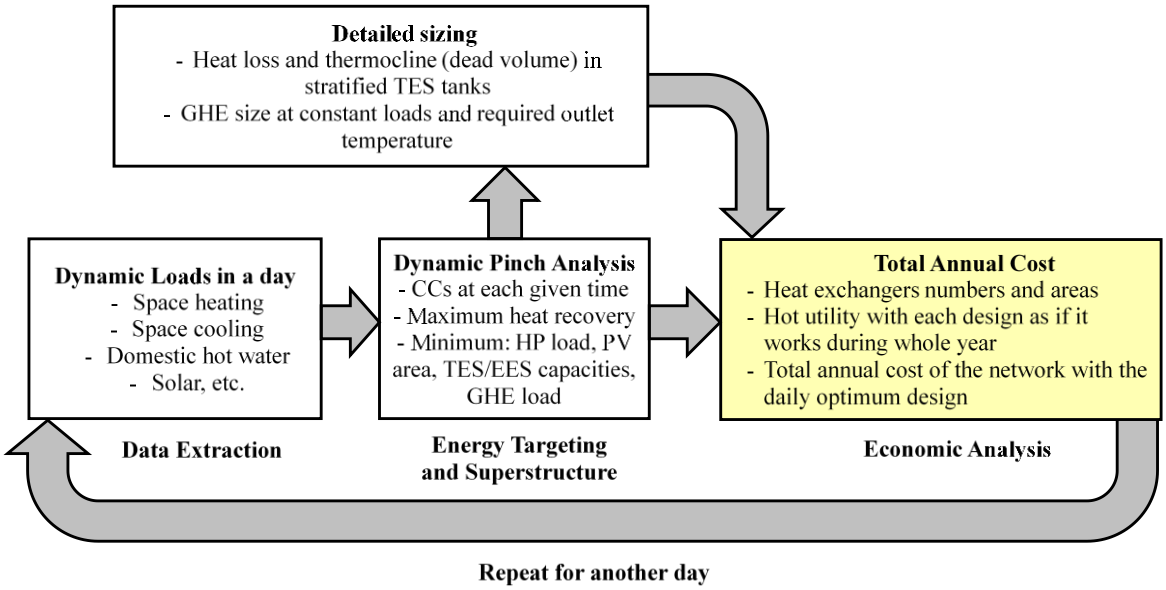

Figure 7-1 The overall dynamic pinch analysis for optimum SAGSHP system, the highlighted section is the subject of this study

The next step is calculating required HCU for each DOD and assumes that this network is the final selected one to work for the entire year. In order to compute the TAC for each daily design, the required HCU (i.e., grid electricity in this case), should be evaluated throughout the year with each fixed-sized daily design. Noticeably, if the DOD for June, as an example, is selected as the final network for the building, then, during other months there might be a need for HCU to meet the building SH, DHW, and space cooling (SC) loads. This makes computing the TAC of each network a complicated task as the size of different components of the network is fixed, but the outdoor condition, e.g., solar irradiance, and the building loads vary. It should be emphasized that this process needs to be performed for each of the 12 DOD. The last step is computing the total annual cost of each design.

The main assumptions regarding the presented techno-economic analysis and buildings are as follows:

- The required space for installing the proposed network is available in the building, or there is a space that (with some modifications) can serve as the required space
- Pressure drops in the components are negligible
- Required area for installing/drilling the vertical GHEs is available
- The system supposed to work for 20 years
- There are auxiliary heating and cooling systems (i.e., conventional or no-heat integration case) available in the building

7.3.3 Computing TAC

TAC can be calculated by adding several parameters. Each component of the system has a capital investment cost (CIC), including the original component purchasing cost plus shipping and installation. Generally, the component needs a regular repair and maintenance to function properly. This is called the capital operational cost (COC), which usually evaluated as a percentage of the corresponding CIC. Finally, each proposed network needs hot/cold utility (i.e., grid electricity) to satisfy the building loads and is named as yearly utility cost (UC). The utility value is extracted by a thermodynamic analysis and energy balance of the system.

The CIC can be annualized ($ACIC$) by considering the project lifetime and the interest rate, as shown in Eq. (7-1).

$$ACIC = CIC \times AF \tag{7-1}$$

Where, AF is the amortization factor, as shown in Eq. (7-2) [166],

$$AF = \frac{i \times (i+1)^n}{(i+1)^n - 1} \tag{7-2}$$

And i is the interest rate assumed as 5% and n is the project lifetime as 20 years. The $ACOC$ can be calculated the same way. Therefore, TAC can be calculated by Eq. (7-3) for each network and m is the number of components. It should be noted that in most cases the COC is assumed 1% of the CIC.

$$TAC = \sum_{j=1}^{j=m} (ACIC + ACOC)_j + UC \tag{7-3}$$

7.4 Results and discussion

The superstructure extracted from the energy targeting phase is presented here in Figure 7-2 for the ease of following the sizing procedure and corresponding related costs. The readers are referred to the energy targeting part [231] for more details.

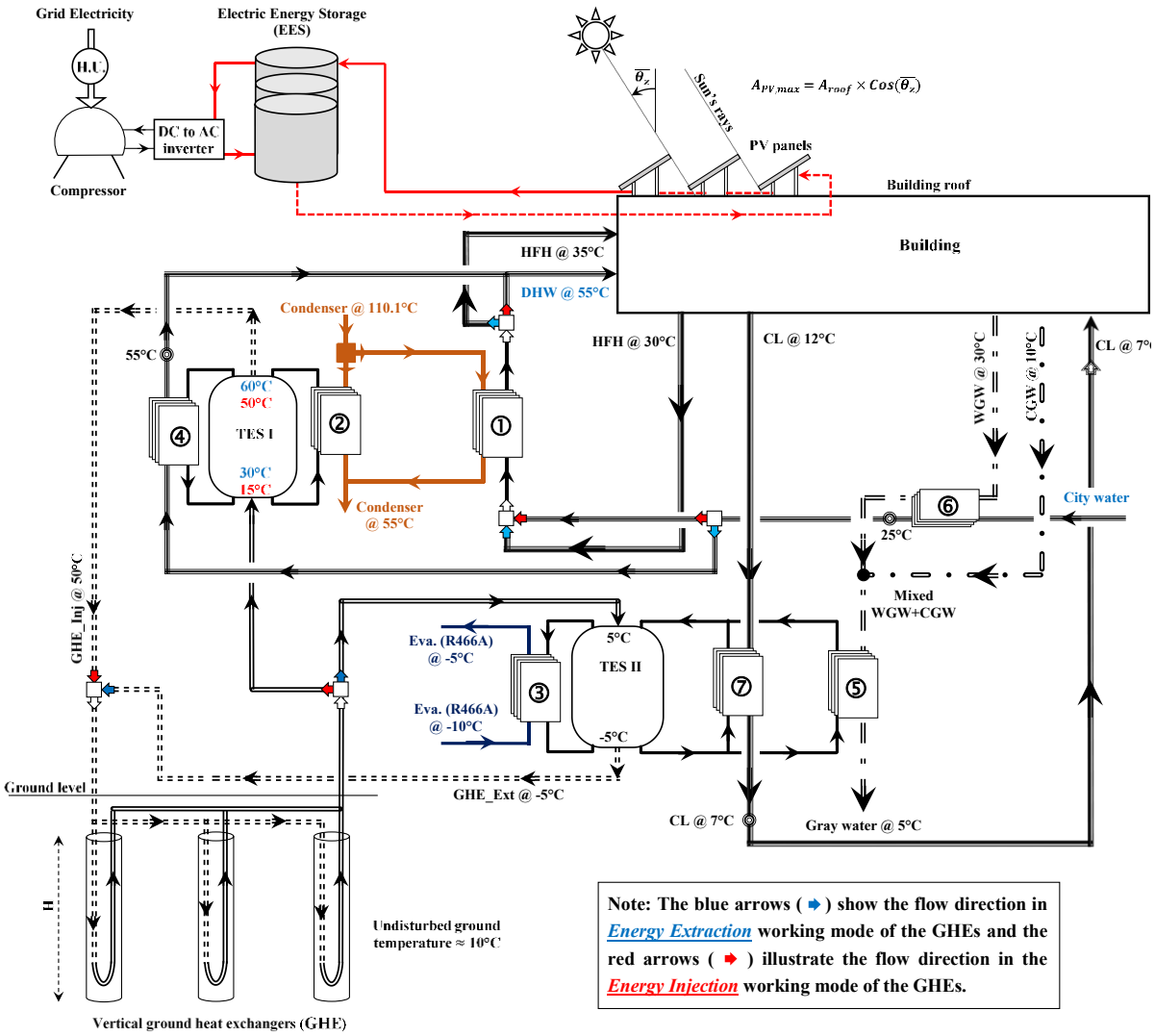

Figure 7-2 Proposed superstructure for the SAGSHP system extracted from the dynamic pinch analysis for both energy extraction/injection working modes

7.4.1 Sizing and cost of different components

The size and cost of the components of the SAGSHP system (illustrated in Figure 7-2) are presented in the following sections.

7.4.1.1 Sizing and cost of HXs (①, ②, ③, ④, and ⑦)

There are two types of heat exchangers in the proposed full network presented in Figure 7-2: the one with phase change and the one with no-phase change heat transfer. The condenser and the evaporator are categorized in the former and they require shell and tube type heat exchangers while plate heat exchangers are suitable for water-water heat exchange which are proposed for the HX with no phase change heat transfer. As the proposed graphical approach provides the

inlet and outlet temperature of each HX at each given time (see Table 7-1), the best method for sizing the required heat transfer area is based on the logarithmic mean temperature difference or LMTD. Eq. (7-4) is used for calculating the required area for each heat exchangers at each given time. The *U* values are set 500 W m^2K^{-1} and 1500 W m^2K^{-1} for shell-and-tube and plate heat exchangers [166], respectively.

$$A(t) = \frac{Q(t)}{U \times \Delta T_{LMTD}} \tag{7-4}$$

Where the LMTD is calculated according to Eq. (7-5):

$$\Delta T_{LMTD} = \frac{\left(T_{h_{in}} - T_{c_{out}}\right) - \left(T_{h_{out}} - T_{c_{in}}\right)}{ln\left(\frac{T_{h_{in}} - T_{c_{out}}}{T_{h_{out}} - T_{c_{in}}}\right)} \tag{7-5}$$

The HP cycle uses R466A as the refrigerant. The pressure-enthalpy diagram is depicted in Figure 7-3. The isentropic efficiency of the compressor is assumed 0.8, as a typical value.

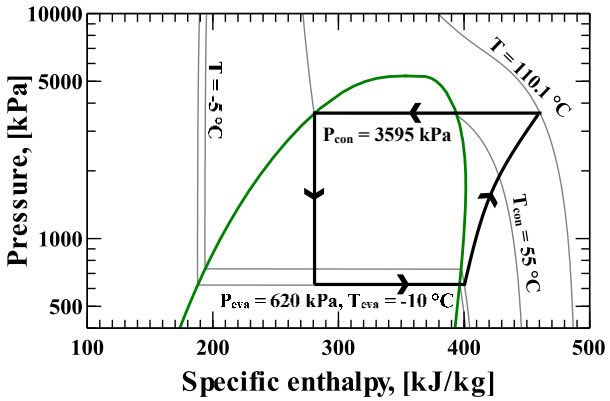

Figure 7-3 P-h diagram of the proposed HP system

Moreover, the main building loads are presented in Appendix F. Figure 7-4 presents two examples of the temperatures of the hot and the cold streams for HX number 2 in two days: one in January and the other in Summer-C1 (i.e., S-C1). As the temperatures are constant and the loads are time-dependent from 0 to 24 hours, the values of ΔH are different but the ΔT_{LMTD} remains constant.

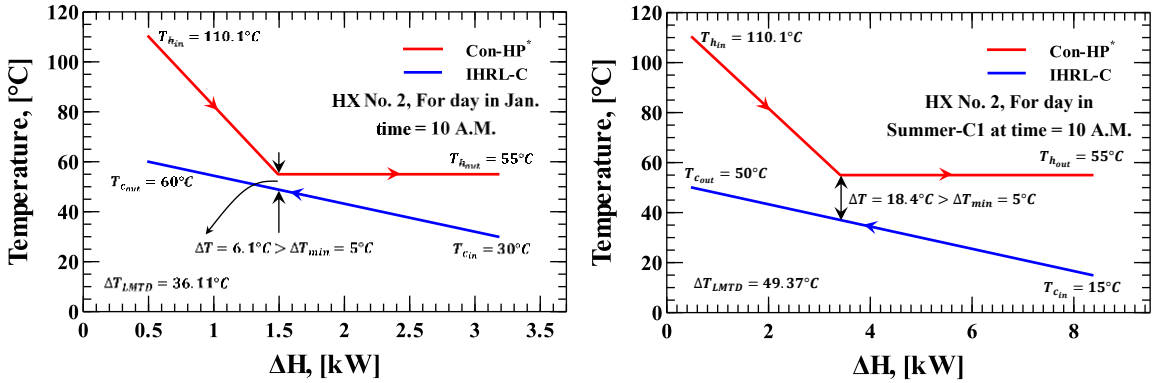

Figure 7-4 Heat transfer between hot and cold stream for HX number 2, time: 10 A.M., left: the day in January right: the day in summer-C1 (S-C1)

It worth mentioning that the minimum temperature difference in the pinch analysis is defined as 5°C. It should be respected during full day in all the heat exchangers.

The dynamic load in Eq (7-4) (i.e., $Q(t)$) is the buildings dynamic load or the load for intermediate heat recovery loops (IHRLs) from 0 to 24 hours. The dynamic area of all other HXs (i.e., ①, ②, ③, ④, and ⑦) is computed in this way. Figure 7-5 presents the time dependent area for HX No. 2 for two selected days, one in January (in energy extraction working mode for the GHE) and another in Summer-C1 (in energy injection working mode of the GHE).

In an effort to guarantee the predicted MHR by the proposed dynamic pinch analysis, the maximum heat exchange area (during 0 to 24 hours) must be selected for each representative day. All maximum areas for all other HXs are computed and illustrated in Table 7-2, like the example showed in Figure 7-4 and Figure 7-5. It worth mentioning that some HXs are not required for some representative day. However, as they should be presented in the superstructure (i.e., Figure 7-2), these HXs are marked as not applicable (NA) in Table 7-2. As it can be seen from Table 7-2, for most of the streams the $LMTD$ is constant in all the representative days, as the supply and target temperatures are constants. Nonetheless, due to variation in the inlet city water temperature for domestic hot water use, the log temperature changes in different representative days.

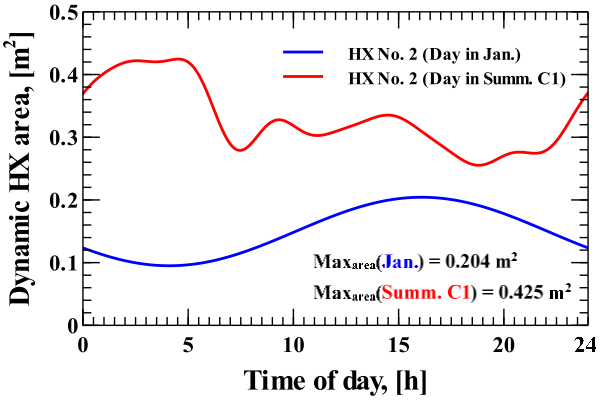

Figure 7-5 Dynamic HX area for HX No.2, as an example, in two selected days

The maximum computed heat recovery can be guaranteed by considering the maximum required area for each HX. Therefore, the price of the plate HXs and the shell and tube ones are computed with the maximum area taken into account. The cost function of the plate heat exchangers is provided in Eq. (7-6) [240].

$$CIC_{HX} = 12000 \times \left(\frac{Area}{100}\right)^{0.6} \tag{7-6}$$

It should be noted that the capital cost of HXs can slightly vary by considering different types of the inlet/outlet connecting ports.

Table 7-2 Maximum load and the corresponding area for the selected heat exchangers (see Figure 7-2), NA indicates Not Applicable

Day ➔		Jan.	Feb.	Mar.	Apr.	May	Jun.	SC1	SC2	Sep.	Oct.	Nov.	Dec.
HX ①	**LMTD**	45.55 (°C)						41.29 (°C)		45.55 (°C)			
	Q_{max}, kW	**11.6**	9.96	8.59	5.9	4.1	2.64	4.53	4.53	2.98	6.1	9.38	9.67
	A_{max}, m²	**0.509**	0.438	0.377	0.259	0.18	0.116	0.219	0.219	0.131	0.268	0.412	0.425
HX ②	**LMTD**	36.11 (°C)						49.4 (°C)		36.1 (°C)			
	Q_{max}, kW	3.69	4.31	4.08	3.97	4.44	4.2	**10.48**	5.67	4.38	3.9	3.92	3.65
	A_{max}, m²	0.204	0.239	0.226	0.22	0.246	0.233	**0.425**	0.23	0.243	0.216	0.217	0.202
HX ③	**LMTD**	7.21 (°C)											
	Q_{max}, kW	**8.85**	7.35	6.59	4.87	3.36	2.6	7.19	4	2.71	5.05	7.22	7.59
	A_{max}, m²	**2.453**	2.037	1.826	1.351	0.932	0.722	1.995	1.109	0.752	1.4	2.002	2.104
HX ④	**LMTD**	**5** (°C)						NA	NA	5 (°C)			
	Q_{max}, kW	**4.53**								4.53			
	A_{max} (m²)	**0.604**								0.604			
HX ⑦	**LMTD**	NA						**9.28** (°C)		NA			
	Q_{max}, kW	NA						**6.4**		NA			
	A_{max}, m²	NA						**1.38**		NA			

7.4.1.2 Drain water heat recovery system (HX ⑤ and ⑥)

As the gray water can be assumed as a gravity driven flow, the drain water heat recovery system is an appropriate heat exchanger for heat recovery in HXs ⑤ and ⑥ (see Figure 7-2). Falling film drain water heat recovery (DWHR) heat exchangers are commercially available and ready to install. They have no moving parts and no need for maintenance. Figure 7-6 shows a typical counter flow DWHR heat exchanger made from two copper pipes.

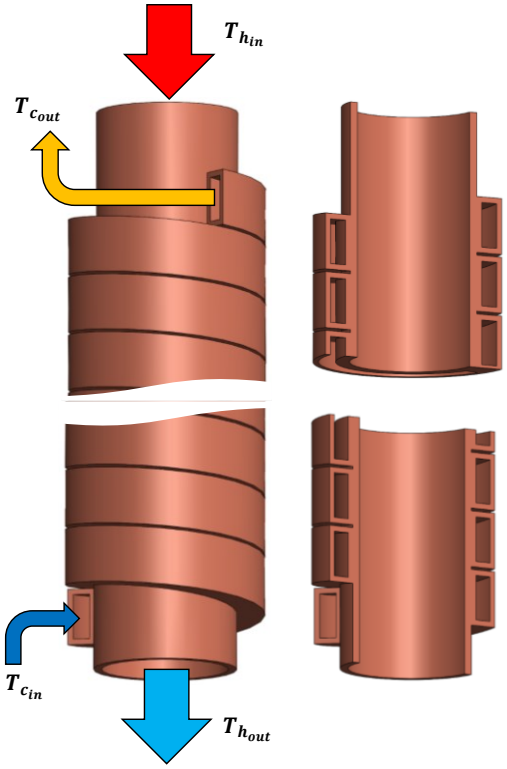

Figure 7-6 3D schematic (left) and cross-section (right) views of a DWRH heat exchanger

Supply/target temperatures and the volumetric flow rate of the waste energy coming from DHW (i.e., warm gray water (WGW) and cold gray water (CGW)) are presented in Figure 7-7.

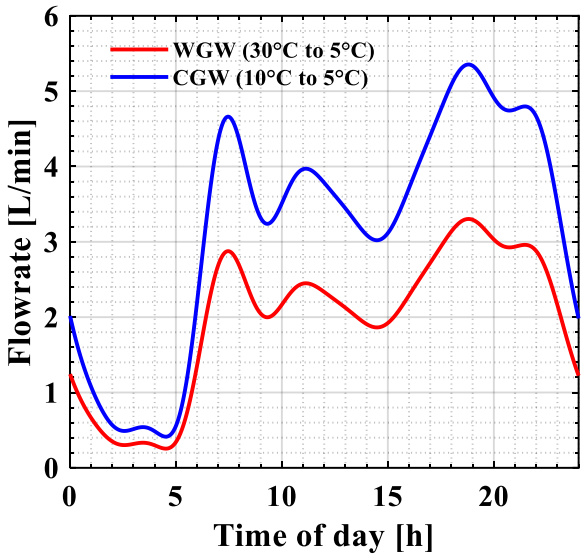

Figure 7-7 Warm and cold gray water flow rate in the test building (day in January)

The gray water flows as a falling film inside the inner larger pipe (e.g., 2 to 4 inches in diameter) and the cold fluid enters from the bottom into the smaller (in diameter) helical pipe. It should be noted that the maximum effectiveness of such a heat exchanger depends on several parameters, namely, the length of the heat exchanger, the mass flow rate of the cold/hot streams and the inlet temperatures of the hot and cold streams. Eq. (7-7) [45] shows the effectiveness as a function of the inlet/outlet temperatures.

$$\varepsilon \cong \frac{T_{c_{out}} - T_{c_{in}}}{T_{h_{in}} - T_{c_{in}}} = \frac{T_{h_{in}} - T_{h_{out}}}{T_{h_{in}} - T_{c_{in}}} \tag{7-7}$$

At appropriate falling film flow rate, e.g., less than 5 liter per minute, the effectiveness (ε) can be as high as 0.72 [43,45], approximately, for a DWHR heat exchanger with a 1.22 m height. The required effectiveness of the DWHR heat exchanger ⑤ (see Figure 7-2) can be computed as:

$$\varepsilon \cong \frac{T_{c_{out}} - T_{c_{in}}}{T_{h_{in}} - T_{c_{in}}} = \frac{5 - (-5)}{12 - (-5)} = 0.59 < 0.72 \tag{7-8}$$

Thus, the outlet temperature of the cold side (IHRL) can easily reach to the required (pre-set) 5°C in HX ⑤. For HX ⑥, the outlet temperature of the cold fluid (i.e., city water) can be computed by considering the maximum possible effectiveness of the DWHR HX, as presented in Eq. (7-9).

$$0.72 = \frac{T_{c_{out}} - 5}{30 - 5} \Longrightarrow T_{c_{out}} = 23°C < 25°C \tag{7-9}$$

Therefore, it is highly unlikely for the city water to reach to the ideal pre-set preheated temperature of 25°C, especially during the cold months of year, with the commercially available DWHR HXs. In a more realistic estimate, it can be preheated up to 23°C, as computed in Eq. (7-9). Hence, the difference between the ideally thermodynamically assumed outlet temperature of 25°C and the realistically possible outlet temperature of 23°C must be provided by the HCU and the extra energy must be added to the HCU value. The maximum load for heating the DHW form 23°C to 25°C is 0.3 kW which is negligible compared to maximum 7.5 kW of the DHW load at its peak demand. Moreover, it worth mentioning that the effectiveness of the HX can be higher than 0.72, if the mass flow rate (falling film side) of the warm gray water (WGW) decreases [45].

For the test building, two commercially available DWHR heat exchangers are considered [241] for both HX ⑤ and ⑥. The hot or drain side is a copper tube with a diameter of 0.102 m (i.e., 4 inches). For HX ⑤, the IHRL (TES II) flows in the helical pipe and for HX ⑥ city water flows in a helical copper tube with diameter of 0.0191 m (i.e., 3/4 inches). The helical pipe is bonded with solder around the drain side pipe to reduce the contact resistance. The overall length of the DWHR is 1.8 m. The capital cost of the selected ones is 920 CAD [241].

7.4.1.3 Compressor and expansion valves

The capital cost of a compressor (Eq. (7-10)) depends on several parameters. The refrigerant mass flow rate ($\dot{m}_{ref}$), the pressure ratio (PR), and the isentropic efficiency (η_{isen}) [242].

$$CIC_{comp} = \frac{71.7\dot{m}_{ref}}{0.92 - \eta_{isen}} \times PR \times \ln(PR) \tag{7-10}$$

The mass flow rate of the refrigerant varies with the compressor load at different HP duties. Eq. (7-11) represents the capital cost of the expansion valves that only depends on the mass flow rate of the refrigerant [242].

$$CIC_{Exp.\ valve} = 114.5\,\dot{m}_{ref} \tag{7-11}$$

Table 7-3 shows the compressor load and the corresponding refrigerant mass flow rate (i.e., $\dot{m}_{ref}$) for each representative day.

Table 7-3 Refrigerant (R466A) mass flow rate (kg s^{-1}) and compressor load (kW) for each representative day

Day	**Jan.**	**Feb.**	**Mar.**	**Apr.**	**May**	**June**	**S. C1**	**S. C2**	**Sep.**	**Oct.**	**Nov.**	**Dec.**
Load	4.47	3.71	3.33	2.46	1.7	1.32	3.64	2.02	1.37	2.55	3.65	3.83
$\dot{m}_{ref}$	0.074	0.062	0.055	0.041	0.028	0.022	0.06	0.033	0.023	0.042	0.06	0.063

Furthermore, the piping and refrigerant (i.e., R466A, in this case) costs can be assumed 1% of the capital investment cost of the HP system [243].

7.4.1.4 PV panel and EES costs

The total cost of the solar PV panels depends on several parameters such as the required area, the quality of PV panels, the average peak power of the selected panel, the repair and maintenance cost, and the installation costs. The required PV panel and the EES capacity are presented in Appendix F. As it was reported in the energy targeting part, the area of the PV panels is limited by the available mounting area (i.e., maximum at 121.1 m^2). The average capital investment cost (including installation costs) and yearly repair and maintenance costs of the PV panels are defined [244] as in Eq. (7-12)

$$\begin{aligned} CIC_{PV\,panel} &= A_{PV}(m^2) \times 0.8 \left(\frac{CAD}{W}\right) \times \frac{330}{2} \left(\frac{W}{m^2}\right) \\ COC_{R\&M/year} &= A_{PV}(m^2) \times 0.014 \left(\frac{CAD}{W}\right) \times \frac{330}{2} \left(\frac{W}{m^2}\right) \end{aligned} \quad (7\text{-}12)$$

The solar PV panels generates an unsteady energy that needs to be stored inside an electric energy storage (EES) or electric batteries. There are two typical types of EES used for building applications: Lead-acid (LA) and Lithium-ion (LI) batteries. Each has its unique features and advantages. As an example, the service life of the LA batteries is considered 4 years less than the useful life of the LI batteries, approximately. Also, the LA batteries require higher repair and maintenance costs in comparison to the LI ones [245]. However, the capital cost of the LA batteries is generally less than the LI batteries at the same capacity [246], though the cost of the LI batteries is gradually going down. Recent investigations [245,247,248] reveals that the overall techno-economic performance of the LI batteries is superior to that of the LA ones. Therefore, in this study the LI batteries are selected as the EES units. Eq. (7-13) shows the capital cost (including the installation costs) of the LI batteries [249] in CAD.

$$CIC_{Li-ion} = \ Storage\ power\ (kWh) \times (127.2\ CAD/kWh) \quad (7\text{-}13)$$

It worth mentioning that the LI batteries need no repair and maintenance, and they must be replaced after 8 years. In other words, there is a need for replacing the LI batteries three times during the 20 years of the lifespan of the project.

7.4.1.5 TES costs

Stratified or thermocline water TES tanks are relatively cheap in comparison to the other storage technologies. The capital cost of the TES tank has been assumed proportional to the stored energy (in kWh) [250,251], as presented in Eq. (14).

$$CIC_{TES} = 24.1 \times \bar{\rho}\bar{c}_p \Delta T_{max-min} \times V_{real} \quad (7\text{-}14)$$

Which $V_{real} = 1.15 \times V_{ideal}$ is in m^3 (see Appendix F) The stratified water tank needs a relatively low maintenance cost, which has been ignored in this study.

It should be noted that the extracted volume in the energy targeting phase for each stratified TES tank is the ideal value. In other words, there is a dead volume (i.e., thermocline thickness) inside each stratified TES tank that needs to be added to the ideal value. Furthermore, the height to diameter of the tank, the heat loss to the ambient and the momentum or turbulent mixing induced by the charging/discharging diffusers are important parameters that increase the dead volume or the thermocline thickness [169]. It has been shown [169] that the minimum thermocline thickness can be achieved at the H/D ratio above 3 in the cylindrical tanks. Additionally, even at the ideal insulation thickness, the thermocline can be as 15% percent of the total volume of the tank. Hence, the real volume is used in the TAC analysis here.

7.4.1.6 GHE sizing and costs

The load and size of the vertical GHE has a great impact on the capital cost of the SAGSHP system. The proposed dynamic pinch approach evaluates the minimum GHE load in connection with the stratified TES tank. However, the depth and configuration of the GHEs needs to be appropriately sized to deliver the predicted constant load at the design temperature range. The total depth of the GHEs or a cluster of GHEs is not a trivial task as the heat transfer mechanism between the ground and the circulating HTF inside the U-tube of the GHEs is transient and three-dimensional. Moreover, the undisturbed ground temperature plays a vital role in the possibility of heat extraction/injection process, especially at constant load and specified inlet/outlet temperatures of HTF. Extensive transient three-dimensional numerical simulation has been performed by the authors [170] that can be utilized in sizing here.

In brief, connecting the GHEs to the stratified TES tank allows it to work in a constant load by charging/discharging stored energy in the intermediate medium during 0 to 24 hours of a day. Due to the requirement of the proposed dynamic pinch approach, the inlet temperatures of the circulating HTF (entering to the GHEs) are fixed as -5°C and 50°C in the energy extraction and injection working mode, respectively. Moreover, the outlet temperature of the circulating HTF has limitations as equal or greater than 5°C and equal or smaller than 15°C in the energy extraction and injection working modes, accordingly. Therefore, not only the GHE load needs to be constant, but it also should be delivered at a certain range of temperatures. The constant load of GHEs for each DOD is depicted in Table 7-4.

To increase the heat transfer area in one GHE (i.e., one borehole), the HTF can pass through a double U-tube instead of single one inside the GHE (depicted in Figure 7-8). Thermal

performance of both single and double U-tube GHEs, in two configurations (i) parallel and (ii) two GHEs connected in series, have been evaluated [170]. It is shown that at high GHE loads (e.g., 1500 W, 2000 W) at fixed borehole depth, the GHE equipped with double U-tube PVC pipes, have superior thermal performance in comparison to the single U-tube ones. Furthermore, at a constant load, two GHEs connected in series, can deliver a higher outlet temperature rather than two GHEs in parallel configuration. However, at small loads (e.g., 250 W, 500 W), the GHEs equipped with single U-tube can deliver the constant design load at the desired outlet temperature which is economically cheaper than that of the double U-tube GHEs.

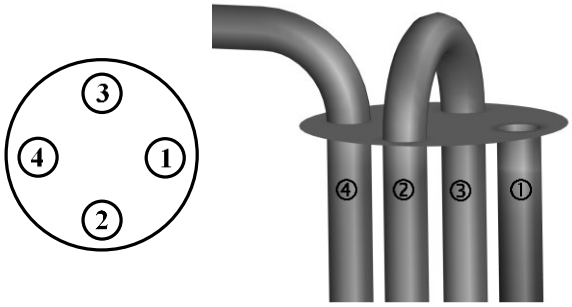

Figure 7-8 3D schematic view of the double U-tube vertical GHE

In light of the numerical results, the required depth and suggested configuration of the GHEs that can meet the minimum GHE loads, are presented in Table 7-4. It worth mentioning that the suggested depth and configuration for each DOD is based on the computational fluid dynamic simulations. Also, a safety margin is taken into account to cover the heat transfer depletion of the ground, especially in a long run working of 20 years.

Table 7-4 Size and suggested configuration of the GHE(s) for each DOD

Day	Load (kW)	Depth (m)	Suggested configuration
Jan.	6.1	400	Four pairs of two 50 m D-U GHEs in series
Feb.	4.6	300	Three pairs of two 50 m D-U GHEs in series
March	3.8	200	Two pairs of two 50 m D-U GHEs in series
April	1.9	150	3× parallel GHEs (each 50 m)
May	0.26	40	One S-U GHE
June	0	0	----------
S-C1	8.1	400	Four pairs of two 50 m D-U GHEs in series
S-C2	3.3	160	Two pairs of two 40 m D-U GHEs in series
Sep.	0	0	----------
Oct.	2	160	4× parallel S-U GHEs (each 40 m)
Nov.	4.3	240	Three pairs of two 40 m D-U GHEs in series
Dec.	4.8	300	Three pairs of two 50 m D-U GHEs in series

The GHE cost depends on four main parameters: i) drilling cost, ii) U tube cost, iii) removing dirt/soil, filling material (i.e., grout and concrete), and iv) installation +labor costs. The total cost can be assumed as a linear function of the GHE depth [170]. Calculating the exact cost is a challenging task as the mentioned parameters can be slightly different based on the geology

of the location and the fluctuation in the market. However, an average total cost can be 69 CAD/m and 57 CAD/m for double and single PVC U-tube vertical GHE, respectively.

7.4.1.7 Hot utility for the entire year with each representative day

According to the proposed dynamic pinch approach, the building can have thermal and electric interaction with the SAGSHP system, as illustrated in Figure 7-9. If the generated energy by the solar PV panels is not sufficient for the compressor of the SAGSHP system due to the cloud or not enough PV area, the rest of the energy needs to be bought from the grid electricity.

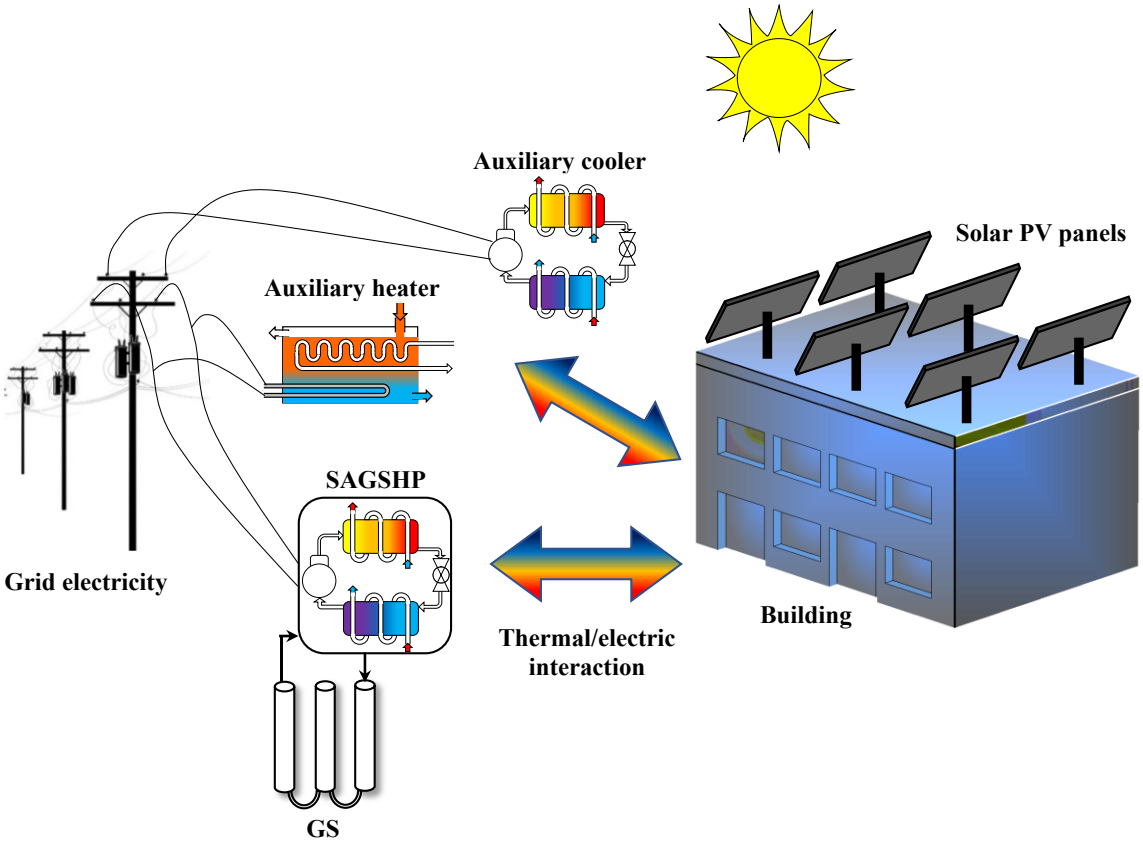

Figure 7-9 Thermal and electric interaction between SAGSHP, grid electricity, and building

It should be noted that the building is also connected to the grid line (not shown in Figure 7-9) for lighting and other miscellaneous plug loads such as refrigerator, oven, computers, etc. The SAGSHP system just provides the required energy for SH/SC + DHW applications. Furthermore, there are two auxiliary heating/cooling systems. The auxiliary heater is simply an electric heating element inside a water tank that can produce the hot water for SH+DHW, if the capacity of the selected SAGSHP system in not sufficient. Also, there is an auxiliary water-cooled heat pump that can satisfy the cooling demand of the building during summer days.

Figure 7-10 shows the required energy to satisfy all DHW, SH, and SC in each representative day (the cumulative energy from 0 to 24 hours). The required energy can be provided by the grid electricity (i.e., no-heat integration case), or by integration of a SAGSHP system. It should be noted that the presented values are daily ones. To compute the average monthly values, the daily one can be multiplied by the number of the days in each month. Furthermore, the DHW loads at different representative days are approximately the same as the variation in the city water temperature is just 5°C from winter to summer.

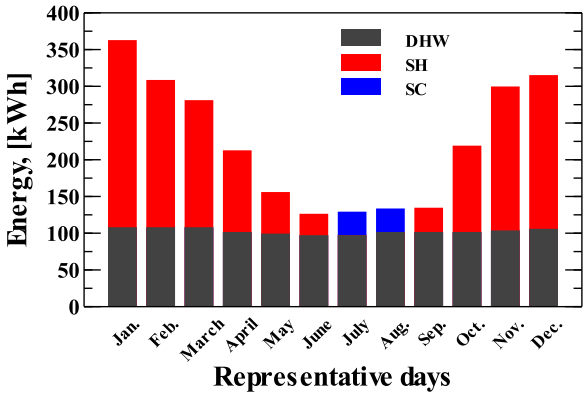

Figure 7-10 Daily energy requirement in no-heat integration case during each representative day

In the energy targeting phase, it was shown that there is a unique and optimum design for each representative day for the test building. The DODs define the minimum capacity of the equipment such as HP, PV area, EES, TES, etc. for the building's energy demands and the solar irradiance of the specific representative days. As the building needs just one design for the whole year, therefore, one final design must be selected among all the daily optimum ones. Each DOD provides a specific amount of energy for the building for the SH/SC and DHW. If the solar energy is not enough to meet the compressor demand of the HP system, the rest of required energy should be provided by the HCU as illustrated in Figure 7-9. Table 7-5 presents the amount of energy that each DOD can provide, with their optimum components' capacities.

Table 7-5 HP daily energy in each DOD for satisfying SH/SC+DHW in kWh

Day	Jan.	Feb.	Mar.	Apr.	May	June	S-C1	S-C2	Sep.	Oct.	Nov.	Dec.
Condenser	319.6	265.4	237.9	176	121.4	94.1	259.9	144.5	97.9	182.4	260.9	274.1
Evaporator	212.3	176.4	158.1	117	80.7	62.5	172.7	96	65.1	121.2	173.3	182.1
Compressor	107.3	89.1	79.8	59.1	40.8	31.6	87.3	48.5	32.9	61.2	87.5	92
COP	2.98											

Therefore, if the DOD of March is selected as the final one for whole year, this design can satisfy the required energy in all days, except days of Jan., Feb., S-C1, Nov., and Dec, where the remaining energy will be provides by the two mentioned auxiliary systems. It should also be noted that the optimum minimum solar panel area generates different amount of energy at

different representative days. Table 7-6 shows the amount of solar energy generated by the PV panels area of each design if it works under solar irradiance of other representative days.

Table 7-6 The amount of possible solar energy that each DOD can generate in other days, (numbers in bold are the daily optimum values)

A_{PV} (m^2)↓ Day →	Jan.	Feb.	Mar.	Apr.	May	June	S-C1/S-C2	Sep.	Oct.	Nov.	Dec.
121.2	**14.6**	**26.1**	**47.1**	68.5	87.6	100.9	104.1	63.8	**37.3**	**19.7**	**11.9**
104.5	12.6	22.5	40.6	**59.1**	75.5	87	89.8	55	32.1	17	10.3
56.5	6.8	12.2	22	32	**40.8**	47	**48.5 (C2)**	29.8	17.4	9.2	5.6
38.1	4.6	8.2	14.8	21.6	27.5	**31.6**	32.7	20.1	11.7	6.2	3.8
101.5	12.2	21.9	39.5	57.4	73.4	84.5	**87.3 (C1)**	53.5	31.2	16.5	10
62.4	7.5	13.4	24.3	35.3	45.1	52	53.6	**32.9**	19.2	10.1	6.1

As an example, if we select the DOD of April, the minimum PV area for April is 104.5 m^2. This PV area can generate 12.6 kWh in day in January, 22.5 kWh in day in February, 40.6 kWh in day in March, and so on, as reported in Table 7-6. However, there is another important factor in each DOD that affect the amount of useful solar energy: EES capacity. According to the proposed dynamic pinch analysis, each daily design has a minimum capacity for the EES. In other words, the capacity of the EES batteries will define the amount of solar energy that can be utilized by the proposed SAGSHP system during a specific day. It can be clarified by an example. Let's consider the DOD of September. The optimal EES capacity for this design is 32.9 kWh. If we use this design for the whole year, thus, in the day in May, where the PV panels can generate up to 45.1 kWh, however, as the EES capacity is 32.9 kWh for May, the design cannot use the extra available solar energy, which increases the utilization of the grid electricity of the day in May.

The main assumptions in computing the HCU for each DOD during the whole year are:

- The extra energy required for SH (beyond the power of the fixed SAGSHP) is provided by an electric heating element.
- The extra energy required for SC (beyond the one that one of the SAGSHP can provide) is delivered via an auxiliary water-cooled HP system with a COP of 3.
- At each DOD the capacity of EES is constant, no matter if there is extra solar energy available at other days of year, in other words, the extra available solar energy cannot be stored/utilized beyond the fixed capacity of the available EES for the DOD.
- When the HP capacity of a DOD is more than what is required for other representative days, the HP system undergoes several on/off processes to meet the loads.

Figure 7-11 illustrates the flowchart for computing the required HCU with each DOD as if it works during a full year. It should be noted that the HCU(s) are presented in electrical power, supplied from grid electricity.

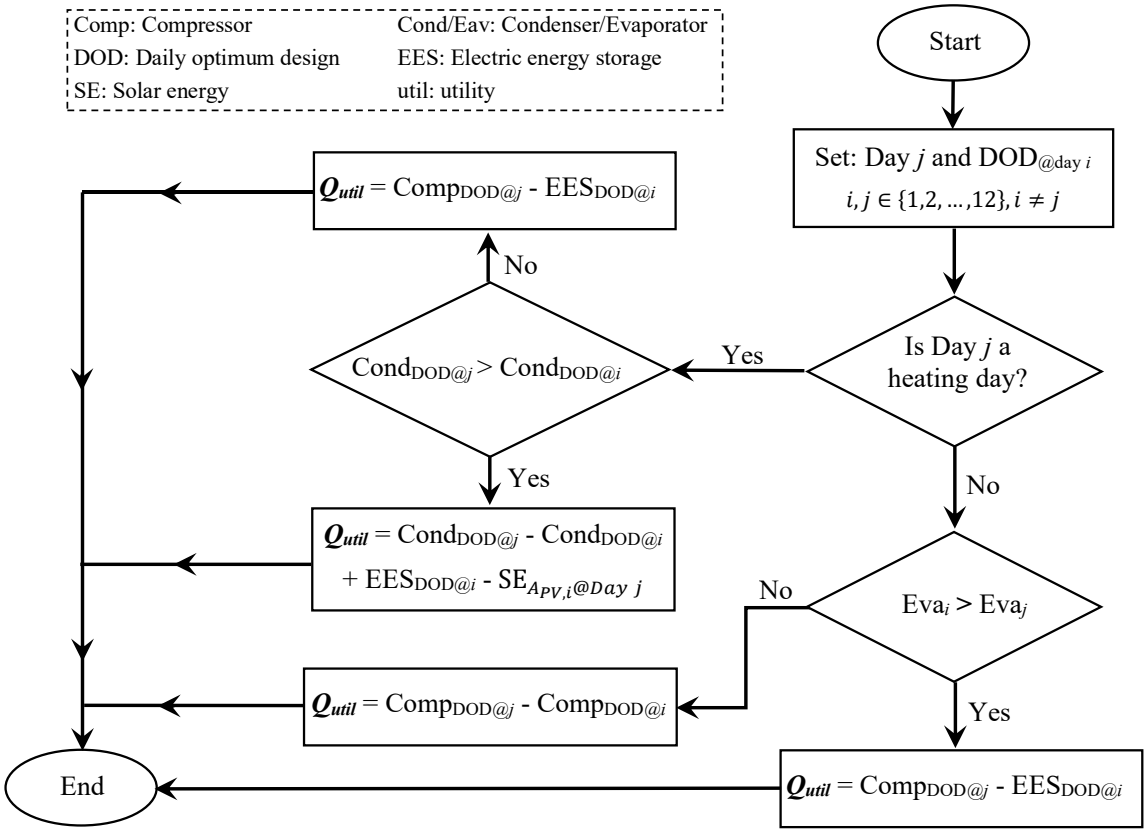

Figure 7-11 Simplified flowchart for computing the HCU with each DOD in all other representative days

By following the given assumptions and restrictions, the required daily HCU of each DOD during the other days are computed and presented in Table 7-7.

Table 7-7 . $Q_{utility}$ for each DOD in all other days

DOD in ↓ Day →	Jan.	Feb.	Mar.	Apr.	May	June	SC1	SC2	Sep.	Oct.	Nov.	Dec.
Jan.	92.7	74.5	65.3	44.5	26.2	17.1	72.6	33.9	18.3	46.7	73.1	80.1
Feb.	128.7	63	53.8	33	14.7	5.6	61.2	22.4	6.8	35.2	61.4	71.7
March	146.9	81.2	32.8	12	0	0	40.2	1.4	0	24	83.1	104.1
April	190.1	126	80.4	0	0	0	28.2	0	0	33.4	127	147
May	232.2	172.6	135.3	63.4	0	0	46.5	7.7	3.1	84.4	171.1	188
June	252.5	194.7	160.6	92	31.3	0	55.7	16.9	15.3	108.2	192.2	207.8
SumC1	134.8	43.4	19.6	1.7	0	0	0	0	0	30	71.8	91.5
SumC2	216.8	157.2	119.9	48	0	0	38.8	0	3.1	81.7	194.7	216
Sep.	247.1	187	148.6	78.1	23.5	0	54.4	15.6	0	98.2	185.8	203
Oct.	183.8	118.1	79.4	21.8	3.5	0	50	11.2	0	24	120	141
Nov.	131.6	72.3	60.1	39.4	21.1	11.9	67.6	28.8	13.2	41.5	68	88.8
Dec.	125.6	77.2	67.9	47.2	28.9	19.7	75.4	36.6	21	49.3	75.6	80

The total annual HCU is calculated based on the number of days in each month, Eq. (7-15).

$$total\ annual\ hot/cold\ utility = \sum_{i=1}^{12} (N_{days} \times Q_{utility})_i \quad (7\text{-}15)$$

The average yearly required HCU with each DOD is illustrated in Figure 7-12. As there are two different scenarios for DOD for summer days, two different yearly hot utilities can be computed. If the summer-C1 (i.e., S-C1) is considered for the summer days, the minimum yearly HCU occurs when the S-C1 DOD is selected for the whole year with 12 MWh. If the summer-C2 (i.e., S-C2) is considered for the summer days, the DOD of March represents the minimum yearly HCU with 14.8 MWh. Furthermore, the yearly total grid electricity in No-HI case is 82.7 MWh, which is 6.9 and 5.6 times higher of the energy required with the mentioned DOD, respectively. It worth mentioning that if all the components are selected with their maximum capacity/area/depth etc., then the final design will fulfill the predicted MHR and the average yearly HCU will be 10.92 MWh. This value can be named as the minimum theoretically possible HCU required for the test building.

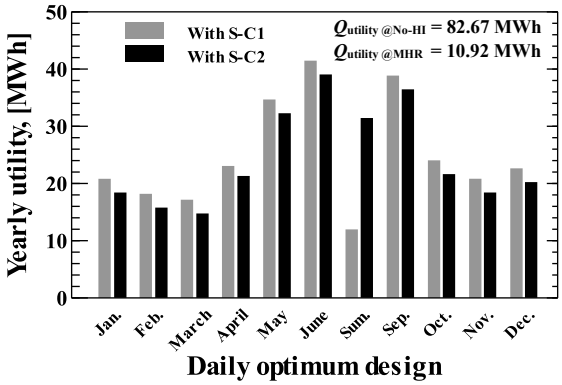

Figure 7-12 Yearly required HCU with each daily optimum design

The HCU is bought from grid electricity for the test building. Therefore, the same exact trend as depicted in Figure 7-12 is expected for the cost of the HCU (i.e., grid electricity). The cost of grid electricity is 0.073 CAD/kWh for the test building location. This value is 0.147 CAD/kWh and 0.18 CAD/kWh as Canada average and global average electricity cost, respectively.

7.4.1.8 Auxiliary systems (heating and cooling)

As the auxiliary heating and cooling or the conventional systems are already available in the energy system of the test building, only the required electricity + repair and maintenance costs should be computed. The required energy has been already derived (i.e., the HCU as computed

in section 7.4.1.7) and the repair and maintenance costs are estimated up to 1% of the yearly electricity cost [243,252].

7.4.2 Total annual cost; different scenarios

Two main scenarios can be considered for selecting the final design for the building:

- The priority can be given to the MHR. In other words, the final design can be defined as a new one when all the components are selected according to their maximum capacity/area/volume, etc. In this way, the predicted MHR for each DOD will be achieved for all days in a year.
- The priority can be given to the minimum TAC among all DODs and MHR cases.

Figure 7-13 presents the TAC for all DODs and the MHR design with two different electricity costs: Quebec (QC) and Canadian average (CA). Considering these two electricity costs is helpful to understand the effect of HCU cost on selecting the final design and the reasons why implementing retrofit options via integrating renewable energies in residential building sector suffer from relatively low penetration factor. Several interesting points can be observed from TAC of each DOD.

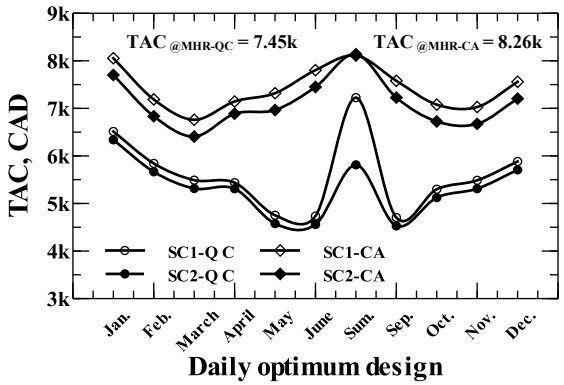

Figure 7-13 Total annual cost of each DOD in two cases: summer-C1 (SC1), summer-C2 (SC2), and MHR designs with both Quebec (QC) and Canadian average (CA) electricity price

Depending on the electricity cost, the minimum TAC can occur at different DOD. For instance, with residential electricity cost of QC, which is the lowest in Canada, the minimum TAC is with DOD of September. However, the DOD of March represents the minimum TAC with the CA electricity cost, which is close to the average global electricity cost. In other words, depending on the HCU cost, the proposed SAGSHP system may not be economically feasible as there is no energy interaction with the ground in DOD of September (i.e., zero require depth of GHE). Furthermore, the TAC of the design representing the highest capacities of each component is maximum with both QC and CA electricity costs. In a broad sense, the cost of solar PV panels

+ EES batteries and the vertical GHEs are still overpriced to effectively penetrate the energy system of residential building sector. The renewable energy integration can be improved, and the other side of the coin is implementation of carbon tax and subsidies in favor of renewable energy integration in buildings, as has been partially iterated in Quebec [253].

Additionally, Figure 7-13 shows that the overall ACIC/ACOC and the utility costs can be the same based on what the electricity cost is. The TAC of SC1 and SC2 are the same when the CA electricity cost is considered.

7.5 Conclusion

Dynamic pinch analysis can be applied to the energy system of buildings. In the energy targeting phase, this approach delivers the DOD according to the available renewable and waste sources of energy and required building loads. Theoretically, there can be 365 DODs extracted for a building for all 365 days of a year, which is the first layer of selecting the optimum design for the building. From a practical point of view, 12 days were selected among 365 days of a year, each representative of each month. The energy targeting results are presented in [231]. Nonetheless, the building needs just one design as the final working ones. This study presents a techno-economic analysis for selecting the final design among all DODs based on the presented techno-economic analysis and the minimum TAC. The capital investment costs, repair and maintenance costs, and operation cost are included in computing TAC. Furthermore, an algorithm is proposed for computing the average yearly HCU (i.e., grid electricity) for each DOD as if it works for the whole year. The results reveal that according to the cost of the electricity (based on location of the building), there can be different DODs with minimum TAC. As the test building is located in the province of Quebec, Canada, the DOD of September with no need to the GHE presents the minimum TAC. By considering the Canadian average electricity cost, the final design changes from DOD of September to the DOD of March, where the ground source provides some part of required evaporator load by 200 m vertical ground heat exchangers. In conclusion, the dynamic pinch and the TAC analyses can set the stage for finding the most cost-effective optimum SAGSHP system for buildings.

7.6 Acknowledgement

The authors acknowledge the financial support of the Natural Sciences and Engineering Research Council of Canada for this project (RGPIN-2019-05826).

7.7 Nomenclature

$\bar{c}_p$	Average heat capacity (kJ kg^{-1} K^{-1})	HFH	Hydronic Floor Heating
H	Enthalpy (kW)	HP	Heat Pump
i	interest rate	HX	Heat Exchanger

j	number of equipment
$\dot{m}_{ref}$	Refrigerant mass flow rate (kg s^{-1})
N	number of days
PR	Compressor pressure ratio
Q	Heat transfer load (kW) or energy (kJ)
T	Temperature (°C or K)
Greek	
ε	DWHR effectiveness
Δ	Difference sign
η_{isen}	Compressor isentropic efficiency
$\bar{\rho}$	Average density [kg m^{-3}]
Subscripts	
c	cold
h	hot
ideal	Thermodynamic based volume
in	inlet
max	maximum
min	minimum
out	outlet
real	practical volume
ref	refrigerant
Acronyms	
ACIC	Annualized Capital Investment Cost
ACOC	Annualized Capital Operation Cost
AF	Amortization Factor
ASGSHP	Solar Assisted Ground Source Heat Pump
CA	Canadian Average
CAD	Canadian Dollar
CIC	Capital Investment Cost
COC	Capital Operation Cost
COP	Coefficient of Performance
DHW	Domestic Hot Water
DOD	Daily Optimum Design
DWHR	Drain Water Heat Recovery
EES	Electric energy storage
Exp.	Expansion
GHE	Ground Heat Exchanger
HCU	Hot/Cold Utility
GS	Ground Source
IHRL	Intermediate Heat Recovery Loop
LA	Lead Acid
LI	Lithium Ion
LMTD	Logarithmic Mean Temperature Difference
MHR	Maximum Heat Recovery
NA	Not Applicable
Pr	Pressure ratio
PV	Photovoltaic
PVC	Polyvinyl Chloride
PVT	Photovoltaic/Thermal panel/collector
QC	Quebec
RPF	Renewable Power Fraction
SC	Space Cooling
SC1	Summer Case 1
SC2	Summer Case 2
SH	Space Heating
SPF	Seasonal Performance Factor
STC	Solar Theraml Collector
TAC	Total Annual Cost
TES	Thermal Energy Storage
UC	Utility Cost (CAD/kWh)
WGW	Warm Gray Water

Chapter 8: A Systematic dynamic pinch approach for thermal energy storage and solar assisted ground source heat pump integration in buildings

Avant-propos

Auteurs et affiliation:

Seyed Mojtaba Hosseinnia: étudiant au doctorat, faculté de génie, département de génie mécanique, Université de Sherbrooke.

Mikhail Sorin: professeur, faculté de génie, département de génie mécanique, Université de Sherbrooke.

Date d'acception: 15 avril 2022

État de l'acceptation: version finale, pp. 1265

Revue: 5th International Conference of Building Energy and Environment (COBEE2022)

Titre français: Une approche de pincement dynamique systématique pour le stockage d'énergie thermique et l'intégration de pompes à chaleur géothermiques assistées par énergie solaire dans les bâtiments

Contribution au document: Cet article montre l'application de l'approche de pincement dynamique proposée pour les panneaux solaires thermiques et photovoltaïques dans les bâtiments.

Résumé français: Il n'y a pas d'approche systématique disponible dans la littérature pour le dimensionnement d'unpompe à chaleur géothermique assistée par énergie solaire (ASGSHP) qui peut entièrement inclure tous les types de sources disponibles, y compris les énergies renouvelables, par exemple, l'énergie solaire, géothermique (GS) et l'énergie résiduelle comme les eaux grises dans les bâtiments, tout en garantissant la réalisation de la récupération de chaleur maximale (MHR). Dans cette étude, une approche de pincement dynamique graphique est proposée qui calcule le MHR en temps réel à chaque instant d'une journée, où l'énergie

solaire est présentée en fonction des capteurs photovoltaïques/thermiques (PVT). De plus, les charges dynamiques de HP et GS sont converties en charges constantes en se connectant à des réservoirs de stockage d'énergie thermique stratifiés. Cette approche inclut toutes les charges dépendantes du temps concernant à la fois les sources d'énergie et les puits ; par conséquent, il peut s'agir d'un cadre solide pour le dimensionnement de la capacité du système, en particulier pour les bâtiments à énergie zéro.

8.1 Summary

There is no systematic approach available in the literature in sizing solar assisted ground source heat pump (ASGSHP) that can fully include all types of available sources including renewable energies, e.g., solar, ground source (GS), and waste energy such a gray water in buildings, while guarantees achieving to the maximum heat recovery (MHR). In this study, a graphical dynamic pinch approach is proposed that computes the real time MHR at each moment during a day, where the solar energy is presented inform of the photovoltaic/thermal (PVT) collectors. Furthermore, the dynamic loads of HP and GS are converted into constant loads by connecting to stratified thermal energy storage tanks. This approach includes all time dependent loads regarding both energy sources and sinks; hence, it can be a solid framework for system capacity sizing, especially for zero energy buildings.

8.2 Introduction

Ground source heat pump (GSHP) system can utilize different sources of renewable energies such as solar photovoltaic, solar thermal, ground source (GS), etc. and waste low-grade sources, e.g., gray water (GW), to meet the required energy demands of buildings. However, selecting the capacity of the GSHP system is not a trivial task [42]. This is mainly due to the dynamism of the energy demands in buildings, e.g., space heating (SH), space cooling (SC) and domestic hot water (DHW), plus the intermittency of renewable sources. In other words, the system capacity can easily be oversized if the maximum total load in the coldest/hottest day in a year is selected as the capacity of the GSHP system, yet it has been practiced [46].

Integration of a stratified thermal energy storage (TES) tank is a practical remedy for avoiding the maximum capacity of the HP system in buildings [123,231]. Hence, the extra HP energy can be stored in an intermediate medium inside the TES tank, and it can be recovered by discharging the tank. Moreover, the functionality of the TES tanks is a good fit for intermittent renewable energy sources [3] as TES tanks can dampen the fluctuations in the intermittent sources. Even so, in the case of solar energy, sizing the area of solar thermal collectors (STC) or the area of PV panels are still a challenging task [254]. Combined photovoltaic and solar thermal (PVT) can provide both electric and thermal energies. From temperature perspective, the circulating

heat transfer fluid (HTF) can reach up to 70°C, which is suitable for domestic hot water application [255].

Utilizing all the mentioned sources of energy into a building energy system and ensuring the maximum heat recovery (MHR) among sources (i.e., hot streams) and sinks (i.e., cold streams) is in the realm of heat integration techniques such as pinch analysis (PA). PA is a useful framework for converting the mentioned sizing problem into a matching among hot/cold streams [6]. Moreover, it provides a heat exchanger (HE) + TES network that can guarantee achieving the predicted MHR. However, steady state PA approach must be adapted for the streams with time-dependent heat flow rate and the prioritization between direct and indirect (via the TES tank) heat exchange needs to be defined [123]. Current application of the PA in buildings is limited to the steady state load assumption [100], the renewable energy is not included [99], and integration of the TES tank is missing [239]. Furthermore, there is no PA based sizing of the GSHP+PVT system in the literature.

In this study a dynamic PA concept is proposed that can handle the dynamic loads of a building and the intermittency of renewable sources. The main outputs of this approach are the load of the GS and HP system. A test building with heating dominated loads is selected to demonstrate the proposed approach. According to the required loads of the test building, the proposed approach delivers the MHR based on direct/indirect heat recovery. It is shown that the proposed sizing approach can reduce the electric input demand of the test building by integrating different renewable and waste sources of energy in the shape of a solar assisted GSHP system.

8.3 Graphical dynamic pinch approach

The proposed dynamic PA follows a series of well-established steps to reach to the final goals: predicting the maximum heat recovery and providing a HX+TES network to make the MHR real. The steps are as follows:

- Extracting the available sources and sinks in an energy system, their loads, supply/target temperatures, heat capacity rate ($CP = \dot{m} \times c_p$) as a continuous function of time during 0 to 24 hours of a day. Regarding the energy streams of buildings, the sources/sinks include, but not limited to, space heating, space cooling, domestic hot water, GW, HP characteristics, solar PVT, and GS.
- Setting the heat exchange possibilities among the mentioned sources/sinks, performing the vertical heat transfer and plotting the hot/cold composite curves (CCs) at a given minimum temperature difference and at a given time, computing the PVT area and the HP capacity for satisfying the building loads, extracting the GS load

- Arranging a network of heat exchangers + TES tanks to make real the promises of the second step. It worth mentioning that the first two steps (i.e., energy targeting) are presented in this study.

8.3.1 Data extraction

Like all pinch analysis performed in industrial sector, there is a need to have reliable data regarding the characteristics of all energy streams in the system. The difference here is the time-dependent nature of the loads in buildings. Moreover, the renewable energies such as solar and GS are time-dependent, too. Therefore, the continuous and time dependent loads need to be extracted as precise as possible. It should be noted that depending on the building types and use, e.g., residential, or commercial, the supply/target temperatures and heating/cooling systems can be different. However, the final goal is to maintain the indoor thermal comfort with minimum usage of external utility.

8.3.2 Buildings basic loads

The basic winter loads in all residential buildings can be categorized as SH and DHW. The loads are shown in Figure 8-1 for the test building. The SH can be satisfied with different heating/cooling systems. In the test building, the SH is a hydronic floor heating (HFH) type. It should be noted that the gray water (GW) loads can be extracted from the DHW. It is practical to divide the GW into warm and cold ones. The details about the test building and the GW loads can be found in [3,123].

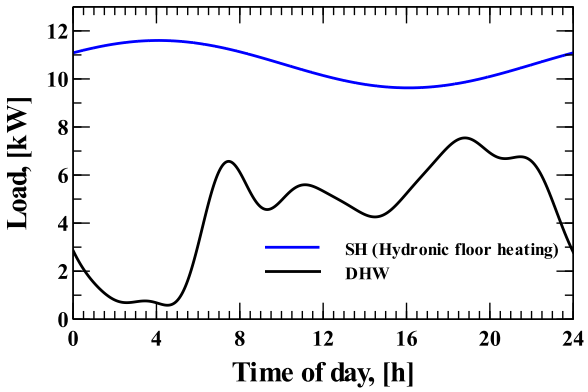

Figure 8-1 Basic loads in the test building in heating mode

8.3.3 Solar PVT

The energy output of PVT collectors is directly proportional to the solar irradiance and the collector area. Both can have limitations depending on the building location and available mounting area. The electric and thermal power outputs are presented in Eq. (8-1). Where, $G(t)$ is the solar irradiance (i.e., Eq. (8-2) [113]), η_e is the electric efficiency of the PV cells, $\eta_0, a_1,$

and a_1 are constants that can be found in the literature or from the collector's manufacturer. $\dot{m}_{CHTF}$ is the mass flow rate of the collector heat transfer fluid. T_{in} is the inlet constant collector heat transfer fluid temperature, equal to 40°C. The outlet temperature of collector heat transfer fluid (CHTF) is assumed 65°C.

$$\begin{gathered} PV\ Electric\ Power = A_{PVT} \times G(t) \times \eta_e \\ Solar\ Thermal\ Collecter\ Power = \eta_c G(t) A_{PVT} \Rightarrow \\ A_{PVT}(\eta_0 G(t) - a_1(T_c - T_{amb}) - a_2(T_c - T_{amb})^2) = \dot{m}_{CHTF} \times c_p \times (T_{out} - T_{in}) \end{gathered} \tag{8-1}$$

$$G(t) = 1362 \times CI \times \left(1 + 0.033 \cos\left(\frac{2\pi d_n}{365}\right)\right) \times \cos(\theta_z(t)) \times \sin\left(\frac{\pi(t - t_{rise})}{t_{set} - t_{rise}}\right) \tag{8-2}$$

The average clearness index (CI) is assumed 0.3 for the day in winter. Details and definitions of the variables can be found in [123]. The outlet temperature of the CHTF needs to reach to 65°C, therefore, several collectors should be connected in series. Figure 8-2 shows the characteristics of 10 PVT panels connected in series, 2 m^2 each, approximately. The area of PVT can be increased, if required, to meet the buildings energy demand. However, the maximum available mounting area is 121.2 m^2 at an average tilt angle of 45°.

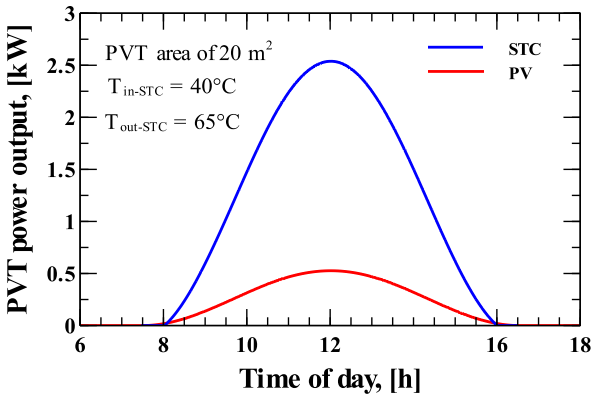

Figure 8-2 . PVT power output for a typical winter day

8.3.4 HP system

R466A is selected as the refrigerant in the proposed HP system, as it is a good replacement for the phased-out R410A [177]. The single stage HP system thermodynamic cycle is presented in the Pressure-Enthalpy graph in Figure 8-3. The COP of the HP system is 3 and the max/min pressure ratio is 5.8. Furthermore, the maximum compressor temperature is 110.1°C, which can easily increase the city water temperature from 5°C to 55°C at an appropriate condenser load.

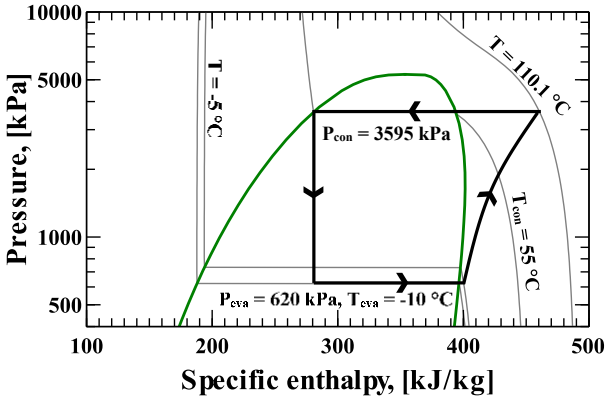

Figure 8-3 P-h diagram for the proposed HP system

8.3.5 Ground source

Depending on the undisturbed underground temperature, certain amount of energy can be extracted/injected from/to the ground by means of several vertical ground heat exchangers (GHE). The heat transfer fluid circulates inside one or several GHE and exchange heat with the ground as shown in Figure 8-4.

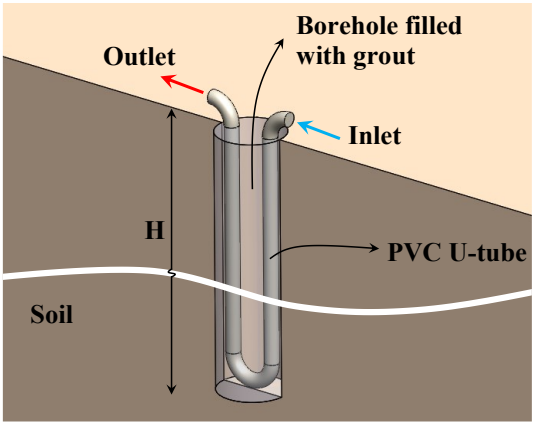

Figure 8-4 Single U-tube ground heat exchanger
(H is the depth of the borehole)

The undisturbed temperature is 10°C for the test building location, approximately. It should be noted that the outlet temperature of the HTF goes down gradually after several days of working in the energy extraction mode. However, the output power of the GS can be held constant by adjusting the mass flow rate of the HTF [170]. Furthermore, if the energy extraction and injection rate are the same, the GS can play the role of a solid TES. In other words, energy will be discharge from GS in the winter and the same amount will charge the GS during the summer, both by heat pumping. Therefore, the system can be sized to set equal the amount of extracted and injected energy regarding the GS.

8.3.6 Stratified TES tank and intermediate heat recovery loops

Stratified TES tank can undergo charge/discharge processes several times per day to load/unload thermal energy effectively. Water or a water + antifreeze mixture is the storage medium due to abundance, good energy storage properties, and being cheap.

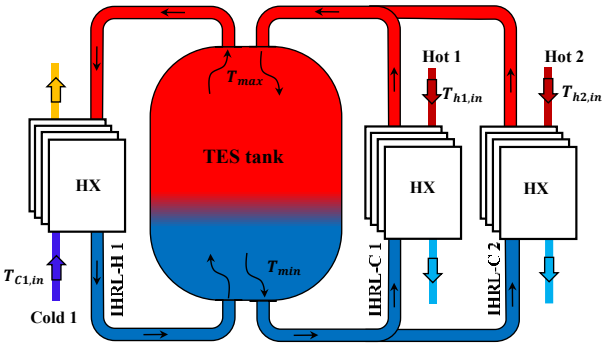

Figure 8-5 Stratified TES tank and IHRLs

The intermediate heat recovery loops (IHRLs) and the heat exchangers (HX) are required to charge/discharge the TES tank, as shown in Figure 8-5. The IHRLs that charge the TES tank are like a cold stream (IHRL-C in Figure 8-5) and the IHRLs that discharge the TES tank can be taken as one hot stream (IHRL-H in Figure 8-5). The supply/target temperatures of the IHRL-C/IHRL-H can be computed based on the supply and target temperature of main hot/cold streams and the heat transfer minimum temperature difference (i.e., $\Delta T_{min} = 5°C$ in this study) [123]. It should be noted that the heat loss to the ambient air and the presence of lost volume or thermocline thickness can be considered in final sizing of the TES volume [169].

8.4 Real time hot/cold composite curves

Table 8-1 presents the supply/target temperatures of different discussed streams in the test building. The vertical heat transfer model ensures the maximum heat recovery among different hot/cold streams. However, the possibility of a viable heat transfer depends on the supply/target temperatures and the priority for the direct/indirect (via TES tank and IHRLs).

Table 8-1 Hot and cold streams with supply/target temperatures

Streams	Hot/Cold	Supply (°C)	Target (°C)	CP (kW/°C)
SH(HFH)	C	30	35	Dynamic
DHW	C	City water	55	Dynamic
WGW	H	30	5	Dynamic
STC	H	65	40	Dynamic
CGW	H	10	5	Dynamic
Con-HP	H	110.1	55	constant
Eva-HP	C	-10	-5	constant
GS-Ext	H	≥5	-5	constant

According to the temperature range of different streams, the heat exchange between them can be realized, as shown in Figure 8-6 Possible energy/heat transfer among hot/cold streams. The

IHRLs are not shown here. Also, the compressor needs the electric output power of PVT collectors (it is not involved in any heat exchange).

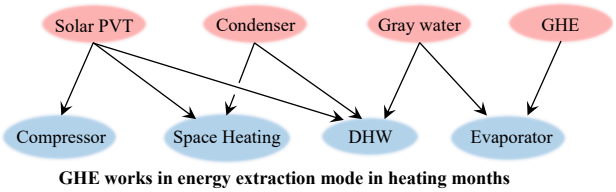

Figure 8-6 Possible energy/heat transfer among hot/cold streams

8.4.1 Composite curves set up

As the supply/target temperatures of the streams involved in the test building are constant, therefore, the time dependent CP resultant at each temperature interval can be extracted by Eq. (8-3).

$$\Delta H = \sum (CP)_i \times \Delta T_{interval} \Rightarrow \left(\frac{dT}{dH}\right)_{interval} = \frac{1}{\sum CP_i} \tag{8-3}$$

Figure 8-7 shows the steps of the proposed PA approach for finding the required $A_{PVT}(t)$, GS load, and HP capacity which can satisfy the loads of the building. As the dynamic loads are continuous function of time during 0 to 24 hours, the proposed algorithm can be applied at each moment during 0 to 24 hours of the selected day.

It should be noted that according to the available solar irradiance, there may be enough energy for satisfying the building loads without heat pumping. In this case, the HP load will be zero. Furthermore, there will be a maximum and minimum for A_{PVT} during 0 to 24 hours. The design area can be selected based on a total annual cost analysis in the future studies. Figure 8-8 shows the computed dynamic A_{PVT}, the constant and dynamic loads of the condenser of the GSHP, and the dynamic and constant loads of the GS. It worth mentioning that if the test building needs to rely just on the PVT panels during the daytime, the required PVT collector area will be around 3390 m^2 at 8 AM, 400 m^2 at 9 AM, and 174.7 m^2 at 10 AM. Around 10:50 AM, the required PVT area falls below the maximum available mounting area of 121.2 m^2. The minimum A_{PVT} is 101.7 m^2 at 12:20 PM. The required A_{PVT} increases by marching further in time towards the sunset in the same pattern as during sunrise.

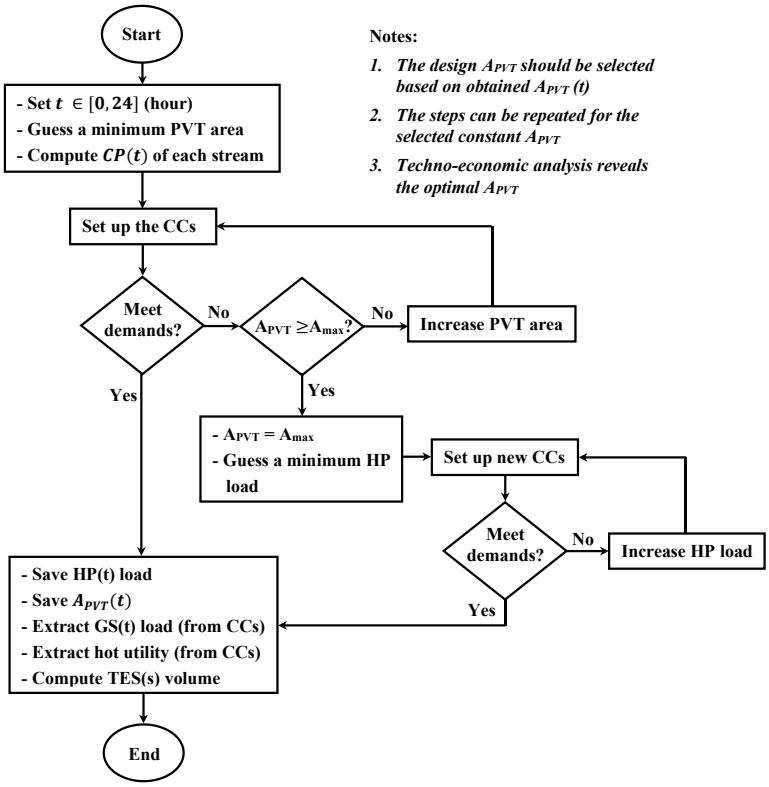

Figure 8-7 PA based algorithm for computing HP load, GS load, and PVT area at a given time

Connection to the TES tanks dampens the fluctuations in the dynamic loads. In other words, it stores the surplus energy (red areas in Figure 8-8) and releases it when it is demanded (blue areas in Figure 8-8). As it can be seen from Figure 8-8, the maximum condenser load is 15.2 kW, and the minimum value is zero (when just solar energy can satisfy building loads). Nonetheless, a constant condenser load at 10.48 kW and connection to a TES tank can provide the required energy of the test building from 0 to 24 hours in combination with solar energy.

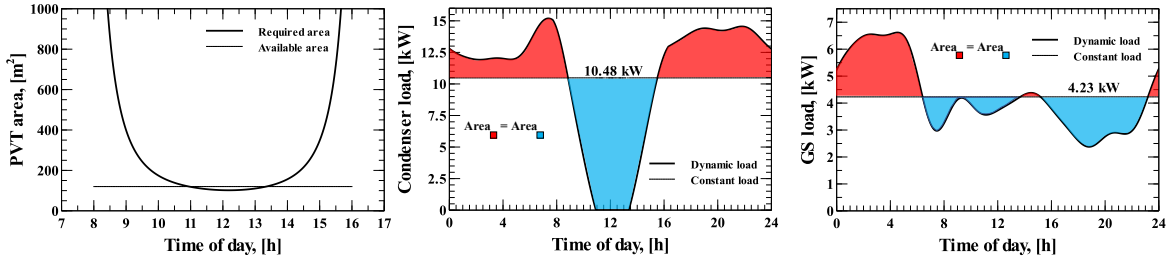

Figure 8-8 Dynamic PVT area, condenser, and GS loads

Similarly, the maximum and minimum GS loads are 6.61 kW and 2.38 kW, respectively. Connecting the GHEs to a TES tank can reduce the maximum GS load to a constant ground load of 4.23 kW. The constant GS together with the gray water can satisfy the require evaporator load. The volume of the stratified TES tank can be calculated from Eq. (8-4).

$$V_{TES} = \frac{Q}{\bar{\rho}\bar{c_p}\Delta T_{max-min}} \quad (8\text{-}4)$$

Where Q is the amount of energy to be stored (blue or read areas in Figure 8-8), $\bar{\rho}$ and $\bar{c_p}$ are the average density and specific heat capacity of the storage fluid. Storable energy must be stored in the high and low temperature TES tanks (i.e., two separate TES tanks). Details of the set points are presented in Table 8-2. The storage medium for both TES tanks is Water + 20% (mass fraction) Ethylene Glycol with freezing point of -7.95°C.

Table 8-2 High and low temperature TES tanks characteristics

Parameter	High-T TES tank	Low-T TES tank
T_{max} (°C)	60	5
T_{min} (°C)	30	-5
$\bar{\rho}$ (kg m^{-3})	1013.4	1029
$\bar{c_p}$ (kJ kg^{-1} °C^{-1})	3.942	3.861
$\Delta T_{max-min}$ (°C)	30	10
Q (kWh)	47.2	12.8
TES Volume (L)	**1418**	**1160**

Moreover, the electric output of the PVT collectors can be stored in electric energy storage units, e.g., lead acid batteries. The stored electric energy can be used for running the compressor of the GSHP system and the installed pumps. The electric energy produced by the PVT collectors reduces the required grid electricity for running the compressor by 18.3%. Additionally, the total energy consumption of the test building reduces from 362.9 kWh to 69 kWh by integrating the proposed SAGSHP + TES tanks into the test building energy system in the single day in January.

8.5 Conclusion

In this study, a dynamic pinch approach is proposed that can consider different dynamic sources/sinks of energy in buildings. The proposed systematic approach can predict the dynamic PVT collector area, the minimum constant loads of the heat pump and the ground source by connecting the heat pump and the vertical ground heat exchangers to the stratified TES tanks. Therefore, the sizing problem can be reduced into matching between predefined hot/cold streams in a graphical approach via hot/cold composite curves. The steps are presented through a novel algorithm and have been applied to a multifamily test building. The integration of the SAGSHP and TES tank in the test building can reduce the required utility (i.e., grid electricity) by a factor of 5. Although the proposed approach is depicted for one day in the heating season for the test building, it can be applied to all days in year, all climate conditions and building types.

8.6 Acknowledgement

The authors acknowledge the financial support of the Natural Sciences and Engineering Research Council of Canada for this project (RGPIN-2019-05826).

Chapter 9: Conclusion and future view

9.1 Conclusion de la thèse et travaux futurs

La principale nouveauté de cette étude est que le concept d'analyse de pincement est adapté pour les systèmes énergétiques dynamiques tels que les bâtiments. L'adaptation mentionnée nécessite l'intégration d'un système de stockage (à la fois thermique et électrique) dans les bâtiments, ce qui signifie la combinaison entre la récupération de chaleur directe et indirecte. En outre, la détermination de la taille minimale des équipements tels que les charges de l'échangeur de chaleur au sol, la surface des panneaux solaires, les charges du condenseur/évaporateur et le volume des unités de stockage d'énergie thermique/électrique est l'intérêt central du bâtiment à énergie nulle. L'approche de pincement graphique proposée inclut tout le dynamisme des charges, peu importe que la charge provienne d'une source d'énergie renouvelable intermittente ou de la demande des bâtiments telle que l'eau chaude sanitaire. Tant que la charge extraite peut être ajustée en fonction continue du temps, les courbes composites chaud/froid en temps réel peuvent prédire la récupération maximale de chaleur en temps réel. Il convient de mentionner qu'une période répétée où tous les flux chauds/froids possibles existent est appelée temps de lot. Les 24 heures d'une journée peuvent être reconnues comme le temps de lot dans les bâtiments. Pendant 0 à 24 heures, l'approche de pincement dynamique graphique proposée peut calculer le surplus/déficit d'énergie à un moment donné. Par conséquent, par intégration, la quantité d'énergie à stocker et, par conséquent, le volume des unités de stockage peuvent être calculés. L'approche par pincement est une approche basée sur la thermodynamique. Ainsi, l'analyse thermodynamique du système de pompe à chaleur est compatible, du point de vue énergétique, avec la méthode du pincement. De cette manière, il est possible de calculer la puissance minimale requise du compresseur et de la relier à la surface des panneaux solaires photovoltaïques et aux unités de stockage électrique.

La phase de ciblage énergétique de l'approche pincée proposée fournit la charge/énergie minimale de chaque composant, comme les unités TES et les GHE, à chaque jour représentatif de 1 à 365 jours par an. Par conséquent, la première couche d'optimisation est effectuée pendant la phase de ciblage énergétique. Néanmoins, le bâtiment n'a besoin que d'un réseau d'équipements avec des tailles fixes. Par conséquent, la deuxième couche d'optimisation est effectuée en considérant le coût annuel total de chaque réseau. Il convient de noter que la quantité d'utilité chaud/froid avec chaque conception optimale quotidienne si elle est exprimée pendant d'autres jours (où elle fonctionne hors conception) doit être calculée. Pour répondre à ce besoin, un algorithme est proposé qui peut calculer la valeur d'utilité annuelle moyenne de

chaque DOD comme s'il fonctionnait pendant toute l'année. En plus de l'utilité chaud/froid, le dimensionnement de certains composants tels que le réservoir TES et les GHE verticaux nécessite une simulation exacte. En d'autres termes, l'approche de pincement proposée donne le volume idéal du réservoir TES et juste la charge minimale des GHE verticaux, pas la taille réelle de ces composants. De plus, la taille réelle de ces composants est nécessaire pour calculer le coût annuel total de la superstructure proposée. En résumé, le coût annuel total de tous les DOD est calculé. Comme ce TAC est la fonction objectif de la deuxième couche d'optimisation, le réseau avec le TAC minimum est déclaré comme le meilleur design pour le bâtiment test. Le TAC minimum est directement affecté par le coût de l'électricité du réseau. A titre d'exemple, avec le coût de l'électricité du QC, l'optimum du réseau dans la journée de septembre est la meilleure conception, qui ne nécessite aucun GHE vertical. Par contre, avec le coût de l'électricité de la moyenne canadienne, la meilleure conception est à la journée en mars avec 200 m de GHE verticaux.

Dans cette étude, la température d'alimentation et la température cible des charges dans le bâtiment (par exemple, la charge de chauffage, la charge de refroidissement, l'eau chaude sanitaire) et les charges extraites pour l'énergie renouvelable telle que l'énergie solaire thermique sont considérées comme fixes. Cependant, il est possible que certains des flux mentionnés représentent une température d'alimentation/cible dépendante du temps. Cette température variable ajoute un autre degré de liberté aux équations résolues (c'est-à-dire la première loi et la deuxième loi de la thermodynamique). Traiter ce nouveau problème nécessite plus de puissance de calcul et de temps d'exécution, cependant, il est intéressant et le nouveau modèle donne un résultat plus réaliste. L'extraction de la fonction de coût dynamique pour chaque courbe composite chaud/froid en temps réel est une autre étude extrêmement utile qui est proposée comme travail futur. De plus, la fonction objectif pour la deuxième couche d'optimisation peut être la quantité d'émissions de gaz à effet de serre plutôt que le coût annuel total. En ce qui concerne l'étude numérique, l'étude des performances hors conception d'un échangeur de chaleur à récupération de chaleur des eaux de drainage (DWHR) est un autre travail futur possible. Ce dernier est extrêmement difficile en raison de la nature turbulente du film d'eau grise tombant à l'intérieur du tube de drainage vertical. De plus, la géométrie de profil hélicoïdal autour du tube ne permet aucune simplification telle que l'utilisation de symétrie ou de conditions aux limites périodiques. En d'autres termes, la géométrie entière doit être considérée comme le domaine de calcul. La taille industrielle de l'échangeur de chaleur DWHR (par exemple, plus d'un mètre de hauteur) et les ressources de calcul disponibles (par exemple, RAM, CPU, disques durs, etc.), augmuntent les diffculté le simulations numériques.

9.2 Thesis conclusions

The main novelty of this study is the point that the concept of pinch analysis is adapted for dynamic energy systems such as buildings. The mentioned adaptation requires integrating of storage system (both thermal and electrical) in buildings which means the combination between direct and indirect heat recovery. Furthermore, determination of the minimum equipment size such as ground heat exchanger loads, solar panel area, condenser/evaporator loads, and the volume of the thermal/electrical energy storage units is the focal interest in the zero-energy building. The proposed graphical pinch approach includes all the dynamism in the loads, no matter the load is coming from an intermittent renewable energy source or from the buildings demand such as domestic hot water. As long as the extracted load can be fitted as a continuous function of time, the real time hot/cold composite curves can predict the real time maximum heat recovery. It worth mentioning that a repeated period when all possible hot/cold streams exist, is called batch time. The 24 hours of a day can be recognized as the batch time in buildings. During 0 to 24 hours, the proposed graphical dynamic pinch approach can compute the energy surplus/deficit at any given time. Therefore, by integration, the amount of energy for storage, and consequently, the volume of the storage units can be computed. The pinch approach is a thermodynamics-based approach. Hence, the thermodynamic analysis of the heat pump system is compatible, from energy perspective, with the pinch method. In this way, it is possible to compute the minimum required compressor power and link it to the solar photovoltaic panel area and electric storage units.

The energy targeting phase of the proposed pinch approach delivers the minimum load/energy of each component such as TES units and GHEs at each representative days in 1 to 365 days in a year. Hence, the first layer of optimization is performed during the energy targeting phase. Nonetheless, the building just need one network of the equipment with fixed sizes. Therefore, the second layer of optimization is performed by considering the total annual cost of each network. It should be noted that the amount of the hot/cold utility with each daily optimum design if it words during other days (where it works off-design) should be computed. To address this need, an algorithm is proposed that can compute the average yearly annual utility value of each DOD as if it works during the full year. In addition to the hot/cold utility, sizing of some components such as TES tank and vertical GHEs needs exact simulation. In other words, the proposed pinch approach gives the ideal volume of the TES tank and just the minimum load of the vertical GHEs, not the real size of these components. Also, the real size of these components is necessary for computing the total annual cost of the proposed superstructure. In summary, the total annual cost of all DOD is computed. As this TAC is the objective function of the second layer of optimization, the network with the minimum TAC is declared as the best design for the test building. The minimum TAC is directly affected by the grid electricity cost. As an example,

with the electricity cost of QC, network optimum in the day in September is the best design, which does not need any vertical GHE. On the other hand, with the electricity cost of Canadian average, the best design is at the day in March with 200 m of vertical GHEs.

9.3 Future work

In this study, the supply and target temperatures of the loads in the building (e.g., heating load, cooling load, domestic hot water), and loads extracted for the renewable energy such as solar thermal energy are considered fixed. This assumption is not far from the hot/cold stream specifications in the building. However, there is a possibility for some of the mentioned stream that represent a time-dependent supply/target temperature. This variable temperature adds another degree of freedom to the solved equations (i.e., first law and second law of thermodynamics). Dealing with this new problem requires more computational power and run time, however, it is interesting and the new model results in a more realistic outcome. Extracting dynamic cost function for each real time hot/cold composite curve is another extremely useful study that is proposed as a future work. Furthermore, the total annual cost analysis in the techno-economic part is selected according to the fact that all the proposed networks of HX+TES+PVT are assumed as retrofit scenarios. Therefore, the TAC is a good indicator for selecting one design among all possible ones. Nevertheless, the objective function for the second layer of optimization can be the amount of the green house gas emission or the payback period of each DOD rather than just TAC. Therefore, the second layer of optimization can vary accordingly. Regarding the numerical study, studying the off-design performance of a drain water heat recovery (DWHR) heat exchanger is another possible future work. The latter is extremely challenging due to the turbulent nature of the graywater falling film inside the vertical drain tube. Furthermore, the geometry of helical profile around the tube does not allow any simplification such as using symmetry or periodic boundary conditions. In other words, the entire geometry should be considered as the computational domain. Considering the industrial size of the DWHR heat exchanger (e.g., more than 1 meter in height) and the available computational resources (e.g., RAM, CPU, hard drives, etc.) exacerbate the numerical simulations.

The results of this Ph.D. study have been published/presented in the following international journals/conference/events:

Journals

1. ***Seyed Mojtaba Hosseinnia***, Mikhail Sorin, "*Economic approach for optimum solar assisted ground source heat pump system in building*" Energy Conversion and Management, under review

2. ***Seyed Mojtaba Hosseinnia***, Mikhail Sorin, "*Energy targeting approach for optimum solar assisted ground source heat pump integration in buildings*" Energy 248 (2022) 123528
3. ***Seyed Mojtaba Hosseinnia***, Mikhail Sorin, "*Numerical approach for sizing vertical ground heat exchangers based on constant design load and desired outlet temperature*" Journal of Building Engineering 48 (2022) 103932
4. Hossein Akbari***, Seyed Mojtaba Hosseinnia,*** Mikhail Sorin, Christopher Reddick, Dominic Laperle "*Adapted Time Slice Model of pinch analysis for direct-indirect heat recovery in buildings*" Journal of Energy and Power Technology. 4 (2022) 1–1
5. ***Seyed Mojtaba Hosseinnia***, Hossein Akbari, Mikhail Sorin, "*Numerical analysis of thermocline evolution during charging phase in a stratified thermal energy storage tank*", Journal of Energy Storage, 40 (2021) 102682
6. ***Seyed Mojtaba Hosseinnia,*** Mikhail Sorin, "*A systematic pinch approach to integrate stratified thermal energy storage in buildings*", International Journal of Energy and Buildings, 232 (2021) 110663

Conference paper/presentations

1. ***Seyed Mojtaba Hosseinnia***, Mikhail Sorin, "*A Systematic Dynamic Pinch Approach for Thermal Energy Storage and Solar Assisted Ground Source Heat Pump Integration in Buildings*" 5th international conference on Building Energy and Environment (COBEE2022) Montreal
2. ***Seyed Mojtaba Hosseinnia***, Mikhail Sorin, "*A systematic pinch approach for thermal energy storage integration in buildings*" CIREQ Interdisciplinary PhD Student Symposium on Climate Change, June 17, 2021 (Online Zoom platform)
3. ***Seyed Mojtaba Hosseinnia***, Mikhail Sorin "*L'approche de « Pincement Intermittent » pour l'intégration de systèmes énergétiques dans les bâtiments*", presented in English in Hydro-Quebec, Summer 2021
4. ***Seyed Mojtaba Hosseinnia***, Mikhail Sorin, "*Direct/Indirect Energy Recovery based on Pinch Analysis and Thermal Energy Storage integration in Buildings*", presented at CANMET energy research center of natural resources Canada, Montreal, March 2020

Appendix A

Numerical details of 1D energy equation

Figure A1 illustrates the effect of segment thickness in the one-dimensional modeling. It shows that the temperature profile with respect to the height of the TES tank does not experience meaningful change by refining the segment thickness from 5 mm to 1 mm. Therefore, segments with 5 mm thickness are selected for the numerical study. The experimental tank in [120] is initially filled with water at 25.4°C and is charged with a flow at 39.8°C from top. The Reynolds number is 1340 and the tank height is 0.6 m. More details can be found in [120].

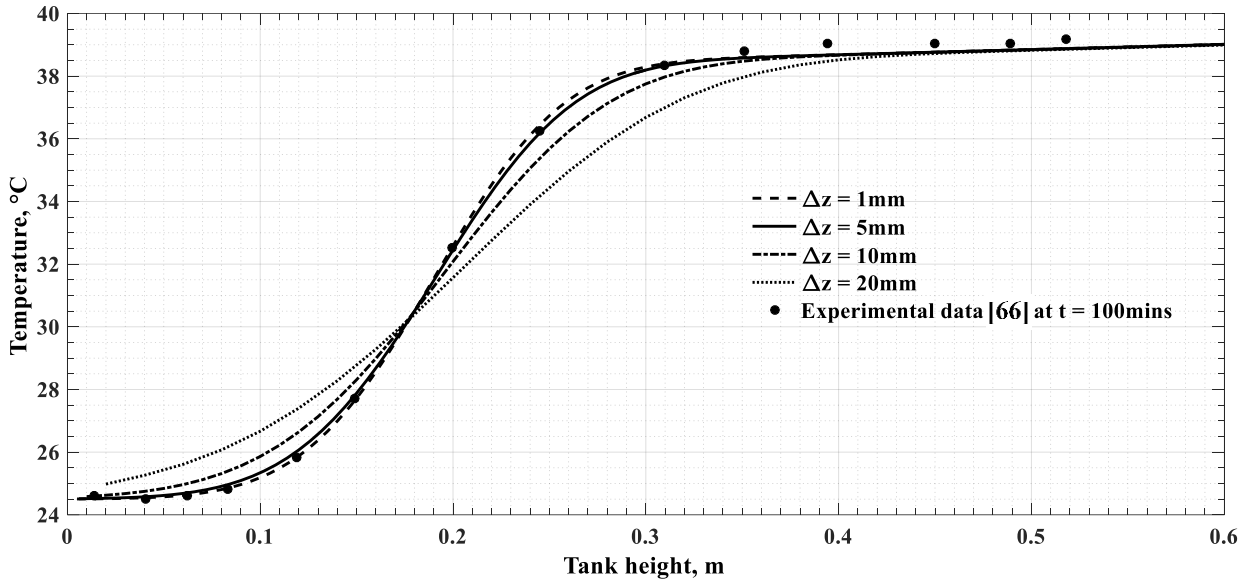

Figure A1 Temperature change with height at different segment thicknesses, as well as experimental [120]]

Figure A2 shows the detailed location of charging and discharging IHRLs inside the TES. Six charging and discharging diffusers are designed as two parallel disks with diameter of 400 mm and a spacing of 5 mm between disks of each diffuser. The spacing between diffusers is designed as 10 mm. With this configuration, inlet and outlet flows have a radial velocity component only, which is helpful to maintain the stratification. Moreover, at least a 40 mm gap has to be considered between the hot and cold zones due to piping/diffusers considerations.

A 1D modeling of the thermal performance of the configuration presented in Figure A2 was studied. To determine the effect of segment thickness (grid resolution) and the time step size on the obtained results, a grid and time step independency analysis was performed. This study was

completed for both validation and for the 1D case with several inlets and outlets as shown in Figure 3-16. The numerical results did not change by reducing grid thickness from 5 mm to 1 mm. Thus, 5 mm was selected for all presented simulation results

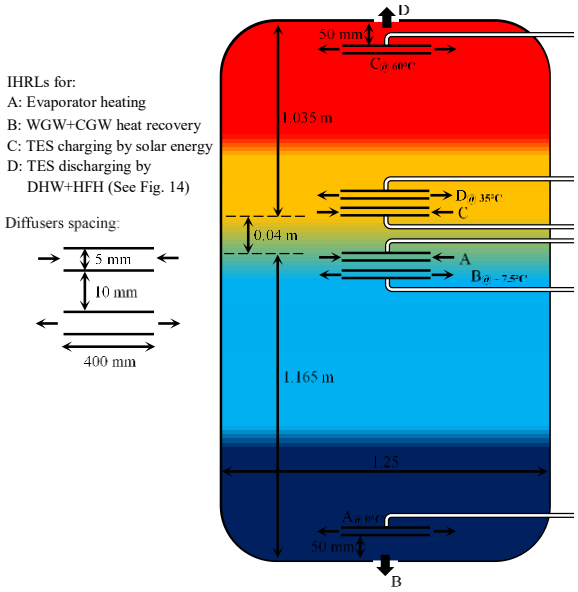

Figure A2 Different dimensions of designed and modeled stratified TES tank for the test building

The mixing and buoyancy effects are artificially produced in the 1D modeling by the algorithm described in Figure A3. This part of the 1D modeling algorithm is shown in Figure A3 as a pseudocode. The node thickness is assumed constant and uniform. In first step, it computes the temperature difference between two consecutive nodes, then the max function detects the presence of a low temperature node above a high temperature one. As this violates the buoyancy effects, in the next step, the calculated difference will be added to the top node and subtracted from the lower node. These steps continue for all nodes at each time step, as long as the maximum temperature difference is below the desired set of error. In this study we set this error as 1e-05.

While the temperature difference between two consecutive nodes is greater than the set error

Compute the maximum between 0 and half of the temperature difference between two consecutive nodes (lower one mines upper one)

For each node with the maximum greater than 0

Add the maximum to the upper node

Subtract the maximum from the lower node

End

Figure A3 Pseudocode for buoyancy and mixing correction in 1D simulation

Appendix B

Water properties used in Chapter 4 of this thesis

Water properties as a continuous function of absolute temperature (K) are used in this numerical study. The functions for density (kg m^{-3}), specific heat capacity (j kg^{-1} K^{-1}), dynamic viscosity (kg m^{-1} s^{-1}), and thermal conductivity (W m^{-1} K^{-1}) are presented here. All values are extracted from Engineering Equation Solver Academic-Commercial V10.836 at constant 101.325 kPa pressure and have been checked for independency from pressure changes. The values are fitted through presented functions with a maximum root mean square error (RMSE) of 0.0014 and R- square values of 1.

The general function form for the viscosity and the thermal conductivity is as Eq. (B1).

$$\mu(T) \; or \; k(T) = \; a \times \exp(b \times T) + c \times \exp\,(d \times T) \tag{B1}$$

Coefficients are presented in Table B1. The absolute temperature range is $273.15 \leq T \leq 372.95$ Kelvin.

Table A1. Coefficients in Eq. (B1)

Property	a	b	c	d
μ	1381	-0.05201	0.01913	-0.01142
k	0.9005	-0.0005152	-6.67	-0.01239

To have accurate values for density and specific heat capacity, the function with a general form presented in Eq. (B2) is applied in the simulation.

$$\rho(T) \; or \; cp(T) = \sum_{i=1}^{5} a_{1i} \times \exp\left(-\left(\frac{T - a_{2i}}{a_{3i}}\right)^2\right) \tag{B2}$$

Coefficients are presented in Table B2. The absolute temperature range is $273.15 \leq T \leq 372.95$ Kelvin.

Table B2. Coefficients in Eq. (B2)

i	a_{1i}		a_{2i}		a_{3i}	
	ρ	cp	ρ	cp	ρ	cp
1	997.2	6295	269	2611	269	3525
2	184.3	653.1	436.6	205.4	77.13	48.89
3	1.09	1.729	364.1	287	24.6	12.83
4	10.55	1.488	340.1	301	40.22	15.04
5	0.5956	71.49	304.5	285.6	25.05	59.95

Appendix C

The superstructure for vertical GHE integration in the test building energy system

According to the pinch approach a superstructure can be derived that can satisfy the predicted maximum heat recovery by including all energy sources and sinks in a building. The details of the approach can be seen in [123,256]. Figure C1 shows the vertical GHEs integrated into the test building energy system. There are several abbreviations that are presented in Table C1. The temperature ranges of each stream in the test building can be seen in Table C1, as well.

In brief, the pinch analysis is based on the first and second laws of thermodynamics and the vertical heat transfer between hot and cold streams. Conventional pinch analysis and the corresponding nomenclature are available in [6]. However, the dynamic nature of the building loads such as the domestic hot water, space heating, and space cooling needs an adapted time slice model to predict the dynamic maximum heat recovery. In this way, the intermittent nature of the renewable sources such as solar energy can be addressed. The stratified thermal energy storage (TES) tanks should be integrated in dynamic systems. Therefore, TES tanks can be charged and discharged to store energy when it is more than required and deliver the stored energy when there is a need for it. The temperature ranges of the top and bottom of a stratified TES tank can be determined according to the charging source, the discharging source, and the minimum temperature difference for a viable heat transfer, 5°C in this study. The pinch analysis for derivation of the superstructure presented in Figure C1 is available in [256].

Heat exchangers are numbered from 1 to 7. There are two stratified TES tanks. The GHEs are connected to just one TES tank. During the heating months of the year, the GHEs are connected to the TES II, where the HTF enters to the GHEs at -5°C. The undisturbed ground temperature is assumed 10°C. Therefore, the configuration and the depth of the GHE should satisfy the load and the HTF outlet temperature should be above or equal to 5°C.

During the cooling months, the GHEs are connected to the TES I, where the HTF enters the GHEs at 50°C. Here it is assumed that the HTF outlet temperature can be less than or equal to 15°C.

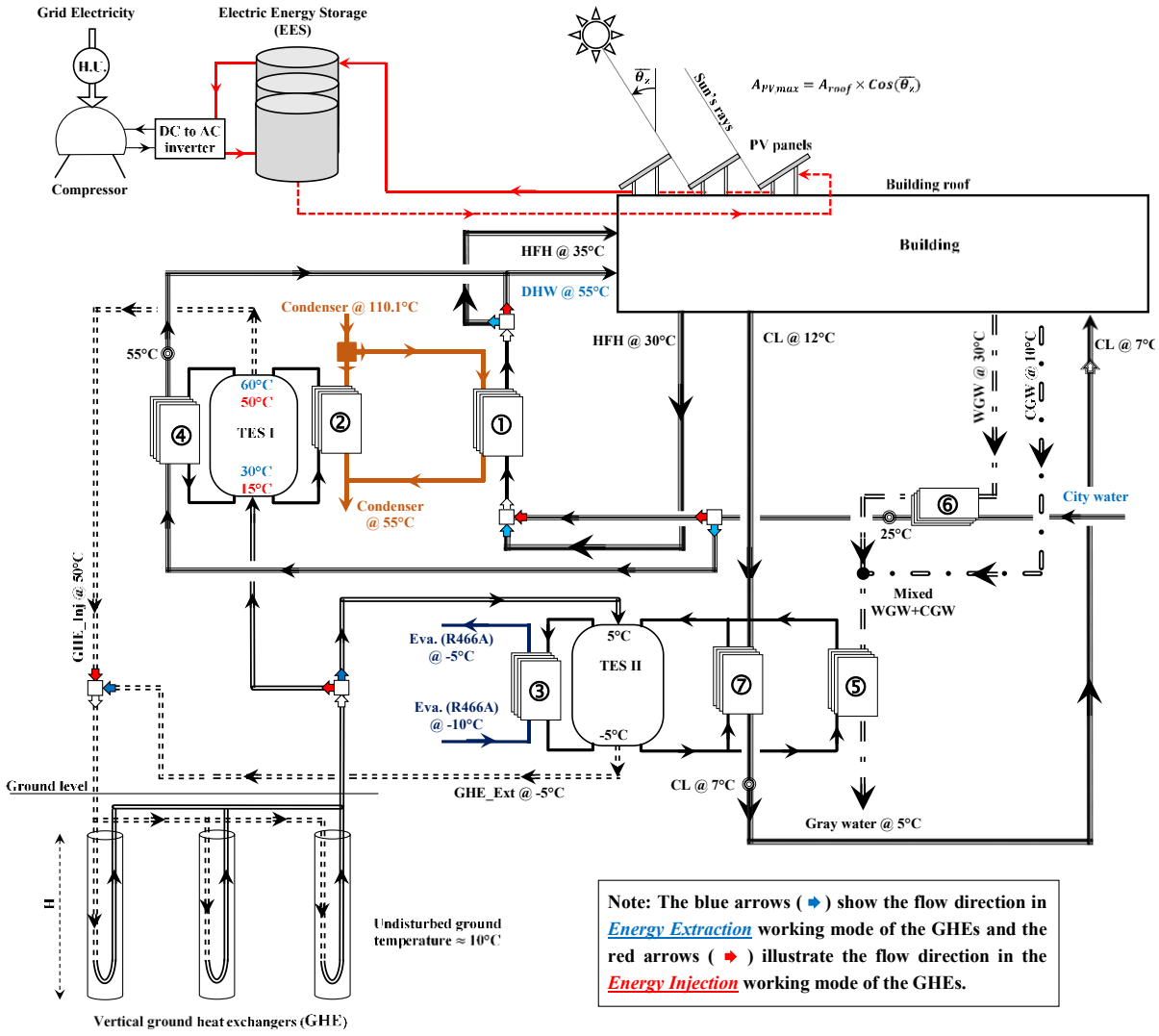

Figure C1. Superstructure of the solar assisted ground source heat pump integration into the test building energy system for both energy extraction and injection working modes [256]

Table C1. Specifications and definition of all the streams in the test building presented in Figure C1

Streams	**Hot/Cold**	**Supply (°C)**	**Target (°C)**	$\dot{m} \times c_p$ **(kW/°C)**
Hydronic Floor Heating (HFH)	C	30	35	Dynamic
Domestic Hot Water (DHW)	C	City water	55	Dynamic
Warm Gray Water (WGW)	H	30	5	Dynamic
Cold Gray Water (CGW)	H	10	5	Dynamic
Cooling Load (CL)	H	12	7	Dynamic
Condenser (Con-HP)	H	110.1	55	constant
Evaporator (Eva-HP)	C	-10	-5	constant
Ground Source in energy Extraction mode (GHE-Ext)	H	≥5	-5	constant
Ground Source in energy Injection mode (GHE-Inj)	C	≤15	50	constant

Appendix D

Water + Ethylene glycol thermophysical properties

Water + 20% (by mass) Ethylene Glycol properties as continuous functions of absolute temperature (in K) are used in this numerical study. The freezing point is -7.95°C, which is below the HTF minimum temperature of -5°C. These properties are hooked to the ANSYS FLUENT software by means of a User Defined Function (UDF). The temperature range is: $268.15\ K \leq T \leq 333.15\ K$. Units of all the properties are in SI system.

Density (kg m^{-3}) function:

$$\rho(T) = 1031 \exp\left(-\left(\frac{T - 249.3}{502.8}\right)^2\right) + 16.24 \exp\left(-\left(\frac{T - 444.7}{90.48}\right)^2\right) \quad \text{(D1)}$$

Thermal conductivity (W m^{-1} K^{-1}) function:

$$k(T) = -5.473 \exp(-0.002045T) + 5.343 \exp(-0.00143T) \quad \text{(D2)}$$

Viscosity (kg m^{-1} s^{-1}) function:

$$\mu(T) = 2973 \exp(-0.05214T) + 0.0311 \exp(-0.00118T) \quad \text{(D3)}$$

Specific heat capacity (J kg^{-1} K^{-1}) function:

$$c_P(T) = 4154 \exp\left(-\left(\frac{T - 508.3}{748.9}\right)^2\right) + 897.1 \exp\left(-\left(\frac{T + 26.33}{200.6}\right)^2\right) \quad \text{(D4)}$$

Appendix E

Four sets of two GHEs in series, computational domain, and grid design

A large computational domain is considered for solving the governing equations. Figure E1 depicts the computational domain, the mesh design, and the dimension of the computational domain. For the area of GHEs and around them, the grids are finer with the same density described earlier in section 6.4.1. The radius of the computational domain is 30 m and the depth of each GHE is 50 m, while the computational domain is 60 m, extended 10 m below the GHE. The two 90-degree sides of the computational domain are set as the periodic boundary condition to make sure the GHEs' thermal interaction are included. The grid distribution, the solving procedure, and the other numerics are exactly as described in section 6.4.3.

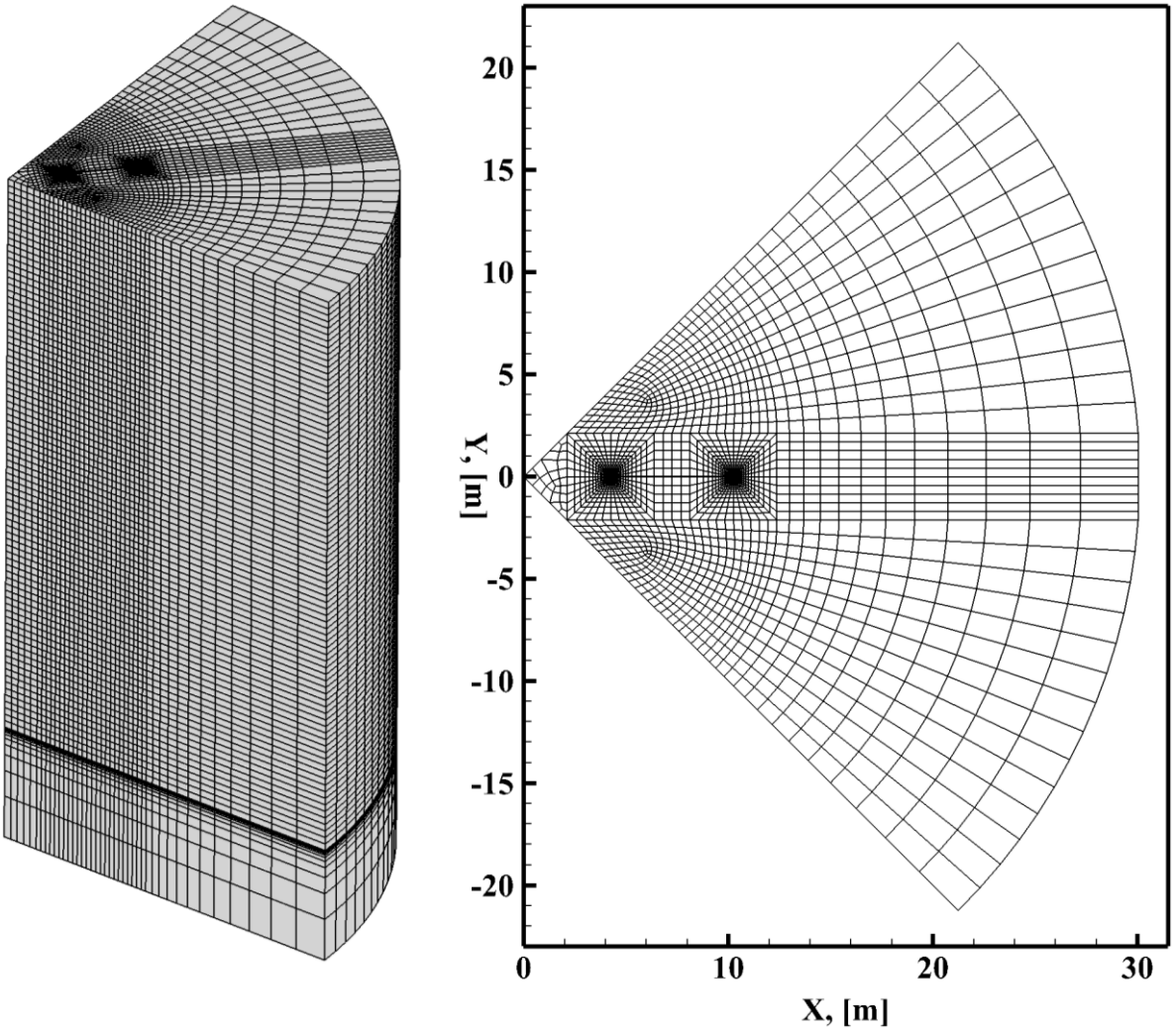

Figure E1. Computational domain and mesh design for arrangement c in Figure 6-14 (mesh details near the boreholes are similar to the one presented in Figure 6-5)

The full 20-year numerical data including the outlet temperature, required mass flowrate, and the pressure loss are presented in Figure E2. The detail or zoom-in data was shown for some selected years in Figure 6-15. As it can be seen from Figure E2, there is no steady state condition, even after 20 years. This is directly related to the imbalanced energy extraction/injection rate. The temperature data is considered as an example, the minimum temperature decreases sharply in the early years, then the reduction rate is gradually smaller after 9 years. The mass flowrate and the pressure loss follow the same pattern.

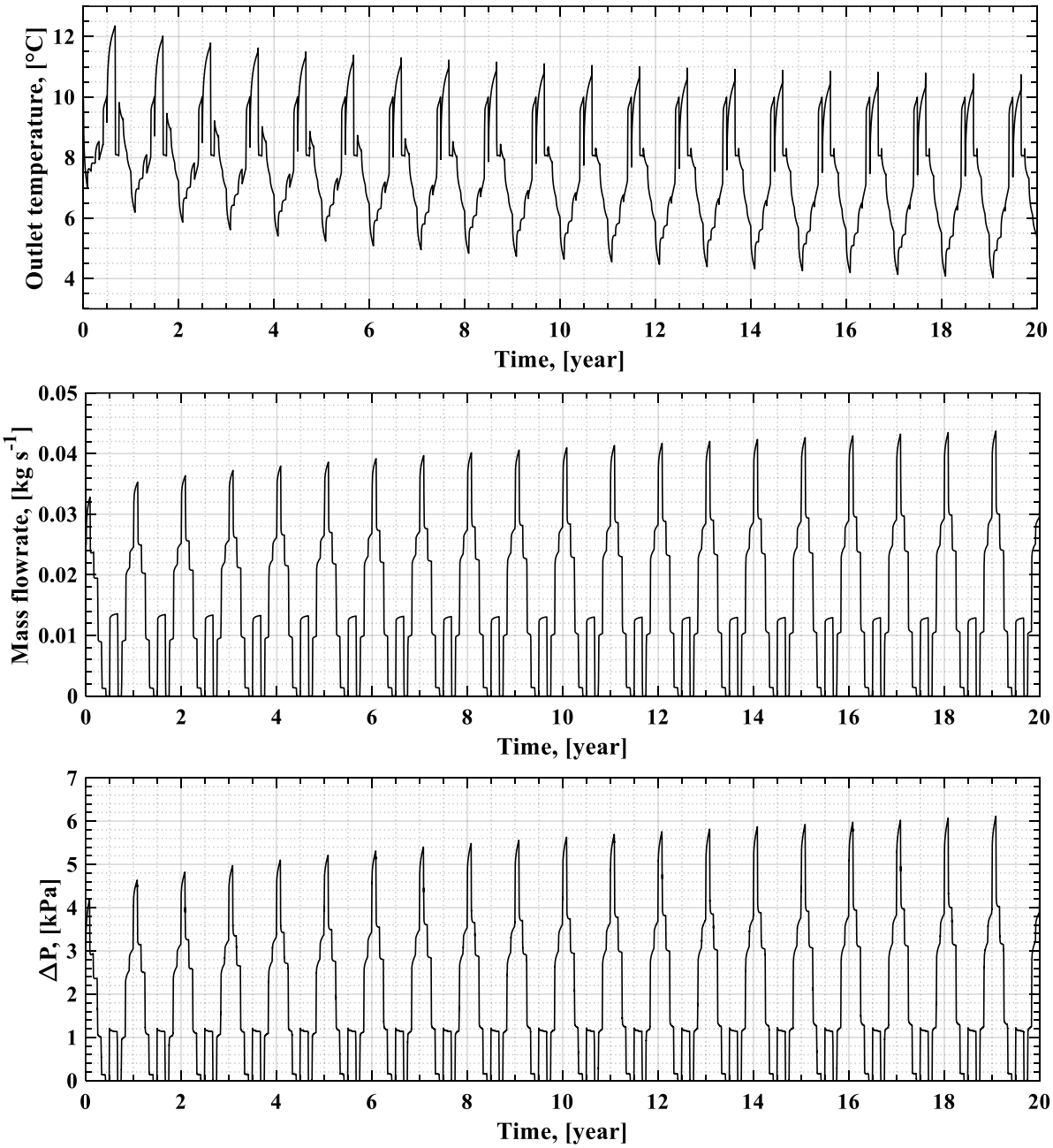

Figure E2. CFD results for full 20 years simulation for the test building

Appendix F

The results of dynamic data extraction and the energy targeting phase are briefly presented in this section. Details of the dynamic pinch approach have been published in a separate article in [231]. Moreover, the test building description and data can be found in [3,123]

The dynamic loads of the building in each representative day are presented in Figure F1. The summer load or cooling load is assumed the same for the entire summer months. The space heating system is hydronic floor heating (HFH) type.

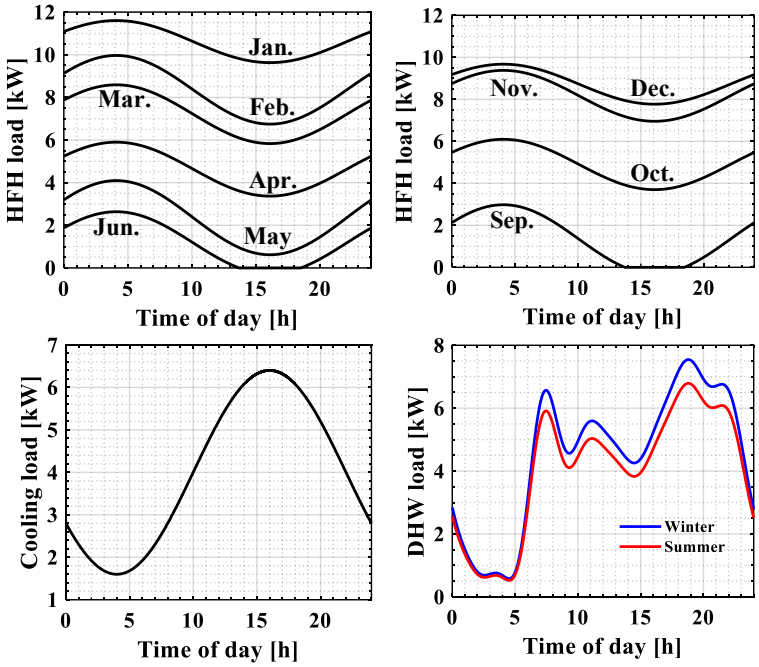

Figure F1. Dynamic loads of the test building in 12 representative days, cooling load extracted for a typical summer day

The output of the energy targeting phase (i.e., the minimum heat pump capacity, the minimum TES tank volume, the minimum PV panel area, etc.) is presented in Figure F2 to Figure F6. These values are used for economic calculations in this study.

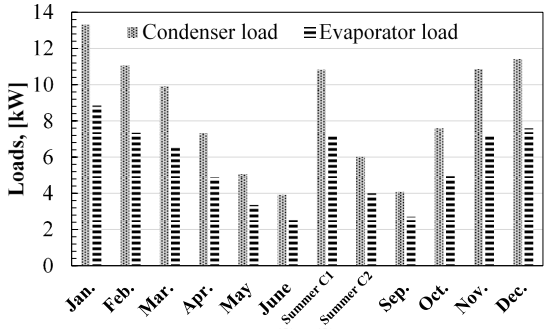

Figure F2. The minimum HP load for each DOD

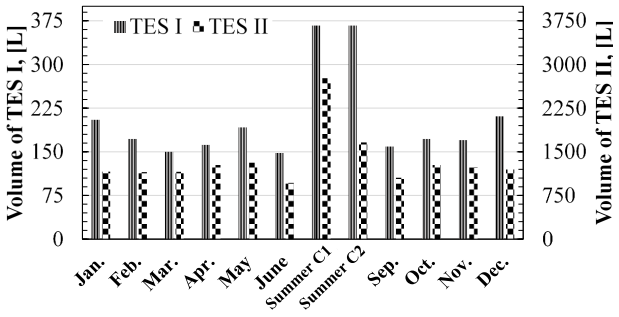

Figure F3. The minimum TES volume for each DOD

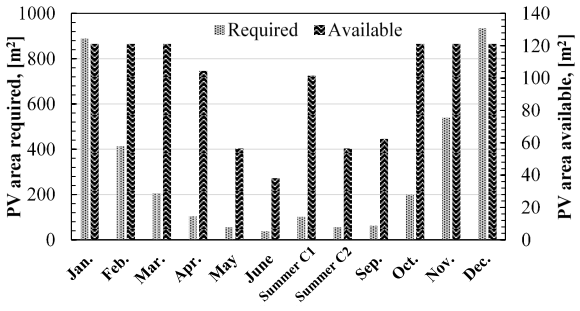

Figure F4. The minimum PV panel area for each DOD

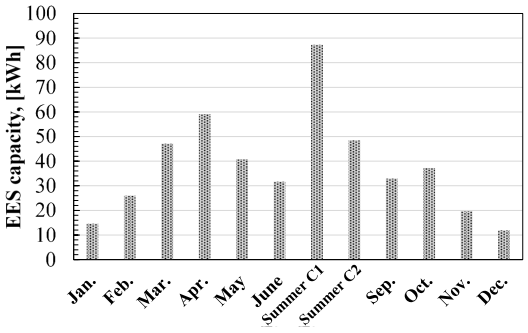

Figure F5. The minimum EES capacity for each DOD

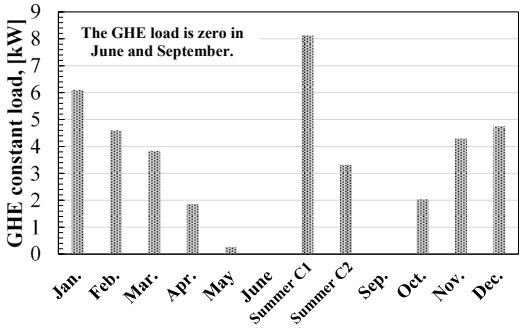

Figure F6. The minimum GHE load for each DOD

References

[1] D. D'Agostino, L. Mazzarella, What is a Nearly zero energy building? Overview, implementation and comparison of definitions, Journal of Building Engineering. 21 (2019) 200–212. https://doi.org/https://doi.org/10.1016/j.jobe.2018.10.019.

[2] M. Santamouris, Innovating to zero the building sector in Europe: Minimising the energy consumption, eradication of the energy poverty and mitigating the local climate change, Solar Energy. 128 (2016) 61–94. https://doi.org/https://doi.org/10.1016/j.solener.2016.01.021.

[3] C. Reddick, M. Sorin, J.-C. Bonhivers, D. Laperle, Waste heat and renewable energy integration in buildings, Energy and Buildings. 211 (2020). https://doi.org/10.1016/j.enbuild.2020.109803.

[4] R. Charron, A. Athienitis, Design and optimization of net zero energy solar homes, in: ASHRAE Transactions, 2006: pp. 285–295.

[5] S.J. Rees, Advances in Ground-Source Heat Pump Systems, Woodhead Publishing, 2016. https://doi.org/10.1016/C2014-0-03840-3.

[6] I. Kemp, Pinch Analysis and Process Integration, 2006. https://doi.org/10.1016/B978-0-7506-8260-2.X5001-9.

[7] I.C. Kemp, A.W. Deakin, Cascade analysis for energy and process integration of batch processes. Part 1. Calculation of energy targets, Chemical Engineering Research and Design. 67 (1989) 495–509.

[8] I.C. Kemp, A.W. Deakin, Cascade analysis for energy and process integration of batch processes. Part 2. Network design and process scheduling, Chemical Engineering Research and Design. 67 (1989) 510–516.

[9] Y.P. Wang, R. Smith, Time pinch analysis, Chemical Engineering Research and Design. 73 (1995) 905–914.

[10] J.A. Stampfli, M.J. Atkins, D.G. Olsen, B. Wellig, M.R.W. Walmsley, J.R. Neale, Industrial heat pump integration in non-continuous processes using thermal energy storages as utility - An NLP enhancement of the graphical approach, Chemical Engineering Transactions. 70 (2018) 1789–1794. https://doi.org/10.3303/CET1870299.

[11] S. Li, G. Foliente, S. Seo, B. Rismanchi, L. Aye, Multi-scale life cycle energy analysis of residential buildings in Victoria, Australia – A typology perspective, Building and Environment. 195 (2021) 107723. https://doi.org/10.1016/j.buildenv.2021.107723.

[12] Explore energy data by category, indicator, country or region, International Energy Agency. (2018) https://www.iea.org/data-and-statistics?country=WO.

[13] R. Vooradi, S.S. Mummana, Cyclic scheduling and heat integration of batch process: Design of heat storage vessels, Chemical Engineering Research and Design. 179 (2022) 130–142. https://doi.org/10.1016/j.cherd.2022.01.002.

[14] I.H. Alhajri, M.A. Gadalla, O.Y. Abdelaziz, F.H. Ashour, Retrofit of heat exchanger networks by graphical Pinch Analysis – A case study of a crude oil refinery in Kuwait, Case Studies in Thermal Engineering. 26 (2021) 101030. https://doi.org/10.1016/j.csite.2021.101030.

[15] K. Ellingwood, K. Mohammadi, K. Powell, Dynamic optimization and economic evaluation of flexible heat integration in a hybrid concentrated solar power plant, Applied Energy. 276 (2020) 115513. https://doi.org/10.1016/j.apenergy.2020.115513.

[16] S.R. Magege, T. Majozi, A comprehensive framework for synthesis and design of heat-integrated batch plants: Consideration of intermittently-available streams, Renewable and Sustainable Energy Reviews. 135 (2021) 110125. https://doi.org/10.1016/j.rser.2020.110125.

[17] C. Reddick, M. Sorin, J.-C. Bonhivers, D. Laperle, Waste heat and renewable energy integration in buildings, Energy and Buildings. 211 (2020). https://doi.org/10.1016/j.enbuild.2020.109803.

[18] A. Osama Radwan, BUILDINGS DESIGN INTEGRATION WITH GEOTHERMAL ENERGY SYSTEM TECHNOLOGIES AND AIR CONDITIONING APPLICATIONS, Journal of Art & Architecture Research Studies - JAARS. 1 (2020). https://doi.org/10.47436/jaarsfa.v1i2.80.

[19] J.J. Klemeš, P.S. Varbanov, T.G. Walmsley, X. Jia, New directions in the implementation of Pinch Methodology (PM), Renewable and Sustainable Energy Reviews. 98 (2018) 439–468. https://doi.org/https://doi.org/10.1016/j.rser.2018.09.030.

[20] S.M. Hosseinnia, M. Sorin, Energy targeting approach for optimum solar assisted ground source heat pump integration in buildings, Energy. 248 (2022) 123528. https://doi.org/10.1016/j.energy.2022.123528.

[21] I.C. Kemp, Pinch Analysis and Process Integration, Second, Elsevier, Oxford, 2007.

[22] Y. Abdelouadoud, E. Lucas, P. Krummenacher, D. Olsen, B. Wellig, Batch process heat storage integration: A simple and effective graphical approach, Energy. 185 (2019) 804–818. https://doi.org/10.1016/j.energy.2019.06.180.

[23] N.S.A. Lopez, D.C.Y. Foo, R.R. Tan, Optimizing regional electricity trading with Carbon Emissions Pinch Analysis, Energy. 237 (2021) 121544. https://doi.org/10.1016/j.energy.2021.121544.

[24] S.M. Hosseinnia, M. Sorin, A systematic pinch approach to integrate stratified thermal storage in buildings, Energy and Buildings. 232 (2021) 110663. https://doi.org/10.1016/j.enbuild.2020.110663.

[25] I.C. Kemp, A.W. Deakin, Cascade analysis for energy and process integration of batch processes. Part 2. Network design and process scheduling, Chemical Engineering Research and Design. 67 (1989) 510–516.

[26] H. Akbari, S.M. Hosseinnia, M. Sorin, C. Reddick, D. Laperle, Adapted Time Slice Model of Pinch Analysis for Direct-Indirect Heat Recovery in Buildings, Journal of Energy and Power Technology. 4 (2022) 1–1. https://doi.org/10.21926/jept.2202013.

[27] Y.P. Wang, R. Smith, Time pinch analysis, Institution of Chemical Engineers. 73, Part A (1995) 905–914.

[28] B. Wang, J.J. Klemeš, P.S. Varbanov, K. Shahzad, M.R. Kabli, Total Site Heat Integration benefiting from geothermal energy for heating and cooling implementations, Journal of Environmental Management. 290 (2021) 112596. https://doi.org/10.1016/j.jenvman.2021.112596.

[29] D. Olsen, P. Liem, Y. Abdelouadoud, B. Wellig, Thermal Energy Storage Integration Based on Pinch Analysis – Methodology and Application, Chemie-Ingenieur-Technik. 89 (2017) 598–606. https://doi.org/10.1002/cite.201600103.

[30] M.A. Paya-Marin, K. Roy, J.-F. Chen, R. Masood, R.M. Lawson, B. Sen Gupta, J.B.P. Lim, Large-scale experiment of a novel non-domestic building using BPSC systems for energy saving, Renewable Energy. 152 (2020) 799–811. https://doi.org/10.1016/j.renene.2020.01.100.

[31] I. Kemp, Pinch Analysis and Process Integration, 2006. https://doi.org/10.1016/B978-0-7506-8260-2.X5001-9.

[32] P. Krummenacher, D. Favrat, Indirect and Mixed Direct-Indirect Heat Integration of Batch Processes Based on Pinch Analysis, International Journal of Applied Thermodynamics. 4 (2001) 135–143.

[33] I.C. Kemp, A.W. Deakin, Cascade analysis for energy and process integration of batch processes. Part 1. Calculation of energy targets, Chemical Engineering Research and Design. 67 (1989) 495–509.

[34] N.D. Chaturvedi, Z.A. Manan, Batch process integration for resource conservation toward cleaner production – A state-of-the-art review, Journal of Cleaner Production. 318 (2021) 128609. https://doi.org/10.1016/j.jclepro.2021.128609.

[35] L. V. Pavão, J.A. Caballero, M.A.S.S. Ravagnani, C.B.B. Costa, A pinch-based method for defining pressure manipulation routes in work and heat exchange networks, Renewable and Sustainable Energy Reviews. 131 (2020) 109989. https://doi.org/10.1016/j.rser.2020.109989.

[36] M.H. Monajati Saharkhiz, B. Ghorbani, A. Ebrahimi, S. Rooholamini, Exergy, economic and pinch analyses of a novel integrated structure for cryogenic energy storage and freshwater production using ejector refrigeration cycle, desalination unit, and natural gas combustion plant, Journal of Energy Storage. 44 (2021) 103471. https://doi.org/10.1016/j.est.2021.103471.

[37] M.J.S. Zuberi, D. Olsen, P. Liem, B. Wellig, M.K. Patel, Heat integration of a multi-product batch process by means of direct and indirect heat recovery using thermal energy storage, Applied Thermal Engineering. 167 (2020) 114796. https://doi.org/10.1016/j.applthermaleng.2019.114796.

[38] M.Z. Pomianowski, H. Johra, A. Marszal-Pomianowska, C. Zhang, Sustainable and energy-efficient domestic hot water systems: A review, Renewable and Sustainable Energy Reviews. 128 (2020) 109900. https://doi.org/https://doi.org/10.1016/j.rser.2020.109900.

[39] C.A. Cruickshank, S.J. Harrison, Heat loss characteristics for a typical solar domestic hot water storage, Energy and Buildings. 42 (2010) 1703–1710. https://doi.org/https://doi.org/10.1016/j.enbuild.2010.04.013.

[40] B. Wang, L.D. Cot, L. Adolphe, S. Geoffroy, J. Morchain, Estimation of wind energy over roof of two perpendicular buildings, Energy and Buildings. 88 (2015) 57–67. https://doi.org/https://doi.org/10.1016/j.enbuild.2014.11.072.

[41] M. Esen, Thermal performance of a solar-aided latent heat store used for space heating by heat pump, Solar Energy. 69 (2000) 15–25. https://doi.org/https://doi.org/10.1016/S0038-092X(00)00015-3.

[42] A. Nguyen, Determination of the ground source heat pump system capacity that ensures the longevity of a specified ground heat exchanger field, Renewable Energy. 169 (2021) 799–808. https://doi.org/https://doi.org/10.1016/j.renene.2021.01.035.

[43] R. Manouchehri, M.R. Collins, An experimental analysis of the impact of temperature on falling film drain water heat recovery system effectiveness, Energy and Buildings. 130 (2016) 1–7. https://doi.org/https://doi.org/10.1016/j.enbuild.2016.08.031.

[44] R. Manouchehri, M.R. Collins, An experimental analysis of the impact of temperature on falling film drain water heat recovery system effectiveness, Energy and Buildings. 130 (2016) 1–7. https://doi.org/https://doi.org/10.1016/j.enbuild.2016.08.031.

[45] I. Beentjes, R. Manouchehri, M.R. Collins, An investigation of drain-side wetting on the performance of falling film drain water heat recovery systems, Energy and Buildings. 82 (2014) 660–667. https://doi.org/https://doi.org/10.1016/j.enbuild.2014.07.069.

[46] Y. Chen, H. Hua, J. Wang, P.D. Lund, Integrated performance analysis of a space heating system assisted by photovoltaic/thermal collectors and ground source heat pump for hotel and office building types, Renewable Energy. 169 (2021) 925–934. https://doi.org/https://doi.org/10.1016/j.renene.2020.12.117.

[47] A.R. Mazhar, S. Liu, A. Shukla, A Key Review of Non-Industrial Greywater Heat Harnessing, Energies . 11 (2018). https://doi.org/10.3390/en11020386.

[48] H. Weeratunge, G.R. Aditya, S. Dunstall, J. de Hoog, G. Narsilio, S. Halgamuge, Feasibility and performance analysis of hybrid ground source heat pump systems in fourteen cities, Energy. 234 (2021). https://doi.org/10.1016/j.energy.2021.121254.

[49] M.C. Rodríguez-Hidalgo, P.A. Rodríguez-Aumente, A. Lecuona, M. Legrand, R. Ventas, Domestic hot water consumption vs. solar thermal energy storage: The optimum size of the storage tank, Applied Energy. 97 (2012) 897–906. https://doi.org/https://doi.org/10.1016/j.apenergy.2011.12.088.

[50] P.C. Eames, B. Norton, The effect of tank geometry on thermally stratified sensible heat storage subject to low Reynolds number flows, International Journal of Heat and Mass Transfer. 41 (1998) 2131–2142. https://doi.org/https://doi.org/10.1016/S0017-9310(97)00349-9.

[51] R. Liberatore, M. Falchetta, W. Gaggioli, D. Mazzei, V. Russo, Power production of an ORC system using a stratified molten salt as thermal energy storage integrated in a CSP plant, AIP Conference Proceedings. 2126 (2019) 140003. https://doi.org/10.1063/1.5117651.

[52] G. Wang, S. Yu, S. Niu, Z. Chen, P. Hu, A comprehensive parametric study on integrated thermal and mechanical performances of molten-salt-based thermocline tank, Applied Thermal Engineering. 170 (2020). https://doi.org/10.1016/j.applthermaleng.2020.115010.

[53] W. Shaikh, A. Wadegaonkar, S.B. Kedare, M. Bose, Numerical simulation of single media thermocline based storage system, Solar Energy. 174 (2018) 207–217. https://doi.org/https://doi.org/10.1016/j.solener.2018.08.084.

[54] R. Bayón, E. Rojas, Simulation of thermocline storage for solar thermal power plants: From dimensionless results to prototypes and real-size tanks, International Journal of Heat and Mass Transfer. 60 (2013) 713–721. https://doi.org/https://doi.org/10.1016/j.ijheatmasstransfer.2013.01.047.

[55] D. Olsen, P. Liem, Y. Abdelouadoud, B. Wellig, Thermal Energy Storage Integration Based on Pinch Analysis – Methodology and Application, Chemie Ingenieur Technik. 89 (2017) 598–606. https://doi.org/10.1002/cite.201600103.

[56] M.J.S. Zuberi, D. Olsen, P. Liem, B. Wellig, M.K. Patel, Heat integration of a multi-product batch process by means of direct and indirect heat recovery using thermal energy storage, Applied Thermal Engineering. 167 (2020) 114796. https://doi.org/https://doi.org/10.1016/j.applthermaleng.2019.114796.

[57] Y.P. Chandra, T. Matuska, Stratification analysis of domestic hot water storage tanks: A comprehensive review, Energy and Buildings. 187 (2019) 110–131. https://doi.org/10.1016/j.enbuild.2019.01.052.

[58] Y. Bai, Z. Wang, J. Fan, M. Yang, X. Li, L. Chen, G. Yuan, J. Yang, Numerical and experimental study of an underground water pit for seasonal heat storage, Renewable Energy. 150 (2020) 487–508. https://doi.org/https://doi.org/10.1016/j.renene.2019.12.080.

[59] D.L. Savicki, H.A. Vielmo, A. Krenzinger, Three-dimensional analysis and investigation of the thermal and hydrodynamic behaviors of cylindrical storage tanks, Renewable Energy. 36 (2011) 1364–1373. https://doi.org/https://doi.org/10.1016/j.renene.2010.10.011.

[60] O. Abdelhak, H. Mhiri, P. Bournot, CFD analysis of thermal stratification in domestic hot water storage tank during dynamic mode, Building Simulation. 8 (2015) 421–429. https://doi.org/10.1007/s12273-015-0216-9.

[61] Y.P. Chandra, T. Matuska, Numerical prediction of the stratification performance in domestic hot water storage tanks, Renewable Energy. 154 (2020) 1165–1179. https://doi.org/10.1016/j.renene.2020.03.090.

[62] A. Mawire, M. McPherson, A feedforward IMC structure for controlling the charging temperature of a TES system of a solar cooker, Energy Conversion and Management. 49 (2008) 3143–3154. https://doi.org/10.1016/j.enconman.2008.06.010.

[63] A. Mawire, S.H. Taole, R.R.J. Van Den Heetkamp, Experimental investigation on simultaneous charging and discharging of an oil storage tank, Energy Conversion and Management. 65 (2013) 245–254. https://doi.org/10.1016/j.enconman.2012.08.011.

[64] K. Wally, G.H. Abernathy, ENERGY STORAGE USING HEAT TRANSFER OIL., Paper - American Society of Agricultural Engineers. (1978).

[65] A.H. Slocum, D.S. Codd, J. Buongiorno, C. Forsberg, T. McKrell, J.-C. Nave, C.N. Papanicolas, A. Ghobeity, C.J. Noone, S. Passerini, F. Rojas, A. Mitsos, Concentrated solar power on demand, Solar Energy. 85 (2011) 1519–1529. https://doi.org/10.1016/j.solener.2011.04.010.

[66] S. Ushak, A.G. Fernández, M. Grageda, 3 - Using molten salts and other liquid sensible storage media in thermal energy storage (TES) systems, in: L.F.B.T.-A. in T.E.S.S. Cabeza (Ed.), Woodhead Publishing Series in Energy, Woodhead Publishing, 2015: pp. 49–63. https://doi.org/https://doi.org/10.1533/9781782420965.1.49.

[67] S. Hatte, C. Mira-Hernández, S. Advaith, A. Tinaikar, U.K. Chetia, K. V Manu, K. Chattopadhyay, J.A. Weibel, S. V Garimella, V. Srinivasan, S. Basu, Short and long-term sensitivity of lab-scale thermocline based thermal storage to flow disturbances, Applied Thermal Engineering. 109 (2016) 936–948. https://doi.org/10.1016/j.applthermaleng.2016.04.138.

[68] D. Ürge-Vorsatz, L.F. Cabeza, S. Serrano, C. Barreneche, K. Petrichenko, Heating and cooling energy trends and drivers in buildings, Renewable and Sustainable Energy Reviews. 41 (2015) 85–98. https://doi.org/https://doi.org/10.1016/j.rser.2014.08.039.

[69] M. Esen, T. Yuksel, Experimental evaluation of using various renewable energy sources for heating a greenhouse, Energy and Buildings. 65 (2013) 340–351. https://doi.org/https://doi.org/10.1016/j.enbuild.2013.06.018.

[70] L. Zeng, G. Li, M. Li, Z. Feng, L. Yang, X. Luo, Design and experimental performance of an off-grid ice storage system driven by distributed wind energy, Energy and

Buildings. 224 (2020) 110252. https://doi.org/https://doi.org/10.1016/j.enbuild.2020.110252.

[71] E. Cetin, A. Yilanci, H.K. Ozturk, M. Colak, I. Kasikci, S. Iplikci, A micro-DC power distribution system for a residential application energized by photovoltaic–wind/fuel cell hybrid energy systems, Energy and Buildings. 42 (2010) 1344–1352. https://doi.org/https://doi.org/10.1016/j.enbuild.2010.03.003.

[72] C.R. Galantino, S. Beyers, C. Lindsay Anderson, J.W. Tester, Optimizing Cornell's future geothermal district heating performance through systems engineering and simulation, Energy and Buildings. 230 (2021) 110529. https://doi.org/https://doi.org/10.1016/j.enbuild.2020.110529.

[73] G. Bode, J. Fütterer, D. Müller, Mode and storage load based control of a complex building system with a geothermal field, Energy and Buildings. 158 (2018) 1337–1345. https://doi.org/https://doi.org/10.1016/j.enbuild.2017.11.026.

[74] E. Saloux, J.A. Candanedo, Modelling stratified thermal energy storage tanks using an advanced flowrate distribution of the received flow, Applied Energy. 241 (2019) 34–45. https://doi.org/https://doi.org/10.1016/j.apenergy.2019.02.075.

[75] H.J. Quintana, M. Kummert, Optimized control strategies for solar district heating systems, Journal of Building Performance Simulation. 8 (2015) 79–96. https://doi.org/10.1080/19401493.2013.876448.

[76] J.D. Kumana, Pinch Analysis for Process Energy Optimization, Energy Engineering. 99 (2002) 18–41. https://doi.org/10.1080/01998590209508900.

[77] J.J. Klemeš, Z. Kravanja, Forty years of Heat Integration: Pinch Analysis (PA) and Mathematical Programming (MP), Current Opinion in Chemical Engineering. 2 (2013) 461–474. https://doi.org/https://doi.org/10.1016/j.coche.2013.10.003.

[78] Y. Abdelouadoud, E. Lucas, P. Krummenacher, D. Olsen, B. Wellig, Batch process heat storage integration: A simple and effective graphical approach, Energy. 185 (2019) 804–818. https://doi.org/https://doi.org/10.1016/j.energy.2019.06.180.

[79] P. Krummenacher, D. Favrat, Indirect and Mixed Direct-Indirect Heat Integration of Batch Processes Based on Pinch Analysis, International Journal of Applied Thermodynamics. 4 (n.d.) 135–143.

[80] S. Stoltze, B. Lorentzen, P.M. Petersen, B. Qvale, A Simple Technique for Analyzing Waste-Heat Recovery with Heat-Storage in Batch Processes BT - Energy Efficiency in

Process Technology, in: P.A. Pilavachi (Ed.), Springer Netherlands, Dordrecht, 1993: pp. 1063–1072. https://doi.org/10.1007/978-94-011-1454-7_94.

[81] T. Majozi, Minimization of energy use in multipurpose batch plants using heat storage: an aspect of cleaner production, Journal of Cleaner Production. 17 (2009) 945–950. https://doi.org/https://doi.org/10.1016/j.jclepro.2009.02.013.

[82] A. Beck, R. Hofmann, A sequential approach for integration of multiple thermal energy storages with fixed mass and variable temperature, Applied Thermal Engineering. 148 (2019) 278–294. https://doi.org/https://doi.org/10.1016/j.applthermaleng.2018.11.039.

[83] N.P. Basán, M.E. Cóccola, A. García del Valle, C.A. Méndez, Scheduling of flexible manufacturing plants with redesign options: A MILP-based decomposition algorithm and case studies, Computers & Chemical Engineering. 136 (2020) 106777. https://doi.org/https://doi.org/10.1016/j.compchemeng.2020.106777.

[84] N.D. Chaturvedi, S. Bandyopadhyay, Indirect thermal integration for batch processes, Applied Thermal Engineering. 62 (2014) 229–238. https://doi.org/https://doi.org/10.1016/j.applthermaleng.2013.09.042.

[85] A. Anastasovski, Design of Heat Storage Units for use in repeatable Time Slices, Applied Thermal Engineering. 112 (2017) 1590–1600. https://doi.org/https://doi.org/10.1016/j.applthermaleng.2016.10.086.

[86] J.-Y. Lee, D.C.Y. Foo, Simultaneous Targeting and Scheduling for Batch Water Networks, Industrial and Engineering Chemistry Research. 56 (2017) 1559–1569. https://doi.org/10.1021/acs.iecr.6b03714.

[87] N.D. Chaturvedi, S. Bandyopadhyay, Targeting for multiple resources in batch processes, Chemical Engineering Science. 104 (2013) 1081–1089. https://doi.org/10.1016/j.ces.2013.10.018.

[88] S. Stoltze, J. Mikkelsen, B. Lorentzen, P.M. Petersen, B. Qvale, Waste-heat recovery in batch processes using heat storage, Journal of Energy Resources Technology, Transactions of the ASME. 117 (1995) 142–149. https://doi.org/10.1115/1.2835330.

[89] C.K.L. Sing, J.S. Lim, T.G. Walmsley, P.Y. Liew, M. Goto, S.A.Z.B.S. Salim, Time-Dependent Integration of Solar Thermal Technology in Industrial Processes, Sustainability. 12 (2020) 2322. https://doi.org/10.3390/su12062322.

[90] N. Sebelebele, T. Majozi, Heat integration of multipurpose batch plants through multiple heat storage vessels, Computers & Chemical Engineering. 106 (2017) 269–285. https://doi.org/https://doi.org/10.1016/j.compchemeng.2017.06.007.

[91] I. Fernández, C.J. Renedo, S.F. Pérez, A. Ortiz, M. Mañana, A review: Energy recovery in batch processes, Renewable and Sustainable Energy Reviews. 16 (2012) 2260–2277. https://doi.org/https://doi.org/10.1016/j.rser.2012.01.017.

[92] A. Nemet, J.J. Klemes, Optimising the Temperature of Heat Storage to Serve Processes with Varying Supply and Demand - Captured Solar Energy Curve, Chemical Engineering Transactions. 25 (2011) 605-610 SE-Research Articles. https://doi.org/10.3303/CET1125101.

[93] T.G. Walmsley, M.R.W. Walmsley, A.H. Tarighaleslami, M.J. Atkins, J.R. Neale, Integration options for solar thermal with low temperature industrial heat recovery loops, Energy. 90 (2015) 113–121. https://doi.org/https://doi.org/10.1016/j.energy.2015.05.080.

[94] T.G. Walmsley, M.R.W. Walmsley, M.J. Atkins, J.R. Neale, Integration of industrial solar and gaseous waste heat into heat recovery loops using constant and variable temperature storage, Energy. 75 (2014) 53–67. https://doi.org/https://doi.org/10.1016/j.energy.2014.01.103.

[95] M.J. Atkins, M.R.W. Walmsley, A.S. Morrison, Integration of solar thermal for improved energy efficiency in low-temperature-pinch industrial processes, Energy. 35 (2010) 1867–1873. https://doi.org/https://doi.org/10.1016/j.energy.2009.06.039.

[96] B. Muster-Slawitsch, C. Brunner, R. Padinger, H. Schnitzer, Methodology for Batch Heat Integration and Storage System Design for Ideal Integration of Solar Process Heat, Chemical Engineering Transactions. 25 (2011) 887-892 SE-Research Articles. https://doi.org/10.3303/CET1125148.

[97] T. Eiholzer, D. Olsen, S. Hoffmann, B. Sturm, B. Wellig, Integration of a solar thermal system in a medium-sized brewery using pinch analysis: Methodology and case study, Applied Thermal Engineering. 113 (2017) 1558–1568. https://doi.org/https://doi.org/10.1016/j.applthermaleng.2016.09.124.

[98] J.-Y. Lee, E.R. Seid, T. Majozi, Heat integration of intermittently available continuous streams in multipurpose batch plants, Computers & Chemical Engineering. 74 (2015) 100–114. https://doi.org/https://doi.org/10.1016/j.compchemeng.2014.12.003.

[99] V. Misevičiūtė, V. Motuzienė, K. Valančius, The application of the Pinch method for the analysis of the heat exchangers network in a ventilation system of a building, Applied Thermal Engineering. 129 (2018) 772–781. https://doi.org/https://doi.org/10.1016/j.applthermaleng.2017.10.051.

[100] A. Herrera, J. Islas, A. Arriola, Pinch technology application in a hospital, Applied Thermal Engineering. 23 (2003) 127–139. https://doi.org/https://doi.org/10.1016/S1359-4311(02)00157-6.

[101] S. Fantucci, A. Lorenzati, G. Kazas, D. Levchenko, G. Serale, Thermal Energy Storage with Super Insulating Materials: A Parametrical Analysis, Energy Procedia. 78 (2015) 441–446. https://doi.org/https://doi.org/10.1016/j.egypro.2015.11.691.

[102] Y.H. Zurigat, P.R. Liche, A.J. Ghajar, Influence of inlet geometry on mixing in thermocline thermal energy storage, International Journal of Heat and Mass Transfer. 34 (1991) 115–125. https://doi.org/https://doi.org/10.1016/0017-9310(91)90179-I.

[103] J. Lago, F. De Ridder, W. Mazairac, B. De Schutter, A 1-dimensional continuous and smooth model for thermally stratified storage tanks including mixing and buoyancy, Applied Energy. 248 (2019) 640–655. https://doi.org/https://doi.org/10.1016/j.apenergy.2019.04.139.

[104] O. Achkari, A. El Fadar, Latest developments on TES and CSP technologies – Energy and environmental issues, applications and research trends, Applied Thermal Engineering. 167 (2020) 114806. https://doi.org/https://doi.org/10.1016/j.applthermaleng.2019.114806.

[105] L. Kocijel, V. Mrzljak, V. Glažar, Numerical analysis of geometrical and process parameters influence on temperature stratification in a large volumetric heat storage tank, Energy. 194 (2020) 116878. https://doi.org/https://doi.org/10.1016/j.energy.2019.116878.

[106] L. Kocijel, V. Mrzljak, V. Glažar, Pressure drop in large volumetric heat storage tank radial plate diffuser, Journal of Energy Storage. 29 (2020) 101350. https://doi.org/https://doi.org/10.1016/j.est.2020.101350.

[107] A. Araújo, R. Silva, Energy modeling of solar water heating systems with on-off control and thermally stratified storage using a fast computation algorithm, Renewable Energy. 150 (2020) 891–906. https://doi.org/10.1016/j.renene.2020.01.026.

[108] E.A. Piana, B. Grassi, L. Socal, A Standard-based method to simulate the behavior of thermal solar systems with a stratified storage tank, Energies (Basel). 13 (2020). https://doi.org/10.3390/en13010266.

[109] M.Y. Haller, R. Haberl, A. Reber, Stratification efficiency of thermal energy storage systems – A new KPI based on dynamic hardware in the loop testing - Part II: Test results, Energy and Buildings. 202 (2019). https://doi.org/10.1016/j.enbuild.2019.109366.

[110] R.J. Sunley, C.J. Atkinson, H.G. Jones, Chill unit models and recent changes in the occurrence of Winter chill and Spring frost in the United Kingdom, The Journal of Horticultural Science and Biotechnology. 81 (2006) 949–958. https://doi.org/10.1080/14620316.2006.11512181.

[111] Canadian Environment and national Resources, Hourly climate data, (n.d.). https://climate.weather.gc.ca/climate_data/hourly_data_e.html (accessed March 25, 2020).

[112] F.S. Goldner, DHW system sizing criteria for multifamily buildings, in: ASHRAE Transactions, 1994: pp. 963–977.

[113] T. Sung, S.Y. Yoon, K.C. Kim, A mathematical model of hourly solar radiation in varying weather conditions for a dynamic simulation of the solar organic rankine cycle, Energies (Basel). 8 (2015) 7058–7069. https://doi.org/10.3390/en8077058.

[114] National Research Council Canada, (n.d.). https://www.nrc-cnrc.gc.ca/eng/services/sunrise/advanced.html (accessed March 25, 2020).

[115] E. Kaloudis, D.G.E. Grigoriadis, E. Papanicolaou, T. Panidis, Large eddy simulation of thermocline flow phenomena and mixing during discharging of an initially homogeneous or stratified storage tank, European Journal of Mechanics - B/Fluids. 48 (2014) 94–114. https://doi.org/https://doi.org/10.1016/j.euromechflu.2014.04.012.

[116] E. Kaloudis, D.G.E. Grigoriadis, E. Papanicolaou, Numerical simulations of constant-influx gravity currents in confined spaces: Application to thermal storage tanks, International Journal of Thermal Sciences. 108 (2016) 1–16. https://doi.org/https://doi.org/10.1016/j.ijthermalsci.2016.04.018.

[117] A.M. Bonanos, E. V Votyakov, Sensitivity analysis for thermocline thermal storage tank design, Renewable Energy. 99 (2016) 764–771. https://doi.org/https://doi.org/10.1016/j.renene.2016.07.052.

[118] S.E.-D. Fertahi, A. Jamil, A. Benbassou, Review on Solar Thermal Stratified Storage Tanks (STSST): Insight on stratification studies and efficiency indicators, Solar Energy. 176 (2018) 126–145. https://doi.org/10.1016/j.solener.2018.10.028.

[119] M. Dehghan, On the numerical solution of the one-dimensional convection-diffusion equation, Mathematical Problems in Engineering. 2005 (2005) 61–74. https://doi.org/10.1155/MPE.2005.61.

[120] R. De Césaro Oliveski, A. Krenzinger, H.A. Vielmo, Comparison between models for the simulation of hot water storage tanks, Solar Energy. 75 (2003) 121–134. https://doi.org/https://doi.org/10.1016/j.solener.2003.07.009.

[121] H. Yoo, E.-T. Pak, Theoretical model of the charging process for stratified thermal storage tanks, Solar Energy. 51 (1993) 513–519. https://doi.org/https://doi.org/10.1016/0038-092X(93)90136-C.

[122] A.S. Kim, Complete analytic solutions for convection-diffusion-reaction-source equations without using an inverse Laplace transform, Scientific Reports. 10 (2020) 8040. https://doi.org/10.1038/s41598-020-63982-w.

[123] S.M. Hosseinnia, M. Sorin, A systematic pinch approach to integrate stratified thermal energy storage in buildings, Energy and Buildings. 232 (2021) 110663. https://doi.org/https://doi.org/10.1016/j.enbuild.2020.110663.

[124] J. Lago, F. De Ridder, W. Mazairac, B. De Schutter, A 1-dimensional continuous and smooth model for thermally stratified storage tanks including mixing and buoyancy, Applied Energy. 248 (2019) 640–655. https://doi.org/https://doi.org/10.1016/j.apenergy.2019.04.139.

[125] R. Bayón, E. Rojas, Simulation of thermocline storage for solar thermal power plants: From dimensionless results to prototypes and real-size tanks, International Journal of Heat and Mass Transfer. 60 (2013) 713–721. https://doi.org/https://doi.org/10.1016/j.ijheatmasstransfer.2013.01.047.

[126] Y.H. Zurigat, P.R. Liche, A.J. Ghajar, Influence of inlet geometry on mixing in thermocline thermal energy storage, International Journal of Heat and Mass Transfer. 34 (1991) 115–125. https://doi.org/https://doi.org/10.1016/0017-9310(91)90179-I.

[127] N. Cadau, A. de Lorenzi, A. Gambarotta, M. Morini, M. Rossi, Development and analysis of a multi-node dynamic model for the simulation of stratified thermal energy storage, Energies (Basel). 12 (2019). https://doi.org/10.3390/en12224275.

[128] J. van Berkel, C.C.M. Rindt, A.A. van Steenhoven, Thermocline dynamics in a thermally stratified store, International Journal of Heat and Mass Transfer. 45 (2002) 343–356. https://doi.org/https://doi.org/10.1016/S0017-9310(01)00161-2.

[129] J. Fan, S. Furbo, Thermal stratification in a hot water tank established by heat loss from the tank, Solar Energy. 86 (2012) 3460–3469. https://doi.org/https://doi.org/10.1016/j.solener.2012.07.026.

[130] M.-S. Shin, H.-S. Kim, D.-S. Jang, S.-N. Lee, Y.-S. Lee, H.-G. Yoon, Numerical and experimental study on the design of a stratified thermal storage system, Applied Thermal Engineering. 24 (2004) 17–27. https://doi.org/https://doi.org/10.1016/S1359-4311(03)00242-4.

[131] M.F. El-AMIN, S. SUN, A. SALAM, Simulation of buoyancy-induced turbulent flow from a hot horizontal jet, Journal of Hydrodynamics, Ser. B. 26 (2014) 104–113. https://doi.org/https://doi.org/10.1016/S1001-6058(14)60012-3.

[132] I.J. Moncho-Esteve, M. Gasque, P. González-Altozano, G. Palau-Salvador, Simple inlet devices and their influence on thermal stratification in a hot water storage tank, Energy and Buildings. 150 (2017) 625–638. https://doi.org/https://doi.org/10.1016/j.enbuild.2017.06.012.

[133] A. Al-Maraffie, A. Al-Kandari, N. Ghaddar, Diffuser design influence on the performance of solar thermal storage tanks, International Journal of Energy Research. 15 (1991) 525–534. https://doi.org/https://doi.org/10.1002/er.4440150702.

[134] J.D. Chung, S.H. Cho, C.S. Tae, H. Yoo, The effect of diffuser configuration on thermal stratification in a rectangular storage tank, Renewable Energy. 33 (2008) 2236–2245. https://doi.org/https://doi.org/10.1016/j.renene.2007.12.013.

[135] F. Findeisen, T. Urbaneck, B. Platzer, Radial diffusers in stratified hot water stores: Ecomtry optimization with CFD, in: ISES Solar World Congress 2017 - IEA SHC International Conference on Solar Heating and Cooling for Buildings and Industry 2017, Proceedings, 2017: pp. 726–734. https://doi.org/10.18086/swc.2017.13.04.

[136] R. Laskowski, The black box model of a double-tube counter-flow heat exchanger, Heat and Mass Transfer. 51 (2015) 1111–1119. https://doi.org/10.1007/s00231-014-1482-2.

[137] M. Bobič, B. Gjerek, I. Golobič, I. Bajsić, Dynamic behaviour of a plate heat exchanger: Influence of temperature disturbances and flow configurations, International Journal of Heat and Mass Transfer. 163 (2020) 120439. https://doi.org/https://doi.org/10.1016/j.ijheatmasstransfer.2020.120439.

[138] A. Kay, Warm discharges in cold fresh water. Part 1. Line plumes in a uniform ambient, Journal of Fluid Mechanics. 574 (2007) 239–271. https://doi.org/10.1017/S0022112006004101.

[139] I. ANSYS, ANSYS fluent user's guide, release 19.1, ANSYS Inc, Canonsburg. (2018).

[140] ANSYS Inc., ANSYS Fluent Theory Guide, ANSYS Inc., USA. 15317 (2013).

[141] D.C. Wilcox, Turbulence modeling for CFD, DCW industries La Canada, CA, 1998.

[142] H. Khurana, S. Tiwari, R. Majumdar, S.K. Saha, Comparative Evaluation of Circular Truncated-Cone and Paraboloid Shapes for Thermal Energy Storage Tank based on Thermal Stratification Performance, Journal of Energy Storage. 34 (2021) 102191. https://doi.org/https://doi.org/10.1016/j.est.2020.102191.

[143] S. V. Patankar, Numerical heat transfer and fluid flow., Taylor & Francis, 1980. https://doi.org/10.13182/nse81-a20112.

[144] Z. Lavan, J. Thompson, Experimental study of thermally stratified hot water storage tanks, Solar Energy. 19 (1977) 519–524. https://doi.org/https://doi.org/10.1016/0038-092X(77)90108-6.

[145] E. Osterman, U. Stritih, Review on compression heat pump systems with thermal energy storage for heating and cooling of buildings, Journal of Energy Storage. 39 (2021) 102569. https://doi.org/https://doi.org/10.1016/j.est.2021.102569.

[146] N. Sommerfeldt, H. Madani, In-depth techno-economic analysis of PV/Thermal plus ground source heat pump systems for multi-family houses in a heating dominated climate, Solar Energy. 190 (2019) 44–62. https://doi.org/https://doi.org/10.1016/j.solener.2019.07.080.

[147] Y. Wang, Z. Quan, H. Jing, L. Wang, Y. Zhao, Performance and operation strategy optimization of a new dual-source building energy supply system with heat pumps and energy storage, Energy Conversion and Management. 239 (2021) 114204. https://doi.org/https://doi.org/10.1016/j.enconman.2021.114204.

[148] A. Pena-Bello, P. Schuetz, M. Berger, J. Worlitschek, M.K. Patel, D. Parra, Decarbonizing heat with PV-coupled heat pumps supported by electricity and heat storage: Impacts and trade-offs for prosumers and the grid, Energy Conversion and Management. 240 (2021) 114220. https://doi.org/https://doi.org/10.1016/j.enconman.2021.114220.

[149] R. Wang, W. Feng, L. Wang, S. Lu, A comprehensive evaluation of zero energy buildings in cold regions: Actual performance and key technologies of cases from China, the US, and the European Union, Energy. 215 (2021) 118992. https://doi.org/https://doi.org/10.1016/j.energy.2020.118992.

[150] B. Hadengue, E. Morgenroth, T.A. Larsen, L. Baldini, Performance and dynamics of active greywater heat recovery in buildings, Applied Energy. 305 (2022) 117677. https://doi.org/https://doi.org/10.1016/j.apenergy.2021.117677.

[151] S.B. Sepúlveda-Mora, S. Hegedus, Making the case for time-of-use electric rates to boost the value of battery storage in commercial buildings with grid connected PV systems, Energy. 218 (2021) 119447. https://doi.org/https://doi.org/10.1016/j.energy.2020.119447.

[152] M. Dongellini, C. Naldi, G.L. Morini, Influence of sizing strategy and control rules on the energy saving potential of heat pump hybrid systems in a residential building, Energy Conversion and Management. 235 (2021) 114022. https://doi.org/https://doi.org/10.1016/j.enconman.2021.114022.

[153] A. Heinz, R. Rieberer, Energetic and economic analysis of a PV-assisted air-to-water heat pump system for renovated residential buildings with high-temperature heat emission system, Applied Energy. 293 (2021) 116953. https://doi.org/https://doi.org/10.1016/j.apenergy.2021.116953.

[154] B. Chwieduk, D. Chwieduk, Analysis of operation and energy performance of a heat pump driven by a PV system for space heating of a single family house in polish conditions, Renewable Energy. 165 (2021) 117–126. https://doi.org/https://doi.org/10.1016/j.renene.2020.11.026.

[155] Y. Cui, J. Zhu, S. Twaha, S. Riffat, A comprehensive review on 2D and 3D models of vertical ground heat exchangers, Renewable and Sustainable Energy Reviews. 94 (2018) 84–114. https://doi.org/https://doi.org/10.1016/j.rser.2018.05.063.

[156] A. Thür, T. Calabrese, W. Streicher, Smart grid and PV driven ground heat pump as thermal battery in small buildings for optimized electricity consumption, Solar Energy. 174 (2018) 273–285. https://doi.org/https://doi.org/10.1016/j.solener.2018.08.087.

[157] E.I. Sakellariou, P.J. Axaopoulos, A.J. Wright, Energy and economic evaluation of a solar assisted ground source heat pump system for a north Mediterranean city, Energy and Buildings. 231 (2021) 110640. https://doi.org/https://doi.org/10.1016/j.enbuild.2020.110640.

[158] L. Lamarche, S. Kajl, B. Beauchamp, A review of methods to evaluate borehole thermal resistances in geothermal heat-pump systems, Geothermics. 39 (2010) 187–200. https://doi.org/https://doi.org/10.1016/j.geothermics.2010.03.003.

[159] A. Pan, L. Lu, P. Cui, L. Jia, A new analytical heat transfer model for deep borehole heat exchangers with coaxial tubes, International Journal of Heat and Mass Transfer. 141 (2019) 1056–1065. https://doi.org/https://doi.org/10.1016/j.ijheatmasstransfer.2019.07.041.

[160] M. Ahmadfard, M. Bernier, A review of vertical ground heat exchanger sizing tools including an inter-model comparison, Renewable and Sustainable Energy Reviews. 110 (2019) 247–265. https://doi.org/https://doi.org/10.1016/j.rser.2019.04.045.

[161] C. Fraga, P. Hollmuller, S. Schneider, B. Lachal, Heat pump systems for multifamily buildings: Potential and constraints of several heat sources for diverse building demands, Applied Energy. 225 (2018) 1033–1053. https://doi.org/https://doi.org/10.1016/j.apenergy.2018.05.004.

[162] H. Chen, S.B. Riffat, Y. Fu, Experimental study on a hybrid photovoltaic/heat pump system, Applied Thermal Engineering. 31 (2011) 4132–4138. https://doi.org/https://doi.org/10.1016/j.applthermaleng.2011.08.027.

[163] R. Thygesen, B. Karlsson, Simulation and analysis of a solar assisted heat pump system with two different storage types for high levels of PV electricity self-consumption, Solar Energy. 103 (2014) 19–27. https://doi.org/https://doi.org/10.1016/j.solener.2014.02.013.

[164] C. Naranjo-Mendoza, M.A. Oyinlola, A.J. Wright, R.M. Greenough, Experimental study of a domestic solar-assisted ground source heat pump with seasonal underground thermal energy storage through shallow boreholes, Applied Thermal Engineering. 162 (2019) 114218. https://doi.org/https://doi.org/10.1016/j.applthermaleng.2019.114218.

[165] L. Belussi, B. Barozzi, A. Bellazzi, L. Danza, A. Devitofrancesco, C. Fanciulli, M. Ghellere, G. Guazzi, I. Meroni, F. Salamone, F. Scamoni, C. Scrosati, A review of performance of zero energy buildings and energy efficiency solutions, Journal of Building Engineering. 25 (2019) 100772. https://doi.org/https://doi.org/10.1016/j.jobe.2019.100772.

[166] R. Smith, Chemical process: design and integration, John Wiley & Sons, 2005.

[167] I.C. Kemp, Pinch Analysis and Process Integration, Second, Elsevier, Oxford, 2007.

[168] P.Y. Lee, P.Y. Liew, T.G. Walmsley, S.R. Wan Alwi, J.J. Klemeš, Total Site Heat and Power Integration for Locally Integrated Energy Sectors, Energy. 204 (2020) 117959. https://doi.org/https://doi.org/10.1016/j.energy.2020.117959.

[169] S.M. Hosseinnia, H. Akbari, M. Sorin, Numerical analysis of thermocline evolution during charging phase in a stratified thermal energy storage tank, Journal of Energy Storage. 40 (2021). https://doi.org/10.1016/j.est.2021.102682.

[170] S.M. Hosseinnia, M. Sorin, Numerical approach for sizing vertical ground heat exchangers based on constant design load and desired outlet temperature, Journal of

Building Engineering. 48 (2022) 103932. https://doi.org/https://doi.org/10.1016/j.jobe.2021.103932.

[171] H. Elhegazy, M.M.M. Eid, A state-of-the-art-review on grey water management: A survey from 2000 to 2020s, Water Science and Technology. 82 (2020) 2786–2797. https://doi.org/10.2166/wst.2020.549.

[172] A. Bonkaney, S. Madougou, R. Adamou, Impacts of Cloud Cover and Dust on the Performance of Photovoltaic Module in Niamey, Journal of Renewable Energy. 2017 (2017) 9107502. https://doi.org/10.1155/2017/9107502.

[173] T. Ma, Z. Guo, L. Shen, X. Liu, Z. Chen, Y. Zhou, X. Zhang, Performance modelling of photovoltaic modules under actual operating conditions considering loss mechanism and energy distribution, Applied Energy. 298 (2021) 117205. https://doi.org/https://doi.org/10.1016/j.apenergy.2021.117205.

[174] J.A. Duffie, W.A. Beckman, Solar Engineering of Thermal Processes: Fourth Edition, 2013. https://doi.org/10.1002/9781118671603.

[175] S. Heibati, W. Maref, H.H. Saber, Developing a model for predicting optimum daily tilt angle of a PV solar system at different geometric, physical and dynamic parameters, Advances in Building Energy Research. 15 (2021) 179–198. https://doi.org/10.1080/17512549.2019.1684366.

[176] J.F. Horn, P.H. Scharf, Design Considerations for Heat Pump Compressors, International Compressor Engineering Conference. (1976) 194–201.

[177] A.G. Devecioğlu, V. Oruç, Energetic performance analysis of R466A as an alternative to R410A in VRF systems, Engineering Science and Technology, an International Journal. 23 (2020) 1425–1433. https://doi.org/https://doi.org/10.1016/j.jestch.2020.04.003.

[178] L.W. Gold, Influence of surface conditions on ground temperature, Canadian Journal of Earth Sciences. 4 (1967) 199–208.

[179] L. Aresti, P. Christodoulides, G.A. Florides, An investigation on the environmental impact of various Ground Heat Exchangers configurations, Renewable Energy. 171 (2021) 592–605. https://doi.org/https://doi.org/10.1016/j.renene.2021.02.120.

[180] V. Trillat-Berdal, B. Souyri, G. Fraisse, Experimental study of a ground-coupled heat pump combined with thermal solar collectors, Energy and Buildings. 38 (2006) 1477–1484. https://doi.org/https://doi.org/10.1016/j.enbuild.2006.04.005.

[181] M. Ouzzane, P. Eslami-Nejad, M. Badache, Z. Aidoun, New correlations for the prediction of the undisturbed ground temperature, Geothermics. 53 (2015) 379–384. https://doi.org/https://doi.org/10.1016/j.geothermics.2014.08.001.

[182] M. Ouzzane, P. Eslami-Nejad, Z. Aidoun, L. Lamarche, Analysis of the convective heat exchange effect on the undisturbed ground temperature, Solar Energy. 108 (2014) 340–347. https://doi.org/https://doi.org/10.1016/j.solener.2014.07.015.

[183] Natural Resources Canada, Energy Efficiency Trends Analysis Tables, residential Sector-Energy Uses Analysis for 2018, (n.d.).

[184] M. Soltani, F. M. Kashkooli, A.R. Dehghani-Sanij, A.R. Kazemi, N. Bordbar, M.J. Farshchi, M. Elmi, K. Gharali, M. B. Dusseault, A comprehensive study of geothermal heating and cooling systems, Sustainable Cities and Society. 44 (2019) 793–818. https://doi.org/https://doi.org/10.1016/j.scs.2018.09.036.

[185] P. Eslami-Nejad, M. Ouzzane, Z. Aidoun, Modeling of a two-phase CO2-filled vertical borehole for geothermal heat pump applications, Applied Energy. 114 (2014) 611–620. https://doi.org/https://doi.org/10.1016/j.apenergy.2013.10.028.

[186] A. Bastani, P. Eslami-Nejad, M. Badache, A.T.A. Nguyen, Experimental characterization of a transcritical CO2 direct expansion ground source heat pump for heating applications, Energy and Buildings. 212 (2020) 109828. https://doi.org/https://doi.org/10.1016/j.enbuild.2020.109828.

[187] H. Esen, M. Inalli, Y. Esen, Temperature distributions in boreholes of a vertical ground-coupled heat pump system, Renewable Energy. 34 (2009) 2672–2679. https://doi.org/https://doi.org/10.1016/j.renene.2009.04.032.

[188] G. Emmi, A. Zarrella, M. De Carli, M. Donà, A. Galgaro, Energy performance and cost analysis of some borehole heat exchanger configurations with different heat-carrier fluids in mild climates, Geothermics. 65 (2017) 158–169. https://doi.org/https://doi.org/10.1016/j.geothermics.2016.09.006.

[189] X. Meng, Z. Han, H. Hu, H. Zhang, X. Li, Studies on the performance of ground source heat pump affected by soil freezing under groundwater seepage, Journal of Building Engineering. 33 (2021) 101632. https://doi.org/https://doi.org/10.1016/j.jobe.2020.101632.

[190] L. Zhang, Q. Zhang, G. Huang, Y. Du, A p(t)-linear average method to estimate the thermal parameters of the borehole heat exchangers for in situ thermal response test,

Applied Energy. 131 (2014) 211–221. https://doi.org/https://doi.org/10.1016/j.apenergy.2014.06.031.

[191] C. Zhang, H. Xu, J. Fan, P. Sun, S. Sun, X. Kong, The coupled two-step parameter estimation procedure for borehole thermal resistance in thermal response test, Renewable Energy. 154 (2020) 672–683. https://doi.org/10.1016/j.renene.2020.03.019.

[192] J.A. Rivera, P. Blum, P. Bayer, A finite line source model with Cauchy-type top boundary conditions for simulating near surface effects on borehole heat exchangers, Energy. 98 (2016) 50–63. https://doi.org/https://doi.org/10.1016/j.energy.2015.12.129.

[193] X. Zhang, T. Zhang, B. Li, Y. Jiang, Comparison of Four Methods for Borehole Heat Exchanger Sizing Subject to Thermal Response Test Parameter Estimation, Energies . 12 (2019). https://doi.org/10.3390/en12214067.

[194] S. Javed, J.D. Spitler, Calculation of borehole thermal resistance, in: Advances in Ground-Source Heat Pump Systems, 2016: pp. 63–95. https://doi.org/10.1016/B978-0-08-100311-4.00003-0.

[195] J.D. Spitler, M. Bernier, Vertical borehole ground heat exchanger design methods, in: Advances in Ground-Source Heat Pump Systems, 2016: pp. 29–61. https://doi.org/10.1016/B978-0-08-100311-4.00002-9.

[196] S. Kavanaugh, K. Rafferty, Geothermal heating and cooling design of ground source heat pump systems, 2nd ed., ASHRAE, 2014.

[197] L.R. Ingersoll, O.J. Zobel, A.C. Ingersoll, Heat Conduction with Engineering, Geological, and Other Applications, 2nd ed., McGraw Hill, New York, 1955. https://doi.org/10.1063/1.3061951.

[198] H. Zeng, N. Diao, Z. Fang, Heat transfer analysis of boreholes in vertical ground heat exchangers, International Journal of Heat and Mass Transfer. 46 (2003) 4467–4481. https://doi.org/https://doi.org/10.1016/S0017-9310(03)00270-9.

[199] E.M. Salilih, N.H. Abu-Hamdeh, H.F. Oztop, Analysis of double U-tube ground heat exchanger for renewable energy applications with two-region simulation model by combining analytical and numerical techniques, International Communications in Heat and Mass Transfer. 123 (2021). https://doi.org/10.1016/j.icheatmasstransfer.2021.105144.

[200] E.D. Kerme, A.S. Fung, Heat transfer simulation, analysis and performance study of single U-tube borehole heat exchanger, Renewable Energy. 145 (2020) 1430–1448. https://doi.org/10.1016/j.renene.2019.06.004.

[201] M. Cimmino, Fluid and borehole wall temperature profiles in vertical geothermal boreholes with multiple U-tubes, Renewable Energy. 96 (2016) 137–147. https://doi.org/https://doi.org/10.1016/j.renene.2016.04.067.

[202] A.A. Serageldin, Y. Sakata, T. Katsura, K. Nagano, Thermo-hydraulic performance of the U-tube borehole heat exchanger with a novel oval cross-section: Numerical approach, Energy Conversion and Management. 177 (2018) 406–415. https://doi.org/https://doi.org/10.1016/j.enconman.2018.09.081.

[203] A.A. Serageldin, Y. Sakata, T. Katsura, K. Nagano, Performance enhancement of borehole ground source heat pump using single U-tube heat exchanger with a novel oval cross-section (SUO) and a novel spacer, Sustainable Energy Technologies and Assessments. 42 (2020) 100805. https://doi.org/https://doi.org/10.1016/j.seta.2020.100805.

[204] H. Zhang, Z. Han, X. Li, M. Ji, X. Zhang, G. Li, L. Yang, Study on the influence of borehole spacing considering groundwater flow and freezing factors on the annual performance of the ground source heat pump, Applied Thermal Engineering. 182 (2021) 116042. https://doi.org/https://doi.org/10.1016/j.applthermaleng.2020.116042.

[205] H. Fatahian, H. Taherian, H. Salarian, E. Fatahian, Thermal performance of a ground heat exchanger in a cold climate: a CFD study, European Physical Journal Plus. 136 (2021). https://doi.org/10.1140/epjp/s13360-021-01265-7.

[206] A. Sharma, R.D. Jilte, S. Dogra, Performance evaluation of ground heat exchanger using novel spirally corrugated pipe geometry - A CFD approach, in: AIP Conference Proceedings, 2020. https://doi.org/10.1063/5.0026240.

[207] A. Jahanbin, Thermal performance of the vertical ground heat exchanger with a novel elliptical single U-tube, Geothermics. 86 (2020). https://doi.org/10.1016/j.geothermics.2020.101804.

[208] A. Jahanbin, G. Semprini, A.N. Impiombato, C. Biserni, E.R. Di Schio, Effects of the circuit arrangement on the thermal performance of double U-tube ground heat exchangers, Energies (Basel). 13 (2020). https://doi.org/10.3390/en13123275.

[209] L. Pu, D. Qi, K. Li, H. Tan, Y. Li, Simulation study on the thermal performance of vertical U-tube heat exchangers for ground source heat pump system, Applied Thermal Engineering. 79 (2015) 202–213. https://doi.org/https://doi.org/10.1016/j.applthermaleng.2014.12.068.

[210] D. Qi, L. Pu, Z. Ma, L. Xia, Y. Li, Effects of ground heat exchangers with different connection configurations on the heating performance of GSHP systems, Geothermics. 80 (2019) 20–30. https://doi.org/https://doi.org/10.1016/j.geothermics.2019.02.002.

[211] A. Bejan, Convection Heat Transfer: Fourth Edition, 2013. https://doi.org/10.1002/9781118671627.

[212] S.B. Pope, S.B. Pope, Turbulent Flows, Cambridge University Press, 2000.

[213] V. Hernandez-Perez, M. Abdulkadir, B.J. Azzopardi, Grid Generation Issues in the CFD Modelling of Two-Phase Flow in a Pipe, The Journal of Computational Multiphase Flows. 3 (2011) 13–26. https://doi.org/10.1260/1757-482X.3.1.13.

[214] N. Aranzabal, J. Martos, M. Stokuca, W. Mazzotti Pallard, J. Acuña, J. Soret, P. Blum, Novel instruments and methods to estimate depth-specific thermal properties in borehole heat exchangers, Geothermics. 86 (2020) 101813. https://doi.org/https://doi.org/10.1016/j.geothermics.2020.101813.

[215] K. Zhou, J. Mao, Y. Li, H. Zhang, Performance assessment and techno-economic optimization of ground source heat pump for residential heating and cooling: A case study of Nanjing, China, Sustainable Energy Technologies and Assessments. 40 (2020) 100782. https://doi.org/https://doi.org/10.1016/j.seta.2020.100782.

[216] Z. Han, M. Zheng, F. Kong, F. Wang, Z. Li, T. Bai, Numerical simulation of solar assisted ground-source heat pump heating system with latent heat energy storage in severely cold area, Applied Thermal Engineering. 28 (2008) 1427–1436. https://doi.org/https://doi.org/10.1016/j.applthermaleng.2007.09.013.

[217] G. Emmi, A. Zarrella, M. De Carli, A. Galgaro, An analysis of solar assisted ground source heat pumps in cold climates, Energy Conversion and Management. 106 (2015) 660–675. https://doi.org/https://doi.org/10.1016/j.enconman.2015.10.016.

[218] H. Monteyne, M. Lazova, Ö. Bağci, F. Luyckx, M. de Paepe, Depletion and regeneration behaviour of a large solar-assisted ground source heat pump system (SAGSHP) for 156 units multi-dwelling, in: Building Simulation Conference Proceedings, 2017: pp. 1460–1469. https://doi.org/10.26868/25222708.2017.803.

[219] Y. Shimada, K. Tokimatsu, T. Asawa, Y. Uchida, A. Tomigashi, H. Kurishima, Subsurface utilization as a heat sink for large-scale ground source heat pump: Case study in Bangkok, Thailand, Renewable Energy. 180 (2021) 966–979. https://doi.org/https://doi.org/10.1016/j.renene.2021.08.116.

[220] R. Lazzarin, Heat pumps and solar energy: A review with some insights in the future, International Journal of Refrigeration. 116 (2020) 146–160. https://doi.org/https://doi.org/10.1016/j.ijrefrig.2020.03.031.

[221] A. James, M. Mohanraj, M. Srinivas, S. Jayaraj, Thermal analysis of heat pump systems using photovoltaic-thermal collectors: a review, Journal of Thermal Analysis and Calorimetry. 144 (2021) 1–39. https://doi.org/10.1007/s10973-020-09431-2.

[222] J. Yao, W. Liu, L. Zhang, B. Tian, Y. Dai, M. Huang, Performance analysis of a residential heating system using borehole heat exchanger coupled with solar assisted PV/T heat pump, Renewable Energy. 160 (2020) 160–175. https://doi.org/https://doi.org/10.1016/j.renene.2020.06.101.

[223] E.I. Sakellariou, P.J. Axaopoulos, Energy performance indexes for solar assisted ground source heat pump systems with photovoltaic-thermal collectors, Applied Energy. 272 (2020) 115241. https://doi.org/https://doi.org/10.1016/j.apenergy.2020.115241.

[224] E.I. Sakellariou, A.J. Wright, P. Axaopoulos, M.A. Oyinlola, PVT based solar assisted ground source heat pump system: Modelling approach and sensitivity analyses, Solar Energy. 193 (2019) 37–50. https://doi.org/https://doi.org/10.1016/j.solener.2019.09.044.

[225] E.I. Sakellariou, A.J. Wright, P.J. Axaopoulos, Energy, economic and emission assessment of a solar assisted shallow earth borehole field heat pump system for domestic space heating in a north European climate, Geothermics. 95 (2021). https://doi.org/10.1016/j.geothermics.2021.102159.

[226] N. Naili, S. Kooli, Solar-assisted ground source heat pump system operated in heating mode: A case study in Tunisia, Renewable and Sustainable Energy Reviews. 145 (2021) 111144. https://doi.org/https://doi.org/10.1016/j.rser.2021.111144.

[227] G. Emmi, S. Bordignon, A. Zarrella, M. De Carli, A dynamic analysis of a SAGSHP system coupled to solar thermal collectors and photovoltaic-thermal panels under different climate conditions, Energy Conversion and Management. 213 (2020). https://doi.org/10.1016/j.enconman.2020.112851.

[228] A. Mehrpanahi, M. Arbabtafti, M.S. Karimi Dastenae, Extraction of optimal SAGSHP sizing based on the various control logic in specific climate condition, Solar Energy. 190 (2019) 576–595. https://doi.org/10.1016/j.solener.2019.08.053.

[229] V. Verma, K. Murugesan, Experimental study of solar assisted ground source heat pump system during space heating operation from morning to evening, Journal of Mechanical

Science and Technology. 32 (2018) 391–398. https://doi.org/10.1007/s12206-017-1239-1.

[230] Y. Ji, L. Duanmu, X. Li, M. Airaksinen, Z. Wang, Simplified method to determine the collector area of solar-assisted ground-source heat pump system, in: Procedia Engineering, 2017: pp. 1138–1145. https://doi.org/10.1016/j.proeng.2017.10.420.

[231] S.M. Hosseinnia, M. Sorin, Energy targeting approach for optimum solar assisted ground source heat pump integration in buildings, Energy. (2022) 123528. https://doi.org/https://doi.org/10.1016/j.energy.2022.123528.

[232] M. Chantal, A. Zoughaib, D. Clodic, Integration of heat pump in district heating and cooling systems, in: Proceedings of the 23rd International Conference on Efficiency, Cost, Optimization, Simulation, and Environmental Impact of Energy Systems, ECOS 2010, 2010: pp. 189–195.

[233] A. Bertrand, R. Aggoune, F. Maréchal, In-building waste water heat recovery: An urban-scale method for the characterisation of water streams and the assessment of energy savings and costs, Applied Energy. 192 (2017) 110–125. https://doi.org/10.1016/j.apenergy.2017.01.096.

[234] S. De-León Almaraz, M. Boix, L. Montastruc, C. Azzaro-Pantel, Z. Liao, S. Domenech, Design of a water allocation and energy network for multi-contaminant problems using multi-objective optimization, Process Safety and Environmental Protection. 103 (2016) 348–364. https://doi.org/https://doi.org/10.1016/j.psep.2016.03.015.

[235] K. Jamaluddin, S.R. Wan Alwi, K. Hamzah, J.J. Klemeš, A Numerical Pinch Analysis Methodology for Optimal Sizing of a Centralized Trigeneration System with Variable Energy Demands, Energies . 13 (2020). https://doi.org/10.3390/en13082038.

[236] Y. Xu, G. Cui, X. Han, Y. Xiao, G. Zhang, Optimization route arrangement: A new concept to achieve high efficiency and quality in heat exchanger network synthesis, International Journal of Heat and Mass Transfer. 178 (2021) 121622. https://doi.org/https://doi.org/10.1016/j.ijheatmasstransfer.2021.121622.

[237] Y. Zhuang, Y. Xing, L. Zhang, L. Liu, J. Du, S. Shen, An enhanced superstructure-based model for work-integrated heat exchange network considering inter-stage multiple utilities optimization, Computers & Chemical Engineering. 152 (2021) 107388. https://doi.org/https://doi.org/10.1016/j.compchemeng.2021.107388.

[238] R. Toffanin, V. Curti, M.C. Barbato, Impact of Legionella regulation on a 4th generation district heating substation energy use and cost: the case of a Swiss single-family

household, Energy. 228 (2021) 120473. https://doi.org/https://doi.org/10.1016/j.energy.2021.120473.

[239] E.A. Pina, M.A. Lozano, J.C. Ramos, L.M. Serra, Tackling thermal integration in the synthesis of polygeneration systems for buildings, Applied Energy. 269 (2020) 115115. https://doi.org/https://doi.org/10.1016/j.apenergy.2020.115115.

[240] S.T. Taleghani, M. Sorin, S. Gaboury, Thermo-economic analysis of heat-driven ejector system for cooling smelting process exhaust gas, Energy. 220 (2021) 119661. https://doi.org/https://doi.org/10.1016/j.energy.2020.119661.

[241] RenewAbility Energy Inc., R4-70 Drain Water Heat Recovery, (n.d.). https://canada.renewability.com/products/r4-72 (accessed January 5, 2022).

[242] Y. Xu, C. Mao, Y. Huang, X. Shen, X. Xu, G. Chen, Performance evaluation and multi-objective optimization of a low-temperature CO2 heat pump water heater based on artificial neural network and new economic analysis, Energy. 216 (2021) 119232. https://doi.org/https://doi.org/10.1016/j.energy.2020.119232.

[243] V. Jain, G. Sachdeva, S.S. Kachhwaha, Energy, exergy, economic and environmental (4E) analyses based comparative performance study and optimization of vapor compression-absorption integrated refrigeration system, Energy. 91 (2015) 816–832. https://doi.org/https://doi.org/10.1016/j.energy.2015.08.041.

[244] R. Cozzolino, D. Chiappini, L. Tribioli, Off-grid PV/URFC power plant fueled with biogas from food waste: An energetic and economic analysis, Energy. 219 (2021) 119537. https://doi.org/https://doi.org/10.1016/j.energy.2020.119537.

[245] A.A. Kebede, T. Coosemans, M. Messagie, T. Jemal, H.A. Behabtu, J. van Mierlo, M. Berecibar, Techno-economic analysis of lithium-ion and lead-acid batteries in stationary energy storage application, Journal of Energy Storage. 40 (2021) 102748. https://doi.org/https://doi.org/10.1016/j.est.2021.102748.

[246] A. Jaiswal, Lithium-ion battery based renewable energy solution for off-grid electricity: A techno-economic analysis, Renewable and Sustainable Energy Reviews. 72 (2017) 922–934. https://doi.org/https://doi.org/10.1016/j.rser.2017.01.049.

[247] S. Dhundhara, Y.P. Verma, A. Williams, Techno-economic analysis of the lithium-ion and lead-acid battery in microgrid systems, Energy Conversion and Management. 177 (2018) 122–142. https://doi.org/https://doi.org/10.1016/j.enconman.2018.09.030.

[248] F.A. v Biggins, S. Homan, D. Roberts, S. Brown, Exploring the economics of large scale lithium ion and lead acid batteries performing frequency response, Energy Reports. 7 (2021) 34–41. https://doi.org/https://doi.org/10.1016/j.egyr.2021.02.058.

[249] E. Tervo, K. Agbim, F. DeAngelis, J. Hernandez, H.K. Kim, A. Odukomaiya, An economic analysis of residential photovoltaic systems with lithium ion battery storage in the United States, Renewable and Sustainable Energy Reviews. 94 (2018) 1057–1066. https://doi.org/https://doi.org/10.1016/j.rser.2018.06.055.

[250] W. Zheng, K. Ma, X. Wang, Exploiting thermal energy storage to reduce data center capital and operating expenses, in: 2014 IEEE 20th International Symposium on High Performance Computer Architecture (HPCA), 2014: pp. 132–141. https://doi.org/10.1109/HPCA.2014.6835924.

[251] I. Khamlich, K. Zeng, G. Flamant, J. Baeyens, C. Zou, J. Li, X. Yang, X. He, Q. Liu, H. Yang, Q. Yang, H. Chen, Technical and economic assessment of thermal energy storage in concentrated solar power plants within a spot electricity market, Renewable and Sustainable Energy Reviews. 139 (2021) 110583. https://doi.org/https://doi.org/10.1016/j.rser.2020.110583.

[252] C. Bernath, G. Deac, F. Sensfuß, Impact of sector coupling on the market value of renewable energies – A model-based scenario analysis, Applied Energy. 281 (2021) 115985. https://doi.org/https://doi.org/10.1016/j.apenergy.2020.115985.

[253] A. Freyre, S. Klinke, M.K. Patel, Carbon tax and energy programs for buildings: Rivals or allies?, Energy Policy. 139 (2020) 111218. https://doi.org/https://doi.org/10.1016/j.enpol.2019.111218.

[254] J.R. Lizárraga-Morazán, G. Martínez-Rodríguez, A.L. Fuentes-Silva, M. Picón-Núñez, Selection of solar collector network design for industrial applications subject to economic and operation criteria, Energy & Environment. 32 (2020) 1504–1523. https://doi.org/10.1177/0958305X20927375.

[255] R.W. Moss, P. Henshall, F. Arya, G.S.F. Shire, T. Hyde, P.C. Eames, Performance and operational effectiveness of evacuated flat plate solar collectors compared with conventional thermal, PVT and PV panels, Applied Energy. 216 (2018) 588–601. https://doi.org/https://doi.org/10.1016/j.apenergy.2018.01.001.

[256] S.M. Hosseinnia, M. Sorin, A dynamic pinch approach for optimum solar assisted ground source heat pump integration in buildings: Energy targeting, (2021) Manuscript submitted for publication.